
Université catholique de Louvain
Faculté d'ingénierie biologique, agronomique et environnementale
Earth and Life Institute - Environmental Sciences

# Soil water content estimation using ground-based active and passive microwave remote sensing

## Ground-penetrating radar and radiometer

François Jonard

Août 2012

Thèse présentée en vue de l'obtention
du grade de docteur en sciences agronomiques
et ingénierie biologique

Jury members:

| | |
|---|---|
| President: | Prof. Jacques Mahillon (UCL, Belgium) |
| Supervisor: | Prof. Sébastien Lambot (UCL, Belgium) |
| Readers: | Prof. Harry Vereecken (FZJ, Germany) |
| | Prof. Pierre Defourny (UCL, Belgium) |
| | Dr. Lutz Weihermüller (FZJ, Germany) |
| | Dr. Thierry Pellarin (LTHE, France) |

*Imagination is more important than knowledge.*
*Knowledge is limited, whereas imagination embraces the entire world,*
*stimulating progress, giving birth to evolution.*
*It is a real factor in scientific research.*

Albert Einstein

# Acknowledgements

The PhD research presented in this dissertation was carried out from March 2009 to March 2012 at Forschungszentrum Jülich (Germany) within the research group "Non-Invasive Methods in Bio-Geosystems" of the Institute of Bio- and Geosciences – Agrosphere. The research project was funded by the German Research Foundation (DFG) through Transregional Collaborative Research Centre 32.

First, I wish to express my warmest thanks to my supervisor, Prof. Sébastien Lambot, for his trust in me and for giving me the opportunity to pursue a PhD in his research group. I thank him for introducing me to the exciting field of hydrogeophysics and for sharing his valuable scientific knowledge. His enthusiasm and his constructive ideas greatly helped me during the PhD process.

I would also like to thank Prof. Harry Vereecken, Director of the Agrosphere Institute of Forschungszentrum Jülich. I am grateful to him for his constant support and guidance, for the very nice working environment and facilities at Forschungszentrum Jülich, and for giving me the opportunity to collaborate with many people and institutions.

I also want to convey a special word of gratitude to Lutz Weihermüller for his valuable help and expert advice throughout the PhD project. It was a pleasure to work with him. His availability and his optimism always helped me through difficulties that I encountered along the way. Many thanks for the time spent discussing my work, solving problems, and supporting me with setting up the field experiments at the TERENO test site in Selhausen.

I would like to thank Peggy O'Neill for welcoming me at NASA in the Hydrological Sciences Branch of Goddard Space Flight Center in Greenbelt (USA) during the period from March to June 2011. I enjoyed working with her in the context of the upcoming Soil Moisture Active and Passive (SMAP) mission. I look forward to continue collaboration with her in the future.

This PhD research has greatly benefitted from the expertise of Mike Schwank, who introduced me to the microwave radiometry community. I thank him for his formative support and for the interesting discussions during his visits to Forschungszentrum Jülich.

I also wish to express my thanks to Prof. Pierre Defourny and Thierry Pellarin, who agreed to read my thesis, as well as to the anonymous reviewers for the time they spent engaging with and commenting on my work. Their comments and suggestions have helped to greatly improve different chapters of this thesis.

I am also very grateful to my colleagues Khan Zaib Jadoon, Marin Dimitrov, Xinxin Li, Normen Hermes, Rainer Harms, Frédéric André, and Stephan Sittig for their support and the pleasant atmosphere during my research period in Germany, and I thank Mehmet Kurum and Alicia Joseph for welcoming me in the United States.

I would like to express my thanks to my parents and my brother for the love, support, and encouragement they have given me over the years.

Finally, I want to reserve a special thanks to my wonderful wife and son for helping me to achieve my project and for their love, affection, and unflagging support!

# Contents

# Abbreviations

| | |
|---|---|
| AIEM | Advanced integral equation model |
| CT | Conventional tillage |
| D-GPS | Differential global positioning system |
| DL | Deep loosening tillage |
| EC | Electrical conductivity |
| $EC_a$ | Apparent electrical conductivity |
| EMI | Electromagnetic induction |
| ERT | Electrical resistance tomography |
| ESA | European Space Agency |
| GIS | Geographic information systems |
| GMCS | Global multilevel coordinate search |
| GPR | Ground-penetrating radar |
| H | Horizontal [polarization] |
| HH | Like-polarized horizontal transmit, horizontal receive [polarization] |
| HV | Cross-polarized horizontal transmit, vertical receive [polarization] |
| IEM | Integral equation model |
| IHS | Intensity-hue-saturation |
| IR | Infrared |
| LAI | Leaf area index |
| MPDI | Microwave polarization difference index |
| MPDT | Microwave polarization difference temperatures |
| MR | Microwave radiometer |
| MVI | Microwave vegetation index |
| NASA | National Aeronautics and Space Administration |
| NDVI | Normalized difference vegetation index |
| NMS | Nelder-Mead simplex |
| PCA | Principal component analysis |
| PEC | Perfect electrical conductor |
| RFI | Radio frequency interference |
| RMSE | Root mean square error |
| RT | Reduced tillage |
| SAR | Synthetic aperture radar |
| SFCW | Stepped-frequency continuous-wave |
| STD | Standard deviation |
| SWC | Soil water content |
| TDR | Time-domain reflectometry |
| TE | Transverse electric |
| TEM | Transverse electromagnetic |
| TM | Transverse magnetic |
| UWB | Ultra-wideband |
| V | Vertical [polarization] |
| VH | cross-polarized vertical transmit, horizontal receive [polarization] |

| | |
|---|---|
| VNA | Vector network analyzer |
| VOD | Vegetation optical depth |
| VV | Like-polarized vertical transmit, vertical receive [polarization] |
| VWC | Vegetation water content |
| 3D | Three-dimensional |

**List of remote sensing system acronyms**

| | |
|---|---|
| AirSAR | NASA's Airborne Synthetic Aperture Radar |
| ALOS | Advanced Land Observing Satellite |
| AMSR-E | Advanced Microwave Scanning Radiometer aboard AQUA |
| AQUA | NASA Earth Science satellite mission, which is part of the Earth Observing System (EOS) |
| AQUARIUS | NASA's sea surface salinity mission aboard SAC-D |
| ASAR | Advanced Synthetic Aperture Radar aboard ENVISAT |
| ASCAT | Advanced Scatterometer aboard MetOp |
| AVIRIS | Airborne Visible and Infrared Imaging Spectrometer |
| Coriolis | American Earth and space observation satellite |
| COSMO-SkyMed | Constellation of small Satellites for Mediterranean basin Observation |
| EnMAP | German hyperspectral Environmental Mapping and Analysis Program |
| ENVISAT | ESA's Environmental Satellite |
| ERS-1 & 2 | European Remote Sensing satellite 1 and 2 |
| FORMOSAT-2 | Taiwan Earth imaging satellite 2 |
| JERS-1 | Japanese Earth Resources Satellite 1 |
| Landsat ETM+ | Landsat Enhanced Thematic Mapper Plus aboard Landsat 7 |
| Landsat TM | Landsat Thematic Mapper aboard Landsat 5 |
| MERIS | Medium Resolution Imaging Spectrometer aboard ENVISAT |
| MetOp | A series of three polar orbiting meteorological satellites |
| MIRAS | Microwave Imaging Radiometer with Aperture Synthesis aboard SMOS |
| MODIS | Moderate-resolution Imaging Spectroradiometer aboard AQUA |
| PALSAR | Phased Array type L-band SAR aboard ALOS |
| PBMR | Push-Broom Microwave Radiometer |
| PolInSAR | Polarimetric Interferometric SAR |
| PORTOS | Six-frequency radiometer of the Institut National de Recherches Agronomiques (INRA), France |
| QuickSCAT | NASA's Quick Scatterometer |
| RADARSAT-1 & 2 | Canadian Space Agency's Earth observation satellite 1 and 2 |
| RapidEye | System of 5 multi-spectral satellites |
| RASAM | Radiometer-Scatterometer to measure microwave signatures of soil, vegetation and snow |
| SAC-D | Satelite de Aplicaciones Cientificas-D (Satellite for Scientific Applications-D) |
| SeeWinds | Specialized microwave radar system aboard QuickSCAT |
| SIR-A | Shuttle Imaging Radar-A aboard the NASA Space Shuttle in 1981 |
| SIR-C/X SAR | Spaceborne Imaging Radar-C/X-Band Synthetic Aperture Radar aboard the NASA Space Shuttle in 1994 |
| SMAP | NASA's Soil Moisture Active Passive mission |
| SMOS | ESA's Soil Moisture and Ocean Salinity mission |
| SPOT | Satellite Pour l'Observation de la Terre (Satellite for Earth Observation) |
| SSM/I | Special Sensor Microwave/Imager |
| Tandem-L | Proposed L-band radar mission |
| TanDEM-X | TerraSAR-X add-on for Digital Elevation Measurement |
| TerraSAR-X | German X-band radar mission |
| WindSAT | Multi-channel multi-frequency microwave radiometer for ocean surface wind detection aboard Coriolis |

# Chapter 1

# Introduction

## 1.1 General context

Soil and groundwater resources are extremely important to maintain life on Earth. Sustainable management of these resources is therefore a major global challenge. Recent developments of agriculture, industry, and infrastructures have significantly increased the pressure on our environment. In agriculture, soil and water resources play a key role to sustain food production. Only 3% of the water on Earth is fresh water, including about 2% of frozen water in glaciers and polar ice caps. Irrigated agriculture, which represents 8% of cropland (i.e., about 277 million hectares) and 40% of the crop production throughout the world, accounts for about 70–75% of global fresh water withdrawals (FAO, 2011). Irrigation of cropland has allowed us to greatly increase agricultural productivity but has also lead to major environmental problems such as soil erosion, groundwater depletion and pollution, and salinization. With the increasing needs of the human population and the expected climate change, a safe and effective use of the subsurface natural resources is the main challenge for our society in the coming years. This could only be achieved by a better understanding of the subsurface environment (Rubin and Hubbard, 2005).

Soil water content is a soil physical state variable which is defined as the water contained in the unsaturated soil zone or vadose zone. Knowledge of soil water content (SWC) is hereby essential as it represents a key variable in many hydrological, climatological, and environmental processes. In hydrology, SWC plays a major role in the water cycle by partitioning rainfall into runoff and infiltration (Tramblay *et al.*, 2010) and by controlling hydrological fluxes such as groundwater recharge. SWC is also a key variable of the climate system as it governs the energy fluxes between the land surface and the atmosphere trough its impact on evapotranspiration (Seneviratne *et al.*, 2006, 2010). In addition, soil water availability influences plant transpiration and photosynthesis, and therefore, has an important effect on the biogeochemical cycles (Jonard *et al.*, 2011a).

Determining the temporal and spatial variability of SWC is therefore essential for many scientific issues and applications (Famiglietti *et al.*, 2008). In

that respect, a large number of SWC sensing techniques have been used and developed in the last 50 years (Robinson *et al.*, 2008b; Vereecken *et al.*, 2008). The standard reference method to determine SWC is the gravimetric technique, which consists of extracting soil samples from the field. The samples are then weighted before and after drying in an oven at 105°C for 24 hours to derive their water content. The amount of water in the soil is classically expressed as volumetric ($m^3$ of water per $m^3$ of soil) or gravimetric (g of water per g of soil) water content. The gravimetric method is the only direct measurement technique but several indirect techniques are also available to measure SWC (e.g., Wagner *et al.*, 2007; Robinson *et al.*, 2008b; Vereecken *et al.*, 2008; Seneviratne *et al.*, 2010). The indirect methods can be distinguished according, for instance, to their spatial extent, namely local scale, field scale, and regional or global scale.

### 1.1.1 Local soil water content sensors

Local indirect methods include mainly electromagnetic sensors, namely time-domain reflectometry (TDR) (Noborio, 2001; Topp *et al.*, 2003; Robinson *et al.*, 2003) and capacitance sensors (Dean *et al.*, 1987; Rosenbaum *et al.*, 2010; Mittelbach *et al.*, 2011). The TDR measurement principle is based on the propagation velocity of guided electromagnetic waves along a probe through the soil, which is dependant on the soil electromagnetic properties. As the dielectric permittivity of liquid water dominates the dielectric permittivity of other soil components, water is the principal factor governing electromagnetic wave propagation in the soil. Such as TDR, capacitance sensors are also based on the dependency of the soil dielectric permittivity on the SWC. Both TDR and capacitance sensors can perform non-destructive measurements of SWC over a wide range of soils and with a very high temporal resolution. However, these instruments are invasive methods, which are restricted to local observation areas ($<1$ $m^2$) and are not expected to be representative of the within field variability.

Other local methods are also available such as: neutron probes (Greacen, 1981; Yao *et al.*, 2004), which are based on the estimation of the number of hydrogen nuclei in soils; heat pulse sensors (Campbell *et al.*, 1991), which are based on the estimation of soil thermal properties; and fiber optic sensors relying on the attenuation or reflection of a light signal in the soil (Garrido *et al.*, 1999) or the characteristics of hydrophilic polymers (Texier *et al.*, 2005). Recently, an emerging new technology, the wireless sensor network using cluster of local sensors, appeared as a promising approach to monitor SWC over large areas and with a high temporal resolution, which is particularly useful for observing hydrological processes (Vereecken *et al.*, 2008; Ritsema *et al.*, 2009; Bogena *et al.*, 2010). However, given the small support scale of the sensors, i.e., the area or volume integrated by an individual measurement, and the relatively large spacing between them, these networks do not allow to reveal the local-scale SWC patterns.

### 1.1.2 Field-scale hydrogeophysical techniques

In the field of hydrogeophysics, electromagnetic induction (EMI) (McNeill, 1980; Pellerin, 2002; Reedy and Scanlon, 2003; Sherlock and McDonnell, 2003), electrical resistance tomography (ERT) (Kemna *et al.*, 2000; Michot *et al.*, 2003; Samouelian *et al.*, 2005; Basso *et al.*, 2011), and ground-penetrating radar (GPR) (Huisman *et al.*, 2003a; Annan, 2005; Lambot *et al.*, 2008a; Slob *et al.*, 2010) are increasingly used for field-scale characterization. EMI and ERT use an electric current to estimate the soil electrical conductivity (or resistivity), which depends simultaneously on different factors including mainly SWC, clay content, and salinity (Rhoades *et al.*, 1976; Corwin and Lesch, 2005; Friedman, 2005). However, since these parameters vary independently within a field, SWC can not be easily estimated from the electrical conductivity. GPR measures the travel time of electromagnetic waves through the ground to estimate the soil dielectric permittivity. In contrast to the TDR technique which uses guided electromagnetic waves along a probe, GPR uses unguided waves, which has the main advantage of allowing noninvasive quantification of soil properties and larger sampling volumes. However, the more complex behavior of unguided waves has limited the interpretation of GPR data. New promising geophysical technologies to characterize the SWC variability at the field scale have also been recently investigated such as the use of ground-based GPS receivers (Larson *et al.*, 2008), cosmic ray probes (Zreda *et al.*, 2008; Desilets *et al.*, 2010), and ground-based time-lapse relative gravity measurements (Naujoks *et al.*, 2010; Christiansen *et al.*, 2011), but their operationally is not yet demonstrated.

Amongst the geophysical techniques, GPR is of major interest to characterize the subsurface with a high resolution (Huisman *et al.*, 2003a; Lambot *et al.*, 2008a). During the last years, several techniques were developed to determine the SWC from GPR measurements. The most commonly used method is based on the analysis of the ground wave propagation velocity. The ground wave, which is the part of the radiated energy that travels from the transmitter to the receiver antenna through the top of the soil, can be identified using a multi-offset acquisition such as the wide angle reflection and refraction (WARR) or the common-midpoint (CMP) method (Huisman *et al.*, 2003a). In this case, the GPR antennas have to be in contact with the soil (on-ground GPR). Although the method has been extensively applied (van Overmeeren *et al.*, 1997; Grote *et al.*, 2003a; Huisman *et al.*, 2002; Grote *et al.*, 2003b; Weihermüller *et al.*, 2007; Steelman and Endres, 2010), accurate SWC estimates were only possible for relatively simple soil conditions (e.g., low clay content, absence of near-surface layering) allowing a clear identification of the ground wave. To overcome this limitation, Lambot *et al.* (2004c) proposed a full-wave forward and inverse modeling approach for off-ground GPR. The electromagnetic model is based on a three-dimensional (3D) solution of Maxwell's equations for waves propagating in multilayered media and on an antenna model based on frequency-dependent transfer functions that also account for antenna-soil interactions. Although this GPR model appeared to accurately reproduce the radar measurements in laboratory experiments (Lambot *et al.*, 2004c, 2006c) and was successfully applied to identify and map surface SWC in the field (Weihermüller *et al.*, 2007; Minet *et al.*, 2011, 2012), it still has to be further developed to

account, for instance, for soil surface roughness and vegetation effects (Serbin and Or, 2005). Recently, the GPR approach of Lambot *et al.* (2004c) was generalized to near-field conditions, including in particular ground-coupled radars (Lambot and André, 2012; Lambot *et al.*, 2012).

### 1.1.3 Large-scale microwave remote sensing

Airborne and spaceborne microwave remote sensing offers the potential to monitor surface soil moisture over large areas (e.g., Schmugge *et al.*, 2002; Wagner *et al.*, 2007; de Jeu *et al.*, 2008; Crow *et al.*, 2012; Shi *et al.*, 2012). Like most local- and field-scale techniques, microwave remote sensing sensors are mostly sensitive to the soil electromagnetic properties. As the dependency of the soil permittivity on SWC is the highest in the low-microwave region (<10 GHz), SWC retrieval is mainly performed using microwave sensors operating in either L-band (frequency $f$ = 1–2 GHz, wavelength $\lambda$ = 30–15 cm), C-band ($f$ = 4–8 GHz, $\lambda$ = 7.5–3.8 cm), or X-band ($f$ = 8–12 GHz, $\lambda$ = 3.8–2.5 cm). A major asset of microwave remote sensing compared to optical remote sensing is its capability to perform all-weather observations due to the low influence of the atmospheric conditions on the microwave signal. Microwave sensors are also able to operate day and night. However, remote sensing methods have several drawbacks compared to ground-based techniques such as the low temporal resolution (few days), the shallow measurement depth (few centimeters), and the difficulty to observe the soil water content below dense vegetation. An other major disadvantage is that the within-pixel variability can not be estimated (Famiglietti *et al.*, 1999, 2008; Vereecken *et al.*, 2008).

Microwave remote sensing sensors include active systems, which transmit electromagnetic waves and monitor the backscattered energy from the land surface and passive systems, which record the electromagnetic radiation naturally emitted from the land surface (Wagner *et al.*, 2007; de Jeu *et al.*, 2008). Since the late 1960s, numerous satellites carrying microwave instruments have been launched which has lead to huge developments with respect to spatial and temporal resolutions and microwave modeling. While scattering and emission phenomena are closely related, active and passive systems have different characteristics leading to different spatiotemporal resolutions and sensitivities to land surface properties.

#### Active microwave remote sensing

Active microwave remote sensing instruments include scatterometer and radar. Synthetic aperture radar (SAR) systems (e.g., ALOS PALSAR, RADARSAT, ERS, ENVISAT ASAR, SIR-C/X SAR, TerraSAR-X) have been specifically designed to provide fine spatial resolution data from space (<30 m). Like for off-ground GPR, the radar backscattered signal is highly sensitive to the land surface characteristics, such as the soil dielectric properties but also the soil surface roughness and the vegetation layer (Verhoest *et al.*, 2008; Shi *et al.*, 2012). Many efforts have been made over the last decades to develop radar backscatter models which account for surface roughness, ranging from empirical to physically-based models. On one hand, empirical scattering models

(e.g., Oh *et al.*, 1992; Dubois *et al.*, 1995; Deroin *et al.*, 1997; D'Urso and Minacapilli, 2006) require site-specific calibrations, which need ground-truth observations or other remote sensing products. These models does not require surface roughness measurements, but are only valid for the same conditions as the calibration. Discrepancies were however observed in several studies between measured and modeled radar backscattered signals (Zribi *et al.*, 1997; Baghdadi and Zribi, 2006). On the other hand, physically-based models use surface roughness parameters which have to be estimated from field measurements. The classical scattering models are the Kirchhoff Approximation (Beckmann and Spizzichino, 1987), the Small Perturbation Method (Beckmann and Spizzichino, 1987), the Small Slope Approximation (Voronovich, 1985), and the Integral Equation Model (IEM) (Fung *et al.*, 1992). The IEM model and its improved versions such as the Advanced Integral Equation Model (AIEM) (Chen *et al.*, 2003) are mostly used to retrieve SWC from SAR data. However, further improvements are still needed in order to provide SWC estimations over rough surface at accuracies that would satisfy typical hydrological application requirements (Wagner *et al.*, 2007; Lievens *et al.*, 2011). The main difficulties are to correctly model the complex natural surfaces and to accurately measure the surface roughness parameters. Most physically-based models assume that the surface roughness is a random stationary process, which is not correct for many natural conditions such as agricultural fields, and field-measurements of surface roughness parameters are often inaccurate (Lievens *et al.*, 2011). As already mentioned, remotely sensed radar data are also greatly affected by vegetation, whereby the plant parts can affect the measurements according to their relative size with respect to the wavelength of the radar signal used (Jackson *et al.*, 1996; Chukhlantsev *et al.*, 2003; Joseph *et al.*, 2010b). A first attempt to model the influence of vegetation on the radar backscattering is the semi-empirical water cloud model treating the canopy as a uniform cloud of water droplets (Attema and Ulaby, 1978; Serbin and Or, 2005). More complicated models were then developed based on the radiative transfer theory describing the vegetation as an ensemble of discrete dielectric scatterers overlying an homogeneous half-space, such as the Michigan Microwave Canopy Scattering (MIMICS) model (Ulaby *et al.*, 1990; Karam *et al.*, 1992; Touré *et al.*, 1994) and the Tor Vergata model (Ferrazzoli and Guerriero, 1995; Bracaglia *et al.*, 1995; Della Vecchia *et al.*, 2004). Phase-coherent scattering models were also developed in order to account for coherent effects caused by the interferences among the different scatterers (Stiles and Sarabandi, 2000; Marliani *et al.*, 2002). But up to now, accurate modeling of scattering and absorption effects in vegetation is not yet available at the spatial resolution of the remote sensing products.

**Passive microwave remote sensing**

Microwave radiometry is also a powerful remote sensing technique to monitor SWC (e.g., Schmugge *et al.*, 1974; Jackson *et al.*, 1982; Schmugge *et al.*, 2002; Shi *et al.*, 2012; Kerr *et al.*, 2012). A major advantage of passive systems (radiometers) compared to active systems is the lower sensitivity to surface roughness and vegetation cover which allows a less complex data processing

for soil moisture retrieval (Jackson *et al.*, 1996; Shi *et al.*, 2012). Spaceborne radiometers (e.g., AQUA AMSR-E, Coriolis WindSAT, SMOS MIRAS) can also provide higher temporal resolution data but with a lower spatial resolution (>5 km) compared to SAR systems (<30 m), which can therefore limit the range of applications. Microwave radiometry in the L-band is a very promising technique to estimate SWC because of its high sensitivity to the soil dielectric permittivity, i.e., a large change in sensor signal (brightness temperature) in response to a change in soil permittivity, and its capability to better penetrate vegetation. Indeed, at long wavelengths (≈21 cm) the soil emission depth is relatively large and the vegetation canopies are semitransparent (Guglielmetti *et al.*, 2008; Grant *et al.*, 2009). In this context, the European Space Agency (ESA) launched in November 2009 the Soil Moisture and Ocean Salinity (SMOS) mission (Kerr *et al.*, 2010). SMOS carries the first L-band radiometer which can provide global SWC estimates at 50 km of spatial resolution and with a 3-day revisiting time. As active and passive systems have complementary assets, the US National Aeronautics and Space Administration (NASA) is scheduling the launch in 2014 of the Soil Moisture Active Passive (SMAP) mission (Entekhabi *et al.*, 2010). SMAP will combine L-band active and passive observations, through which the spatial resolution is expected to reach to 9 km.

The influence of surface roughness and vegetation cover, while less important for passive compared to active soil moisture retrieval, has been investigated by many scientists (Choudhury *et al.*, 1979; Mo and Schmugge, 1987; Wigneron *et al.*, 2001; Lawrence *et al.*, 2011; Mialon *et al.*, 2012). The semi-empirical Q/H model (Wang and Choudhury, 1981) has been widely used to account for roughness and is currently applied in the SMOS soil moisture algorithm due to its simplicity (Wigneron *et al.*, 2007; Panciera *et al.*, 2009; Joseph *et al.*, 2010a). This model is based on two fitting parameters ($Q$ and $H$) which are calibrated with *in-situ* data. Recent studies indicated possible relationships between the empirical roughness parameters and the measurable surface roughness characteristics, i.e., the standard deviation of the surface height, the correlation length and the autocorrelation function (Mialon *et al.*, 2012). However, several scientists observed some discrepancies using this model (Shi *et al.*, 2002). Other approaches were developed such as the air-to-soil transition model introduced by Schwank and Mätzler (2006) and the reflectivity model of Shi *et al.* (2002) based on the IEM model. Algorithms for estimating surface SWC from vegetated areas using radiometry are also available in the literature such as the Tau-Omega model (Jackson, 1993; Wigneron *et al.*, 1995, 2007) which has been successfully applied in a wide range of conditions (Jackson *et al.*, 1996; Saleh *et al.*, 2007; Guglielmetti *et al.*, 2008; Schwank *et al.*, 2012). In addition to surface roughness and vegetation effects, several studies have analyzed the impact of forest litter (Schwank *et al.*, 2008; Lawrence *et al.*, 2011), soil temperature (Choudhury *et al.*, 1982; Chanzy *et al.*, 1997), freezing soil (Schwank *et al.*, 2004; Rautiainen *et al.*, 2012), snow cover (Mätzler, 1994b; Pulliainen and Hallikainen, 2001; Jiang *et al.*, 2007), and topography (Mätzler and Standley, 2000; Monerris *et al.*, 2008; Pierdicca *et al.*, 2010; Pulvirenti *et al.*, 2011; Völksch *et al.*, 2011) on the SWC retrieval from passive microwave data.

Even if there are various experiments reported in literature analyzing the effect of soil surface roughness and vegetation on the retrieved radiometer signal, ambiguous findings and explanations are reported. The reasons for this are manifold. On one hand, the spatial scale of observation limited the understanding of involved processes, which is especially the case if airborne or spaceborne data were used. On the other hand, the experiments were performed under non-controlled conditions, whereby especially the spatial horizontal and vertical heterogeneity of the influencing factors (such as water content) are not known. Therefore, ground-based radiometer has proven to be of particular interest to improve and validate retrieval algorithms used for large-scale passive remote sensing of SWC due to the ability of controlling and/or characterizing the observed footprint.

## 1.2 Research objectives

In order to characterize the spatiotemporal variability of SWC at the field scale, GPR and ground-based radiometer show particularly promising potentialities for high-resolution mapping and monitoring. Yet, for both techniques, still research is needed to further improve and validate SWC products.

In that context, the main objective of this research project is to develop and evaluate new forward and inverse modeling approaches for surface SWC retrieval using active and passive remote sensing. In particular, ground-based microwave radiometer and ground-penetrating radar were investigated for SWC sensing and mapping at the field scale. This is illustrated in Figure 1.1 showing the key elements of the overall estimation problem around which this thesis is organized. The soil dielectric properties and the related soil water content can either be derived from radiometer signal by inverting a radiative transfer model or from GPR signal by inverting an electromagnetic model. Both active and passive microwave signals are affected by soil roughness and vegetation, which have to be accounted for in the forward models. The soil hydraulic properties are then estimated from time-lapse soil water content data using an appropriate hydraulic model.

This research is expected to provide new insights into the development and application of field-scale characterization techniques that can be used for characterizing the within variability of field-scale SWC and also improving large-scale SWC estimates obtained from, for instance, the SMOS or the upcoming SMAP satellites. Within that framework, the key objectives of the thesis are:

- to test, validate, and apply existing modeling approaches for GPR and radiometer SWC mapping;
- to improve GPR and radiometer retrieval algorithms in order to account for soil surface roughness effects;
- to estimate soil hydraulic properties from GPR and radiometer data, and evaluate the uncertainty associated with the estimations;

- to investigate the effect of vegetation on the passive and active microwave signals and the potential use of microwave remote sensing to characterize vegetation.

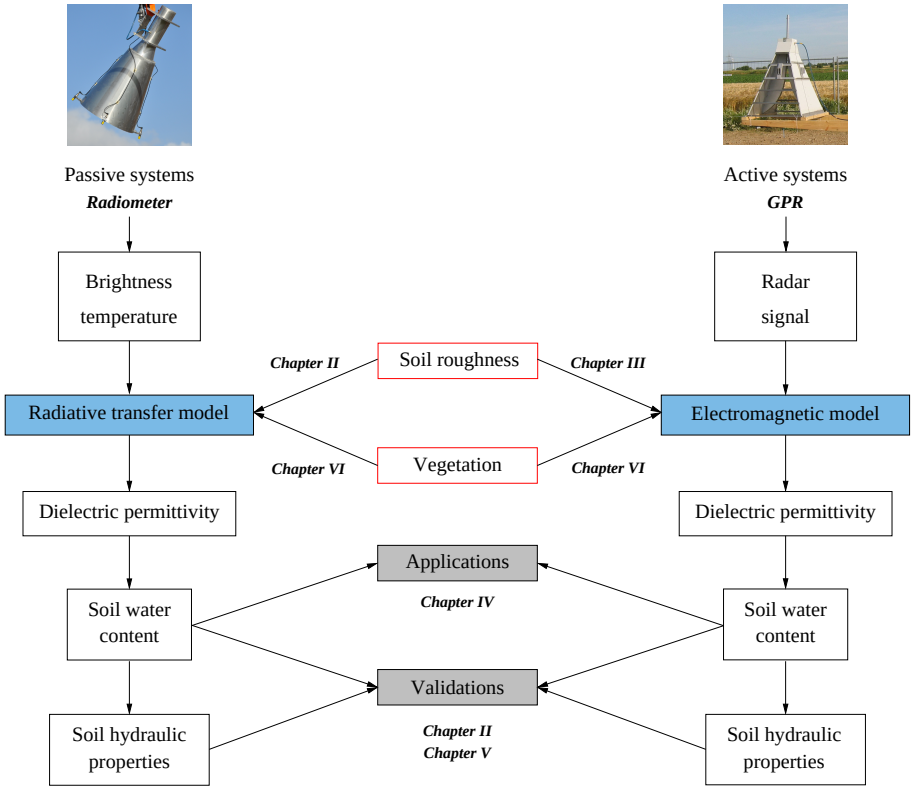


Figure 1.1: General sketch of SWC retrieval using passive and active microwave systems, from which the thesis is structured. Black outlined boxes denote geophysical data and variables inverted for, blue boxes denote geophysical models, red outlined boxes represent investigated effects to account for in geophysical models for accurate soil characterization, and grey boxes represent activities to validate and apply both microwave systems.

## 1.3 Outline of the thesis

The thesis is organized in 7 chapters. In Chapter 2, we compare L-band radiometer and off-ground GPR to map surface SWC at the field scale over bare soil. The effect of soil roughness on the passive microwave signal is addressed by using a semi-empirical roughness model and the sensitivity of the model parameters with respect to the number of ground truths is evaluated using Monte Carlo simulations. The uncertainty related to radiometer and GPR estimates

is also appraised and discussed by comparing both characterization techniques to reference TDR.

Soil surface roughness constitutes a major source of noise in the GPR signal when roughness amplitude is relatively large with respect to wavelength, which typically applies in the hyperfrequency range. In Chapter 3, we combine the full-wave GPR model of Lambot *et al.* (2004c) with a roughness model that we derived from the Kirchhoff scattering theory to retrieve surface SWC through signal inversion. This approach is validated using laboratory data and by performing numerical experiments.

In Chapter 4, we analyze the effects of tillage practices on the spatial variation of soil properties using GPR data. In addition, we also use EMI data to provide insights into the variability of the soil properties within the entire root zone. In particular, the tillage effects on surface SWC, bulk soil electrical conductivity, and mechanical resistance are investigated. The spatial distribution of the SWC is also analyzed using geostatistical approaches.

A crucial issue in soil science and hydrology is the characterization of the vadose zone hydraulic properties. In this context, we experimentally investigate in Chapter 5 the potential of GPR and L-band radiometer to remotely infer the hydraulic properties of a sand subject to hydrostatic equilibrium with a range of water table depths.

Vegetation constitutes an additional factor that affects both GPR and radiometer measurements. In Chapter 6, we present a literature review of the use of passive and active microwave remote sensing methods for characterizing crop canopies with specific attention to stress-related properties such as vegetation water content and leaf water potential. Future avenues of research related to water stress recognition in vegetation using microwave methods are also formulated.

Finally, conclusions and perspectives are drawn in the last chapter, thereby providing insights with respect to both future research needs and potential applications.

# Chapter 2

# Mapping field-scale soil moisture with L-band radiometer and ground-penetrating radar over bare soil*


## Abstract

Accurate estimates of surface soil moisture are essential in many research fields, including agriculture, hydrology and meteorology. The objective of this study was to evaluate two remote sensing methods for mapping the soil moisture of a bare soil, namely L-band radiometry using brightness temperature and ground-penetrating radar using surface reflection inversion. Invasive time-domain reflectometry measurements were used as a reference. A field experiment was performed in which these three methods were used to map soil moisture after heterogeneous irrigation that ensured a wide range of water content. The heterogeneous irrigation pattern was reasonably well reproduced by both remote sensing techniques. However, significant differences in the absolute moisture values retrieved were observed. This discrepancy was attributed to different sensing depths and areas, and different sensitivities to soil surface roughness. For GPR, the effect of roughness was excluded by operating at low frequencies (0.2–0.8 GHz) that were not sensitive to the field surface roughness. The root mean square error (RMSE) between soil moisture measured by GPR and TDR was 0.038 $m^3$ $m^{-3}$. For the radiometer, the RMSE decreased from 0.062 (hor-


*This chapter is adapted from:
Jonard, F.; Weihermüller, L.; Jadoon, K. Z.; Schwank, M.; Vereecken, H. & Lambot, S. Mapping field-scale soil moisture with L-band radiometer and ground-penetrating radar over bare soil, in *IEEE Transactions on Geoscience and Remote Sensing*, **2011**, 49(8), 2863–2875.

izontal polarization) and 0.054 (vertical polarization) to 0.020 $m^3$ $m^{-3}$ (both polarizations) after accounting for roughness using an empirical model that required calibration with reference TDR measurements. Monte Carlo simulations showed that around 20% of the reference data were required to obtain a good roughness calibration for the entire field. It was concluded that relatively accurate measurements were possible with both methods, although accounting for surface roughness was essential for radiometry.

## 2.1 Introduction

Surface water content is a key variable for estimating water and energy fluxes at the land surface. Knowledge of the spatial distribution and dynamics of the soil water content is essential in agricultural, hydrological, meteorological, and climatological research and applications. Soil sampling, time-domain reflectometry, as well as neutron and capacitance probes, are common methods used to characterize soil water content at the point scale. In general, these techniques are restricted to small observation areas and are tedious and time-consuming. Furthermore, these techniques may disturb the soil structure and may not allow repeated measurements at the same point. Finally, point measurements are not expected to be representative of the within field variability or even average field moisture (Western *et al.*, 2002).

Airborne and spaceborne remote sensing techniques with either passive microwave radiometry or active radar instruments are the most promising methods for mapping surface soil moisture over larger areas (Ulaby *et al.*, 1986; Jackson *et al.*, 1996; Huisman *et al.*, 2003a; Wagner *et al.*, 2007). Active radar instruments, especially synthetic aperture radar, can provide high spatial resolution data from space (<30 m). However, the radar signal is highly sensitive to the geometric structure of the soil surface (Verhoest *et al.*, 2008). To account for roughness effects, empirical radar scattering models have been developed by several authors (Oh *et al.*, 1992; Dubois *et al.*, 1995; Deroin *et al.*, 1997), but all these models require site-specific calibrations (D'Urso and Minacapilli, 2006). Currently, no widely applicable radar model accounting for roughness effects is able to provide soil moisture estimations at accuracies that would satisfy typical hydrological application requirements (Wagner *et al.*, 2007). In addition, remote sensing radar measurements are greatly affected by vegetation (Jackson *et al.*, 1996). Active systems are therefore limited to flat areas with bare soils or low vegetation. On the other hand, numerous studies have also demonstrated the potential of passive microwave remote sensing to retrieve geophysical parameters such as soil moisture (Schmugge *et al.*, 1974; Jackson *et al.*, 1982, 1995; Schmugge *et al.*, 2002; Wagner *et al.*, 2007). Passive methods provide coarser spatial resolution data (>5 km), but are less influenced by surface roughness and vegetation cover (Jackson *et al.*, 1996). Microwave radiometry in the L-band (1 to 2 GHz) is a promising technique to estimate soil moisture and has the advantage of being unaffected by cloud cover and independent of solar radiation (Njoku and Entekhabi, 1996), which allows all-weather and continuous (day and night) observations. The frequency band 1.400–1.427 GHz is a protected radio astronomy band thus reducing radiometric measurement

errors due to radio frequency interferences (RFI). Additionally, at these wavelengths (≈21 cm) the soil emission depth is relatively large and the vegetation canopies are semitransparent (Guglielmetti *et al.*, 2008; Grant *et al.*, 2009).

Few techniques are presently available to measure soil water content at an intermediate scale between the local and remote sensing scales, namely, the field scale. However, they are particularly necessary for improving and validating large-scale remote sensing data products (Famiglietti *et al.*, 1999). In this respect, ground-penetrating radar and ground-based microwave radiometry techniques are specifically suited for field-scale characterization.

Over the past decade, GPR technology has made significant progress and has shown great potential for mapping surface soil moisture at the field scale with high spatial resolution. Reviews on the use of GPR in soil and hydrological sciences are given by Huisman *et al.* (2003a) and Annan (2005). As the dielectric properties of water outweigh those of other soil components, the spatial distribution of water decisively controls GPR wave propagation in the subsurface. However, the forward model describing the radar backscatter measurements is usually subject to relatively strong simplifications with respect to electromagnetic wave propagation phenomena. This results in inherent errors in the water content retrieval, and moreover, this does not permit the exploitation of all the information contained in the radar data. To overcome this limitation, it is necessary to resort to full-waveform forward and inverse modeling of the GPR data, which has become the logical choice due to the computing resources now available (Ernst *et al.*, 2006; Gloaguen *et al.*, 2007; Soldovieri *et al.*, 2007). Lambot *et al.* (2004c) proposed a full-waveform forward and inverse modeling approach, which particularly applies to off-ground GPR. The electromagnetic model is based on a solution of the 3D Maxwell equations for waves propagating in multilayered media and correctly accounts for antenna effects and antenna-soil interactions. The model was shown to accurately reproduce the radar measurements, and model inversion was successfully applied to identify and map surface soil moisture in the field (Weihermüller *et al.*, 2007; Lambot *et al.*, 2008b).

In the past, several experiments were performed using ground-based and airborne L-band radiometers to better understand the effects of vegetation cover (Ferrazzoli *et al.*, 1992; Saleh *et al.*, 2007; Wigneron *et al.*, 2007; Schwank *et al.*, 2008), soil temperature (Choudhury *et al.*, 1982; Chanzy *et al.*, 1997), soil surface roughness (Choudhury *et al.*, 1979; Mo and Schmugge, 1987), snow cover (Mätzler, 1994b), and topography (Mätzler and Standley, 2000) on the microwave emission from the Earth's surface. These effects have to be considered in the interpretation of the signatures measured, otherwise soil water content retrieval becomes inaccurate. Algorithms for estimating surface soil moisture from passive data are available in the literature (Jackson, 1993; Wigneron *et al.*, 1995). These models include corrections for the surface roughness as well as for the vegetation cover and have been successfully applied in a wide range of conditions in ground-based and airborne experiments (Jackson *et al.*, 1996).

In this context, the further development of algorithms for soil moisture retrievals based on passive and/or active remote sensing techniques is essential to fully benefit from ESA's SMOS mission launched in November 2009

and NASA's upcoming SMAP mission scheduled for launch in 2014. For the proper calibration of such algorithms, ground-truth measurements collected at relevant scales are necessary. In this respect, both ground-based GPR and radiometer show great promise for mapping spatiotemporal variations of soil moisture at scales ranging from a few square meters to several hectares and with a spatial resolution in the order of one meter (Vereecken *et al.*, 2008). These ground-based GPR and radiometer techniques overcome the limitations of the present ground truths (point information, see above) and constitute a promising solution for bridging the spatial scale gap between point information and large-scale remote sensing data.

The objective of this chapter is to compare L-band radiometer and off-ground ultra-wideband GPR (Lambot *et al.*, 2004c, 2006c) to map surface soil moisture at the field scale over bare soil. The effect of soil roughness on the passive microwave signal is also addressed by using an empirical roughness model. The uncertainty related to, respectively, radiometer, GPR, and TDR estimates is appraised and discussed by comparing the three characterization techniques, as absolute uncertainty quantification is relatively complex when dealing with unknown heterogeneities over different scales. In addition, Monte Carlo simulations were performed to evaluate the sensitivity of the roughness parameters with respect to the number of ground truths used for the model calibration, thereby providing valuable insights into the roughness calibration uncertainty. To the best of our knowledge, this study represents the first attempt to compare field-scale maps of soil moisture over a bare rough surface using radiometer and advanced GPR.

## 2.2 Materials and methods

### 2.2.1 Experimental setup

The experiment was conducted on July 14, 2009 on an agricultural field at the TERENO test site in Selhausen, Germany (latitude 50°87 N, longitude 6°45 E, and elevation 105 m above sea level). The measurements were performed three months after the last plowing event on a compacted bare soil. The test site has a maximum inclination of 4 in the east-west direction. The ground water depth shows seasonal fluctuations between 3 m and 5 m below the surface. The soil type is a Haplic Luvisol developed in silt loam according to the USDA textural classification. In the upper horizons of the soil (0–30 cm), the grain size distribution is largely dominated by the silt fraction (mean value of 65.0%). The mean clay and sand contents are 14.9 and 20.1%, respectively. In the upper part of the field, stones are observed. Due to the geomorphology and soil texture variation (around 5% within the experimental plot), a large natural variability in surface soil water content is present (around 0.10 $cm^3$ $cm^{-3}$) (Weihermüller *et al.*, 2007).

GPR, radiometer and TDR data were collected on a 72 × 16 $m^2$ experimental plot located in the upper part of the test site (Figure 2.1). This plot consists of 8 transects each consisting of 18 measurement points (measurement spacing: 2 and 4 m in the $x$- and $y$-direction, respectively). In order to produce

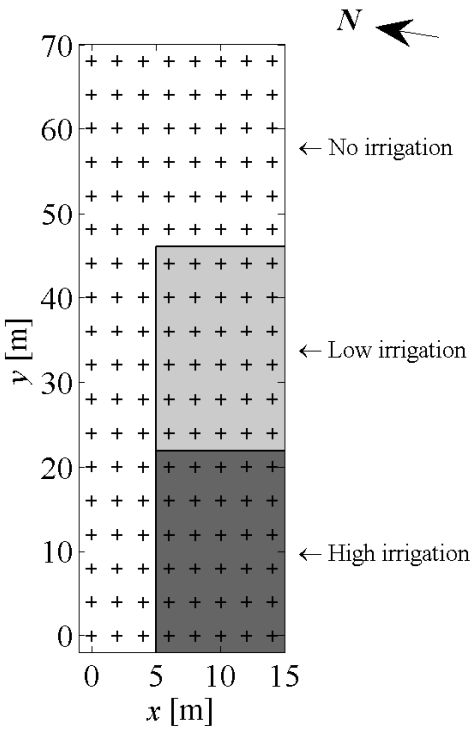


Figure 2.1: Sampling grid (72 × 16 $m^2$) consisting of 8 transects, each comprising 18 measurement points (in total 144 measurement points). The delineated areas correspond to areas with different levels of irrigation with a mean of 8 l $m^{-2}$ for the high irrigation (dark-gray) and a mean of 4 l $m^{-2}$ for the low irrigation (light-gray).

a wide range of water contents, the plot was partially irrigated with different quantities of water in two different areas using a fire hose one day before the experiment. Figure 2.1 shows the location of the irrigated area. The dark-gray area was irrigated with a mean of 8 l $m^{-2}$, while the light-gray area was irrigated with a mean of 4 l $m^{-2}$.

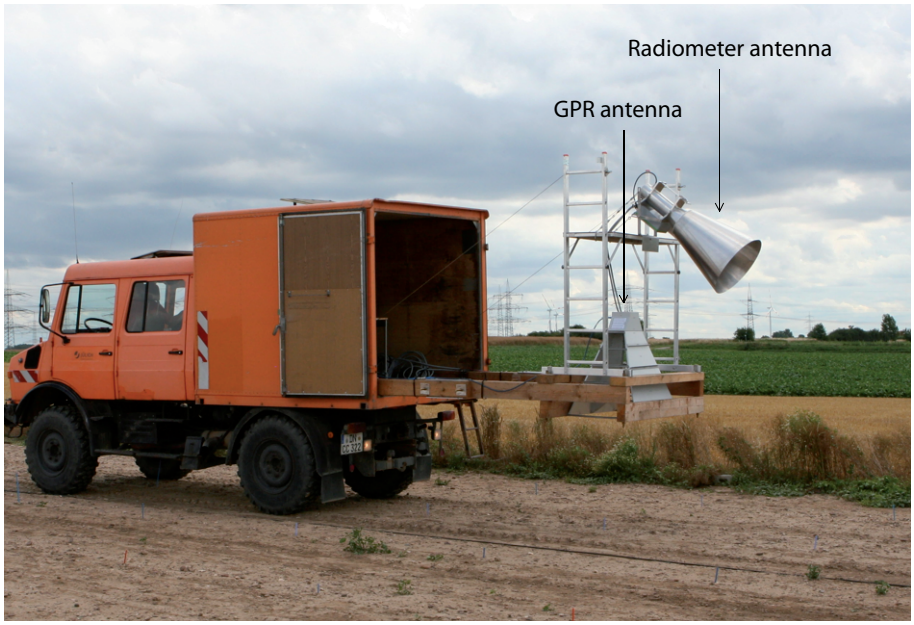


Figure 2.2: GPR and L-band radiometer mounted on a truck to measure surface soil relative dielectric permittivity.

Measurements were performed with a radiometer and a GPR mounted on the back of a truck (see Figure 2.2). The truck moved backwards to avoid the effects of the tracks on the radiometer and radar measurements. Single radiometer and radar measurements were performed at each position. The radiometer antenna aperture was situated about 2 m above the soil surface and directed with an observation angle of $\vartheta = 53°$ relative to the vertical direction. The GPR antenna aperture was about 1.2 m above the ground with normal incidence. This setup resulted in an elliptic $-3$ dB footprint of approximately $3.2 \times 1.9$ $m^2$ for the radiometer and a $-3$ dB footprint of approximately $1.8 \times 1.8$ $m^2$ for the GPR (see Section 2.3.3).

### 2.2.2 Ground-truth measurements

Subsequent to each GPR and radiometer measurement, four TDR and temperature measurements were performed in the center of the GPR and the radiometer antenna footprints, at distances of about 20 cm from each other. Only four measurements were collected due to a time constraint during the mapping experiment, in particular to avoid significant temporal variations of surface soil

moisture (evaporation). Data measured within each footprint were averaged for comparison with the permittivities derived from the GPR and radiometer. TDR measurements of soil dielectric permittivity were performed using a custom-made, three-rod probe with a length of 10 cm which was inserted vertically into the soil. The TDR probe was connected to a TDR100 cable tester (Campbell Scientific, Logan, Utah, USA). The raw data of the waveform were stored and automatically analyzed by the commonly used tangent method in the time domain (Heimovaara and Bouten, 1990). Due to the low clay content of the soil at the site, the frequencies of the TDR measurements are expected to be in the frequency range of 200–1000 MHz (Robinson *et al.*, 2005), which is similar to the GPR frequency band. Soil temperature measurements were performed using a temperature sensor (Testo110, Testo Industrial Services, Lenzkirch, Germany) inserted vertically at a depth of 5 cm. This sensor provides the soil temperature with an accuracy of $\pm 0.2$ K.

### 2.2.3 Remote sensing instruments

#### Ground-penetrating radar

The radar system was set up using a ZVL vector network analyzer (VNA, Rohde & Schwarz, Munich, Germany), thereby providing an ultra-wideband (UWB) stepped-frequency continuous-wave (SFCW) radar. The antenna system consisted of a transverse electromagnetic (TEM), double-ridged broadband horn antenna (BBHA 9120 F, Schwarzbeck Mess-Elektronik, Schönau, Germany). The antenna was 95 cm long with a $68 \times 96$ cm$^2$ aperture area and a $-3$ dB full beamwidth in the E-plane and the H-plane of 46° (at 400 MHz). The antenna nominal frequency range was 0.2–2 GHz and its isotropic gain ranged from 9–14 dBi.

The raw GPR data consist of the frequency-dependent complex ratio $S_{11}$ between the backscattered electromagnetic field and the incident electromagnetic field and were measured sequentially at 301 stepped operating frequencies over the range 0.2–2 GHz with a frequency step of 6 MHz. Only lower frequency data (0.2–0.8 GHz), which were not affected by soil surface roughness according to Rayleigh's criterion ($h_c = \lambda/8$, where $h_c$ is the critical height of the surface protuberances and $\lambda$ is the wavelength), were used for the inversions.

#### Microwave radiometer

The L-band microwave radiometer JÜLBARA from Forschungszentrum Jülich was designed for field-scale application in surface soil moisture experiments. JÜLBARA is a Dicke-type radiometer which operates at the central frequency of 1.414 GHz and is based on a similar concept (with respect to the filter characteristics and calibration sources) as the ELBARA radiometer (Mätzler *et al.*, 2003). To distinguish interferences from natural thermal radiance, the radiometer measured quasi-simultaneously at the two following frequency ranges: 1.400–1.414 GHz and 1.414–1.427 GHz. The radiometer was equipped with a dual-mode conical horn antenna (aperture diameter = 60 cm, length = 67 cm) with symmetrical and identical beams and a $-3$ dB full beamwidth in the

far-field of 23°, which allowed the received radiance to be confined to a well defined and narrow footprint area. The radiometer was equipped with internal cold (278 K) and hot (338 K) loads for calibration preceding each measurement. The measurements were recorded with 10 s integration time. The estimated absolute accuracy of the radiometer was ±1 K with a sensitivity better than 0.1 K. External calibration was done to correct for losses in the antenna cables and for noise generated by the physical temperature of the antenna and cables. This external calibration was performed by directing the radiometer towards the sky with an elevation angle of 60° above the horizon and by correcting the measured brightness temperature to the theoretical value as described by Pellarin *et al.* (2003).

### 2.2.4 Signal processing

#### GPR full-waveform forward and inverse modeling

Assuming the distribution of the electromagnetic field measured by the antenna to be independent of the scatterer, i.e., only the phase and amplitude of the field change (plane wave approximation over the antenna aperture), the antenna can be modeled using the following equation in the frequency domain, owing to the linearity of Maxwell's equations (Lambot *et al.*, 2004c):

$$S_{11}(\omega) = H_{\mathrm{i}}(\omega) + \frac{H(\omega)\, G^{\uparrow}_{\mathrm{xx}}(\omega)}{1 - H_{\mathrm{f}}(\omega)\, G^{\uparrow}_{\mathrm{xx}}(\omega)} \tag{2.1}$$

where $S_{11}(\omega)$ is the international standard quantity measured by the VNA, $H_{\mathrm{i}}(\omega)$ is the antenna return loss, $H(\omega)$ is the antenna transmitting-receiving transfer function ($H(\omega) = H_{\mathrm{t}}(\omega)H_{\mathrm{r}}(\omega)$), $H_{\mathrm{f}}(\omega)$ is the antenna feedback loss, $G^{\uparrow}_{\mathrm{xx}}(\omega)$ is the transfer Green's function of the air-soil system, and $\omega$ is the angular frequency. The antenna transfer functions and the Green's function are dimensionless. The Green's function represents a solution of the 3D Maxwell equations for electromagnetic waves propagating in multilayered media with smooth interfaces (Michalski and Mosig, 1997; Slob and Fokkema, 2002; Lambot *et al.*, 2004c). The characteristic antenna transfer functions can be determined by solving a system of equations such as Eq. (2.1) to the unknowns $H_{\mathrm{i}}(\omega)$, $H(\omega)$, and $H_{\mathrm{f}}(\omega)$ for different well-defined model configurations, i.e., with the antenna at different heights above a perfect electrical conductor (PEC). The Green's functions can therefore be computed and $S_{11}(\omega)$ can be readily measured.

In order to identify the surface dielectric permittivity, inversion of the Green's function is performed in the time domain, focusing on a time window containing the surface reflection only (Lambot *et al.*, 2006c). The inverse problem is formulated in the least-squares sense and the objective function to be minimized is accordingly defined as follows:

$$\phi(\mathbf{b}) = \left(\mathbf{g}^{\uparrow *}_{\mathrm{xx}} - \mathbf{g}^{\uparrow}_{\mathrm{xx}}\right)^{T} \cdot \left(\mathbf{g}^{\uparrow *}_{\mathrm{xx}} - \mathbf{g}^{\uparrow}_{\mathrm{xx}}\right) \tag{2.2}$$

where

$$\mathbf{g}^{\uparrow *}_{\mathrm{xx}} = g^{\uparrow *}_{\mathrm{xx}}(t)\big|^{t_{\max}}_{t_{\min}} \quad \text{and} \quad \mathbf{g}^{\uparrow}_{\mathrm{xx}} = g^{\uparrow}_{\mathrm{xx}}(t)\big|^{t_{\max}}_{t_{\min}} \tag{2.3}$$

are the vectors containing, respectively, the observed and simulated time-domain windowed Green's functions, and $\mathbf{b} = [\varepsilon_\mathrm{r}, h_\mathrm{a}]$ is the parameter vector to be estimated with $\varepsilon_\mathrm{r}$ [–] being the surface soil relative dielectric permittivity and $h_\mathrm{a}$ [m] being the distance between the antenna phase center and the soil surface. The antenna phase center represents the origin of the radiated field from which the far-field spherical divergence is initiated (Jadoon *et al.*, 2011). Although the soil electrical conductivity, magnetic permeability, and soil layering can be taken into account in the inversion process, their effect was initially assumed to be negligible for the estimation of $\varepsilon_\mathrm{r}$ (Lambot *et al.*, 2006c).

The objective function (Eq. (2.2)) is minimized using the local Levenberg-Marquardt algorithm. An initial guess for the antenna elevation $h_\mathrm{a}$ is derived from the surface reflection arrival time $t_\mathrm{i}$ [s], which is automatically detected. Given the simple topography of the objective function (not oscillating and containing a single minimum) dealt with in this particular inverse problem, the initial guess for $\varepsilon_\mathrm{r}$ can be made arbitrarily, and it was set as 5 in this study (the solution found by the algorithm is independent of the initial guess). The GPR methodology has been fully validated in previous studies, both in the laboratory and in the field (Lambot *et al.*, 2004c, 2006c, 2008b). However, a validated ultra-wideband GPR model that accounts for soil surface roughness is not yet available (Lambot *et al.*, 2006a).

### Passive microwave signal modeling

**Radiative transfer model** The basic principle of microwave radiometry is a measurement of the thermal radiance emitted at the Earth's surface in a given frequency band (Njoku and Entekhabi, 1996). Planck's radiation law describes the radiation spectrum of a black body at a given physical temperature. At microwave frequencies, and for temperatures typical of the Earth's surface, Planck's law can be approximated by the Rayleigh-Jeans equation. According to this equation, the radiance is proportional to the physical temperature, and denoted as brightness temperature, $T_\mathrm{B}$ [K] (Njoku and Entekhabi, 1996).

The brightness temperature of a soil surface observed by the L-band radiometer can then be expressed as (Jackson, 1993; Wigneron *et al.*, 2001):

$$T_{\mathrm{B},p} = E_p\, T_\mathrm{eff} + (1 - E_p)\, T_\mathrm{sky} \tag{2.4}$$

where $E$ [–] is the surface emissivity, $T_\mathrm{sky}$ [K] is the sky radiometric temperature calculated as in Pellarin *et al.* (2003), $T_\mathrm{eff}$ [K] is the effective physical temperature of the soil (Ulaby *et al.*, 1986) and $p$ refers to the polarization (H or V). In this study, the effective soil temperature is assumed to be the temperature at a depth of 5 cm. The impact of this assumption on the emissivity values is negligible. Indeed, even if an error of 5 K is assumed for $T_\mathrm{eff}$, this would result in an error for the emissivity of less than 3%.

Under local thermodynamic equilibrum, Kirchhoff's law states that the emissivity ($E$) of a given object is equal to its absorptivity. The soil emissivity can then be related to the soil reflectivity, $R$ [–] by:

$$E = 1 - R \tag{2.5}$$

The reflectivity is described by the Fresnel equations that express the behavior of electromagnetic waves at a smooth dielectric boundary (Ulaby *et al.*, 1981; Kong, 1990). By solving the Fresnel equations, $\varepsilon_{\mathrm{r}}$ of the emitting layer can be retrieved from the observed $R$ at each polarization. However, the Fresnel equations are only valid for an ideal smooth air-soil interface which is never found in typical agricultural fields. To include the effects of roughness in the modeling of the microwave emission from soil surface, a simple model based on the semi-empirical approach of Wang and Choudhury (Wang and Choudhury, 1981) was applied. This model is described below.

**Roughness model** The Wang and Choudhury model (Wang and Choudhury, 1981) expresses the rough surface reflectivity $R_{\mathrm{R},p}(\vartheta)$ at a polarization $p$ (H or V) and an incidence angle $\vartheta$ in relation to the specular reflectivity $R_{\mathrm{F},p}(\vartheta)$ as:

$$R_{\mathrm{R},p}(\vartheta) = [(1-Q)\,R_{\mathrm{F},p}(\vartheta) + Q\,R_{\mathrm{F},p}(\vartheta)]\,\exp(-h\,\cos(\vartheta)^n) \tag{2.6}$$

where $Q$ is the polarization mixing factor, $n$ expresses the angular dependence of roughness, and $h$ is the roughness parameter.

In our study, only a single incidence angle is used ($\vartheta = 53°$), and thus the angular dependence of roughness will then not be considered ($n = 0$). In most studies, polarization crosstalk is assumed to be negligible at L-band, and thus $Q = 0$ is used (Wigneron *et al.*, 2001; Njoku *et al.*, 2003). In Eq. (2.6), the roughness parameter $h$ is generally considered to be independent of polarization (Wigneron *et al.*, 2001; Wang and Choudhury, 1981). However, various studies have pointed out that the roughness affects the two polarizations differently as a result of the anisotropy of the effective permittivity $\varepsilon_{\mathrm{r}}$ in the air to soil transition zone (Shi *et al.*, 2002; Schwank *et al.*, 2010a). Several studies have also shown that the roughness effect might change with soil moisture. Wigneron *et al.* (2001), Schwank and Mätzler (2006), and Escorihuela *et al.* (2007) did indeed observe a negative correlation between their estimated roughness parameter and the surface soil moisture. The apparently increasing roughness with decreasing soil moisture was explained by an increase of the dielectric heterogeneity (dielectric roughness) as the soil dries out. However, a recent study by Escorihuela *et al.* (2010) showed that the dependence of the soil roughness parameter on soil moisture is due to the difference between the L-band radiometer sensing depth and the ground-truth sampling depth used for the calibration. Based on these assumptions, a simplified bare soil reflectivity model accounting for roughness was derived:

$$R_{\mathrm{R},p} = R_{\mathrm{F},p}\,\exp(-(a_p + b_p\,\varepsilon_{\mathrm{r}})) \tag{2.7}$$

where $a$ and $b$ are the soil roughness model parameters depending on polarization $p$. Parameter $b$ is multiplied by $\varepsilon_{\mathrm{r}}$ instead of the volumetric soil water content to avoid any inaccuracy due to the petrophysical relationship. Given that the model parameters are determined by best fit, they include the measurements errors and their physical meaning is not straightforward (Escorihuela *et al.*, 2007).

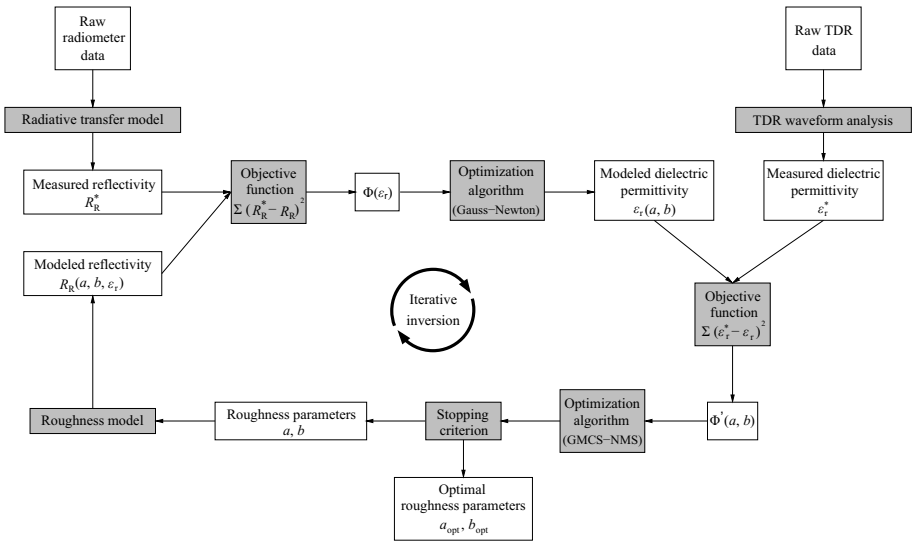


Figure 2.3: Flowchart representing the calibration procedure for the roughness parameters $a$ and $b$ of Eq. (2.7) for estimating the soil relative dielectric permittivity. Shaded boxes denote operators and white boxes denote variables.

The inversion procedure adopted for the estimation of the roughness parameters is depicted in Figure 2.3. In this optimization process, only radiometer and reference TDR data are used. Inversion is composed of two sequential optimization steps. The first inverse problem consists of solving a non-linear least squares problem. In this case, the Gauss-Newton algorithm is used to minimize the objective function:

$$\Phi(\varepsilon_{\mathrm{r}}) \;=\; \sum (R_{\mathrm{R}}^* - R_{\mathrm{R}})^2 \tag{2.8}$$

This objective function represents the cumulative squared error between the measured and modeled reflectivity radiometer data ($R_{\mathrm{R}}^*$ and $R_{\mathrm{R}}(a, b)$, respectively). The measured reflectivity data are obtained from the brightness temperature measurements by using the radiative transfer model presented above (Eqs. (2.4) and (2.5)). The radiometer data from each polarization are used separately in the inversion procedure to obtain specific roughness parameters for each polarization. The second inverse problem consists in minimizing the objective function:

$$\Phi'(a, b) \;=\; \sum (\varepsilon_{\mathrm{r}}^* - \varepsilon_{\mathrm{r}})^2 \tag{2.9}$$

The objective function $\Phi'$ represents the cumulative squared error between the measured and modeled dielectric permittivity data ($\varepsilon_{\mathrm{r}}^*$ and $\varepsilon_{\mathrm{r}}(a, b)$ respectively) and is minimized by means of the global multilevel coordinate search optimization algorithm combined with the local Nelder-Mead simplex algorithm (GMCS-NMS, see Lambot *et al.* (2004b)). Measured permittivity data are obtained from raw TDR data while modeled permittivity data are obtained

from the solutions of the first inverse problem. At each iteration, new roughness parameters are generated, which are used in the roughness model (Eq. (2.7)) to produce new modeled reflectivity data and then new modeled dielectric permittivity data. The optimal roughness parameters $a$ and $b$ are finally obtained after numerous iterations. For the optimization convergence criteria, the default values of the implementation of the Nelder-Mead Simplex algorithm in Matlab (The MathWorks Inc.) were used (i.e., termination tolerance on the function value set to $10^{-4}$ and termination tolerance on the optimized parameters set to $10^{-4}$). It has to be noted that more stringent conditions did not affect the fitting results.

### 2.2.5 Petrophysical relationship

For each type of measurement (GPR, radiometer, and TDR), the model of Topp *et al.* (1980) was used to relate the soil volumetric water content ($\theta$ [$m^3$ $m^{-3}$]) to the soil relative dielectric permittivity:

$$\theta = -5.3 \times 10^{-2} + 2.92 \times 10^{-2}\,\varepsilon_r - 5.5 \times 10^{-4}\,\varepsilon_r^2 + 4.3 \times 10^{-6}\,\varepsilon_r^3 \quad (2.10)$$

The Topp model is a widely used empirical relationship mainly applied for TDR measurements with some restrictions for highly clayic and organic-rich soils as well as soils with high bulk electrical conductivity. For our study site, Topp's model was shown to perform well by Weihermüller *et al.* (2007). The authors found a root mean square error of 0.021 $m^3$ $m^{-3}$ between volumetric soil samples and TDR estimates.

## 2.3 Results and discussion

### 2.3.1 Off-ground GPR

Figure 2.4 presents the frequency and time-domain GPR Green's functions for the 144 measurement points. The Green's function is computed from the $S_{11}$ scatter function using Eq. (2.1), thereby filtering antenna effects. In the frequency domain, we observe that the amplitude of the Green's function ($G_{xx}^{\uparrow}$) increases monotonically up to approximately 0.8 GHz. This behavior indicates that the surface reflection dominates the radar backscatter (this corresponds to a single reflection in the time domain) (Lambot *et al.*, 2006c). For higher frequencies, $G_{xx}^{\uparrow}$ presents a highly oscillating behavior. This is to be attributed to the effect of soil surface roughness (Lambot *et al.*, 2006a). Indeed, for this particular radar setup, the frequency at which a surface appears to be smooth agrees with the Rayleigh criterion (Chanzy *et al.*, 1996). Accordingly, the critical height of the surface protuberances below which the soil surface can be considered smooth corresponds to one eight of the wavelength. In our case, the threshold frequency is around 0.8 GHz, corresponding to a maximum height of the surface protuberances of about 0.047 m, which is consistent with the conditions visually observed in the field. In the time domain (Figure 2.4b), the Green's function ($g_{xx}^{\uparrow}$) does indeed present a single reflector (the soil surface). The time zero corresponds to the antenna phase center. The variations of the

reflection over time are due to the inherent variations of the antenna height above the soil during the measurements. It is worth noting that the soil moisture retrieved from the reflection at the air-soil interface is a surface property and not a volume property (reflection coefficient)(Lambot *et al.*, 2006c; Minet *et al.*, 2010). Hence, the retrieved soil moisture does not directly depend on the penetration depth of the GPR electromagnetic waves. However, when dielectric contrasts are present near the soil surface, and in particular at depths which are a fraction of the wavelength (typically less than a quarter the wavelength), constructive or destructive interferences occur and affect the results, leading to, respectively, over- or underestimations of soil surface dielectric permittivity (Lambot *et al.*, 2006c; Minet *et al.*, 2010).

### 2.3.2 Soil moisture maps

In the first step, off-ground GPR and radiometer data were analyzed without taking soil roughness into account. Surface soil moisture estimated from GPR ($\theta_{\mathrm{GPR}}$), radiometer ($\theta_{\mathrm{MR}}$), and TDR ($\theta_{\mathrm{TDR}}$) measurements are plotted in Figure 2.5. As expected, the soil water content map based on the GPR measurements (Figure 2.5a) shows the lowest water contents in the upper part of the field, which was not irrigated. Intermediate water contents are observed in the area of low irrigation and highest water contents in the area of high irrigation (Figure 2.1). Although the left part of the field was not irrigated, a water content gradient is detectable from the upper to the lower left part. This is associated with the slope of the field. GPR-derived water content values range between 0.12 and 0.26 $\mathrm{m^3\ m^{-3}}$.

In comparison to the GPR-derived water content map, the results of the radiometer measurements, considering the average between the horizontal (subscript H) and vertical (subscript V) polarizations ($\theta_{\mathrm{MR},\overline{\mathrm{HV}}}$) (Figure 2.5b), show a smaller water content range (0.13–0.20 $\mathrm{m^3\ m^{-3}}$). However, a similar moisture pattern to that of GPR is observed with the lowest water contents in the upper non-irrigated area, intermediate water contents in the area of low irrigation, and the highest water contents in the area of high irrigation. Additionally, the spatial correlation is much higher compared to the GPR, with smoother transitions between drier and wetter parts. This may partly be attributed to the larger footprint of the radiometer, and as shown below, to the polarization averaging.

The map based on the reference TDR measurements ($\theta_{\mathrm{TDR}}$, Figure 2.5c) shows a large range of water contents over the entire field with values from 0.09 $\mathrm{m^3\ m^{-3}}$ in the upper non-irrigated area to a maximum of 0.23 $\mathrm{m^3\ m^{-3}}$ in the area of high irrigation. This is due to a significant local variability at the GPR and radiometer footprint scales, as observed from the repeated TDR measurements within the footprints (average standard deviation (STD) of 0.02 $\mathrm{m^3\ m^{-3}}$). It is also worth noting that TDR measurements were affected by the presence of numerous stones in the field, especially in the upper part, thereby also leading to significant measurement errors (typically underestimations). Nevertheless, the same general moisture pattern as for the GPR and the radiometer is obtained.

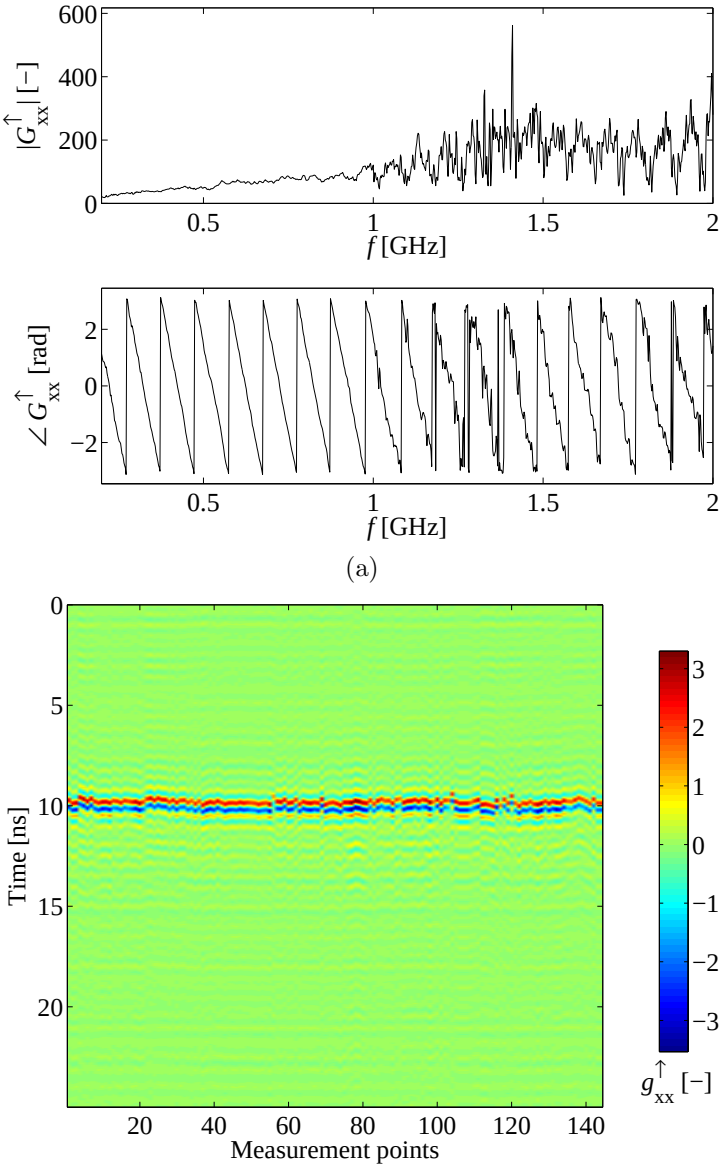


Figure 2.4: Representation of the Green's function (a) in the frequency domain for one measurement point ($|G_{xx}^{\uparrow}|$ denotes the amplitude and $\angle G_{xx}^{\uparrow}$ represents the phase of the Green's function) and (b) the time domain for all measurement points. The oscillations observed with respect to time (above and below the reflection observed around 10 ns) are an artefact of the inverse Fourier transform when data is used in a limited frequency window.

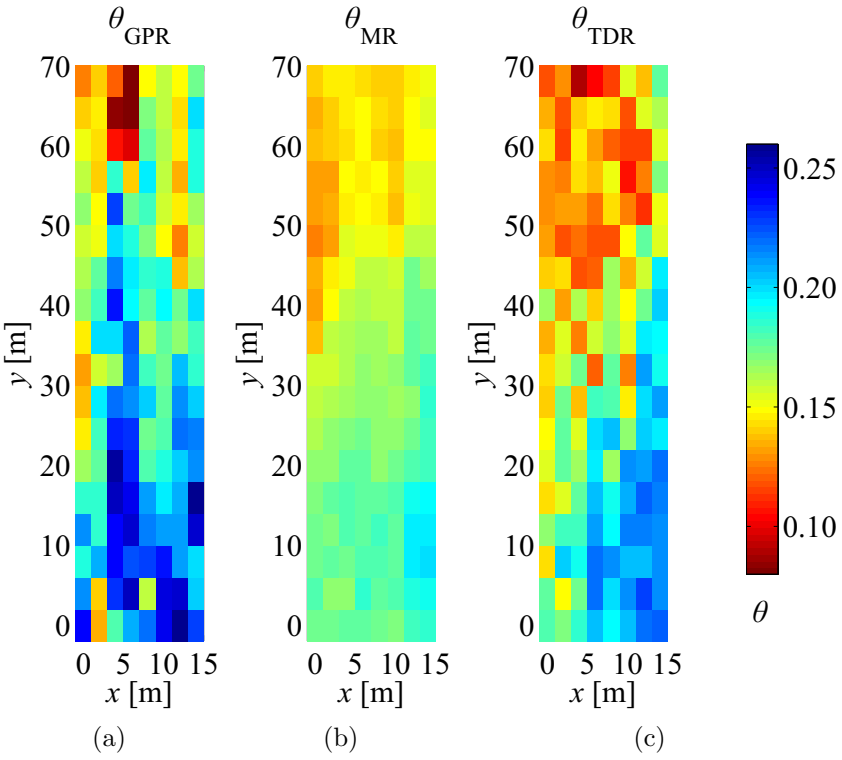


Figure 2.5: Volumetric water content maps obtained using (a) off-ground GPR, (b) radiometer, and (c) TDR measurements at the TERENO test site in Selhausen, Germany (July 14, 2009).

As already stated above, two polarizations were measured by the radiometer, namely horizontal and vertical. For the horizontal polarization, water content values ($\theta_{\mathrm{MR,H}}$) range between 0.08 $m^3$ $m^{-3}$ and 0.15 $m^3$ $m^{-3}$, and for the vertical polarization the water content values ($\theta_{\mathrm{MR,V}}$) range between 0.16 $m^3$ $m^{-3}$ and 0.25 $m^3$ $m^{-3}$ (data not shown). Radiometer measurements at horizontal and vertical polarizations provide large differences in water content estimations in terms of absolute values. This discrepancy can be ascribed to the different sensitivities to the soil surface roughness with respect to the polarization. Indeed, Mo *et al.* (1987) and Shi *et al.* (2002) showed that roughness effects on the surface effective reflectivity differ at different polarizations for the same roughness characteristics. For both polarizations, Figure 2.6 presents the corresponding normalized water content value ($\theta^*_{\mathrm{MR},p}$) defined as follows:

$$\theta^*_{\mathrm{MR},p} = \frac{\theta_{\mathrm{MR},p} - \overline{\theta_{\mathrm{MR},p}}}{\overline{\theta_{\mathrm{MR},p}}} \tag{2.11}$$

where $\overline{\theta_{\mathrm{MR},p}}$ is the water content estimated by the radiometer at polarization $p$ and spatially averaged over the entire field. This shows that although the absolute water contents are under- or overestimated with the horizontal and vertical polarizations, the spatial pattern is similar for the two normalized maps (coefficient of determination $R^2 = 0.74$) and consistent with the GPR and TDR maps (wetter and drier zones). The remaining differences between the two polarizations in the spatial distribution of the retrieved water content may be attributed to variations in soil roughness within the field, which are not fully removed by normalization (only the linear bias is removed).

### 2.3.3 Comparison of the measurement methods

For a direct comparison of the results obtained from the different measurement methods, the GPR- and radiometer-derived water contents are plotted with respect to the TDR results (Figure 2.7). To facilitate interpretation, the data sets were divided into three classes, corresponding to the high (dark-gray), low (light-gray), and non-irrigated (white) parts as plotted in Figure 2.1.

In Figure 2.7a, it can be observed that GPR-derived water contents systematically overestimate the TDR measurements. Additionally, the data points are highly scattered resulting in a low coefficient of determination ($R^2$) of 0.39 and an RMSE in terms of water content of 0.038 $m^3$ $m^{-3}$ (see Table 2.1). However, compared to the radiometer, the slope of the regression (0.63) is much closer to 1. The relatively large STD (0.029) observed for the GPR measurements with respect to the TDR reference measurements may be attributed to soil heterogeneity and the different support scales of the techniques ($\approx$5 cm for TDR compared to >1.5 m for GPR). In Lambot *et al.* (2004c), laboratory results are presented for a quite homogeneous medium with two layers and the STD is indeed much smaller (0.007). For field conditions, Lambot *et al.* (2008b) obtained an STD of 0.023. The observed discrepancies are similar for the three differently irrigated areas of the field. GPR data were analyzed using the surface reflection analysis, which is sensitive mainly to the top few centimeters of the soil. This shallow surface is inherently more heterogeneous in terms of

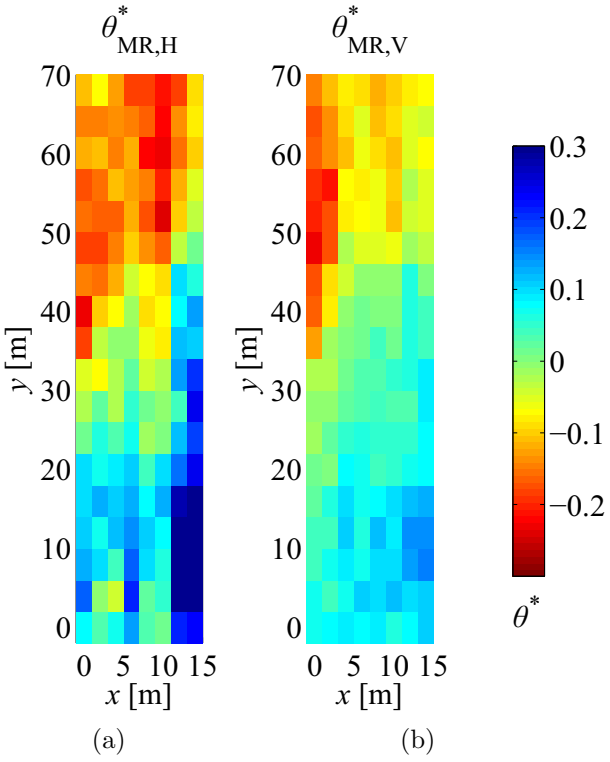


Figure 2.6: Maps of the normalized water content (Eq. (2.11)) with respect to the spatially averaged water content obtained using the radiometer at (a) horizontal and (b) vertical polarizations.

water content than the deeper soil layers investigated by the TDR probe (up to 10 cm depth). It is also worth noting that the GPR measurements may be affected by dielectric layering near the soil surface, which may lead to constructive and destructive interferences, and, thereby, to over- or underestimations of the surface dielectric permittivity (Minet *et al.*, 2010). The effect of roughness on the radar backscatter could not be fully excluded by using low frequency data (<0.8 GHz), and therefore contributes as well to the scattering of the data points in Figure 2.7a. The apparent soil electrical conductivity (including dielectric losses) can also affect the GPR measurements. As showed by Lambot *et al.* (2006c), the effect of the soil electrical conductivity on the surface reflection and dielectric permittivity estimates is negligible for conductivity values below 0.03 S $m^{-1}$ which is larger than the apparent electrical conductivity observed in the field during the experiment (<0.025 S $m^{-1}$). Lastly, soil moisture estimates from TDR measurements can be affected by measurement errors, in particular due to the difficulties encountered in properly inserting the TDR probe into the soil, especially in the drier and stone-rich non-irrigated part of the field.

The comparison of averaged radiometer results (not accounting for roughness) and TDR data presented in Figure 2.7b shows less scattering, with a higher $R^2$ of 0.67 and a lower RMSE of 0.022 $m^3$ $m^{-3}$. The slope of the regression line is 0.4. Figures 2.7c and 2.7d clearly show that the radiometer-derived water contents with horizontal polarization significantly underestimate the TDR-derived values, while those with vertical polarization systematically lead to an overestimation. These discrepancies can be attributed to the different sensitivities of the two polarizations with respect to roughness. In general, the horizontal polarization better predicts the lower water contents in the non-irrigated areas compared to the higher water contents from the irrigated parts. Indeed, in Figure 2.7c, the low water content data are closer to the 1:1 line compared to the higher water content data, whereas the opposite is observed in Figure 2.7d. However, the $R^2$ is still 0.66 $m^3$ $m^{-3}$ for the horizontal and 0.59 $m^3$ $m^{-3}$ for the vertical polarizations, respectively, whereby the high RMSE of 0.062 and 0.054 $m^3$ $m^{-3}$ clearly indicate the systematical mismatch between the two techniques. This explains the small RMSE obtained by averaging the two polarizations.

The frequency dependence of the soil dielectric permittivity over the frequency range covered by the three methods (GPR, radiometer, TDR) is expected to be rather small (Lambot *et al.*, 2004c) as all methods operate at frequencies well below the relaxation frequency of free water (approximately 16 GHz). However, as the soil is inherently heterogeneous, differences in soil moisture retrieved by the three techniques can also be partly explained by the different characterized soil volumes.

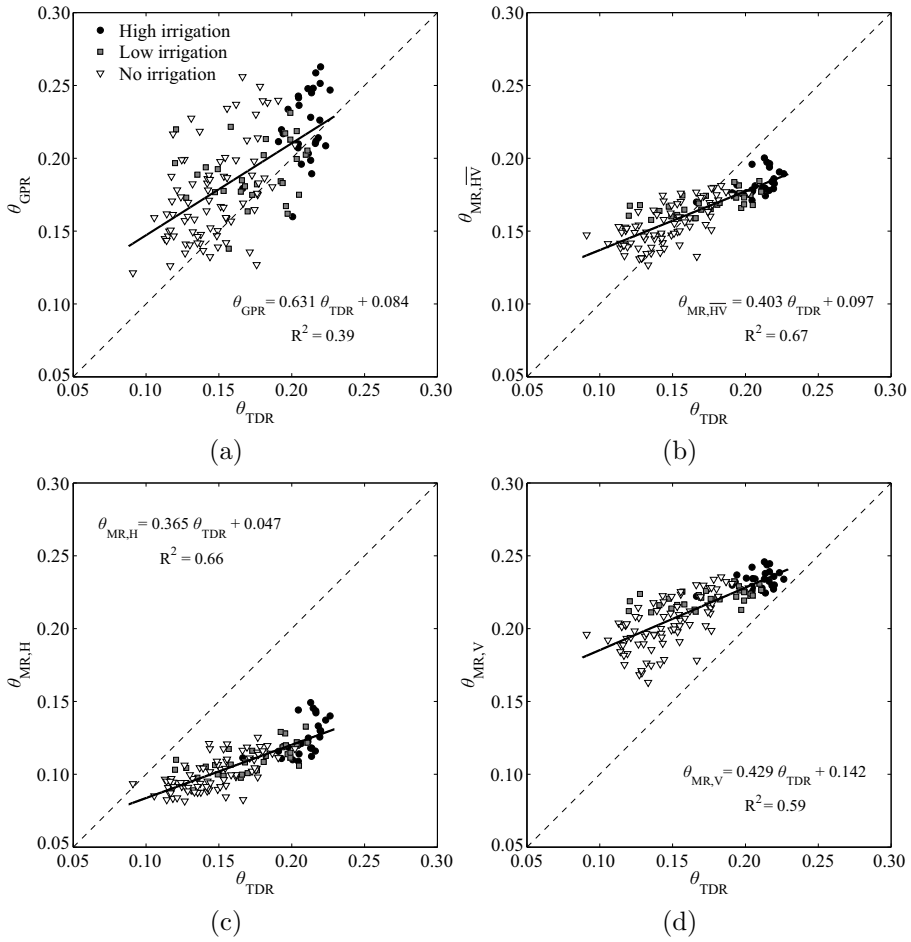


Figure 2.7: Volumetric soil water content from (a) off-ground GPR versus TDR, (b) radiometer (averaged over both polarizations) versus TDR, (c) radiometer (horizontal polarization) versus TDR, and (d) radiometer (vertical polarization) versus TDR.

Table 2.1: Diagonal matrixes of RMSE in terms of water content (RMSE $\theta$) and relative dielectric permittivity (RMSE $\varepsilon_r$) for the GPR, TDR, and radiometer averaged ($\overline{\text{HV}}$-pol), horizontal (H-pol) and vertical (V-pol) polarization, respectively.

| | RMSE $\theta$ | | | | RMSE $\varepsilon_r$ | | | |
|---|---|---|---|---|---|---|---|---|
| | Radiometer $\overline{\text{HV}}$-pol | Radiometer H-pol | Radiometer V-pol | TDR | Radiometer $\overline{\text{HV}}$-pol | Radiometer H-pol | Radiometer V-pol | TDR |
| GPR | 0.038 | 0.084 | 0.041 | 0.038 | 1.933 | 4.065 | 2.065 | 1.881 |
| Radiometer $\overline{\text{HV}}$-pol | | 0.056 | 0.050 | 0.022 | | 2.580 | 2.580 | 1.096 |
| Radiometer H-pol | | | 0.106 | 0.062 | | | 5.160 | 2.941 |
| Radiometer V-pol | | | | 0.054 | | | | 2.658 |

### 2.3.4 Accounting for soil surface roughness for the radiometer

As already stated, soil surface roughness plays an important role in the retrieval of soil water content from the radiometer data. In this section, soil surface roughness is accounted for using the empirical roughness model (see Eq. (2.7)). The optimal roughness parameters obtained by the inversion scheme in Figure 2.3 are $a = 0.1818$ and $b = 0.0013$ for the horizontal polarization, and $a = -1.1480$ and $b = 0.0913$ for the vertical polarization, respectively. The value of $b$ is close to 0 for the horizontal polarization, which means that the model dependence on $\varepsilon_r$ is negligible for this polarization. It is worth noting that, as they are empirical, no constraint on the value of the estimated parameters during the inversion process was applied and their physical meaning is not straightforward. The values of these parameters depend on all electromagnetic phenomena that are not properly accounted for by the Fresnel model, in particular roughness effects, and measurement errors.

Figure 2.8 shows the logarithm of the objective function ($\log_{10}(\Phi')$) as a function of the roughness parameters $a$ and $b$. The aim of this analysis was to verify that the adopted optimization approach was able to find the global minimum of the parameter space correctly and accurately and also to analyze the uniqueness of the inverse solution and the parameter sensitivities, as well as the correlations between the two parameters. The objective function was calculated on 122500 discrete points within the range $[-5 \leq a, b \leq 5]$ and plotted in Figure 2.8. For both polarizations, the objective function shows a well-defined minimum (indicated by a white star), which is found by the global optimization procedure. The model is much less sensitive to $a$ than to $b$, in particular for the vertical polarization, which may result in some uncertainty in the estimation of $a$.

Based on the optimal parameter values, the RMSE between the TDR- and radiometer-derived (accounting for roughness) soil water contents is 0.020 $m^3$ $m^{-3}$ for both polarizations. In general, the accuracy of the soil water content retrieval is significantly improved by using the roughness model. In fact, the RMSE significantly decreased compared to those obtained without the roughness correction, namely, 0.062 $m^3$ $m^{-3}$ and 0.054 $m^3$ $m^{-3}$ for the horizontal and vertical polarizations, respectively (see Table 2.1). The radiometer-derived water contents corrected for the roughness effect are plotted with respect to the TDR estimates in Figure 2.9. Compared to Figures 2.7c and 2.7d, the measurements for both polarizations are much closer to the 1:1 line with a regression slope of 0.6 for the horizontal polarization and 0.7 for the vertical polarization. Without the roughness correction, the regression slope was around 0.4 for both polarizations. However, the $R^2$ of the regression has not improved with the roughness model and the data scattering is similar. This means that random errors are not removed by using the roughness model, showing that it does not perfectly account for all propagation phenomena (not only due to roughness but also to soil water content variability, measurement errors, calibration errors, etc.).

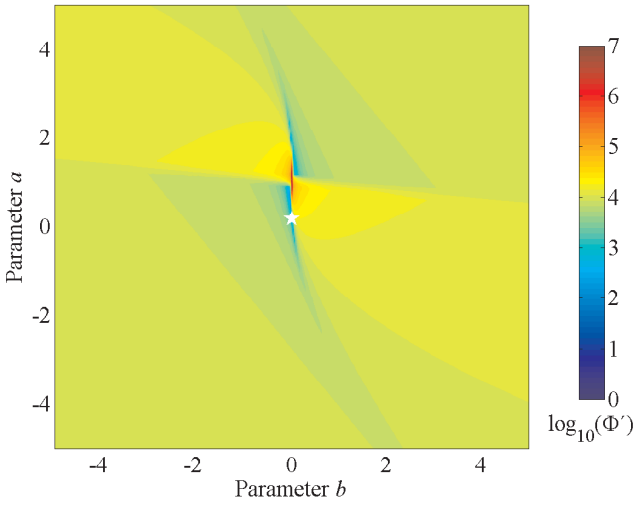


(a)

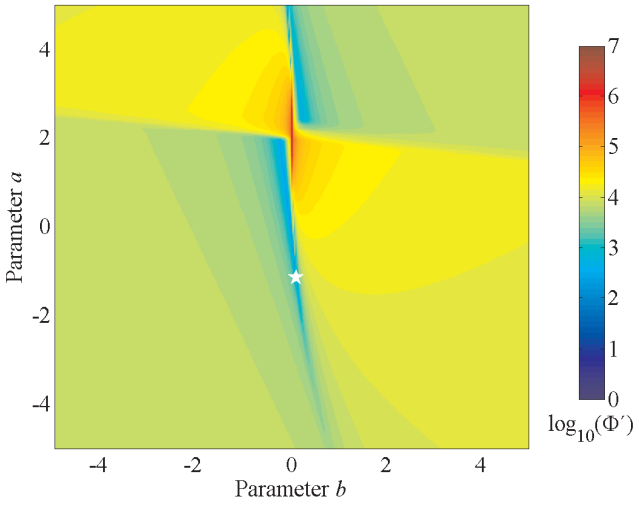


(b)

Figure 2.8: Logarithm of the objective function ($\log_{10}(\Phi')$) as a function of the roughness parameters $a$ and $b$. (a) Horizontal polarization and (b) vertical polarization. The star represents the global minimum of $\Phi'$. The optimal roughness parameters are $a = 0.1818$ and $b = 0.0013$ for the horizontal polarization, and $a = -1.1480$ and $b = 0.0913$ for the vertical polarization.

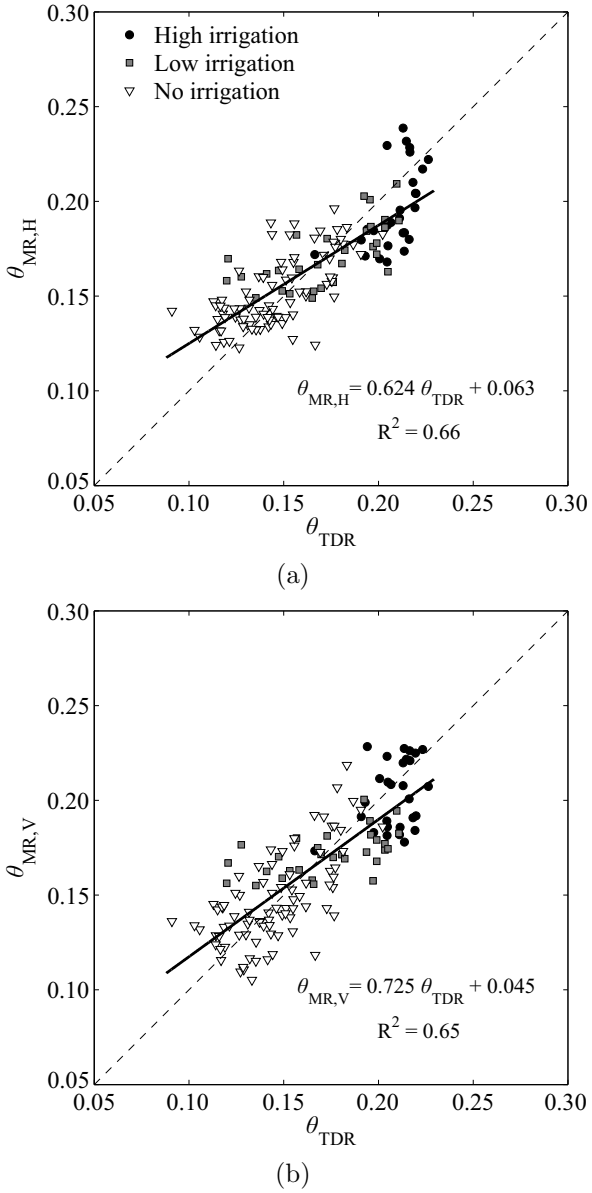


Figure 2.9: Volumetric soil water content from (a) radiometer (horizontal polarization) versus TDR, and (b) radiometer (vertical polarization) versus TDR. Radiometer-derived water contents were estimated by taking roughness into account.

### 2.3.5 Monte Carlo simulations

In most remote sensing applications, ground-truth measurements are sparse. In general, only a few reference points are sampled for the estimation of the roughness parameters, and those values are then used to estimate the soil dielectric permittivity and/or water content for the rest of the area (Panciera *et al.*, 2009). To analyze the associated uncertainty, Monte Carlo simulations were performed, whereby a certain percentage of calibration points were randomly sampled from the total ensemble of reference measurements. In our case, the percentage of calibration points varied from 1 to 100%. For each percentage, 30 independent model runs were performed with randomly chosen reference points. For all these runs, independent roughness parameters $a$ and $b$ were fitted following the inversion procedure depicted in Figure 2.3, based on the TDR measurements associated with the randomly sampled points. In the next step, these roughness parameters were used to predict $\varepsilon_{\mathrm{r}}$ of all the remaining points using the measured $T_{\mathrm{B}}$. The RMSE between radiometer-predicted and the TDR-derived $\varepsilon_{\mathrm{r}}$ was then calculated. Finally, the arithmetic mean and STD of the RMSE were obtained from the 30 model runs of each percentage. The evolution of the mean and STD of the RMSE with increasing percentage of calibration points is plotted in Figure 2.10 (note that the left ordinate is split for better visualization).

The mean RMSE shows a sharp decrease with increasing number of calibration points for both polarizations, whereby the decrease is largest between 1 and ≈20%. Beyond this threshold the mean RMSE changes only slightly approaching the value of 0.95 for the horizontal polarization and 0.98 for the vertical polarization. Additionally, the STD also decreases with the increasing number of calibration points.

These results indicate that even for a relatively homogeneous soil without any vegetation, a large number of calibration points are needed for a robust estimation of the field-scale soil water content. These results indicate that calibrating roughness parameters such as $a$ and $b$ for regional scales is expected to require many more ground-truth measurements than reported above because regional scales show a higher degree of heterogeneity in terms of soil properties (texture, structure, chemical properties, etc.) and vegetation.

## 2.4 Summary and conclusion

Radiometer and GPR measurements were collected over an area of $72 \times 16$ m$^2$ at the TERENO test site in Selhausen, Germany. As a reference ground truth, additional TDR measurements were performed within the footprints of the radiometer and the GPR. The overall moisture patterns were satisfactory reproduced by the three techniques, whereby significant differences were observed between the absolute estimations. The observed discrepancies were attributed to different sensing depths and areas, and different sensitivities with respect to soil surface roughness.

For GPR, the effect of roughness was excluded by operating at low frequencies (0.2–0.8 GHz) that are not sensitive to the field surface roughness. The

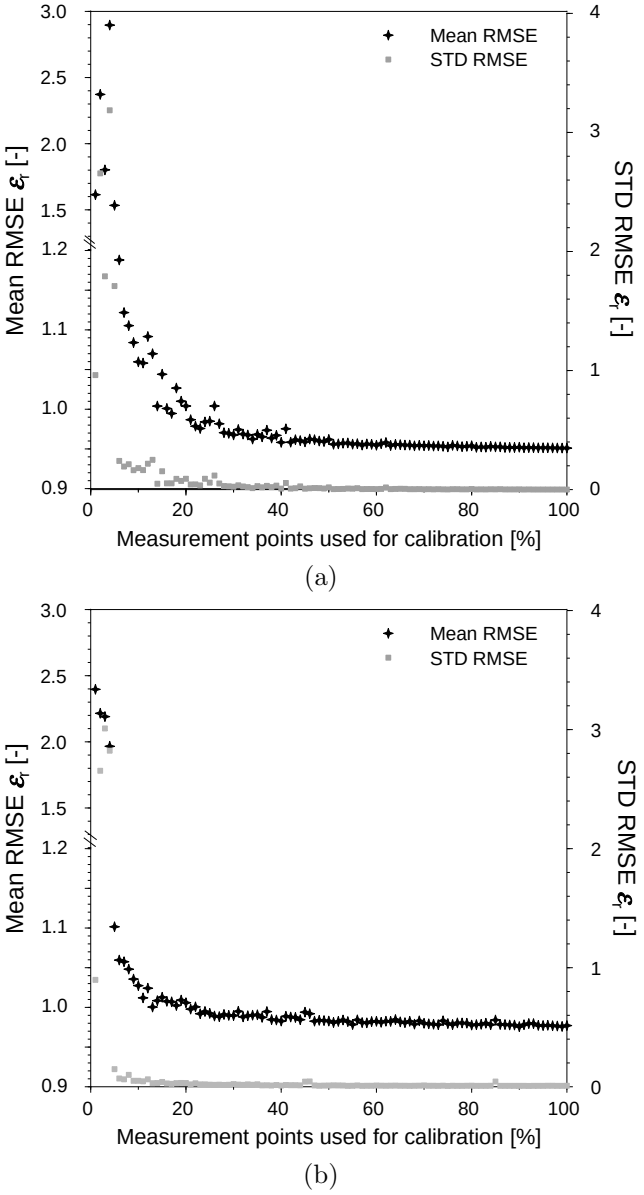


Figure 2.10: RMSE with respect to the percentage of randomly sampled measurement points used for the calibration of the empirical roughness parameters $a$ and $b$ of Eq. (2.7). The mean and STD of the RMSE in terms of dielectric permittivity are estimated on the basis of 30 Monte Carlo runs (a) for horizontal polarization and (b) for vertical polarization. Note that the left ordinate is split for better visualization.

RMSE between soil moisture measured by GPR and TDR was 0.038 $m^3$ $m^{-3}$. For the radiometer, the RMSE significantly decreased from 0.062 (horizontal polarization) and 0.054 (vertical polarization) to 0.020 $m^3$ $m^{-3}$ (both polarizations) after accounting for roughness using an empirical model that required calibration with reference TDR measurements.

Because it is common practice in field and regional radiometer applications to estimate empirical roughness parameters on relatively small numbers of ground-truth measurements, Monte Carlo simulations were performed to estimate the associated uncertainty. These investigations showed that around 20% of the ground-truth information is required to obtain a good roughness calibration to be applied to the entire field.

This study showed that relatively accurate soil moisture estimates were possible with L-band radiometer and off-ground GPR, although accounting for surface roughness was essential for the L-band radiometer. However, comparing different characterization techniques operating at different scales remains a difficult task in heterogeneous environments. The results of this study in particular provide valuable insights into the development and application of field-scale characterization techniques that could be used for improving remote sensing data products for the retrieval of surface soil moisture. Future research will focus on the potential radiometer and GPR synergies for improving soil moisture estimates, to be applied, for instance, in the upcoming SMAP mission.

# Chapter 3

# Accounting for soil surface roughness in the inversion of ultra-wideband off-ground GPR signal for soil moisture retrieval*


## Abstract

We combined a full-waveform ground-penetrating radar model with a roughness model to retrieve surface soil moisture through signal inversion. The proposed approach was validated under laboratory conditions with measurements performed above a sand layer subjected to seven different water contents and four different surface roughness conditions. The radar measurements were performed in the frequency domain in the range of 1–3 GHz and the roughness amplitude standard deviation was varied from 0 to 1 cm. Two inversion strategies were investigated: (1) Full-waveform inversion using the correct model configuration, and (2) inversion focused on the surface reflection only. The roughness model provided a good description of the frequency-dependent roughness effect. For the full-waveform analysis, accounting for roughness permitted us to simultaneously retrieve water content and roughness amplitude. However, in this approach, information on soil layering was assumed to be known. For the surface reflection analysis, which is applicable under field conditions, accounting for roughness only enabled water content to be reconstructed, but with an RMSE in terms of water content of 0.034 $m^3$ $m^{-3}$ compared to an RMSE of


*This chapter is adapted from:
Jonard, F.; Weihermüller, L.; Vereecken, H. & Lambot, S. Accounting for soil surface roughness in the inversion of ultrawideband off-ground GPR signal for soil moisture retrieval, in *Geophysics*, **2012**, 77(1), H1–H7.

$0.068\ \mathrm{m}^3\ \mathrm{m}^{-3}$ for an analysis where roughness is neglected. However, this inversion strategy required a priori information on soil surface roughness, estimated, e.g., from laser profiler measurements.

## 3.1 Introduction

Knowledge of surface water content is essential in the fields of agricultural and environmental engineering, hydrology, meteorology, and climatology (Vereecken *et al.*, 2008; Seneviratne *et al.*, 2010). As the dielectric permittivity of liquid water dominates the dielectric permittivity of other soil components, water is the principal factor governing electromagnetic wave propagation in the soil. This allows us to use geophysical techniques to indirectly measure the surface water content of the soil (Ulaby *et al.*, 1982b).

Many studies have investigated the potential of microwave radar systems to monitor the spatiotemporal variation of the surface and subsurface soil water content. Spaceborne and airborne synthetic aperture radars yield soil moisture estimates on a large spatial scale (1–100 km), which are particularly relevant for catchment-scale studies (Moran *et al.*, 2004). At the field scale, ground-penetrating radar has proven to be successful in many hydrological applications. Reviews on the uses and recent developments of GPR are given by Huisman *et al.* (2003a) and Slob *et al.* (2010). Compared to local measurements such as soil sampling and time-domain reflectometry, GPR has the advantage of allowing noninvasive quantification of soil properties with a high spatial resolution at the field scale. Lambot *et al.* (2004c) proposed a full-waveform forward and inverse modeling approach which applies to off-ground GPR. The electromagnetic model is based on a solution of the 3D Maxwell equations for waves propagating in multilayered media and correctly accounts for antenna effects and antenna-soil interactions. The model was shown to be applicable for reproducing the radar measurements, and model inversion was successfully applied to identify and map surface soil moisture in the field (Jonard *et al.*, 2011b).

Electromagnetic wave reflection on a bare soil is highly dependent on the surface roughness. A distinction can be made between smooth and rough surfaces with respect to the wavelength of the signal based on the Rayleigh criterion ($h_c = \lambda/8\cos(\gamma)$, where $h_c$ is the critical height of the surface protuberances, $\gamma$ is the incidence angle, and $\lambda$ is the wavelength) (Ulaby *et al.*, 1982b). If the surface is smooth and homogeneous (in terms of electrical properties), most of the energy reflected will be in the specular direction (coherent component), while if the surface is rough, diffuse reflections or scattering (incoherent component) can occur leading to less energy being recorded in the specular direction. These diffuse reflections and the reduction of energy in the specular direction should be accounted for to accurately retrieve the surface soil moisture. Previous studies carried out with airborne and spaceborne remote sensing radars also demonstrated the need to take surface roughness into account in signal processing for soil moisture retrieval (Quesney *et al.*, 2000; Baghdadi *et al.*, 2008; Verhoest *et al.*, 2008). The roughness effect has also been shown for GPR (Sai and Ligthart, 2004; Yarovoy *et al.*, 2004; Lambot *et al.*, 2006a; Giannopoulos and Diamanti, 2008; van der Kruk *et al.*, 2010).

Nevertheless, the issue remains poorly investigated for the retrieval of the soil electromagnetic properties by off-ground GPR and no GPR model accounting for roughness is currently available in the literature.

In this chapter, we combine the full-waveform GPR model of Lambot *et al.* (2004c) with the Ament roughness model derived from the Kirchhoff scattering theory (Ament, 1953; Beckmann and Spizzichino, 1987) to retrieve surface soil moisture through signal inversion. To account for surface roughness, the global surface reflection coefficient is multiplied by a scattering loss factor. The proposed approach was validated under laboratory conditions with measurements performed above a sand layer subjected to seven different water contents and four different surface roughness conditions. Numerical experiments were also performed to analyze the well-posedness of the inverse problem.

## 3.2 Experiment

### 3.2.1 Experimental setup

Radar measurements were performed under laboratory conditions above a rectangular wooden container (1.45 x 1.30 $m^2$ area) homogeneously filled with a sand layer 0.09 m in thickness (Figure 3.1) (Lambot *et al.*, 2006a). Below the sand layer, a horizontal metal sheet was installed to control the bottom boundary condition in the electromagnetic model. Indeed, materials underneath this metal sheet have no influence on the measured backscattered signal. The sand was subjected to seven different water contents ranging from dry to wet conditions ($\theta_i$ with $i = 1$ to 7) and four different surface roughness heights ($R_j$ with $j = 1$ to 4), including a smooth surface ($R_1$), resulting in 28 independent configurations ($\theta_i R_j$). For each water content level, the sand was mixed manually to obtain a homogeneous distribution of the water within the whole sand layer and the desired roughness topographies were produced by pressing a cylinder with stones randomly glued onto the surface over the smooth sand surface. Independent surface roughness characterization was performed using a 1 m long mechanical needle-like profiler.

### 3.2.2 Radar system

The radar system was set up using a vector network analyzer (VNA, ZVRE, Rohde and Schwarz, Munich, Germany) as transmitter and receiver, thereby providing an ultra-wideband stepped-frequency continuous-wave system. The antenna system consisted of a linear polarized double-ridged broadband horn antenna (BBHA 9120 D, Schwarzbeck Mess-Elektronik, Schönau, Germany). Antenna dimensions are 22 cm length and 14 x 24 $cm^2$ aperture area, and the $-3$ dB full beamwidth of the antenna is 27° in the E-plane and 22° in the H-plane (at 2 GHz). The antenna nominal frequency range is 1–18 GHz and its isotropic gain ranges from 6–18 dBi. Measurements were performed with the antenna aperture situated at an average height of 23 cm above the soil surface with a normal incidence (Figure 3.1) and by operating frequencies over the range 1–3 GHz (4 MHz step).

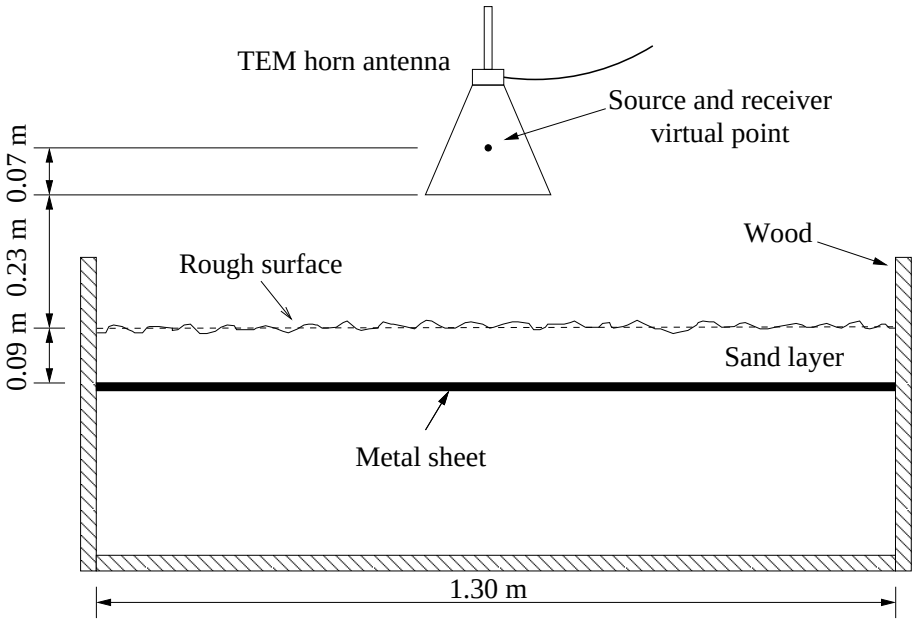


Figure 3.1: Laboratory experimental setup including the sand box made of wood, the off-ground horn antenna, the sand layer subject to different water content and roughness conditions, and a metal sheet at the bottom to control the boundary condition in the electromagnetic model (Lambot *et al.*, 2006a).

## 3.3 Models

### 3.3.1 Radar model

The raw GPR data consist of the frequency-dependent complex ratio $S_{11}(\omega)$ between the backscattered electromagnetic field ($b(\omega)$) and the incident electromagnetic field ($a(\omega)$), with $\omega$ being the angular frequency. Assuming the distribution of the electromagnetic field measured by the antenna to be independent of the scatterer, i.e., only the phase and amplitude of the field change (plane wave approximation over the antenna aperture), Eq. (2.1) is applied to filter out the antenna effects (Lambot *et al.*, 2004c). We derived the specific Green's function using a recursive scheme to compute the transverse electric (TE) and magnetic (TM) global reflection coefficients of the multilayered medium in the spectral domain (Slob and Fokkema, 2002). The transformation back to the spatial domain is performed by numerically evaluating a semi-infinite, complex integral (Lambot *et al.*, 2007).

Full-waveform inverse modeling of the GPR data was performed in the frequency domain to identify the electromagnetic properties (i.e., the relative dielectric permittivity $\varepsilon_\mathrm{r}$ [–] and the electrical conductivity $\sigma$ [S m$^{-1}$]) of the soil (Lambot *et al.*, 2004c). The inverse problem was formulated in the least-squares sense and the objective function to be minimized was accordingly defined as follows

$$\phi_1(\mathbf{b}) = \left|\mathbf{G}_{\mathrm{xx}}^{\uparrow *} - \mathbf{G}_{\mathrm{xx}}^{\uparrow}\right|^T \left|\mathbf{G}_{\mathrm{xx}}^{\uparrow *} - \mathbf{G}_{\mathrm{xx}}^{\uparrow}\right| \tag{3.1}$$

where $\mathbf{G}_{\mathrm{xx}}^{\uparrow *}(\omega)$ and $\mathbf{G}_{\mathrm{xx}}^{\uparrow}(\mathbf{b},\omega)$ are, respectively, the measured and modeled Green's functions in the frequency domain, and $\mathbf{b}$ is the parameter vector to be estimated (e.g., $\mathbf{b} = [\varepsilon_\mathrm{r}, \sigma]$, depending on the unknowns). Because the Green's functions are complex vectors, the difference between observed and modeled data is expressed by the magnitude of the errors in the complex plane, thereby inherently accounting for both amplitude and phase information. Optimization was performed using the global multilevel coordinate search algorithm (Huyer and Neumaier, 1999) combined sequentially with the local Nelder-Mead simplex algorithm (Lagarias *et al.*, 1998) as proposed by Lambot *et al.* (2004b). For this inversion, the distance between the soil surface and the metal sheet $h$ [m] was assumed to be known (Figure 3.1).

Inversion in the time domain also was performed by focusing on a time window containing the surface reflection only (Lambot *et al.*, 2006c; Jonard *et al.*, 2011b). The measured and modeled frequency domain Green's functions were first transformed in the time domain using the inverse Fourier transform. The inverse problem consisted of finding the minimum of the objective function defined as Eq. (2.2). Optimization was performed using the local Levenberg-Marquardt algorithm (Marquardt, 1963).

A sand-specific empirical model (third-order polynomial) derived in Lambot *et al.* (2006a) was used to relate GPR-derived relative dielectric permittivity to the volumetric water content $\theta$

$$\theta = 2.30 \times 10^{-4}\,\varepsilon_\mathrm{r}^3 - 6.28 \times 10^{-3}\,\varepsilon_\mathrm{r}^2 + 7.50 \times 10^{-2}\,\varepsilon_\mathrm{r} - 1.51 \times 10^{-1} \tag{3.2}$$

### 3.3.2 Surface roughness model

In general, the surface is assumed to be stationary with a random Gaussian height distribution. The soil surface can therefore be described by the following statistical quantities: the standard deviation of the surface height $s_{\mathrm{r}}$ [m], the spatial autocorrelation function, and the spatial correlation length (Fung *et al.*, 1992).

To account for roughness effects on radar electromagnetic wave propagation, the Ament model (Ament, 1953; Beckmann and Spizzichino, 1987) was used. This model, which is derived from the Kirchhoff scattering theory, describes the scattering losses in the specular direction due to the reflection on a rough interface. This model has been applied in several studies investigating the roughness effect on electromagnetic wave scattering, e.g., by Pinel *et al.* (2007) for radar reflection over sea surfaces and Landron *et al.* (1996) for radar reflection on rough building materials. In this model, the global surface reflection coefficient is multiplied by a scattering loss factor ($\rho$), which is based on the Rayleigh parameter as a function of frequency, namely,

$$\rho = e^{-\frac{g}{2}} \tag{3.3}$$

with

$$g = \left(\frac{4\pi\, s_{\mathrm{r}}\, \cos\gamma_{\mathrm{i}}}{\lambda}\right)^2 \tag{3.4}$$

where $s_{\mathrm{r}}$ is the standard deviation of the surface height, $\gamma_{\mathrm{i}}$ is the angle of incidence, and $\lambda$ is the free space wavelength of the incident wave. The modified reflection coefficient $R^{\mathrm{R}}$ that models the reduction of the signal power in the specular direction is then defined as

$$R^{\mathrm{R}}_{\mathrm{TE}} = \rho\, R^{\mathrm{F}}_{\mathrm{TE}} \tag{3.5}$$

$$R^{\mathrm{R}}_{\mathrm{TM}} = \rho\, R^{\mathrm{F}}_{\mathrm{TM}} \tag{3.6}$$

where $R^{\mathrm{F}}_{\mathrm{TE}}$ and $R^{\mathrm{F}}_{\mathrm{TM}}$ are, respectively, the global TE- and TM-mode surface reflection coefficients for a smooth surface. Equations (3.5) and (3.6) assume that the surface heights have a Gaussian distribution with negligible sharp edge and shadowing effects. The model also assumes that there is no multiple scattering (Beckmann and Spizzichino, 1987). In our case, the incidence is normal ($\gamma_i = 0$) and the model is applied to the spectral-domain global reflection coefficients of the first interface (sand surface) of the 3D layered medium.

## 3.4 Results and discussion

### 3.4.1 Response surface analysis

To analyze the well-posedness of the inverse problem, we calculated response surfaces of the objective function using synthetic error-free data and real data. Real data correspond to intermediate water content and roughness conditions ($\theta$ = 0.14 m$^3$ m$^{-3}$; $s_{\mathrm{r}}$ = 0.49 cm), but similar results were obtained for the other conditions. Inversions were performed in a relatively large parameter

space ($2 < \varepsilon_r < 12$; $0 < h < 0.25$ m; $1 \times 10^{-5} < \sigma < 1 \times 10^{-1}$ S m$^{-1}$; $0 < s_r < 0.025$ m), which contained the exact solutions. The range of each parameter was divided into 200 discrete values resulting in 40000 objective function values for each contour plot.

Figures 3.2 and 3.3 show the response surfaces of the logarithm of the objective function values in four parameter planes $\varepsilon_r$–$h$, $h$–$s_r$, $\sigma$–$s_r$, and $\varepsilon_r$–$s_r$ and for the full-waveform inversion case (Eq. (3.1)). For the synthetic data (left panel), each response surface shows a well-defined global minimum, which reveals that sufficient information is contained in the inverse problem to estimate the parameters of interest simultaneously. In the $\varepsilon_r$–$h$ parameter plane, the global minimum region exhibits a banana shape, which suggests an important negative correlation between these parameters. A similar signal can indeed be obtained for either a low dielectric permittivity with a high-layer thickness, or a high dielectric permittivity with a low-layer thickness. The $h$–$s_r$ and $\varepsilon_r$–$s_r$ response surfaces show an elliptical global minimum region parallel to the $s_r$ axis. Additionally, local minima can also be observed. In general, the response surfaces suggest that the two parameter pairs are uncorrelated. Indeed, $s_r$ determines the attenuation of the wave while $h$ and $\varepsilon_r$ determine the propagation time of the wave throughout the layer. These parameters then independently determine the amplitude ($s_r$) and the phase ($h$ or $\varepsilon_r$) of the radar electromagnetic waves propagating through the soil. In the $\sigma$–$s_r$ parameter plane, no local minima can be observed and the parameters are negatively correlated. In fact, a high $\sigma$ will strongly attenuate the signal throughout the layer as well as a high $s_r$. Response surfaces pertaining to the real data (right panel) exhibit the same general shape as the synthetic response surfaces. For each parameter plane, the position of the global minimum is unchanged, which demonstrates the stability of the inverse problem with respect to measurement and modeling errors. As expected, the values of the objective function are systematically higher and the global minimum regions are flatter for the real data, resulting in an increase in parameter uncertainty (note that the color scale differs for the single response surfaces). In the $\varepsilon_r$–$h$ parameter plane, given the negative correlation of the parameters and the larger global minimum region, compared to the synthetic case, an accurate estimation of $\varepsilon_r$ will require a priori information about the layer thickness ($h$).

Figure 3.4 shows the response surfaces of the logarithm of the objective function (Eq. (2.2)) in the $\varepsilon_r$–$s_r$ parameter plane for the surface reflection inversion. Figures 3.4a and 3.4b show the response surface with synthetic data and real data, respectively. The synthetic response surface shows a well-defined minimum. However, for the real data, the values of the objective function are higher and the global minimum region is flatter, resulting in larger uncertainty in the estimation of the parameters. For both response surfaces, a significant positive correlation between $s_r$ and $\varepsilon_r$ can be observed. As a result, an increase in $s_r$ has a similar effect on the objective function as a decrease in $\varepsilon_r$, which increases parameter estimation uncertainty. In fact, the reflection coefficient will decrease with an increase of the surface roughness or a decrease of the water content/dielectric permittivity. An accurate estimation of $\varepsilon_r$ is therefore not possible without knowledge of any soil roughness parameters, especially

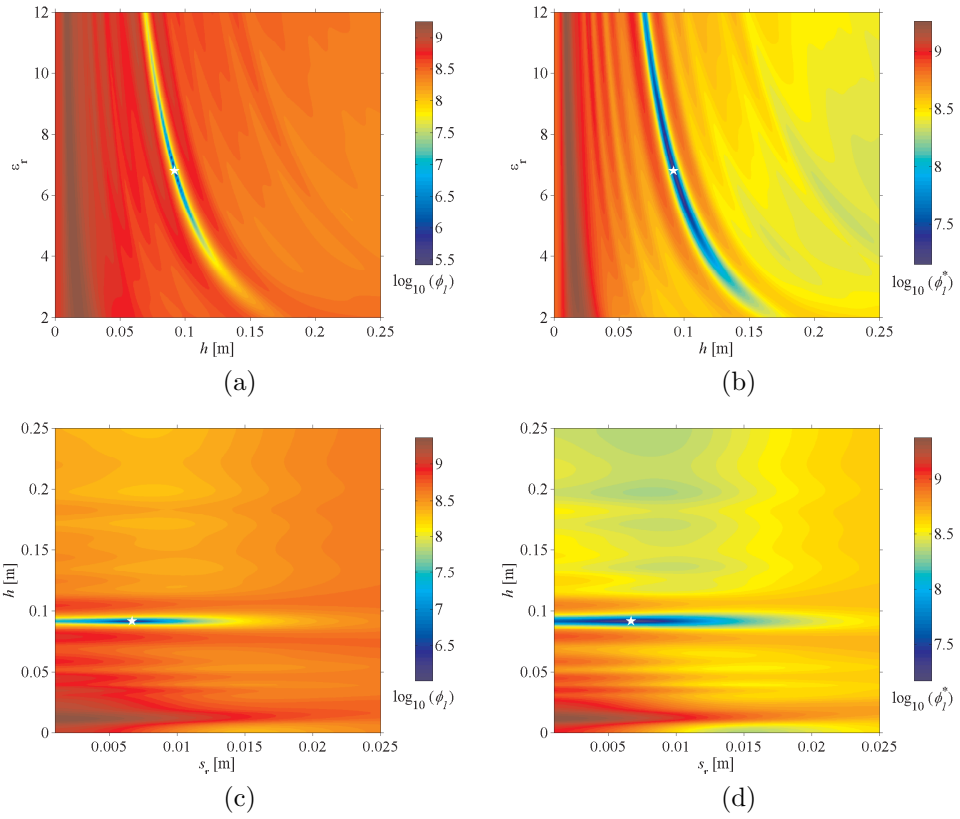


Figure 3.2: Response surfaces of the objective function logarithm $\log_{10}(\phi_1(\mathbf{b}))$ for the full-waveform inversion in the $\varepsilon_\mathrm{r}$ –$h$ and $h$–$s_\mathrm{r}$ parameter planes. Left-hand plots correspond to numerically generated error-free data ($\phi_1(\mathbf{b})$) and right-hand plots correspond to real data ($\phi_1^*(\mathbf{b})$). The asterisk represents the global minimum of the objective function. Note that the color scale differs for the single response surfaces.

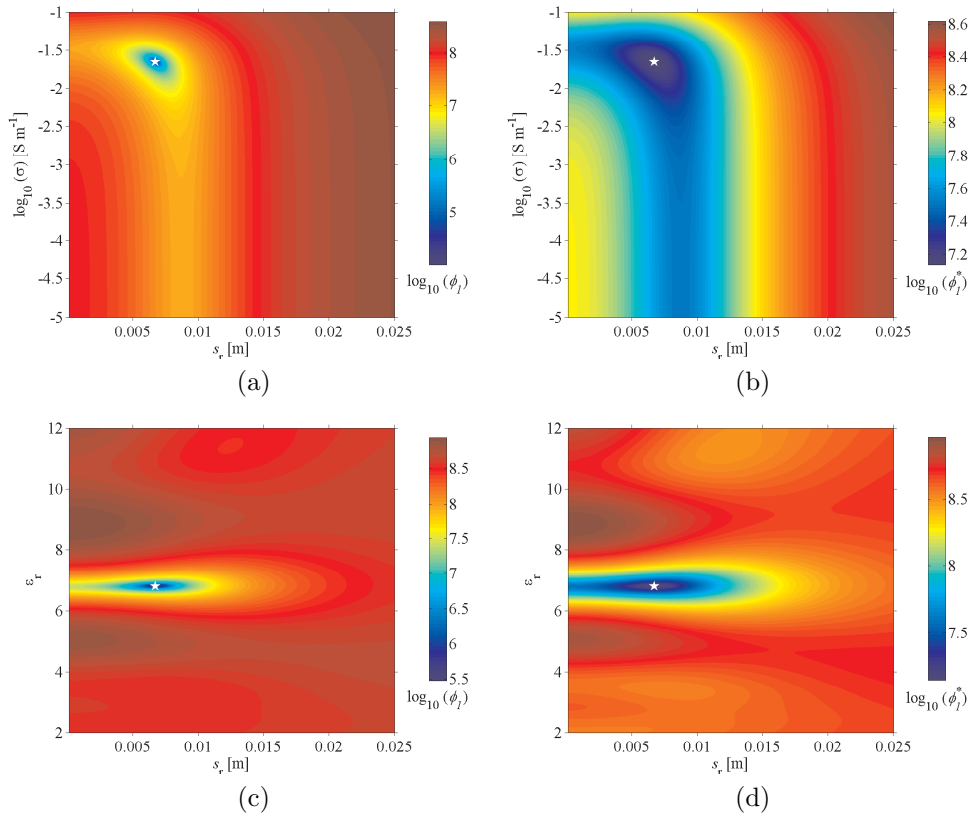


Figure 3.3: Response surfaces of the objective function logarithm $\log_{10}(\phi_1(\mathbf{b}))$ for the full-waveform inversion in the $\sigma$–$s_\mathrm{r}$ and $\varepsilon_\mathrm{r}$–$s_\mathrm{r}$ parameter planes. Left-hand plots correspond to numerically generated error-free data ($\phi_1(\mathbf{b})$) and right-hand plots correspond to real data ($\phi_1^*(\mathbf{b})$). The asterisk represents the global minimum of the objective function. Note that the color scale differs for the single response surfaces.

for the real data case. Compared to the full-waveform inversion, this increase in uncertainty comes from the lower information content in the radar data when focusing on the surface reflection only. Indeed, for the surface reflection inversion, $\varepsilon_r$ and $s_r$ information is obtained from the surface reflection only. As a consequence, information about $\varepsilon_r$ and $s_r$ is correlated. For the full-waveform inversion, similar information is obtained from the surface reflection. However, information about $\varepsilon_r$ is also obtained from the two-way travel time through the soil layer. This additional information allows us to estimate $\varepsilon_r$ with higher accuracy and without a priori information about $s_r$. The surface reflection inversion strategy is particularly useful under field conditions for which layering is a priori unknown.

### 3.4.2 Green's functions

Figure 3.5 depicts the measured and modeled Green's function in the frequency domain for two different combinations of water content and roughness level (Figure 3.5a: $\theta = 0.15$ m$^3$ m$^{-3}$–$s_r = 0.33$ cm; Figure 3.5b: $\theta = 0.20$ m$^3$ m$^{-3}$–$s_r = 0.88$ cm). Other scenarios are similar and show intermediate results. Figures 3.5a and 3.5b show that the modeled amplitude of the Green's function does not fit measurements above 2 GHz if no roughness correction is applied for both water content and roughness conditions. The modeled amplitude of the Green's function overestimates the measurements and this overestimation, as expected, increases with frequency (Lambot *et al.*, 2006a). We observe that the roughness model describes this behavior relatively well, although some discrepancies remain due to oscillations in the Green's function amplitude that cannot be described by the scattering loss factor (exponential behavior only). Indeed, the scattering loss factor applied in this study accounts only for the reduction of energy in the specular direction. As a result, only the coherent component is assumed to contribute to the reflected signal. The remaining Green's functions oscillations could therefore be attributed to the contribution of the incoherent components. In both cases, the phase of the Green's function is properly reproduced and corresponds to the propagation times in air and sand layer.

### 3.4.3 Full-waveform inverse estimations

In Figure 3.6, the roughness standard deviation $s_r$ measured by the needle-like profiler was compared to values inverted using the full-waveform inversion (Eq. (3.1), $\mathbf{b} = [\varepsilon_r, \sigma, s_r]$). In total, twenty-one configurations (3 roughness levels combined with 7 water content levels) were analyzed. Although the inversion failed for one scenario ($\theta_2 R_2$), a relatively good agreement was obtained between the real and GPR-derived values ($R^2 = 0.55$ and RMSE = 0.22 cm). In general, inverted data slightly overestimated the measured $s_r$. To estimate the sand dielectric permittivity, the use of the roughness model did not improve the estimations compared to the smooth model. This is due to the fact that the permittivity information is not only contained in the surface reflection, but also in the two-way travel time between the sand surface and the underlying

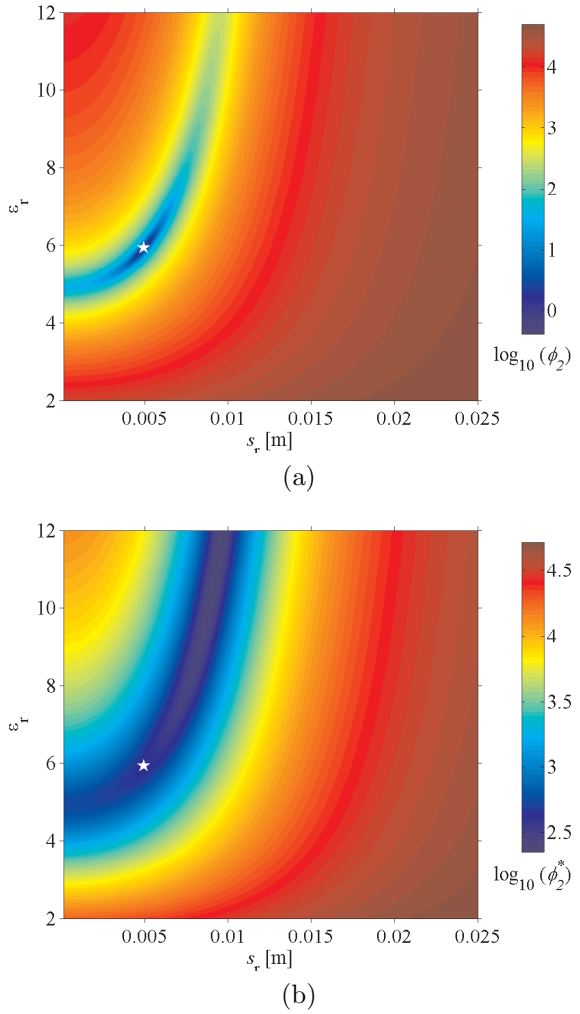


Figure 3.4: Response surfaces of the objective function logarithm $\log_{10}(\phi_2(\mathbf{b}))$ for the surface reflection inversion in the $\varepsilon_r$–$s_r$ parameter plane using (a) numerically generated error-free data ($\phi_2(\mathbf{b})$) and (b) real data ($\phi_2^*(\mathbf{b})$). The asterisk represents the global minimum of the objective function. Note that the color scale differs for the two response surfaces.

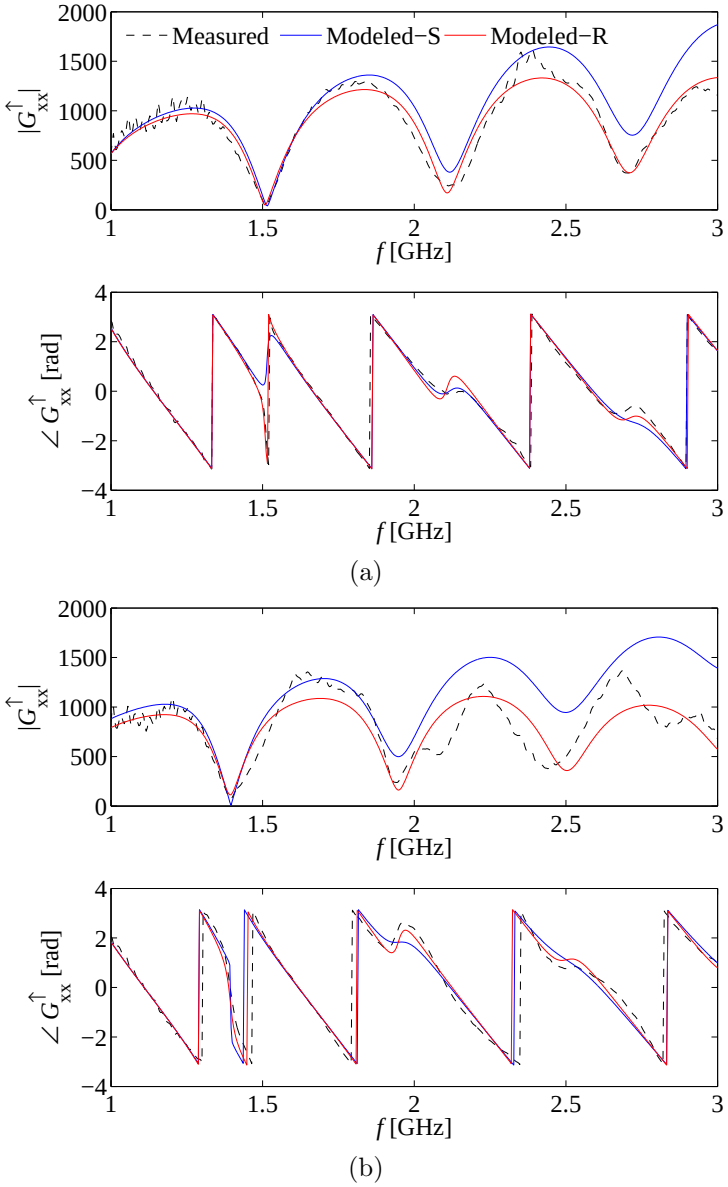


Figure 3.5: Measured (dashed black line) and modeled (Modeled-S: without using a roughness correction and Modeled-R: with a roughness correction; solid blue and red lines, respectively) amplitude and phase of the frequency-domain Green's function. Data are presented for two water content and roughness height combinations ($\theta = 0.15$ m$^3$ m$^{-3}$–$s_r = 0.33$ cm (a), and $\theta = 0.20$ m$^3$ m$^{-3}$–$s_r = 0.88$ cm (b)).

perfect electrical conductor. Only the estimation of the electrical conductivity was affected, which is due to energy loss by surface scattering.

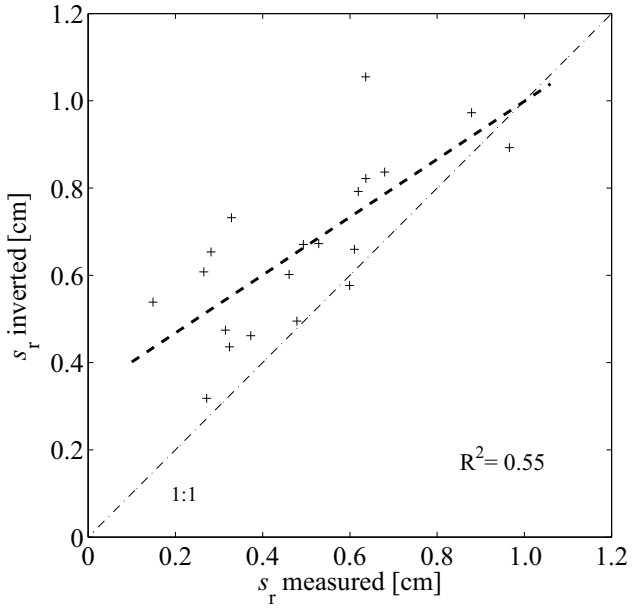


Figure 3.6: Standard deviation of the GPR-derived roughness amplitude with respect to the real values.

### 3.4.4 Surface reflection inverse estimations

For this scenario, only the surface dielectric permittivity was inverted for (Eq. (2.2), $\mathbf{b} = [\varepsilon_r]$). The results for the largest roughness level ($s_r$ between 0.6 and 1.0 cm) are presented in Figure 3.7 and are expressed in terms of water content using the sand-specific petrophysical relationship (Eq. (3.2)). The errors in the estimation of water content are presented for both models. The errors are defined as the absolute difference between the estimation of water content using the smooth or roughness model and the GPR-derived water content for the same water content level but with a smooth surface. Following the results presented in Lambot *et al.* (2004c), the radar approach can indeed be used as a reference to accurately estimate the medium permittivity for the smooth case and this experimental setup. In all cases, the use of the roughness model significantly decreases the estimation errors, with variable benefits depending on actual water content. With the roughness model, the error is 1.2–13.2 times smaller compared to the smooth model. The RMSE in terms of water content is 0.068 $m^3$ $m^{-3}$ when considering the smooth model, while with the roughness model the RMSE is only 0.034 $m^3$ $m^{-3}$. In this last case, the roughness was known a priori.

To evaluate the impact of the unknown roughness on the water content retrieval, inversions were also performed using the roughness model and by assuming the roughness unknown (Eq. (2.2), $\mathbf{b} = [\varepsilon_\mathrm{r},\, s_\mathrm{r}]$). The RMSE in terms of water content is 0.057 $\mathrm{m}^3\ \mathrm{m}^{-3}$, which is similar to the results obtained without accounting for roughness, i.e., with the smooth model. The roughness model significantly improves the retrieval of the water content compared to the smooth model when roughness is known. However, without a priori knowledge of the roughness, the accuracy of the retrieval does not differ significantly between the two models. Similar results were obtained for the lower roughness levels, but with smaller effects.

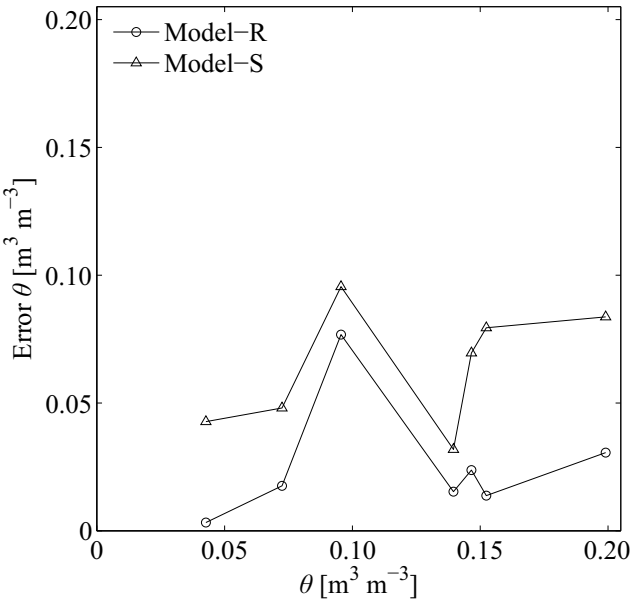


Figure 3.7: Error in the estimation of water content $\theta$ with the surface reflection inversion using the roughness model (Model-R) and the smooth model (Model-S).

## 3.5 Conclusions

The Ament model accounting for scattering losses in the specular direction for rough surfaces was applied to invert off-ground GPR data using Lambot's model. Full-waveform inversion permitted simultaneous reconstruction of the sand dielectric permittivity and the standard deviation of the surface roughness. For this inversion, information about the soil layering was assumed to be known. A practical field inversion strategy based on surface reflection permitted the retrieval of the surface permittivity with a significantly higher accuracy compared to a smooth model. However, in that case, roughness should be

independently measured, e.g., by a laser profiler. The proposed method appears to be promising for surface soil moisture mapping in reasonably rough environments (roughness amplitude $< 1/4$ of the wavelength).

# Chapter 4

# Characterization of tillage effects on the spatial variation of soil properties using GPR and EMI*


## Abstract

Tillage practices influence physical, chemical, and biological soil properties, which also affect soil quality and consequently plant growth. In this study, the main objective was to evaluate the effects of different tillage systems on soil physical properties by using geophysical methods, namely, ground-penetrating radar and electromagnetic induction. Additional measurements such as soil sampling, capacitance probes, and soil penetrometer data were acquired as ground truths. The study was performed on three contrasting tillage systems, i.e., conventional tillage (CT), deep loosening tillage (DL), and reduced tillage (RT), implemented on different plots of an agricultural field. The data showed that tillage influences the soil resistance in the shallow soil layers (deeper tillage decreases soil resistance), which could be partly seen in the on-ground GPR data. In addition, reference soil water content measurements (capacitance probes and soil sampling) were in fairly good agreement with the water content estimates from off-ground GPR. We also observed that the tillage influences shallow surface SWC, while deeper SWC seems to be unaffected by tillage. Mean surface SWC was significantly lower for CT than for DL and RT, which was partly explained by lower pore connectivity between the topsoil and the deeper layers after conventional tillage. Moreover, the variance of the SWC


*This chapter is adapted from:
Jonard, F.; Mahmoudzadeh, M.; Roisin, C.; Weihermüller, L.; André, F.; Minet, J.; Vereecken, H. & Lambot, S. Characterization of tillage effects on the spatial variation of soil properties using ground-penetrating radar and electromagnetic induction, in *Geoderma*, **2012**, under review.

within the conventional tillage plots was larger than within the other plots. This larger SWC variability could be explained by a larger soil heterogeneity induced by the plowing process. Overall, this study confirms the potential of GPR and EMI for the determination of the soil physical properties at the field scale and for the assessment of agricultural management practices.

## 4.1 Introduction

Agricultural management practices can affect soil physical, chemical, and biological properties with consequences for the movement of water, nutrients, and pollutants in the vadose zone, and for plant growth (Strudley *et al.*, 2008). Alternative management practices such as conservation tillage or reduced tillage are encouraged to prevent environmental risks like soil erosion, flooding, and pesticide leaching in the groundwater. However, these practices are weakly adopted by the producers as their effects on soil and crop production are not yet well-understood (Alletto *et al.*, 2011). The impact of tillage practices on soil hydraulic properties (Sauer *et al.*, 1990; Ndiaye *et al.*, 2007; Strudley *et al.*, 2008; Schwen *et al.*, 2011a,b) and their consequences on preferential flow (Kulasekera *et al.*, 2011; Elliott *et al.*, 2000), soil state-variables (soil water content and soil temperature) (Kovar *et al.*, 1992; Tan *et al.*, 2002), soil physical properties (soil penetration resistance, soil bulk density, soil porosity) (Jabro *et al.*, 2009), and plant growth (Alletto *et al.*, 2011; Zhang *et al.*, 2011) has been subject to more intensive research over the last decade. However, according to the recent review of Strudley *et al.* (2008), experimental results from field and laboratory studies do not show consistent effects of tillage practices on soil properties. Moreover, to get information about the soil properties, most of these studies have used invasive methods such as time-domain reflectometry, capacitance sensor, or soil sampling, which are time-consuming and offer only local information. Therefore, these techniques are limited to a small spatial extent. In addition, time-lapse measurements are not feasible within agricultural fields, which would provide valuable insights into the changes of the state variables (e.g., soil water content and soil temperature) or processes involved.

In that respect, ground-penetrating radar and electromagnetic induction are non-invasive geophysical techniques which can be used for the characterization of the shallow subsurface properties at the field scale and with high temporal and spatial resolutions (Huisman *et al.*, 2003a; Slob *et al.*, 2010; Jonard *et al.*, 2011b; André *et al.*, 2012). EMI is sensitive to soil electrical conductivity, which is mainly affected by soil water content, clay content, and salinity (Corwin and Lesch, 2005; Friedman, 2005), while GPR is sensitive to both soil electrical conductivity and dielectric permittivity, the latest primarily depending on SWC (Huisman *et al.*, 2003a). Yet, until now, very few studies have used geophysical techniques to investigate the impact of tillage practices (e.g., Oleschko *et al.*, 2008; Richard *et al.*, 2010; Basso *et al.*, 2011). Recently, Müller *et al.* (2009) compared different geophysical techniques to characterize tillage effects on SWC and electrical resistivity. However, their sampling scheme was limited to two transects, which did not permit to fully explain their observations. Basso *et al.* (2011) used electrical resistivity tomography applied to an entire field area,

which permitted to study spatiotemporal dynamics of soil physical properties. Nevertheless, a high resolution could not be achieved, especially at the soil surface.

The general objective of this study is to analyze the effects of tillage practices on the spatial variation of soil properties by using geophysical techniques. In particular, we focused on surface soil water content, bulk soil electrical conductivity, and mechanical resistance. The study was conducted on an agricultural field in the loess belt of central Belgium (Gentinnes). GPR and EMI measurements were performed over three contrasting tillage systems, i.e., conventional tillage, deep loosening tillage, and reduced tillage. In this chapter, we first present on-ground GPR images and soil strength maps to characterize the tillage effects on soil penetration resistance. Soil electrical conductivity and SWC maps from EMI and off-ground GPR data, respectively, are then presented and interpreted in the light of *in-situ* observations. Finally, the tillage effects on SWC and its spatial distribution are discussed.

## 4.2 Materials and methods

### 4.2.1 Experimental site

The study was conducted on an agricultural field in Gentinnes, located in the loess belt of central Belgium (50°35' N 4°35' E). The soil is a loam soil classified as an Orthic Luvisol according to the FAO classification. Elevation varies between 137 and 145 m above sea level. The silt fraction dominates largely the clay and sand fractions (20.0, 74.5, and 5.5% for clay, silt, and sand, respectively) in the topsoil (0–25 cm) and the organic carbon content was 8.67 g $kg^{-1}$. The exact water table depth is unknown, but is in general deeper than 2 m. Since fall 2005, a soil tillage experiment was implemented on the field to compare three contrasting tillage systems: (1) conventional tillage with mouldboard ploughing to ≈27 cm depth, (2) deep loosening tillage with a heavy tine cultivator to ≈30 cm depth, and (3) reduced tillage with a spring tine cultivator to ≈10 cm depth (Figure 4.1). The field was divided into 20 plots of 30 × 18 $m^2$ and each plot was characterized by one of the three tillage systems (Figure 4.2). Only 12 plots were used for the geophysical measurements (4 replications per tillage) and 3 other plots were used for the soil strength measurements. These 3 plots were located next to the 12 other plots, at about 15 m on the south-western part of the field (not shown in Figure 4.2). The geophysical measurements were performed on April 13, 2010, while the soil strength measurements were performed on April 27, 2010. Average monthly rainfall recorded at a meteorological station located about 7 km apart from the field, was 75.3 mm in February, 36.0 mm in March, and 23.4 mm in April 2010. No rain was observed during the two measurement days and the daily reference evapotranspiration was close to 3 mm for both dates (Figure 4.3).

(a)

(b)


(c)

Figure 4.1: Tillage systems implemented at the Gentinnes study site : (a) conventional tillage with mouldboard ploughing, (b) deep loosening tillage with a heavy tine cultivator, and (c) reduced tillage with a spring tine cultivator.

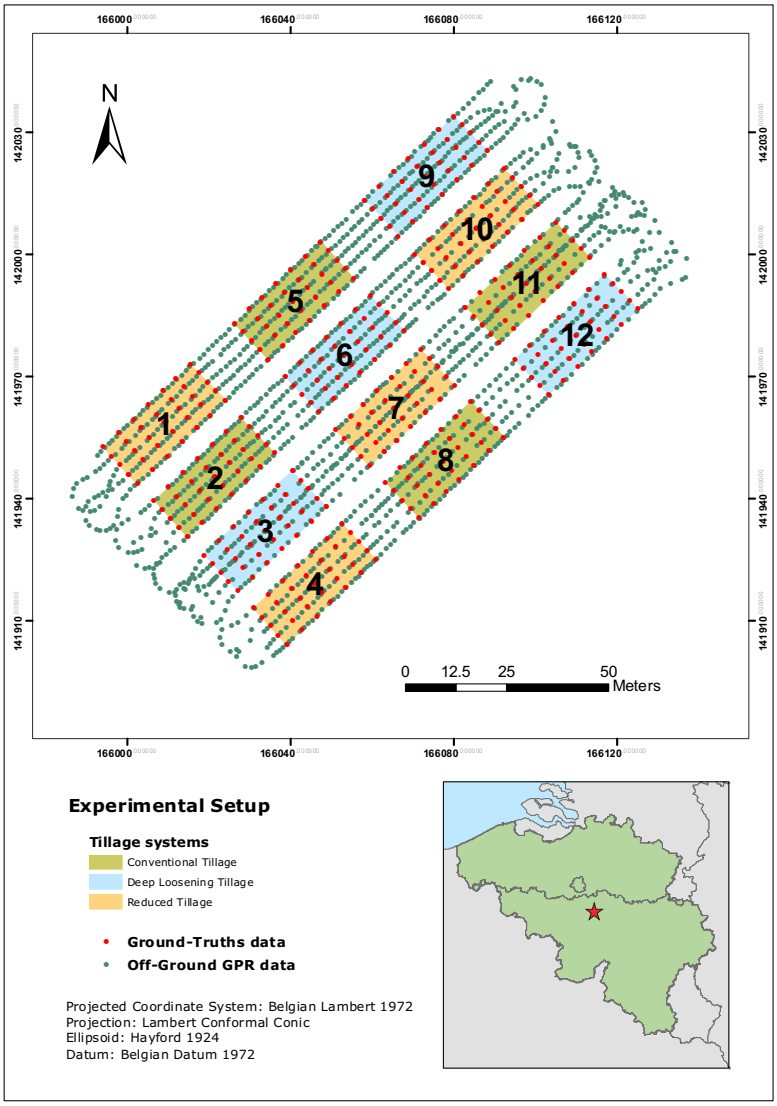


Figure 4.2: Study site of Gentinnes, Belgium. Sampling points for the ground-truth measurements and the off-ground GPR data acquisition are shown. Background colors represent the three tillage systems: conventional tillage, deep loosening tillage, and reduced tillage.

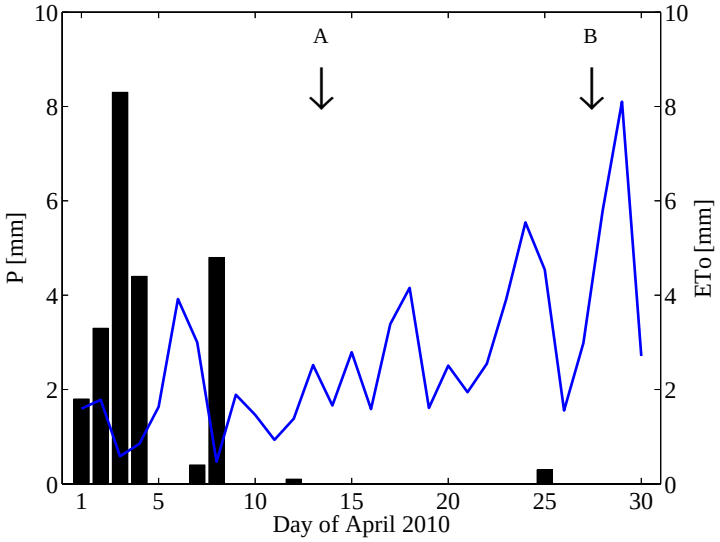


Figure 4.3: Daily rainfall ($P$) and daily reference evapotranspiration ($ETo$) in mm measured at the Ernage-Gembloux weather station during April 2010. Arrows indicate the first (A) and second (B) measurement day.

### 4.2.2 Agricultural practices

Initially, the study field was entirely ploughed for several decades. Since 2005, it has been divided according to three tillage systems (CT, DL, and RT) and the same tillage treatment was implemented every year at the same plot, excepted in 2006 and 2008, where the tillage systems DL was replaced by the tillage system RT. In 2006 and 2008, sugar beet was planted in April after seed bed preparation (with rotary harrow and drill), while winter wheat was sown in November (also with rotary harrow and drill). The wheat straws were chopped during the harvest and then mixed within the top soil layer by a stubble harrowing. White mustard was used as cover crop for all the plots during three fallow periods (2005–2006, 2007–2008, 2009–2010), i.e., before sugar beet planting. White mustard was always sown in September by using rotary harrow and drill. The three tillage treatments (CT, DL, and RT) were systematically implemented before white mustard or winter wheat sowing. In April 2010, one day before the geophysical measurements, a minimum tillage was implemented to all the plots with a disc harrow (depth to 5 cm) in order to reduce soil surface roughness for the radar measurements (Jonard *et al.*, 2012). The day after the geophysical measurements, the whole field was prepared for seed bed with disc harrow (depth to 3 cm) and flax was sown.

### 4.2.3 Reference soil water content measurements

Undisturbed soil samples (100 $cm^3$ Kopecky-rings) were used as reference measurement for the volumetric SWC. Soil samples were collected between 0–5 cm

depth on a regular grid in each plot ($5 \times 3$ m spacing, i.e., 35 samples per plot and 420 samples in total). Soil samples were also taken at two locations in each plot between 0–75 cm depth at 5 cm step. The volumetric water content of the soil samples was obtained by the weight loss after oven-drying at 105°C for at least 48h. At each sampling point, dielectric permittivity was measured using two capacitance water content sensors, namely, the ThetaProbe ML2x sensor (Delta-T Devices Ltd, Cambridge, England) and the 5TE sensor (Decagon Devices, Inc., Pullman, Washington, USA). The soil water content was then determined from the soil dielectric permittivity using Topp's model (Eq. (2.10)).

### 4.2.4 Geophysical measurements

#### Ground-penetrating radars

Two different ground-penetrating radar systems were used in this study: (1) monostatic off-ground radar for SWC retrieval and (2) bistatic common on-ground radar for soil stratigraphy imaging, whereby both radar systems were carried by an all-terrain vehicle (Figure 4.4).

**Off-ground GPR** The radar system was set up using a ZVL vector network analyzer (VNA, Rohde & Schwarz, Munich, Germany), thereby providing an UWB SFCW radar. The antenna system consisted of a transverse electromagnetic, double-ridged broadband horn antenna (BBHA 9120 F, Schwarzbeck Mess-Elektronik, Schönau, Germany) and the antenna aperture was situated at 1.1 m above the ground. The antenna was 95 cm long with a $68 \times 96$ cm$^2$ aperture area and a $-3$ dB full beamwidth in the E-plane and the H-plane of 46° (at 400 MHz). The antenna nominal frequency range was 0.2–2 GHz and its isotropic gain ranged from 9–14 dBi.

With this radar system, the raw data consist of the frequency-dependent complex ratio $S_{11}$ between the backscattered electromagnetic field ($b(\omega)$) and the incident electromagnetic field ($a(\omega)$), with $\omega$ being the angular frequency. The raw GPR data were performed sequentially at 301 stepped operating frequencies over the range 0.2–2 GHz with a frequency step of 6 MHz. Only lower frequency data (0.2–0.4 GHz), which were not affected by soil surface roughness, were used for the inversions. Assuming the distribution of the electromagnetic field measured by the antenna to be independent of the scatterer, i.e., only the phase and amplitude of the field change (plane wave approximation over the antenna aperture), Eq. (2.1) is applied to filter out the antenna effects (Lambot *et al.*, 2004c).

In order to identify the surface dielectric permittivity, inversion of the Green's function is performed in the time domain, focusing on a time window containing the surface reflection only (Lambot *et al.*, 2006c). The inverse problem is formulated in the least-squares sense and the objective function to be minimized is accordingly defined as Eq. (2.2). As for the capacitance water content sensors, the soil water content was then derived from the soil dielectric permittivity using Topp's model (Eq. (2.10)).

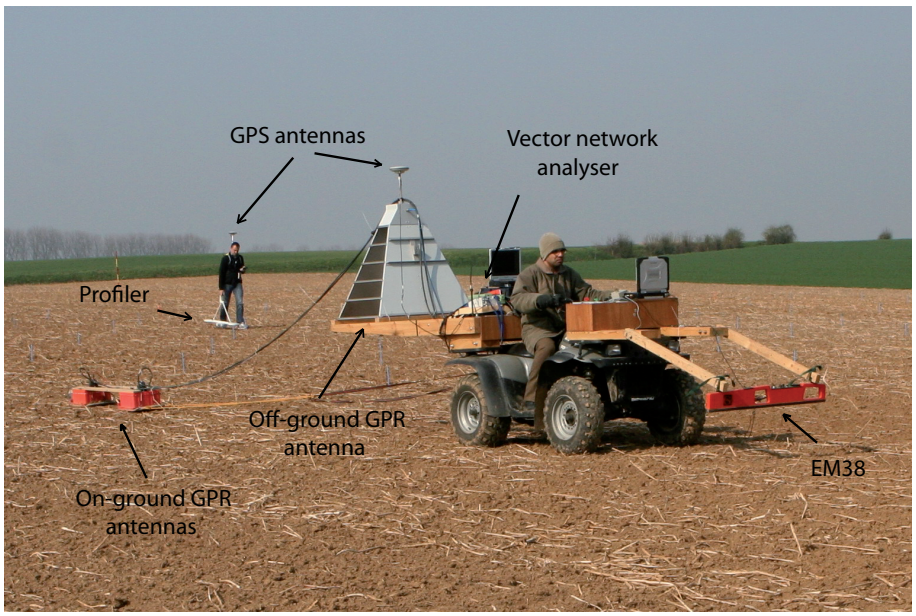


Figure 4.4: Off-ground GPR (horn antenna linked to a vector network analyser, D-GPS device, and a PC), on-ground GPR, and EM38 sensor mounted on an all-terrain vehicle as well as Profiler sensor carried manually.

**On-ground GPR** We used a time-domain GPR system (model SIR-20, Geophysical Survey Systems, Inc., Salem, Massachusetts, USA) combined with a transmitting ($Tx$) and receiving ($Rx$) 400 MHz center-frequency shielded bowtie antenna with a $Tx$ and $Rx$ offset of 0.16 m. GPR data were collected with a sampling interval of 5 cm and 512 samples per scan were recorded with 16 bits per sample. The GPR produces a Ricker-type pulse with frequency bandwidth of 100–800 MHz. The gain function was enabled in 5 points in order to highlight deeper reflections. Time window was limited to 50 ns.

### Electromagnetic induction

Electromagnetic induction data were acquired with the Profiler EMP-400 (Geophysical Survey Systems, Inc., Salem, Massachusetts, USA) and the EM38 (Geonics Limited, Mississauga, Ontario, Canada) sensors. The Profiler was manually carried (at about 0.10 m above the ground surface) and allowed to perform measurements simultaneously at three different frequencies (5, 10, and 15 kHz). The data were recorded every second, corresponding to an average sampling interval of about 0.80 m. In contrast, the EM38 was mounted on the front of the all-terrain vehicle (at about 0.30 m above the ground surface) (see Figure 4.4) and the data were only recorded at one frequency (14.7 kHz). Profiler data were collected with horizontal and vertical dipole orientations, while EM38 measurements were performed with vertical dipole orientation only. The use of different frequencies and dipole orientations permitted to investigate dif-

ferent soil depths. All equipments (GPR and EMI sensors) were georefferenced by means of a differential GPS (D-GPS).

### 4.2.5 Soil strength measurements

The soil strength measurements were performed in three plots characterized by the three tillage methods and located just next to the investigated plots. These measurements were performed two weeks after the geophysical measurements. A fully automated penetrometer (30° angle cone with a base area of 1 $cm^2$) mounted on a small vehicle was used as described by Roisin (2007) (Figure 4.5). Two areas of $80 \times 80$ $cm^2$ placed side by side were investigated. These two squares were divided along a $16 \times 16$ lattice (with 5-cm spacing between neighboring points) yielding a total of 256 nodes each. At each node, a penetration was performed, and data were collected every centimeter from the surface down to a depth of 45 cm. This procedure resulted in a $32 \times 32$ matrix of resistance values at each of 45 depth levels.

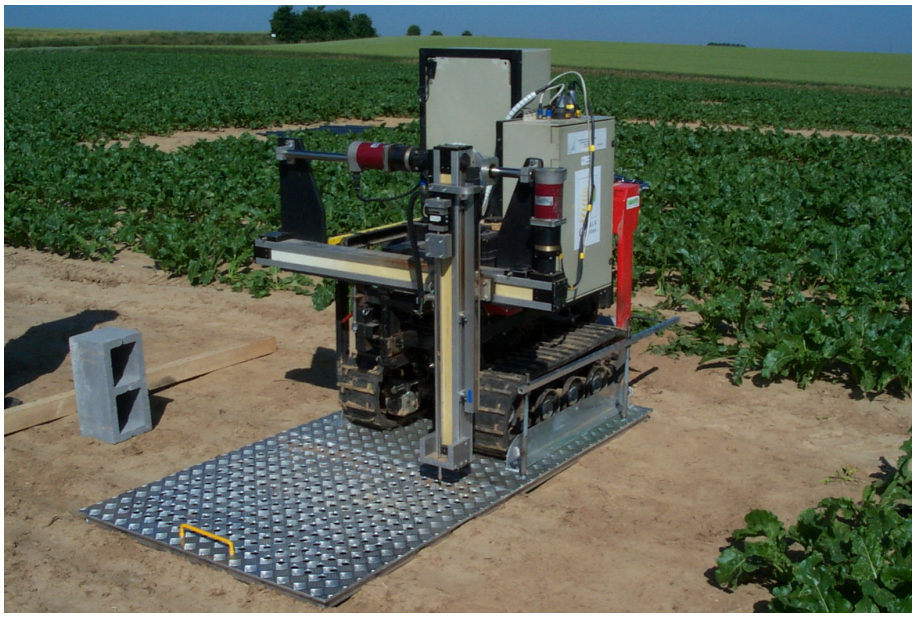

Figure 4.5: Fully automated penetrometer used for the soil strength measurements.

## 4.3 Results and discussion

### 4.3.1 Shallow soil stratigraphy imaging

First, we analyzed the shallow soil stratigraphy using the 2D soil strength maps as depicted in Figure 4.6 obtained by the penetrometer for the three different tillage systems (CT, DL, and RT). It has to be noted that the 2D

vertical profiles were calculated by averaging the data collected in 3D over one direction (y-axis) for better visualization. For all cases, the profiles are depicted in the perpendicular direction of the tillage practice to highlight the tillage effects on soil resistance. Figure 4.6a clearly shows two distinct layers for the CT, whereby the first layer (0–25 cm depth) is characterized by lower resistance values (<2.5 MPa) compared to the second layer with resistance values exceeding 2.5 MPa. The lower resistance value of the first layer can be explained by the plowing which generally reduces soil compaction in the top layer. In general, the resistance of the first layer is quite homogeneous but on the top left (between 20 and 80 cm distance) two blocks with higher resistance can be observed which correspond to areas of compaction below the tractor tracks. The second layer with generally higher compaction values indicates a clear stratigraphic increase of resistance over depth. The map of the DL (Figure 4.6b) also shows two distinct layers but with less clear separation and larger heterogeneity. The uneven separation of the layering can also be explained by the tillage practice, whereby the two main prongs of the heavy tine cultivator caused the local changes during the deep loosening. Nevertheless, a layer separation can be detected between 20 and 25 cm depth. In comparison to CT and DL, RT (Figure 4.6c) shows a much finer top layer (≈10 cm depth), which can be related to the smaller penetration depth of the tine cultivator used for the reduced tillage. Additionally, the top layer is highly homogeneous. The irregularities observed in the second layer at ≈20 cm depth can be attributed to the historical tillage practices before 2005. These irregularities are not visible in the CT and DL plots because the plowing and the deep loosening are both below 20 cm depth. In general, penetrometer can be used to clearly distinguish the different tillage practices and their effects on soil strength, but due to the time consuming data acquisition only a small area (or volume) can be sampled.

On the other hand, on-ground GPR allows non-invasive data acquisition over large areas within relative short time. As an example, Figure 4.7 shows selected radargrams for the three tillage practices. Hereby, each radargram corresponds to a transect over one plot (CT, DL, and RT) in the tillage direction. Although some slight variability could be observed, comparable results were obtained between the different transects within one tillage practice (results are not shown). In general, all transects show a clear reflection at 4 ns indicating the soil surface as well as a clear reflection at 9–10 ns indicating the interface between the disturbed surface layer and deeper soil. In the case of CT, a deeper soil layer at 14–15 ns can also be clearly observed which corresponds to a sharp transition between two different horizons. Unfortunately, this layer is less visible for DL and RT. For RT plotted in Figure 4.7c, the first interface becomes much clearer, which may be attributed to the shallower interface and larger contrast between the loose and compacted soil layers. Additionally to the major reflections at the interface between tilled and non-tilled soil layers, local heterogeneities can be observed at greater depths (>20 ns), which may be caused by the presence of stones, or variations of local water content due to textural changes.

In the next step, we calculated the actual depth of the reflectors using the travel times and the first layer averaged dielectric permittivity obtained from

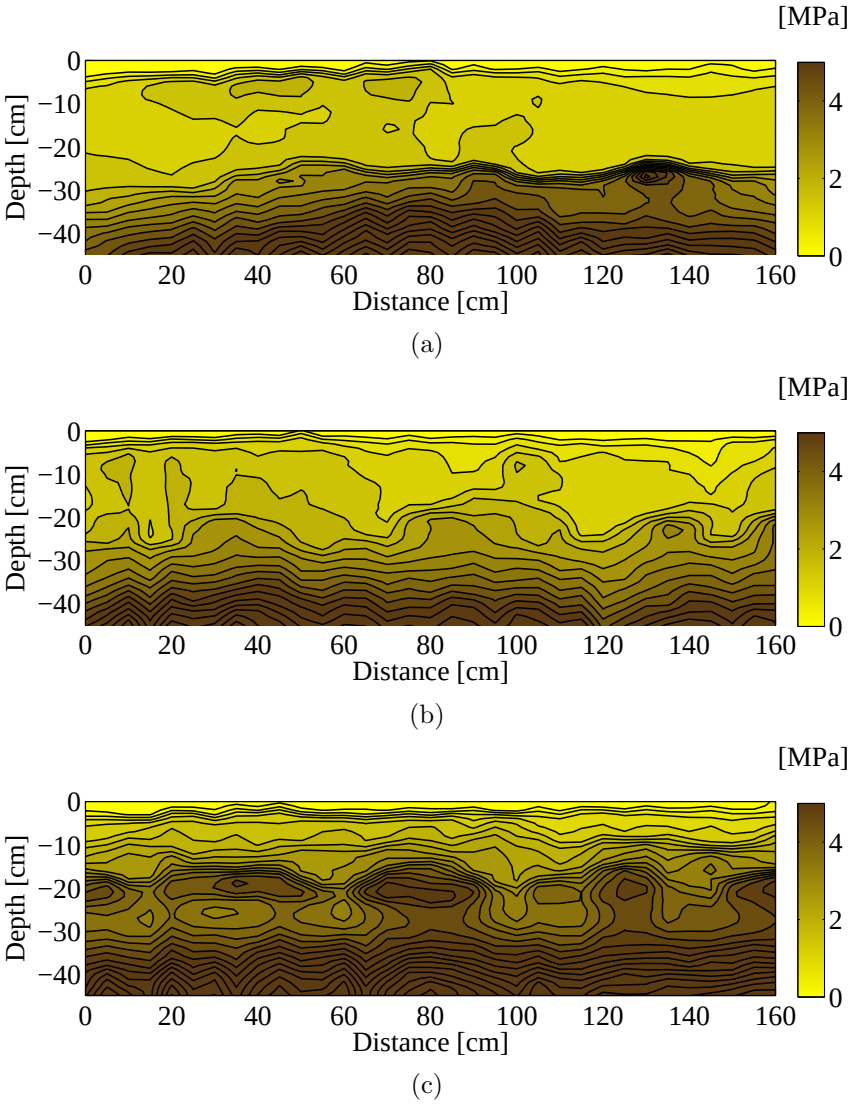


Figure 4.6: 2D soil strength maps obtained by penetrometer after (a) conventional tillage, (b) deep loosening tillage, and (c) reduced tillage.

the SWC information. Classically, the water content of the shallow (tilled) layer can be also calculated directly from the radar data using the direct ground wave as proposed by Huisman *et al.* (2003a,b) and Galagedara *et al.* (2005). Unfortunately, the direct ground wave was not always separable from the radargram which was already observed for silty or clayic soil by other authors such as Huisman *et al.* (2001) and Weihermüller *et al.* (2007). Therefore, we decided to use auxiliary water content data from *in-situ* measurements. Consequently, we averaged all water content data for all plots of the same tillage practice from ThetaProbe readings (mean $\theta_{\mathrm{ThetaProbe}} = 0.23$, 0.26, and 0.27 $\mathrm{m^3\ m^{-3}}$ for CT, DL, and RT, respectively) and finally calculated the reflector depth. It is worth noting that some uncertainty is introduced by this procedure because only the mean surface water content for each tillage is used for each point in space. The first reflection interface (observed at 9–10 ns) in addition to the surface interface (observed at 4 ns) is estimated to occur at a depth of ≈22 cm for CT, 20 cm for DL, and 19 cm for RT which is in a good agreement with the penetrometer maps. This interface is expected to result from the tillage which affects shallow soil density. The second interface observed at 14–15 ns in CT plots is estimated to occur at a depth of ≈43 cm and can be explained by the presence of a more compacted soil layer below this depth. It is worth noting that the interpretation of the radargrams with respect to the tillage practices is hampered by the relatively low depth resolution obtained by the used 400 MHz antenna ($\lambda/4 \cong 5$ cm, assuming a mean SWC of 0.25 $\mathrm{m^3\ m^{-3}}$). In conclusion, on-ground GPR seems to be a helpful tool for easy and timeless imaging of larger areas with respect of identifying shallow soil layers induced by different tillage practices. As shown, a large variability was already observed between the different treatments, whereby better results are expected to be obtained using higher frequencies or multi-channel GPR systems (e.g., Westermann *et al.*, 2010; Wollschläger *et al.*, 2010).

### 4.3.2 Apparent soil electrical conductivity

Apparent soil electrical conductivity mainly depends on soil clay content, SWC, soil salinity, soil temperature, and indirectly on soil compaction due to changes on SWC (Corwin and Lesch, 2005; Friedman, 2005). As already stated, two different EMI sensors (Profiler and EM38) were used to map the apparent soil electrical conductivity to provide insights into the spatial variability of the soil properties within the root zone. In general, EMI sensors measure a depth-weighted average of the electrical conductivity (EC), referred as apparent electrical conductivity ($\mathrm{EC_a}$). Figure 4.8 shows $\mathrm{EC_a}$ maps retrieved by the Profiler and the EM38 sensors. Figures 4.8a and 4.8b are obtained from Profiler operating with horizontal and vertical dipoles, respectively, at a frequency of 15 kHz and with a coil separation of 1.22 m. Figure 4.8c is obtained from EM38 at 14.7 kHz with vertical dipoles and a coil separation of 1 m. The different frequencies and dipole orientations provide different nominal depths of investigation, which is defined as the depth to which approximately 70% of the measured response is generated. For the Profiler, the nominal depth of investigation is 1.9 m and 0.9 m when operated in the vertical and horizontal

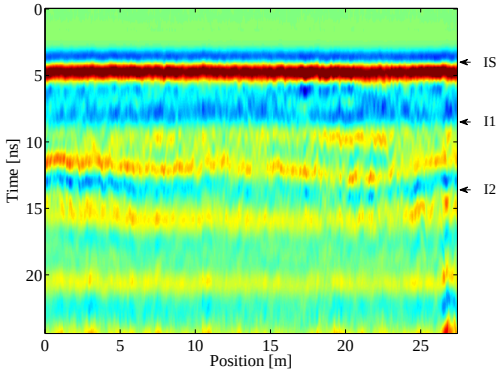


(a)

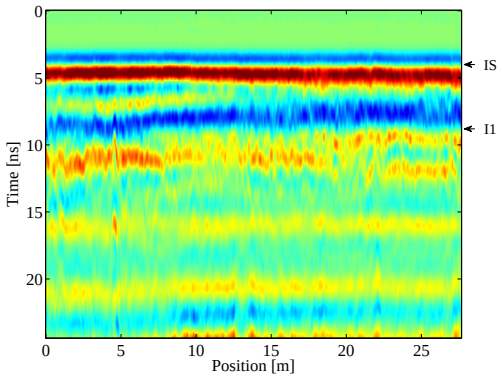


(b)

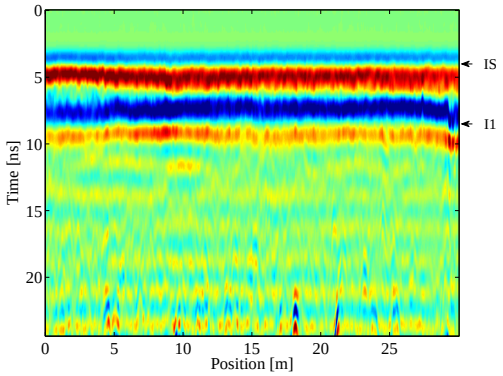


(c)

Figure 4.7: Time-domain representation (b-scan) of the amplitude of the reflected signal measured by the on-ground GPR on a 30 m transect for each tillage system: (a) conventional tillage, (b) deep loosening tillage, and (c) reduced tillage. IS indicates the reflection at the soil surface. I1 and I2 indicate a reflection at the interface between two distinct soil layers.

modes, respectively, while the EM38 nominal depth of investigation is 1.6 m (McNeill, 1980; Reedy and Scanlon, 2003). The EM38 data were collected in one direction only while the Profiler data were collected in two perpendicular directions.

In general, a decline trend in $EC_a$ from the lower left to the upper right corner (from south to north) can be observed (Figure 4.8), whereby this trend is independent of the underlying soil tillage practice of the different plots. This suggests that the tillage does not significantly affect the deeper SWC. For the entire field $EC_a$ varies between 10 to 30 mS $m^{-1}$, which is a relatively small range of variation for agricultural fields (Brosten *et al.*, 2011). This small variability of the EMI derived $EC_a$ can be explained by the small variability of clay content over the entire field (15.8–22.7 mass %). The $EC_a$ derived from vertical dipole orientation of the Profiler significantly shows higher values compared to the horizontal dipole measurements, which indicates an increase of $EC_a$ with depth. Indeed, the sensitivity of the measurements in horizontal dipole orientation is mostly affected by $EC_a$ changes within the near surface layer (<0.40 m), whereas the vertical dipole mode shows a maximum sensitivity at deeper layers (0.8–1.0 m) (McNeill, 1980). On the other hand, the EM38 derived $EC_a$ map is relatively similar to the Profiler map measured at vertical dipole orientation, which is expected as both instruments are operating at similar frequencies (15 kHz and 14.7 kHz) and dipole orientations. Unfortunately, both measurements (Profiler and EM38) were not performed at the same location because the EM38 was mounted on the all-terrain vehicle and the Profiler was moved manually (see Figure 4.2), and therefore, a straight forward comparison was not possible. To overcome this drawback, all Profiler data points within a neighborhood of 1 m to each consecutive EM38 data point were averaged. Even though, a significant correlation ($R^2 = 0.5$) between both data sets exists, whereby the RMSE is relatively low with 2.14 mS $m^{-1}$ (Figure 4.9). As indicated by the regression, Profiler data tend to slightly overestimate the EM38 data. One explanation may be the difference in coil separation (1.22 m for the Profiler and 1 m for EM38) leading to a slightly deeper sensitivity of the Profiler.

To analyze the spatial variability of the apparent electric conductivity measured by the EMI sensors, we computed the corresponding semivariograms. We used a class distance from 0 to 120 m with a step of 5 m, and we fitted an exponential model. Figure 4.10 shows the semivariogram for the apparent electrical conductivity obtained by the Profiler operating at 15 kHz with vertical dipoles. Similar semivariograms were observed for the data collected by the EM38 and the Profiler with horizontal dipole orientation. It can be seen in Figure 4.10 that the semivariogram raises over distance and never levels off, which results in a correlation length larger than the field size. The nugget effect is relatively large (3.6 [mS $m^{-1}$]$^2$) and the nugget/sill ratio is equal to 23%, which indicates a relatively strong spatial dependence (Cambardella *et al.*, 1994). This spatial correlation is to be attributed to the relatively smooth variations of soil texture and water content within the field. The tillage effects on the bulk soil electrical conductivity within the root zone are not visible.

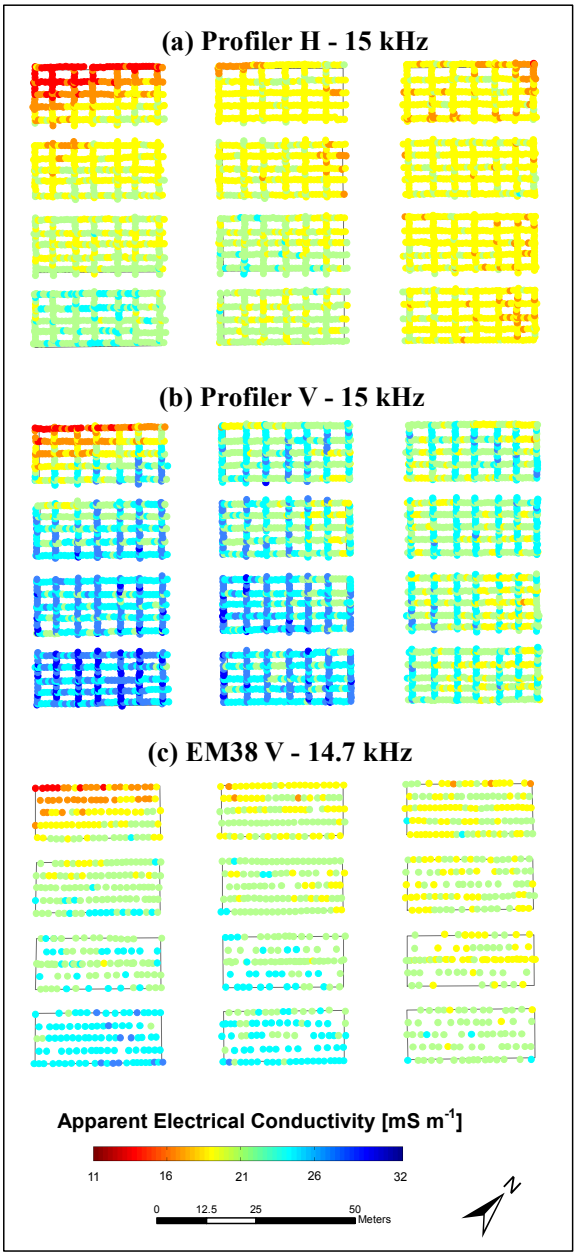


Figure 4.8: Map of the apparent soil electrical conductivity retrieved by Profiler using (a) horizontal dipoles (15 kHz), and (b) vertical dipoles (15 kHz), and (c) by EM38 using vertical dipoles (14.7 kHz) at the Gentinnes study site (13th April 2010).

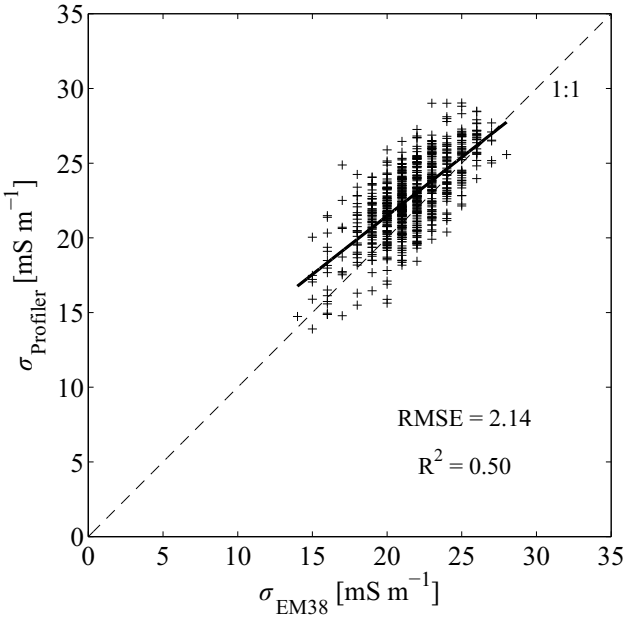


Figure 4.9: Apparent soil electrical conductivity ($\sigma$) from EM38 (14.7 kHz, vertical dipoles) versus Profiler (15kHz, vertical dipoles).

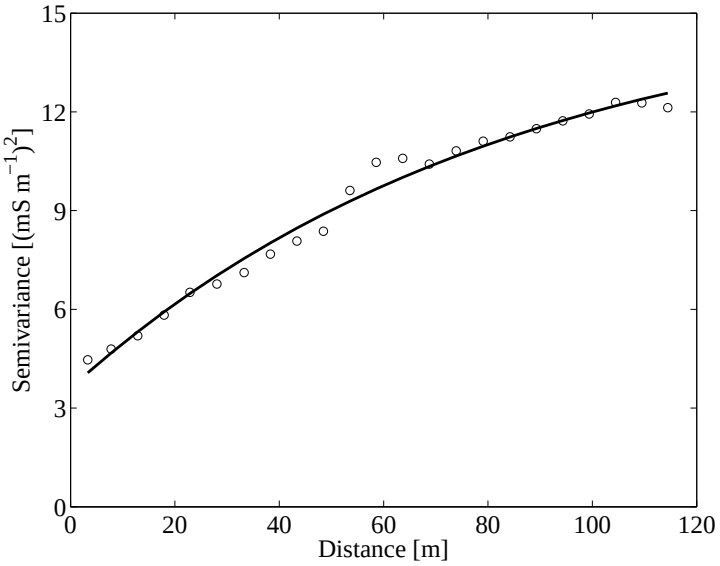


Figure 4.10: Semivariogram for the apparent electrical conductivity obtained by Profiler operating at 15 kHz and with vertical dipoles. The semivariogram was computed for the whole field with a class distance from 0 to 120 m by a step of 5 m and fitted with an exponential model ($R^2 = 0.98$)

### 4.3.3 Root zone water content

Figure 4.11 depicts the gravimetric SWC profiles obtained for each plot. Soil samples were collected at every 5 cm from the surface to 75 cm depth and at two locations for each plot. It is worth noting that gravimetric water content instead of volumetric water content were measured for these profiles as some uncertainties arose in the estimation of the sample volumes. The gravimetric water content profiles obtained within the plots characterized by a conventional tillage show the same trends (Figure 4.11a). In particular, the profiles show a sharp increase of the water content between the surface and 10–15 cm depth. The water content is then decreasing up to a depth of 30 cm, and below, water content is relatively constant. The water content profiles observed within the plots characterized by a deep loosening tillage show an opposite behavior within the top layers (Figure 4.11b) with decreasing values from the surface to 20–30 cm depth. The water content at deeper locations stays then fairly constant. For the reduced tillage system, the water content profiles are more heterogeneous (Figure 4.11c). In general, water content decreases from the soil surface to 15–25 cm depth and then stays constant below. For all tillages, the deep SWC variation range is relatively small and the absolutes values are very similar (mean SWC below 40 cm depth is equal to 0.23 g $g^{-1}$ for each tillage). This confirms that the electrical conductivity variations originate mainly from clay content and not from differences in water content. In addition, SWC in the deeper horizons seems to be unaffected by tillage practices.

### 4.3.4 Surface soil water content

Figure 4.12 presents SWC maps retrieved by (a) volumetric soil sampling, (b) ThetaProbe, (c) 5TE, and (d) off-ground GPR. To allow for a better comparison between the different techniques all maps have the same color scale ranging from 0.12 to 0.41 $m^3$ $m^{-3}$. In general, all four SWC maps show similar spatial patterns irrespectively of the different sensing depths. The SWC map derived from 5TE shows however lower SWC values with a mean of 0.21 $m^3$ $m^{-3}$ compared to mean SWC of 0.27, 0.25, and 0.25 $m^3$ $m^{-3}$ for soil sampling, ThetaProbe, and off-ground GPR, respectively. It is worth noting that different numbers of data points were used: 420 measurement points for the invasive methods (soil sampling, ThetaProbe, and 5TE) while 927 measurements were collected by the off-ground GPR. Although some trends can be observed, the spatial correlation of surface SWC (see below) is much smaller than for the EMI images (see Section 4.4.2). This can be attributed to (1) the effect of the shallow tillage practices (see below) and (2) to inherent local heterogeneities. The EMI sensors are less sensitive to local heterogeneities due to the larger sensing volume (1–3 $m^3$). In comparison, for the GPR and the invasive techniques, the sampling volume is below 0.1 $m^3$.

For a direct comparison of the results obtained from the different measurement methods, off-ground GPR-derived water content is plotted versus water content derived from ThetaProbe, 5TE, and volumetric soil sampling (Figures 4.13 and 4.14). As the GPR measurements were continuously performed at predefined transects with high density, all GPR data points within a neighbor-

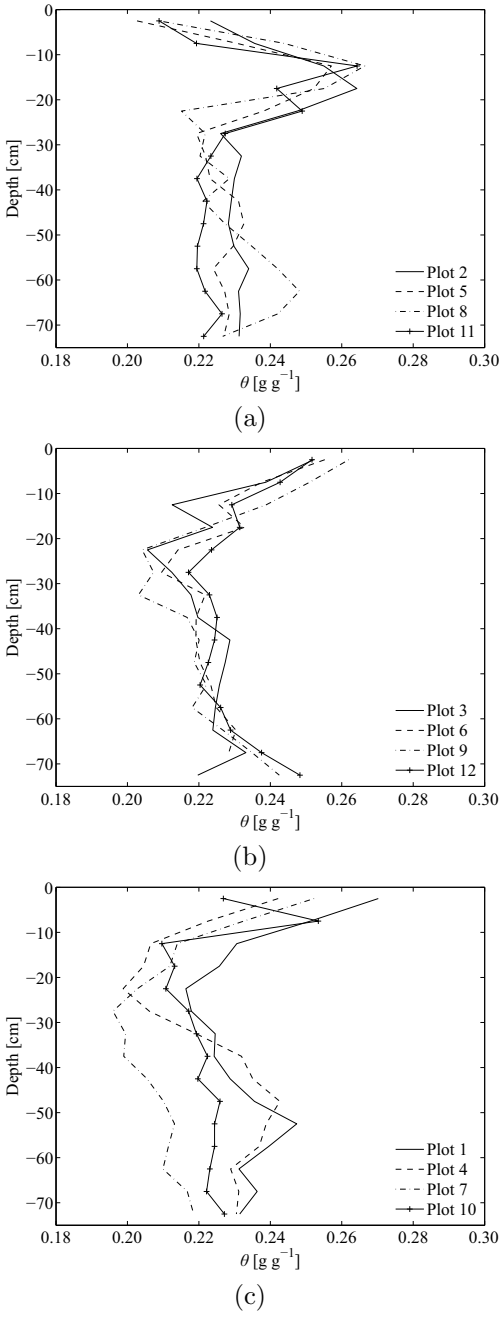


Figure 4.11: Gravimetric soil water content profiles from surface down to 75 cm depth (5 cm step). Each depicted profile consists of a mean of two measured SWC profiles. Four SWC profiles per tillage system are shown: (a) conventional tillage, (b) deep loosening tillage, and (c) reduced tillage.

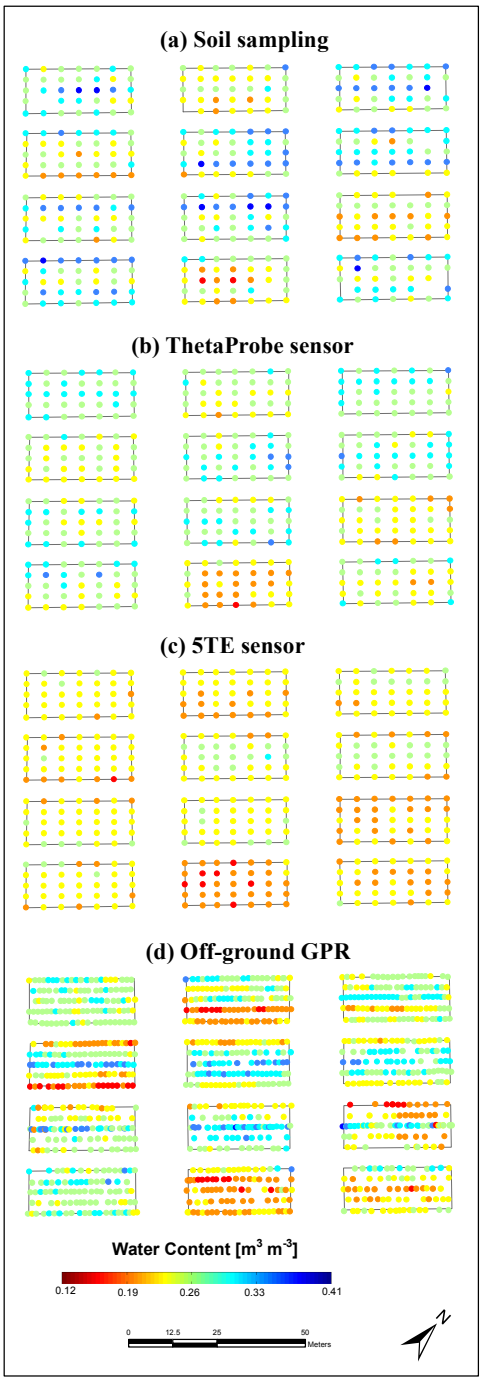


Figure 4.12: Soil water content maps obtained using (a) volumetric soil sampling, (b) ThetaProbe capacitance sensor, (c) 5TE capacitance sensor, and (d) off-ground GPR at the Gentinnes study site (13th April 2010).

hood of 1 m to the invasive measurement points were averaged. In general, GPR-derived water contents are much better correlated to the soil sensors derived water contents $\theta_{\mathrm{ThetaProbe}}$ ($R^2 = 0.31$, RMSE = 0.040 $m^3\ m^{-3}$) and $\theta_{\mathrm{5TE}}$ ($R^2 = 0.39$, RMSE = 0.045 $m^3\ m^{-3}$) than to the soil sampling ($\theta_{\mathrm{Sampling}}$) data ($R^2 = 0.10$, RMSE = 0.060 $m^3\ m^{-3}$). Not only the correlation between $\theta_{\mathrm{GPR}}$ and $\theta_{\mathrm{Sampling}}$ is weak but also the scattering is high and the regression is far off the 1:1 line. Additionally, the range of SWC values is much smaller for the 5TE sensor (0.14–0.28 $m^3\ m^{-3}$) compared to the other methods with 0.15–0.34, 0.16–0.41, and 0.13–0.36 $m^3\ m^{-3}$ for the ThetaProbe, soil sampling, and GPR, respectively.

The intention of using three different ground-truth measurement techniques was to provide insights into the effect of the sensors specific measurement volume and/or measurement accuracy. Therefore, we also analyzed the correlation between the sensors (Figure 4.15). The correlation between $\theta_{\mathrm{ThetaProbe}}$ and $\theta_{\mathrm{Sampling}}$ is relatively weak with a $R^2$ of 0.24, and the correlation between $\theta_{\mathrm{5TE}}$ and $\theta_{\mathrm{Sampling}}$ is also weak with a $R^2$ of 0.13. Additionally, both correlations are far off the 1:1 line with a slope of 0.35 for the $\theta_{\mathrm{ThetaProbe}}$ and $\theta_{\mathrm{Sampling}}$, and 0.19 for the $\theta_{\mathrm{ThetaProbe}}$ and $\theta_{\mathrm{Sampling}}$ relationship. In contrast, correlation between $\theta_{\mathrm{5TE}}$ and $\theta_{\mathrm{ThetaProbe}}$ shows fairly good agreement with an $R^2$ of 0.50 (RMSE = 0.046) and only a parallel shift to the 1:1 line indicating a systematic overestimation of the ThetaProbe data. The differences between the three methods can be partly explained by the different sensing volumes (100 $cm^3$ for the soil sampling, ≈75 $cm^3$ for the ThetaProbe, and ≈50 $cm^3$ for the 5TE sensor) as well as differences in the sensing depths with 5, 6, and 5.2 cm for the soil sampling, ThetaProbe, and 5TE sensor, respectively. Nevertheless, it is still questionable why the method integrating over the largest volume (namely, soil sampling) deviates so much from the sensor based data. On the other hand, it seems now logical that also the correlation between $\theta_{\mathrm{GPR}}$ and $\theta_{\mathrm{Sampling}}$ is weak (Figure 4.14), because the soil samples do show a clear difference compared to the sensor based data.

### 4.3.5 Tillage effects on surface soil water content

To get a better insight on the tillage effects on surface SWC as measured by the invasive methods as well as the off-ground GPR system, the mean SWC and the associated confidence interval ($\alpha_t = 0.05$) have been computed and plotted in Figure 4.16. As shown, a significantly lower mean SWC was observed in the conventional tillage plots compared to all other plots, irrespectively of the measurement techniques used, whereby the 5TE data generally indicate the lowest mean water contents and the soil sampling data indicate the largest. In-between are the ThetaProbe and the off-ground GPR data with comparable results as already indicated above. This lower mean water content in the CT plots can be partly explained by lower pore connectivity between the topsoil and the deeper layers after plowing, which reduces capillary upward water flow from the deeper wetter layers. This is in agreement with the findings of Mahboubi *et al.* (1993) and Kosutic *et al.* (2001) who observed a higher soil water retention with no-tillage treatment compared with conventional tillage treatment. On

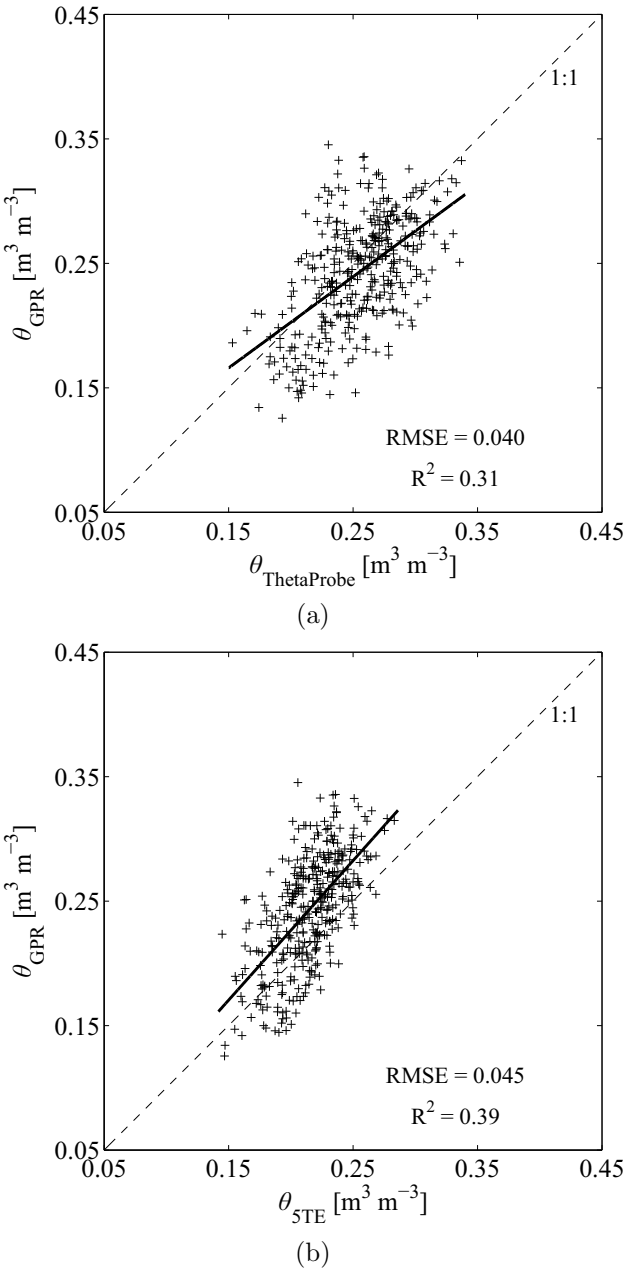


Figure 4.13: Volumetric soil water content from (a) ThetaProbe capacitance sensor and (b) 5TE capacitance sensor versus off-ground GPR. For each method, water content estimates were derived from the dielectric permittivity measurements using Topp's model.

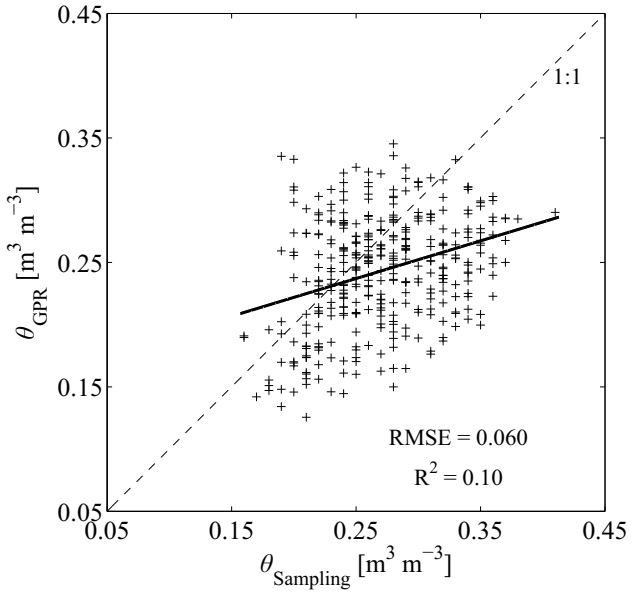


Figure 4.14: Volumetric soil water content from soil sampling versus off-ground GPR-dervied water content.

the other hand, DL and RT show no significant difference in surface soil water content with the three invasive methods and a very slight difference with the off-ground GPR system, which indicates a comparable evaporation loss and/or infiltration capacity.

In the next step, we plotted the mean SWC of each plot for all sensors versus the STD of the measurements (Figure 4.17). In general, the STD increases with increasing mean SWC in the observed range of variation. This general trend is in good agreement with observations of Ryu and Famiglietti (2005) and Choi and Jacobs (2007) who showed that the spatial variability of SWC increases from very dry to wet conditions, reaches a maximum at specific water contents, and then decreases with further wetting until saturation. Vereecken *et al.* (2007) found that the soil hydraulic properties itself control the shape of this curve and the point where the maximum will occur. Unfortunately, the SWC values observed are probably below the critical value (maximum STD point) described by the authors, and therefore, a detailed analysis of the differences in terms of soil hydraulic properties due to the tillage systems is restricted. Nevertheless, each tillage system shows a distinct shape of the curve (Figure 4.17), which could be a hint of different hydraulic properties and/or different spatial variabilities of water content within the surface layer.

Finally, we analyzed the spatial variability of the surface SWC measured by off-ground GPR for the different tillage systems. Semivariograms were computed using GPR-derived SWC estimates from cluster of plots characterized by the same tillage system. The resulting semivariograms are depicted in Figure 4.18 for the conventional tillage, deep loosening tillage, and reduced tillage.

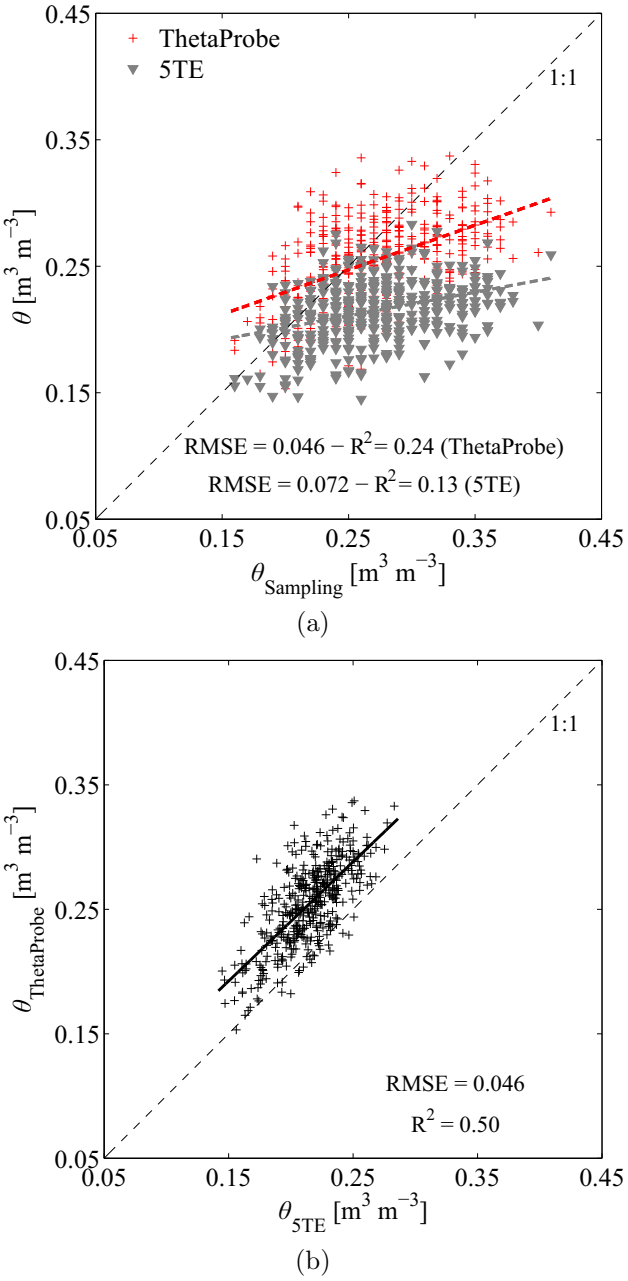


Figure 4.15: Volumetric soil water content from (a) volumetric soil sampling versus ThetaProbe and 5TE capacitance sensors and (b) 5TE capacitance sensor versus ThetaProbe capacitance sensor. For the two capacitance sensors, water content estimates were derived from the dielectric permittivity measurements using Topp's model.

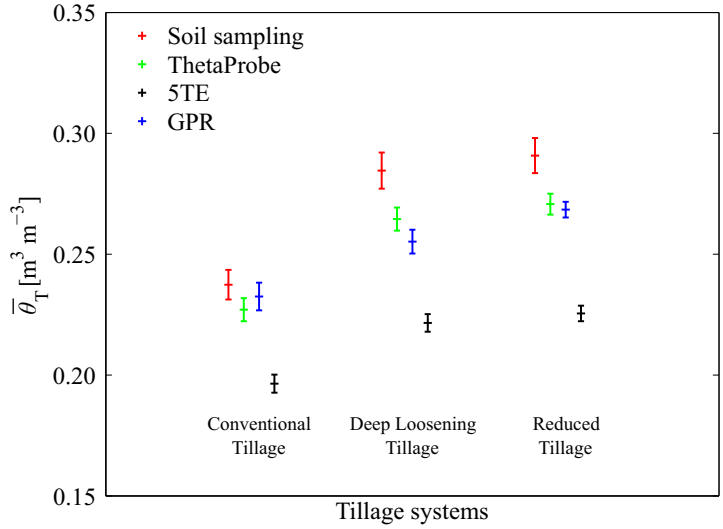


Figure 4.16: Mean soil water content per tillage $\overline{\theta}_T$ (conventional tillage, deep loosening tillage, and reduced tillage). Error bars represent confidence interval ($\alpha_t = 0.05$) between the four plots for each tillage. Colors represent the measurement techniques (red: volumetric soil sampling, green: ThetaProbe capacitance sensor, black: 5TE capacitance sensor, and blue: off-ground GPR).

Each semivariogram was computed with a class distance from 0 to 60 m by a step of 5 m and fitted with an exponential model. In general, the quality of the fit is reasonable with a $R^2$ between 0.54 and 0.62. These graphs point out distinct spatial behavior of the SWC within the three tillage systems. SWC within reduced tillage plots appears to have less spatial structure compared to conventional tillage plots as illustrated by the smaller nugget effect and the smaller range of its semivariogram (see Table 4.1). The nugget effect can be attributed to measurement errors and/or spatial sources of variation at distances smaller than the shortest sampling interval while the range is the distance beyond which two SWC values can be considered as statistically independent and the sill is the level at which the variogram flattens out (Goovaerts, 1999; De Lannoy *et al.*, 2006). For each semivariogram, the range is larger than the plot size (>30 m) and the spatial correlation is moderate, with nugget/sill ratios of 49, 61, and 40% for the CT, DL, and RT, respectively (Cambardella *et al.*, 1994). The larger sill of the conventional tillage semivariogram indicates that the variance of the SWC within the conventional tillage plots is larger than within the other plots. This larger SWC variability could be explained by a larger soil heterogeneity induced by the plowing process. Indeed, using a mold board plough, soil blocks from deeper layers characterized by higher bulk densities (in general, the soil bulk density increases with depth) are locally transferred to the surface, and therefore, increase the variability in SWC. Additionally, the plowing creates also local compaction which modifies the SWC

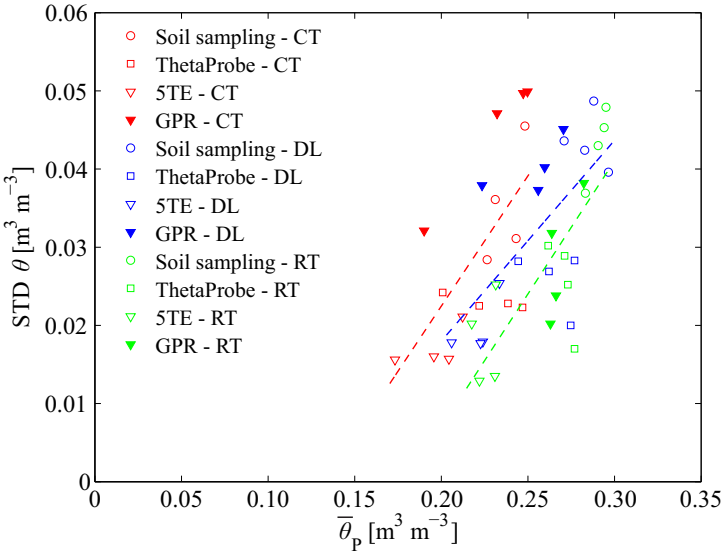


Figure 4.17: Soil water content standard deviation, STD $\theta$, with respect to mean soil water content per plot, $\overline{\theta}_{\mathrm{P}}$, obtained from measurements made using volumetric soil sampling (circles), ThetaProbe capacitance sensor (squares), 5TE capacitance sensor (triangle), and off-ground GPR (filled triangles) at the Gentinnes study site (13th April 2010). Colors represent tillage systems (red: conventional tillage, blue: deep loosening tillage, and green: reduced tillage). Dashed lines represent linear regression lines for each tillage system.

distribution. An intermediate sill value is observed for the deep loosening tillage which could be explained by lower soil mixing compared to the conventional tillage (especially between the tines), but higher soil mixing compared to the reduced tillage (on the tines ways).

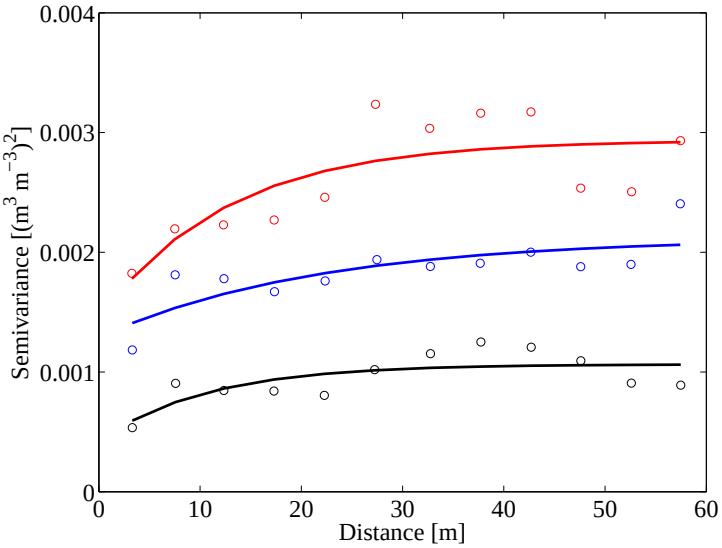


Figure 4.18: Semivariograms for off-ground GPR-derived soil water content computed for the plots prepared with conventional tillage (red), deep loosening tillage (blue), and reduced tillage (black). All semivariograms were computed with a class distance from 0 to 60 m by a step of 5 m and fitted with an exponential model.

Table 4.1: Semivariogram parameters for off-ground GPR-derived SWC computed for the plots prepared with conventional tillage, deep loosening tillage, and reduced tillage.

| | **Nugget** [m$^3$ m$^{-3}$]$^2$ | **Sill** [m$^3$ m$^{-3}$]$^2$ | **Nugget/Sill** [%] | **Range** [m] | **R$^2$** |
|---|---|---|---|---|---|
| Conventional Tillage | 0.00144 | 0.00294 | 49 | 38 | 0.62 |
| Deep Loosening Tillage | 0.00129 | 0.00212 | 61 | 65 | 0.61 |
| Reduced Tillage | 0.00042 | 0.00106 | 40 | 32 | 0.54 |

## 4.4 Summary and conclusion

In this study, we used geophysical methods to analyze the effects of tillage on surface soil water content, bulk soil electrical conductivity, and mechanical

resistance. GPR and EMI data were collected on three contrasting tillage systems implemented on an agricultural field: (1) conventional tillage, (2) deep loosening tillage, and (3) reduced tillage. As additional measurements, soil sampling, capacitance probes, and soil penetrometer data were acquired as ground truth. The data showed that tillage influences the soil resistance (deeper tillage decreases soil resistance), which could be partly seen in the GPR data. Additionally, reference SWC measurements (capacitance probes and soil sampling) were in a relatively good agreement with the water content estimates from off-ground GPR. We also observed that the tillage influences shallow surface water content, while deeper SWC seems to be unaffected. Surface soil water retention was significantly larger in the reduced tillage and the deep loosening tillage compared to the conventional tillage, which was partly explained by lower pore connectivity between the topsoil and the deeper layers after conventional tillage, which reduces capillary upward water flow from the deeper wetter layers. The variance of the SWC within the conventional tillage plots was larger than within the other plots. This larger SWC variability could be explained by a larger soil heterogeneity induced by the plowing process. This study confirms the potential of GPR and EMI sensors for soil physical properties determination at the field scale and for the characterization of agricultural management practices. These geophysical techniques could also help us to apply precision agricultural practices for efficient resource management and crop yield enhancement.

# Chapter 5

# Estimation of the hydraulic properties of a sandy soil using passive and active microwave remote sensing*


## Abstract

In this study, we experimentally analyzed the feasibility of estimating the soil hydraulic properties from L-band radiometer and ground-penetrating radar data. L-band radiometer and ultra-wideband off-ground GPR measurements were performed above a sand box in hydrostatic equilibrium with a water table located at different depths. The results of the inversions showed that the radar and radiometer signals contain sufficient information to estimate the soil water retention curve and its related hydraulic parameters with a relatively good accuracy compared to time-domain reflectometry estimates. However, an accurate estimation of the hydraulic parameters was only obtained by considering the saturated water content parameter as known during the inversion.


## 5.1 Introduction

Soil hydraulic properties are of major interest for estimating water and energy fluxes at the land surface. In general, estimation of these properties relies on the measurement of soil water content within the soil profile usually performed by soil sampling or with *in-situ* sensors such as time-domain reflectometry or capacitance probes. Unfortunately, these methods do not account for the high

*This chapter is adapted from:
Jonard, F.; Weihermüller, L.; Schwank, M.; Jadoon, K. Z.; Vereecken, H. & Lambot, S. Estimation of the hydraulic properties of a sandy soil using passive and active microwave remote sensing, in *Remote Sensing of Environment*, in preparation.

spatial variability, especially over large areas. On the other hand, proximal sensors such as ground-based microwave radiometer and ground-penetrating radar can be used to obtain information at the field scale with high spatial resolution, but these measurements may be biased by confounding factors such as soil surface roughness (Lambot et al., 2004; Jonard et al., 2011; Jonard et al., 2012).

The objective of this study is to experimentally analyze the feasibility of measuring a soil water content profile using off-ground GPR and L-band radiometer data. In particular, we investigated the potential of GPR and radiometer to identify the hydraulic properties of a sandy soil in hydrostatic equilibrium with a water table at different depths. In this condition, the soil water content profile corresponds to the soil water retention curve, which can be related to the soil hydraulic parameters by using a simple soil hydraulic model. The uncertainty related to the estimation of the soil hydraulic parameters from GPR, radiometer, and TDR will be also addressed. To the best of our knowledge, this study represents a first attempt to compare the estimation of soil hydraulic parameters from active and passive microwave remote sensing data.

## 5.2 Experimental setup

The experiment was conducted at the TERENO test site in Selhausen, Germany (latitude 50°87 N, longitude 6°45 E, and elevation 105 m above sea level). L-band radiometer and off-ground GPR measurements were performed over a 1.00-m-deep and 2.00 x 2.00 $m^2$ area wooden box filled with sand. The L-band radiometer was fixed on an aluminium arc at 4 m height above the ground and the antenna was pointed towards the sand box with an observation angle of 36° relative to the vertical direction (Figure 5.1). The off-ground GPR antenna was fixed above the sand box on a wooden frame and the GPR antenna aperture was situated at about 0.35 to 0.40 m above the soil surface with normal incidence (Figure 5.2). To avoid interferences between the two instruments, the radiometer and GPR were not operated simultaneously.

The sides of the wooden box were covered with aluminium foils as well as a PVC sheet to avoid transmission of electromagnetic waves and water fluxes. To increase the sensitivity of the radiometer to radiations emitted from the sand within the box and reduce the influence of radiance originating from areas outside, the surrounding soil surface was covered by a metal grid (area of 116 $m^2$) with a mesh size of 0.5 cm (Figure 5.1), thereby setting up a perfect electrical reflector. In that respect, the mesh size was significantly smaller than the operating L-band microwave wavelength (≈21 cm).

Radiometer and GPR measurements were performed with the water table at 7 different depths, ranging from the bottom of the box to the sand surface. For each water table depth, hydrostatic equilibrium was waited for during 6 to 11 days in order to produce a vertical water content profile above the water table in agreement with the sand water retention curve. Distilled water was used to saturate the sand in order to limit the electrical conductivity of the medium and therefore electrical losses. Precipitation and evaporation at the

(a)

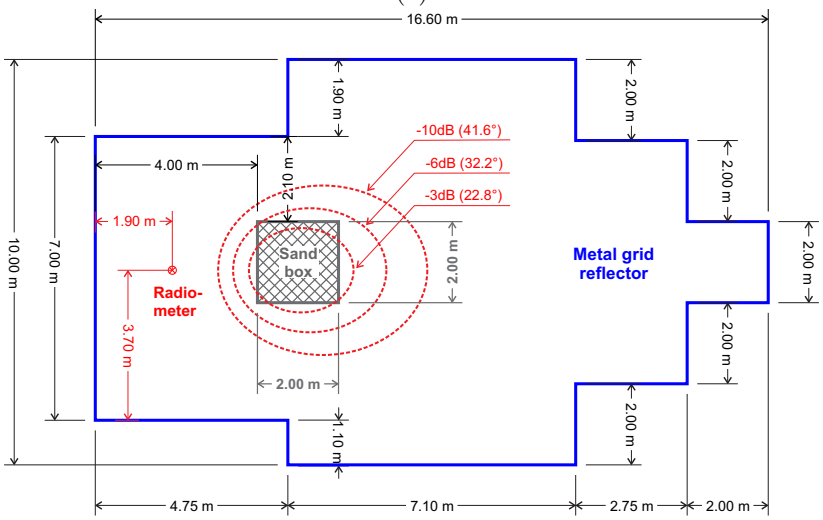


(b)

Figure 5.1: (a) Picture of the experimental setup including a radiometer fixed on an arc and a sand box in the centre of a metal grid at the TERENO test site in Selhausen (Germany), (b) detailed sketch of the experimental setup showing the location and dimensions of the sand box and the metal grid. Dashed ellipses indicate the radiometer footprints at $-3$, $-6$, and $-10$ dB.

Figure 5.2: Picture of the VNA and radar antenna fixed at about 0.35–0.40 m above the sand surface.

sand surface were prevented using a metal cover that was just removed during measurements.

### 5.2.1 TDR and capacitance sensors

Time-domain reflectometry and capacitance sensors were inserted at 7 depths, i.e., 5, 10, 20, 30, 40, 60, and 80 cm depth of two opposite sides of the box to measure the dielectric permittivity and bulk electrical conductivity within the sand box (Figure 5.3). TDR measurements were performed every 20 min using custom-made three-rod probes with a length of 20 cm that were inserted horizontally into the sand. TDR probes were connected to a TDR100 cable tester (Campbell Scientific, Logan, Utah, USA). The raw data of the waveform were stored and automatically analyzed by the commonly used tangent method in the time domain (Heimovaara and Bouten, 1990). Capacitance measurements were performed every 15 min using 5TE sensors (Decagon Devices, Inc., Pullman, Washington, USA) composed of 3 prongs of 5.2 cm length and that were inserted horizontally into the sand. Additionally, soil temperature was also recorded by the capacitance sensors. A piezometer and 5 tensiometers were used to monitor the water level in the box (Figure 5.3). Unfortunately, the tensiometers did not work properly during the experiment, and therefore, the ground water level was only measured by the piezometer.

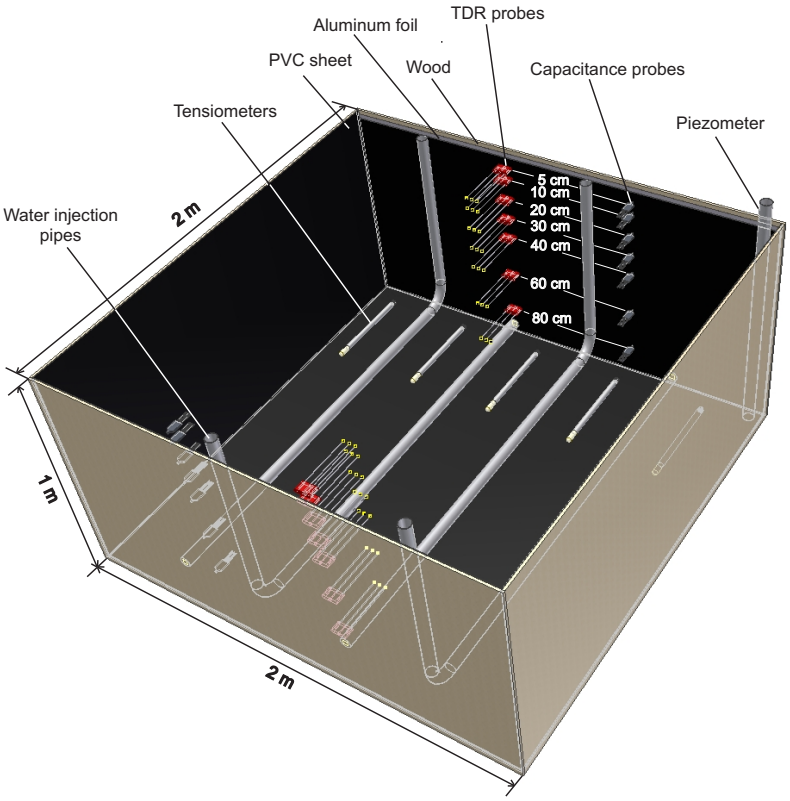


Figure 5.3: Detailed sketch of the sand box showing the location of the TDR probes, capacitance probes, tensiometers, water infiltration pipes, and the piezometer.

### 5.2.2 Remote sensing systems

**L-band radiometer** The L-band radiometer ELBARA II operating at the TERENO test site in Selhausen (Germany) is an identical copy of the three ELBARA II radiometers deployed by ESA for calibration and validation activities related to the SMOS mission. ELBARA II is sensitive within the protected frequency band 1400–1424 MHz of the microwave L-band. The internal calibration used to derive brightness temperature from raw radiometer data is performed by periodically switching between two instrument internal reference noise sources: a resistive noise source (hot reference noise temperature) and an active cold source (cold reference noise temperature). The noise temperature measured at the radiometer input ports was also corrected for the noise added by the lossy feed cables. A detailed description of the ELBARA II system and the calibration procedure is given in Schwank *et al.* (2010b). Every day of measurement, the radiometer was calibrated by measuring sky radiance at an elevation angle of 55° above the horizon and oriented approximately toward the north. Each radiometer measurement was recorded with 3 s integration time. The accuracy of the measured brightness temperature is estimated to be lower than 1 K (Schwank *et al.*, 2012). Simultaneously to each radiometer measurement, air temperature at the height of the radiometer was also recorded. The radiometer was equipped with a dual-mode conical horn antenna (aperture diameter = 60 cm, length = 67 cm) with symmetrical and identical beams (Figure 5.4) and a −3 dB full beamwidth of 23° in the far-field. The antenna directivity was derived from time series of brightness temperatures measured with the sun passing through the antenna field of view as described in Schwank *et al.* (2010b) (Figure 5.5).

**Ground-penetrating radar** The radar system was set up using a vector network analyzer (VNA, ZVRE, Rohde and Schwarz, Munich, Germany) as transmitter and receiver, thereby providing a monostatic ultra-wideband stepped-frequency continuous-wave system (Lambot *et al.*, 2004c; Jonard *et al.*, 2012). The antenna system consisted of a linear polarized double-ridged broadband horn antenna (BBHA 9120 A, Schwarzbeck Mess-Elektronik, Schönau, Germany). Antenna dimensions are 22 cm length and 14 x 24 $cm^2$ aperture area, and the −3 dB full beamwidth of the antenna is 26° in the E-plane and 20° in the H-plane (at 2 GHz). The antenna nominal frequency range is 0.8–5.2 GHz and its isotropic gain ranges from 4.4–10.5 dBi. Measurements were performed between 0.8–2.6 GHz and with a frequency step of 8 MHz.

## 5.3 Modeling approach

### 5.3.1 Soil hydraulic model

In this study, radiometer and radar measurements were only performed when the sand was in hydrostatic equilibrium with a water table located at a position $z_w$ [m]. In hydrostatic conditions, the water content profile can be described

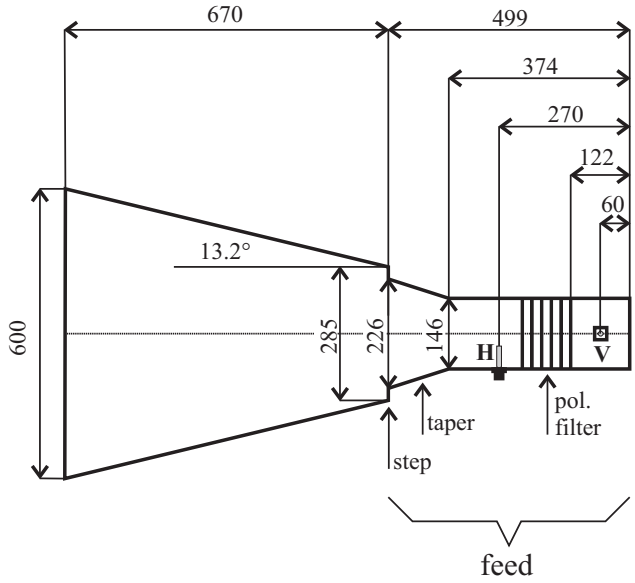


Figure 5.4: Sketch of the L-band radiometer antenna. The antenna system consists of a dual-mode conical horn antenna fixed to a feed. Dimensions are in units of millimeters.

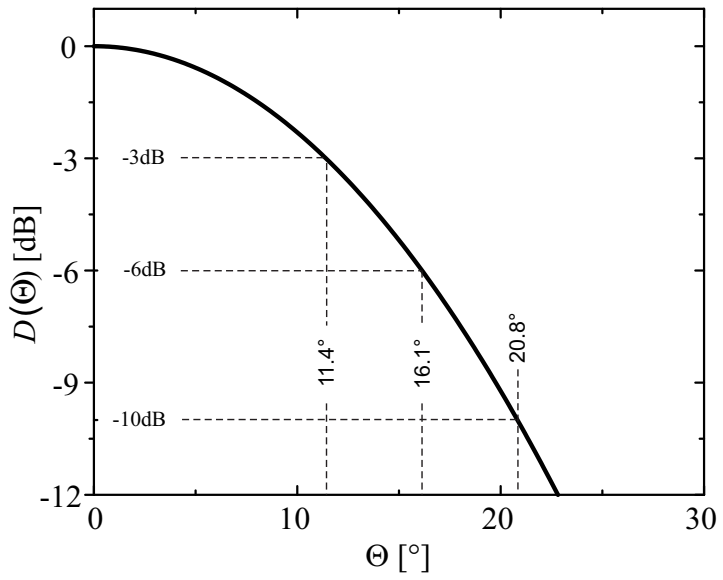


Figure 5.5: Normalized antenna directivity $D(\Theta)$ derived from time series of brightness temperatures measured with the sun passing through the antenna field of view. $\Theta$ corresponds to the angle between the antenna main direction and the sun position.

by the water retention curve of the soil, which was modeled in this study using the van Genuchten model (van Genuchten, 1980):

$$\theta(h) = \begin{cases} \theta_\mathrm{r} + (\theta_\mathrm{s} - \theta_\mathrm{r})\,[1 + |\alpha h|^n]^{-m} & \text{for} \quad h < 0 \\ \theta_\mathrm{s} & \text{for} \quad h \geq 0 \end{cases} \tag{5.1}$$

where $\theta$ [$\mathrm{m}^3\ \mathrm{m}^{-3}$] is the volumetric water content, $\theta_\mathrm{r}$ and $\theta_\mathrm{s}$ [$\mathrm{m}^3\ \mathrm{m}^{-3}$] are the residual and saturated water contents, respectively, $h$ [m] is the pressure head and is related to the vertical position $z$ [m] by $h = z - z_\mathrm{w}$, $\alpha$ [$\mathrm{m}^{-1}$] and $n$ [–] are curve shape parameters which are, respectively, inversely related to the air entry value and the width of the pore size distribution, and $m$ is restricted by the Mualem condition with $m = 1 - 1/n$ and $n > 1$.

### 5.3.2 Petrophysical relationships

To relate soil water content $\theta$ to soil relative dielectric permittivity $\varepsilon_\mathrm{r}$, the model of Ledieu *et al.* (1986) was used:

$$\varepsilon_\mathrm{r} = \left(\frac{\theta - b}{a}\right)^2 \tag{5.2}$$

where $a$ and $b$ are soil specific empirical parameters. In this study, we used the parameters $a = 12.64 \times 10^{-2}$ and $b = -19.33 \times 10^{-2}$ as determined by Lambot *et al.* (2004c) for a very similar sandy soil.

Additionally, the model of Rhoades *et al.* (1976) was used to relate soil water content to apparent soil electrical conductivity $\sigma$ [$\mathrm{S\ m}^{-1}$], namely:

$$\sigma = \left(c\theta^2 + d\theta\right)\sigma_\mathrm{w} + \sigma_\mathrm{s} \tag{5.3}$$

where $c$ and $d$ are soil specific empirical parameters, $\sigma_\mathrm{w}$ [$\mathrm{S\ m}^{-1}$] is the soil solution electric conductivity, and $\sigma_\mathrm{s}$ [$\mathrm{S\ m}^{-1}$] is the electric conductivity of the dry sand. In this study, we set $c = 1.85$, $d = 3.85 \times 10^{-2}$, and $\sigma_\mathrm{s} = 5.89 \times 10^{-4}$ $\mathrm{S\ m}^{-1}$ which are characteristic values for sandy soils. The soil solution electric conductivity $\sigma_\mathrm{w}$ was computed using the DC electrical conductivity measured in the top part of the piezometer ($3.88 \times 10^{-2}$ $\mathrm{S\ m}^{-1}$ at 9°C) and the Debye model (Debye, 1929) to account for frequency dependent dielectric losses.

### 5.3.3 Radiative transfer model

**Brightness temperature** The thermal L-band emission, also called brightness temperature $T_\mathrm{B}$, is classically expressed using a zero-order radiative approach (Mätzler, 2006). In this study, $T_\mathrm{B}$ is assumed to be a linear combination of the radiance emitted from the sand box and the radiance emitted from the surrounding area. Consequently, $T_\mathrm{B}$ can be expressed by:

$$T_\mathrm{B}^p = \eta^p[(1 - R_\mathrm{s}^p)\,T_\mathrm{s} + R_\mathrm{s}^p\,T_\mathrm{sky}] + (1 - \eta^p)[(1 - R_0^p)\,T_0 + R_0^p\,T_\mathrm{sky}] \tag{5.4}$$

where $\eta$ is the fractional amount of the measured radiance which was emitted from the sand box, $R_\mathrm{s}$ [–] is the reflectivity of the sand box, $R_0$ [–] is the reflectivity of the surrounding area, $T_\mathrm{sky}$ [K] is the sky radiance (≈4.8 K according

to Pellarin *et al.* (2003)), $T_s$ [K] is the effective physical temperature of the soil in the box, $T_0$ [K] is the effective physical temperature of the ground surrounding the box, and $p$ refers to the polarization (H or V). Under thermodynamic equilibrium, $(1-R_s)$ and $(1-R_0)$ represent the emissivity of the sand box ($E_s$) and the surrounding area ($E_0$), respectively (Kirchhoff's law).

In this study, $T_s$ was estimated as the mean value between the soil temperature at 5 cm depth and 40 cm depth while $T_0$ was approximated by the air temperature at the radiometer height. The values for $\eta^p$ were determined from $T_B$ measurements with the sand box successively covered by a reflector (copper sheet) ($T_{B,refl}$) and an absorber ($T_{B,abs}$). The reflector is characterized by a reflectivity ($R_{s,refl}$) of 1 while the absorber is characterized by a reflectivity ($R_{s,abs}$) of 0 (Figure 5.6). Considering $T_B = T_{B,refl}$ and $R_s = R_{s,refl}$ in Eq. (5.4) provides $\eta^p$ as a function of $R_0$. In a similar way, considering $T_B = T_{B,abs}$ and $R_s = R_{s,abs}$ in Eq. (5.4) provides a second equation with $\eta^p$ as a function of $R_0$. Solving these two equations for the two unknowns yielded $\eta^H = \eta^V = 0.54$, $R_0^H = 0.94$, and $R_0^V = 0.90$. Finally, $R_s$ can be computed from $T_B$ measurements.

**Reflectivity model** $R_s$ represents the soil reflectivity from the sand box and can be modeled using two different approaches: a non-coherent approach considering the sand box system as a homogeneous soil with a constant water content over depth or a coherent approach considering the sand box system as planar layered medium (N horizontal layers). As stated above, in the non-coherent approach, the soil is characterized by a single permittivity/water content and the reflectivity can be simply modeled using the Fresnel equations as the sand surface is assumed to be smooth. In the coherent approach, the medium of the $n^{th}$ layer is homogeneous and characterized by the dielectric permittivity $\varepsilon_n$, the electric conductivity $\sigma_n$, and the thickness $h_n$ (Figure 5.7). The reflectivity model is based on a matrix formulation of the boundary conditions at the layer interfaces derived from Maxwell's equations (Dobrowolski, 1995). To derive the reflectivity of the layer stack, the model was evaluated for dielectric layers with a thickness of 1 cm, which is much smaller than the wavelength. The soil permittivity/water content profiles were described using the van Genuchten model (Eq. (5.1)).

### 5.3.4 GPR model

**Radar equation** The radar signal $S(\omega)$ can be expressed as the ratio between the backscattered field $b(\omega)$ and incident field $a(\omega)$ at the radar transmission line reference plane, with $\omega$ being the angular frequency. In far-field conditions, the spatial distribution of the backscattered electromagnetic field measured by the antenna can be assumed to be independent of the layered medium, i.e., only the phase and amplitude of the field change (plane wave approximation over the antenna aperture). In that case, the following radar equation applies (Lambot *et al.*, 2004c; Lambot and André, 2012):

$$S(\omega) = \frac{b(\omega)}{a(\omega)} = R_0(\omega) + \frac{T(\omega)\, G_{xx}^{\uparrow}(\omega)}{1 - R_s(\omega)\, G_{xx}^{\uparrow}(\omega)} \tag{5.5}$$

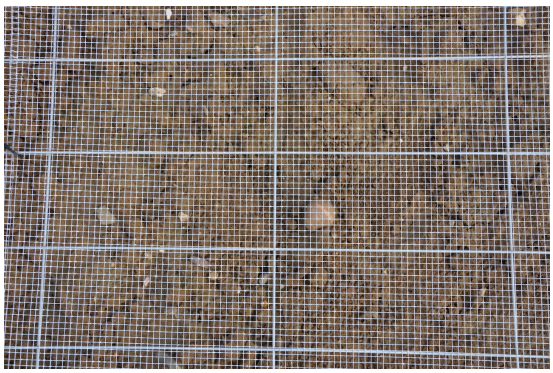

(a)

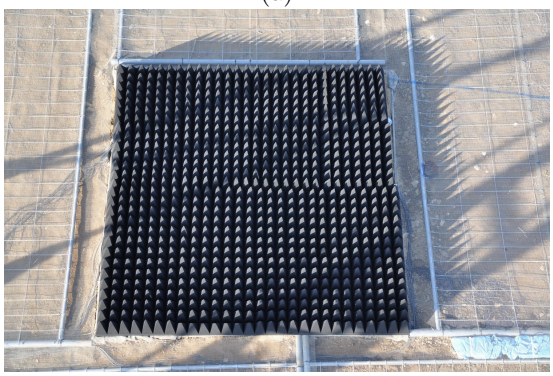

(b)

(c)

Figure 5.6: (a) Metallic mesh grid used to cover the surroundings of the sand box with a mesh-size of 0.5 cm, (b) electromagnetic absorber, and (c) perfect reflector (copper plate) placed on the top of the sand box.

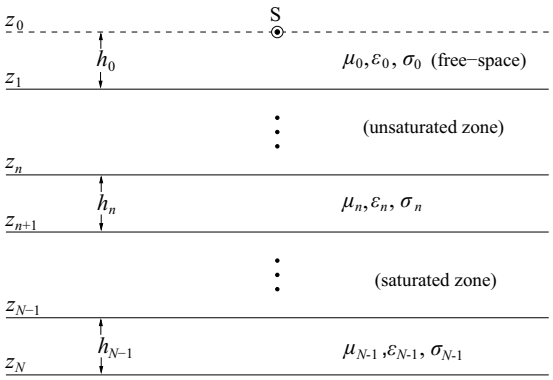


Figure 5.7: Three-dimensional planar layered medium with a radar point source and receiver or a radiometer point receiver (S). Each layer is characterized by the dielectric permittivity $\varepsilon_n$, the electric conductivity $\sigma_n$, the magnetic permeability $\mu_n$, and the thickness $h_n$.

where $R_0(\omega)$ is the global reflection coefficient of the antenna in free space, $T(\omega) = T_i(\omega)T_s(\omega)$, $T_i(\omega)$ is the global transmission coefficient for fields incident from the radar reference plane onto the point source, $T_s(\omega)$ is the global transmission coefficient for fields incident from the field point onto the radar reference plane, $R_s(\omega)$ is the global reflection coefficient for the field incident from the layered medium onto the field point, and $G^{\uparrow}_{xx}(\omega)$ is the planar layered medium Green's function.

The global reflection and transmission coefficients ($R_0(\omega)$, $T(\omega)$, and $R_s(\omega)$) are determined by solving a system of equations (Eq. (5.5)) for different model configurations. We used several well-defined configurations with the antenna at different heights above a copper plane playing the role of an infinite perfect electrical conductor. The Green's functions can therefore be computed from $S(\omega)$ measurements.

**Green's function** The radar model used to inverse the GPR signal consists of a 3D planar layered medium (N horizontal layers) with a point source and receiver (Figure 5.7). The use of a 3D model is essential to take into account spherical divergence (geometric spreading) in wave propagation. The medium of the $n^{\text{th}}$ layer is homogeneous and characterized by the dielectric permittivity $\varepsilon_n$, the electric conductivity $\sigma_n$, and the thickness $h_n$. In this study, the thickness of the layers was set to 1 cm as for the radiometer (reflectivity model). The magnetic permeability ($\mu$) is considered constant and equal to the permeability of free space ($\mu_0 = 4\pi 10^{-7}$ H m$^{-1}$). The Green's function, i.e., the solution of the 3D Maxwell equations for electromagnetic waves propagating in multilayered media, is derived by computing with a recursive scheme the TE and TM global reflection coefficients of the multilayered medium in the spectral domain (Slob and Fokkema, 2002). The transformation back to the spatial domain is performed by numerically evaluating a semi-infinite, complex integral (Lambot *et al.*, 2007).

### 5.3.5 Inversion procedure

Inversion of the radiometer and GPR data was performed to identify the van Genuchten hydraulic parameters ($\theta_r$, $\theta_s$, $\alpha$, and $n$) of the soil, which define the water content profile. $\theta_r$, which is defined as the residual water content with a pressure head $h$ of $-\infty$, was used as fixed parameter set to 0. The water table level was also assumed to be known and used as fixed parameter during the inversions. Inversions were performed in a relatively large parameter space given by $[0.25 \leq \theta_s \leq 0.45;\ 1 \leq \alpha \leq 20;\ 1.1 \leq n \leq 10]$. The inverse problem was formulated in the least-squares sense and the objective function to be minimized was accordingly defined for the different sensing methods.

For the radar (GPR), the objective function is:

$$\phi_{\mathrm{GPR}}(\mathbf{b}) = \left|\mathbf{G}_{\mathrm{xx}}^{\uparrow *}(\omega) - \mathbf{G}_{\mathrm{xx}}^{\uparrow}(\mathbf{b},\omega)\right|^{\mathrm{T}} \left|\mathbf{G}_{\mathrm{xx}}^{\uparrow *}(\omega) - \mathbf{G}_{\mathrm{xx}}^{\uparrow}(\mathbf{b},\omega)\right| \tag{5.6}$$

where $\mathbf{G}_{\mathrm{xx}}^{\uparrow *}(\omega)$ and $\mathbf{G}_{\mathrm{xx}}^{\uparrow}(\mathbf{b},\omega)$ are, respectively, the measured and modeled complex Green's functions in the frequency domain, and $\mathbf{b}$ is the parameter vector to be estimated ($\mathbf{b} = [\theta_s,\ \alpha,\ n]$). Both measured and modeled Green's functions are vectors containing values for each frequency (from 0.8 to 2.6 GHz with a step of 8 MHz, i.e, 1101 frequencies) and each water table depth (7), resulting in 7707 complex values.

To limit the dimensionality of the inverse problem, the distance between the soil surface and the GPR antenna phase center $h_0$ [m] was previously estimated by performing inversion of the electromagnetic model in the time domain (Lambot *et al.*, 2006c; Jonard *et al.*, 2011b). The vector $\mathbf{h}_0$ was then used as a fixed parameter during the inversion.

For the radiometer (MR), the objective function is:

$$\phi_{\mathrm{MR}}(\mathbf{b}) = \left(\mathbf{R}_s^* - \mathbf{R}_s(\mathbf{b})\right)^{\mathrm{T}} \left(\mathbf{R}_s^* - \mathbf{R}_s(\mathbf{b})\right) \tag{5.7}$$

where $\mathbf{R}_s^*$ and $\mathbf{R}_s(\mathbf{b})$ are, respectively, the measured and modeled reflectivity and $\mathbf{b}$ is the parameter vector to be estimated. The fractional amount of the measured radiance which was emitted from the sand box ($\eta$) was also estimated during the inversion ($\mathbf{b} = [\theta_s,\ \alpha,\ n,\ \eta]$). For this inversion, we used the coherent approach (see above) to model the soil reflectivity. Both measured and modeled reflectivities are vectors containing values for each polarization (H and V) and each water table depth (7), resulting in 14 real values.

Hydraulic parameters were also estimated in the same way from TDR and capacitance probes water content data. The respective objective functions are:

$$\phi(\mathbf{b}) = \left(\theta^* - \theta(\mathbf{b})\right)^{\mathrm{T}} \left(\theta^* - \theta(\mathbf{b})\right) \tag{5.8}$$

where $\theta^*$ and $\theta(\mathbf{b})$ are, respectively, the measured and modeled water contents from TDR or capacitance probes, and $\mathbf{b}$ is the parameter vector to be estimated ($\mathbf{b} = [\theta_s,\ \alpha,\ n]$). Both measured and modeled water contents are vectors containing values for each measurement depth (7 depths) and each water table depth (7), resulting in 49 real values.

The objective functions were minimized using the GMCS algorithm combined sequentially with the NMS algorithm as introduced by Lambot *et al.* (2002).

## 5.4 Results and discussion

### 5.4.1 TDR and capacitance sensors data

Although only TDR- and capacitance-derived soil water content at the time of radar and radiometer measurements are considered in this study, continuous measurements were performed to analyze the behavior of the *in-situ* sensors and confirm the hydrostatic equilibrium of the sand box at the times of radar and radiometer measurements. The water table level measured at hydrostatic equilibrium by using the piezometer was at 0.86 m depth on DOY 294, 0.57 m depth on DOY 304, 0.50 m depth on DOY 311, 0.41 m depth on DOY 319, 0.30 m depth on DOY 325, 0.18 m depth on DOY 332, and 0.17 m depth on DOY 343. Figure 5.8 represents the SWC as a function of time monitored by capacitance sensors at different depths. The times where the radar and radiometer were performed are also shown and correspond to hydrostatic equilibrium. We can clearly observe the successive water content increases in relation to the water table increases. As expected, the water content increases faster at the deeper depths. We can also observe that in fully saturated conditions, the sensors do not provide the same saturated water content. This may be attributed to inherent heterogeneities in the medium and artefact related to both sensor calibration and installation. The observed saturated water content ranges from about 0.33 to 0.38.

Figure 5.9 depicts the SWC readings from TDR versus capacitance sensors. Only data collected during the radar and radiometer measurements were used. In general, SWC derived from capacitance probes slightly overestimates SWC derived from TDR sensors below 0.20 $m^3$ $m^{-3}$ and underestimate TDR-derived SWC above 0.20 $m^3$ $m^{-3}$. Yet, the regression line between both SWC is close to the 1:1 line with a $R^2$ of 0.95.

### 5.4.2 Brightness temperature

Figure 5.10 shows the brightness temperature ($T_B$) measured by the L-band radiometer above the experimental setup with the free sand surface ($T_{B,sand}$), the sand surface covered by an absorber ($T_{B,abs}$), and the sand surface covered by a perfect reflector ($T_{B,refl}$). Each $T_{B,sand}$ value corresponds to a mean of at least 20 measurements performed over 45 min. The STD of the repeated $T_{B,sand}$ measurements is systematically lower than 0.3 K, which confirms the repeatability of the measurements and the stability of the instrument and the experimental setup during the measurement period. $T_{B,sand}$ decreases with increasing water table level from 150 K to 112 K for V-pol and from 138 K to 88 K for H-pol, which results from the progressive wetting of the sand. As shown, $T_{B,sand}$ at H-pol is systematically lower than at V-pol. $T_{B,refl}$ and $T_{B,abs}$ measurements were performed twice, at the beginning and in the middle of the measurement campaign, to characterize the setup. $T_{B,refl}$ measured above the entirely grid covered setup (including the sand box covered by a copper sheet) shows similar values (15–17 K at V-pol and 12 K at H-pol) to the sky brightness temperature (≈4.8 K), which confirms that the metal grid used as reflector to block the emission from the surrounding area of the sand box worked

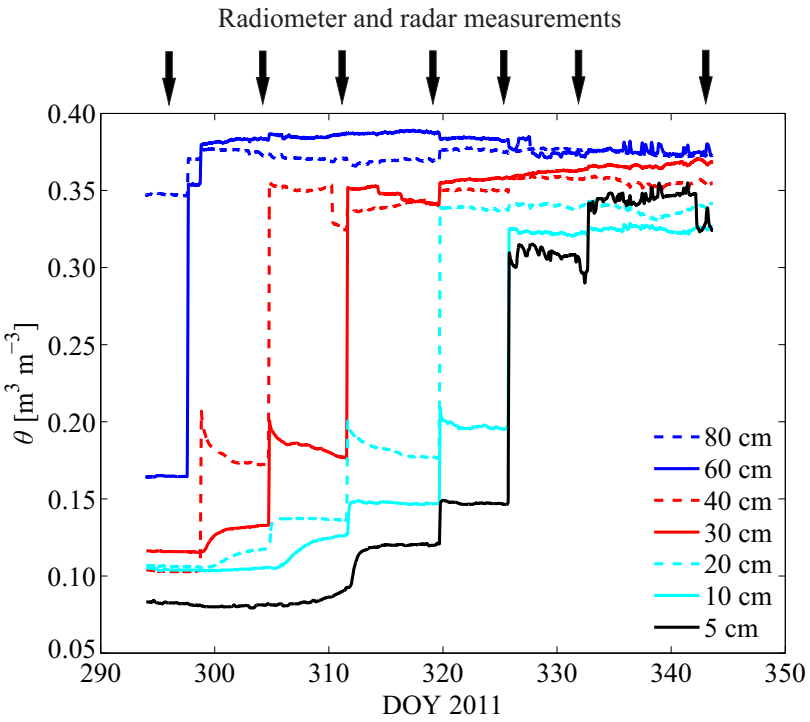


Figure 5.8: Soil water content as a function of time monitored by capacitance sensors at different depths in the sand box. Black arrows indicate the radiometer and radar measurement times.

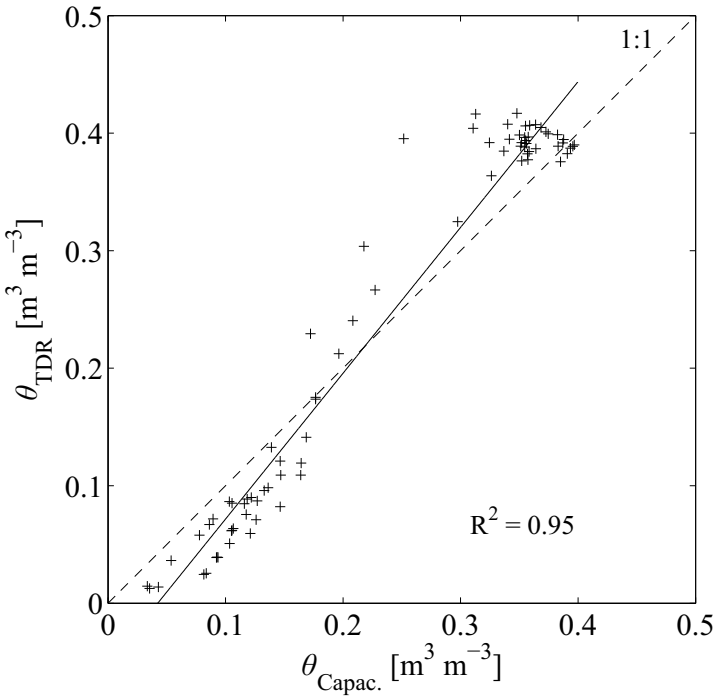


Figure 5.9: TDR-derived versus capacitance sensor-derived soil water content.

properly. The remaining difference between $T_{\mathrm{B,refl}}$ and $T_{\mathrm{sky}}$ may come from (1) influences from areas not covered by the metal grid, and (2) multiple refections and emissions from the aluminium arc. Additionally, $T_{\mathrm{B,refl}}$ stayed relatively constant between the two calibration periods, with a difference of 0.6 K and 2.1 K for H- and V-pol, respectively. This confirms that the setup did not change significantly between the two calibrations. $T_{\mathrm{B,abs}}$ shows the largest brightness temperature values with 167–168 K for V-pol and 161–162 K for H-pol. The similar $T_{\mathrm{B,abs}}$ values retrieved for the two calibration periods are explained by a similar physical temperature of the absorber, as the radiation of an absorber is only driven by its physical temperature, and a similar emission from areas surrounding the sand box. Finally, the large differences between $T_{\mathrm{B,refl}}$, $T_{\mathrm{B,abs}}$, and $T_{\mathrm{B,sand}}$ proves that the size of the sand box (2.00 x 2.00 $\mathrm{m}^2$ area) was large enough to significantly detect different L-band radiation from the sand box for different configurations (reflector, absorber, and sand) and, therefore different soil water contents of the sand within the box.

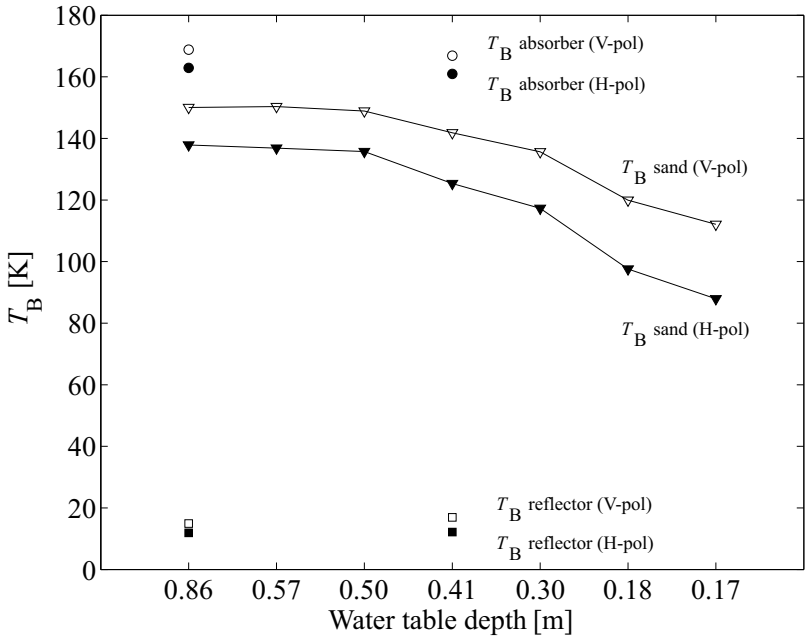


Figure 5.10: Brightness temperature $T_{\mathrm{B}}$ measured by the L-band radiometer above the free sand surface (triangles) for both horizontal and vertical polarizations as a function of water table depth (depth scale is not linear). $T_{\mathrm{B}}$ measurements above the sand surface covered by an absorber (circles) and a reflector (squares) are also shown for two calibration periods. Note that the STD of the $T_{\mathrm{B}}$ measurements is not shown as the STD values are too small (<0.3K) to be visible on the graph.

### 5.4.3 Radar data

Figure 5.11 represents the observed radar Green functions in the frequency domain ($G^{\uparrow}_{xx}$) for 2 water table depths and Figure 5.12 shows the observed radar Green functions in the time domain ($g^{\uparrow}_{xx}$) for the 7 water table depths. The Green's function is computed from the $S$ scatter function for frequencies between 0.8–2.6 GHz using Eq. (5.5) to filter out antenna effects. As expected for the frequency range used, the frequency dependence of the Green function amplitude is linear. In the time domain, the time zero corresponds to the antenna phase center. The reflection from the soil surface is clearly visible between 2–3 ns. The remaining oscillations on the time-domain signal are caused by the inverse Fourier transform, since only the signal frequencies between 0.8–2.6 GHz were measured. The surface reflection does not exactly occur at the same time for each measurement as the height of the antenna (0.35 to 0.40 m) was slightly different for the different measurements. The amplitude of the reflection is increasing with increasing water table level, which means that the dielectric contrast between the air layer and the surface soil layer increased. No clear reflection can be observed below the surface reflection and the water table interface is also not detectable. This means that the sand dielectric profile is continuous for the frequencies used and that the electromagnetic waves are almost totally attenuated in the unsaturated zone. The assumption of a continuous dielectric profile for the unsaturated zone and an infinite lower half-space for the saturated zone in the electromagnetic model can therefore be confirmed.

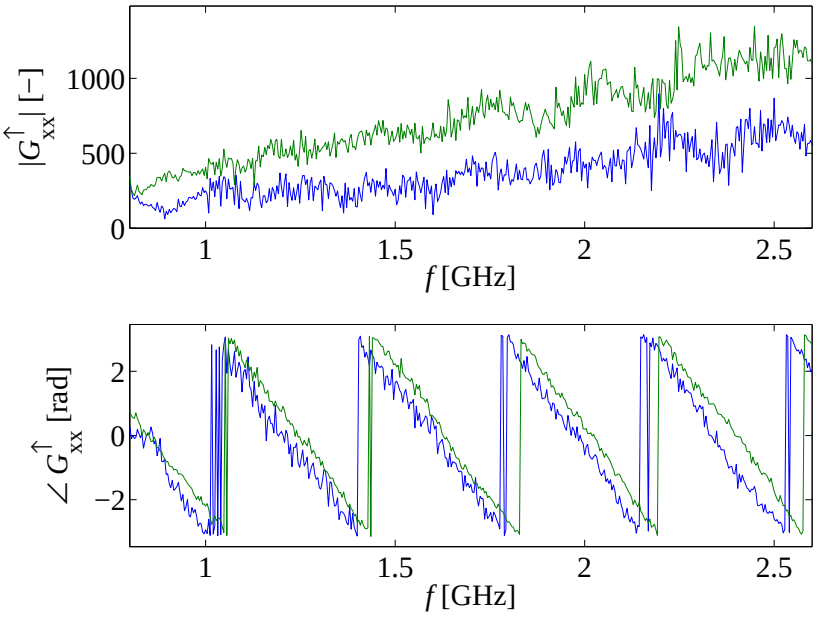


Figure 5.11: Green's function in the frequency domain for measurements performed in the frequency range 0.8–2.6 GHz and for two water table depths, 0.57 (blue) and 0.17 m (green), respectively.

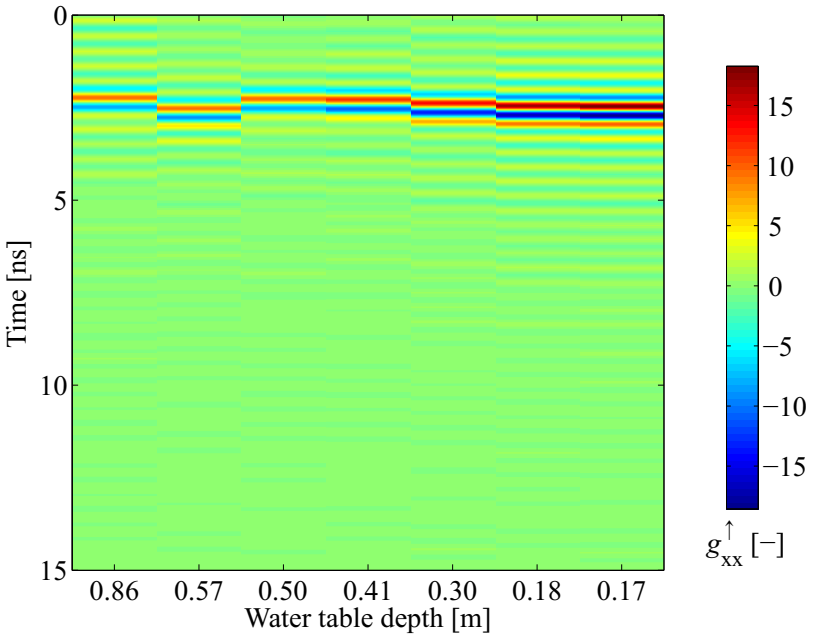


Figure 5.12: Green's function in the time domain for measurements performed in the frequency range 0.8–2.6 GHz and for the seven water table depths (depth scale is not linear).

### 5.4.4 Surface soil water content

In a first step, we derived surface SWC from radiometer and radar data. For the radiometer, the surface soil layer was considered as homogeneous and the Fresnel equations were used to compute the dielectric permittivity of the surface soil layer. For the radar, the data were analyzed using full-wave inversion in the time domain of the surface reflection. Figure 5.13 shows radiometer-, GPR-, and TDR-derived surface SWC for the 7 water table depths. Surface SWC from radiometer was derived from both polarizations. V-pol-derived SWC shows slightly higher SWC compared to H-pol derived SWC. The frequency range 0.8–2.0 GHz was used to derive SWC from GPR data in order to have the same central frequency (1.4 GHz) as for radiometer. For TDR, we used the measurements performed at 5 cm depth. In general, radiometer- and GPR-derived SWC are in close agreement with TDR estimates for lower water contents but the GPR estimates differ substantially for higher water contents.

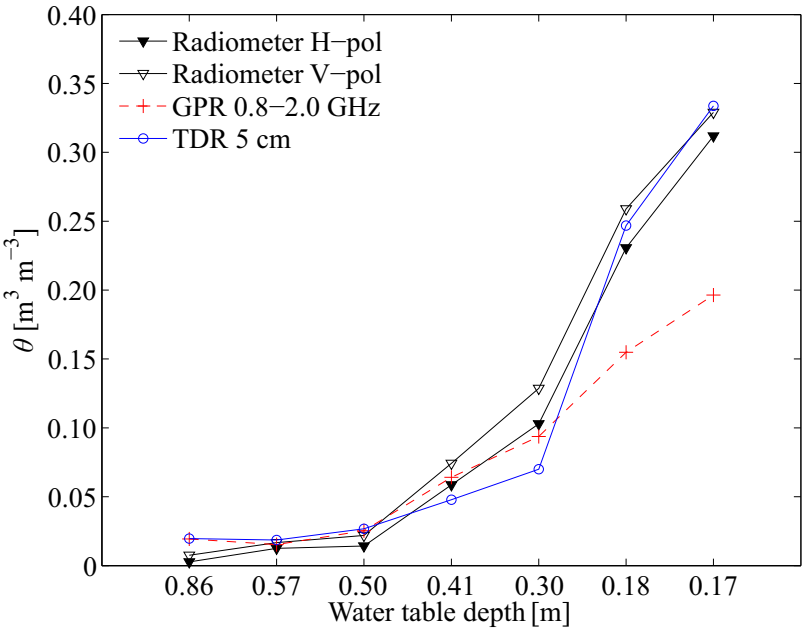


Figure 5.13: Radiometer- and GPR-derived surface soil water content $\theta$ as a function of water table depth (depth scale is not linear).

### 5.4.5 Water content profile and hydraulic parameters

In a second step, the objective was to retrieve the SWC profile and the related hydraulic parameters of the van Genuchten model. Figures 5.14 and 5.15 represent the water content measured by the TDR and capacitance sensors, respectively, at different depths and for different water table levels as well as the directly fitted SWC profile using the van Genuchten model.

The inversely estimated hydraulic parameters for the four measurement techniques, namely, TDR, capacitance probes, radiometer, and GPR, and their corresponding confidence intervals are presented in Table 5.1. As TDR is widely recognized in hydrology as a reference for SWC measurement, TDR-derived parameters are considered in this study as reference parameters. For the capacitance probes, parameter $\theta_s$ is significantly underestimated with a value of 0.36 considering the information from all sensors installed in the sand box. The $\alpha$ parameter is slightly larger compared to the TDR estimate and the $n$ parameter slightly lower. The value of $\theta_s$ obtained from the inversion of the radiometer data is 0.37 $m^3$ $m^{-3}$, which is slightly smaller compared to the value of 0.40 $m^3$ $m^{-3}$ obtained from the inversion of the TDR data. As the confidence interval is relatively large, inversion of the hydraulic parameters was also performed by fixing $\theta_s$ to 0.40 $m^3$ $m^{-3}$ in order to reduce the number of unknowns. Radiometer-derived $\alpha$ and $n$ show slightly different values compared to TDR-derived parameters but the confidence intervals are relatively small ($\pm 0.6$ $m^{-1}$ for $\alpha$ and $\pm 0.7$ for $n$). Parameter $\eta$, which is the fractional amount of the measured radiance emitted from the sand box, was also inverted simultaneously with the hydraulic parameters. The estimated value of $\eta$ is $0.49 \pm 0.0013$. This value is relatively close to the one obtained using the absorber and reflector measurements (0.54) and the confidence interval is very small. The value of $\theta_s$ obtained from the inversion of GPR data is 0.27 $m^3$ $m^{-3}$, which is significantly lower compared to the reference value. As for the radiometer data, inversion of the hydraulic parameters from GPR data was also performed by fixing $\theta_s$ to 0.40 $m^3$ $m^{-3}$. GPR-derived $\alpha$ and $n$ are slightly closer to TDR-derived parameters compared to radiometer-derived parameters and the confidence intervals are also smaller. This can be explained by the larger information contained in the GPR signal (1101 frequencies x 1 polarization) compared to the radiometer signal (1 frequency x 2 polarizations). However, the differences in terms of accuracy for the parameter retrieval are relatively small compared to the large differences in terms of information contained in the radar and radiometer data. In addition, $\theta_s$ was much better estimated by the radiometer compared to GPR. This is to be attributed to the absence of significant radar reflection from the saturated zone due to the smooth transition zone within the water profile. A correct estimate could have been achieved for saturated conditions at the soil surface.

Figure 5.16 compares the soil water retention curves retrieved by the different techniques. To compute these curves, results considering $\theta_s$ as fixed parameter for the inversion of the GPR and radiometer data were used. As shown, GPR- and radiometer-derived water retention curves are in close agreement with the reference TDR-derived water retention curve with a maximum water content difference of 0.04 and 0.05 for, respectively, GPR- and radiometer-derived water content with respect to TDR-derived water content.

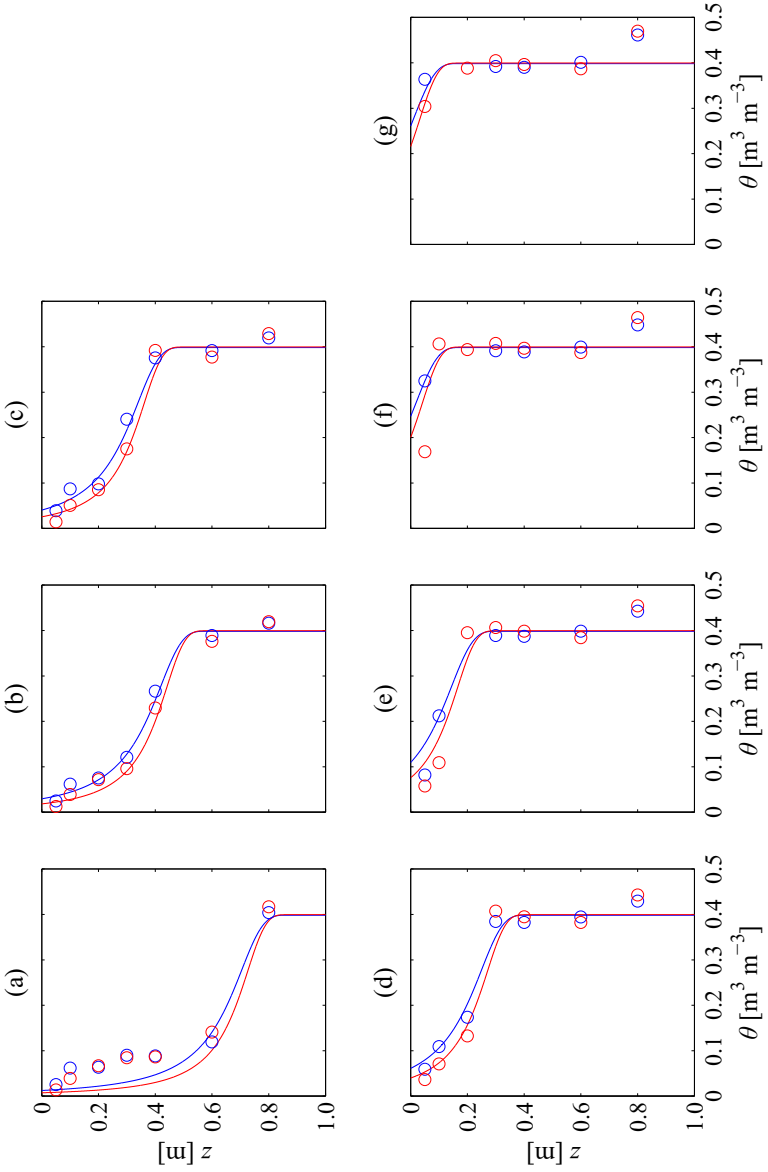


Figure 5.14: Water content profiles for 7 water table depths, i.e., (a) 0.86 m, (b) 0.57 m, (c) 0.50 m, (d) 0.41 m, (e) 0.30, (f) 0.18 m, and (g) 0.17 m depth. Solid lines represent the fitted van Genuchten model and markers represent TDR measurements. Blue and red colors represent the two respective measurement profiles.

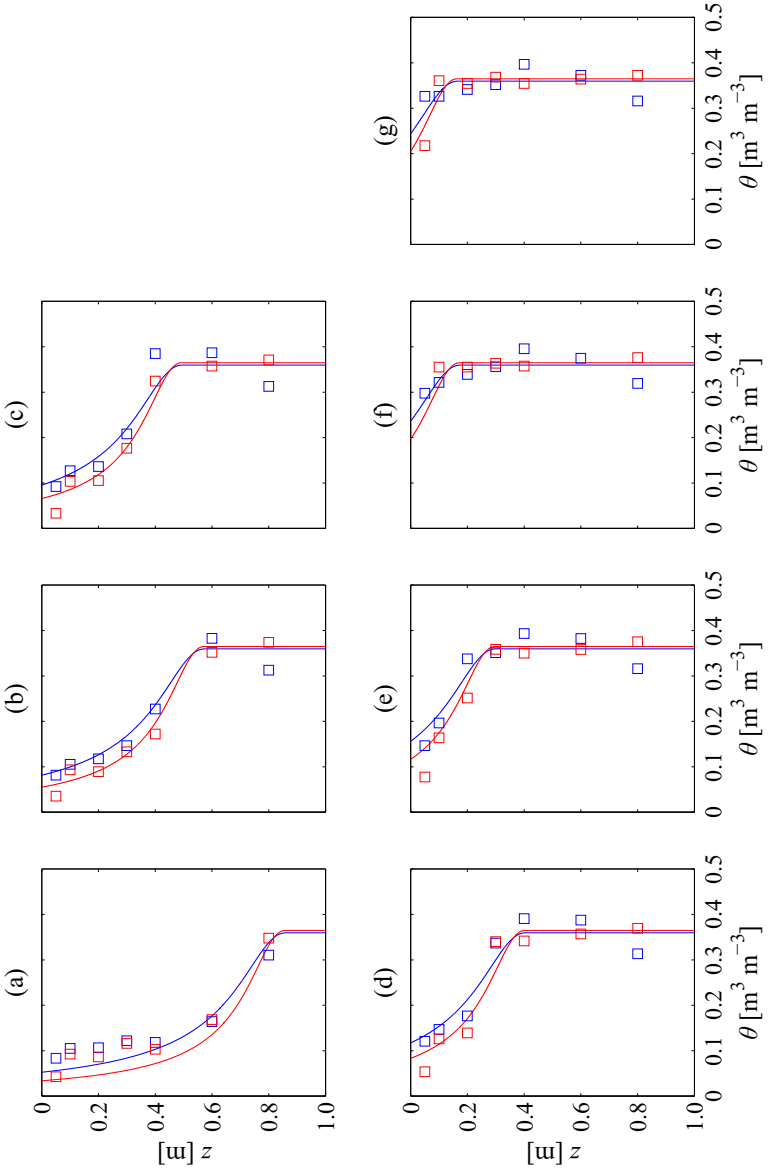


Figure 5.15: Water content profiles for 7 water table depths, i.e., (a) 0.86 m, (b) 0.57 m, (c) 0.50 m, (d) 0.41 m, (e) 0.30, (f) 0.18 m, and (g) 0.17 m depth. Solid lines represent the fitted van Genuchten model and markers represent capacitance sensor measurements. Blue and red colors represent the two respective measurement profiles.

Table 5.1: Inversely estimated van Genuchten parameters. Confidence intervals are presented in brackets ($\alpha_t = 0.05$).

| | $\theta_s$ $m^3\ m^{-3}$ | $\alpha$ $m^{-1}$ | $n$ – |
|---|---|---|---|
| TDR - Profile 1 | 0.398 (0.012) | 5.740 (0.666) | 3.166 (0.495) |
| TDR - Profile 2 | 0.400 (0.018) | 6.717 (1.123) | 3.274 (0.745) |
| TDR - All sensors | 0.399 (0.011) | 6.258 (0.694) | 3.160 (0.456) |
| Capacitance sensors - Profile 1 | 0.360 (0.013) | 6.233 (1.388) | 2.135 (0.307) |
| Capacitance sensors - Profile 2 | 0.365 (0.012) | 7.896 (1.578) | 2.237 (0.288) |
| Capacitance sensors - All sensors | 0.362 (0.009) | 7.025 (1.112) | 2.177 (0.220) |
| Radiometer | 0.371 (0.183) | 4.778 (2.403) | 3.945 (2.175) |
| Radiometer | 0.400 (fixed) | 5.106 (0.551) | 3.746 (0.679) |
| GPR | 0.272 (0.072) | 5.133 (1.317) | 3.714 (0.616) |
| GPR | 0.400 (fixed) | 7.142 (0.436) | 3.247 (0.200) |

## 5.5 Summary and conclusion

In this study, we investigated the feasibility of measuring a continuous dielectric profile in a sandy soil using off-ground GPR and L-band radiometer data. In particular, measurements were performed above a sand box in hydrostatic equilibrium with a water table located at different depths. The results of the inversions showed that the radar and radiometer signals contain sufficient information to estimate the sand water retention curve and its related hydraulic parameters with a relatively good accuracy compared to TDR estimates. However, an accurate estimation of the hydraulic parameters was only obtained by considering the saturated water content parameter as known during the inversion.

Additionally, further issues still need to be investigated such as the estimation of the hydraulic parameters of the sand from laboratory measurements in order to have a sensor-independent information, and the application of a dielectric mixing model to account for the imaginary part of the dielectric permittivity in the radar as well as in the radiometer model. Further research will also focus on the inversion of GPR and radiometer data at transient conditions which are much more natural-like conditions. Finally, the setup also allows us to study the impact of soil surface roughness and vegetation on the radar and radiometer signal and its influence on the retrieval of the soil hydraulic properties.

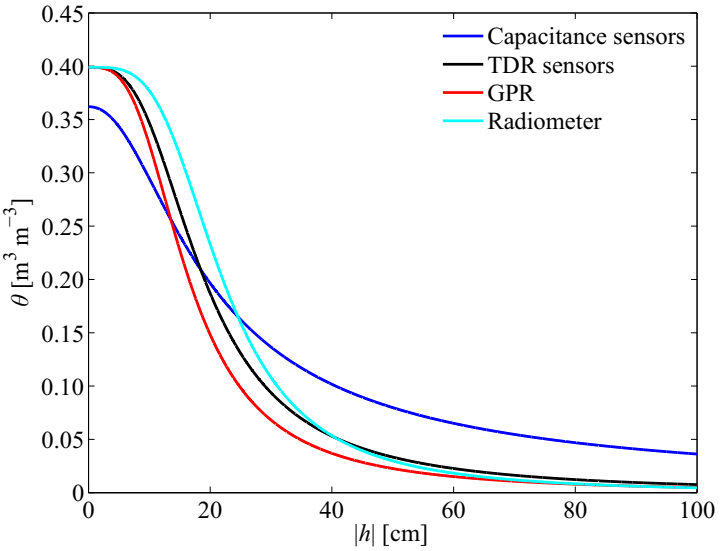


Figure 5.16: Water retention curves based on the van Genuchten parametrization and estimated by the different sensing methods (capacitance sensors, TDR sensors, GPR, and radiometer).

# Chapter 6

# Characterization of crop canopies and water stress related phenomena using microwave remote sensing methods: A review*


## Abstract

In this chapter we reviewed the use of microwave remote sensing methods for characterizing crop canopies and vegetation water-stress related phenomena. Our analysis includes both active and passive systems that are ground-based, airborne, or spaceborne. Most of the published results that have examined crop canopy characterization and water stress have used active microwave systems. In general, quantifying the effect of dynamic vegetation properties and particularly water-stress related processes on the measured microwave signals can still benefit from improved models and more observational data. Integrated data sets providing information on both soil status and plant status are lacking, which has hampered the development and validation of mathematical models. There is a need to link 3D functional-structural crop models with radiative transfer models in order to better understand the effect of environmental and related physiological processes on microwave signals and to better quantify the impact of water stress on microwave signals. Such modeling approaches should incorporate both passive and active microwave methods. Studies that combine different sensor technologies that cover the full-spectral range from optical to


*This chapter is adapted from:
Vereecken, H.; Weihermüller, L.; Jonard, F. & Montzka, C. Characterization of crop canopies and water stress related phenomena using microwave remote sensing methods: A review, in *Vadose Zone Journal*, **2012**, 11(2). My contributions to this chapter are Sections 6.2–6.3–6.4.

microwave have the potential to move forward our knowledge on the status of crop canopies and particularly water related stress phenomena. Assimilation of remotely sensed properties such as backscattering coefficients or brightness temperature in terms of estimating biophysical crop properties using mathematical models is also an unexplored avenue.

## 6.1 Introduction

Over the last three decades there has been a growing awareness of the importance of land surface processes and their value in predicting climate change and its subsequent impact on the terrestrial system, managing water resources, and predicting and monitoring floods and droughts. Remote sensing from Earth observation platforms has played a key role by providing valuable data from local to global scales and at different time scales to the scientific community. Given the importance of the land surface for terrestrial processes and for agricultural activity, the characterization and monitoring of vegetation and crops has been an important focus area in the remote sensing of the Earth surface. Historically, remote sensing of vegetation has focused primarily on the use of spectral measurements in the visible, near infrared, and shortwave infrared region of the spectrum. This region is important because the reflectance measurements are governed primarily by the scattering and absorption characteristics of the leaf internal structure and biochemical constituents. Overviews of the satellite-based results can be found in Lu (2006) for biomass estimation, Moskal and Zheng (2009) for leaf area (LAI) index retrieval, Govender *et al.* (2009) for multispectral detection of plant water stress, and Pinter *et al.* (2003) for crop management.

During the last decade, satellite and spaceborne SAR systems (i.e., ALOS PALSAR, RADARSAT-1 and 2, ERS-1 and 2, ENVISAT ASAR, SIR-C/X SAR, TerraSAR-X) and microwave radiometers (i.e., AQUA AMSR-E, Coriolis WindSAT, SMOS MIRAS) have been available. A list of spaceborne microwave sensors is given in Table 6.1 and a list of microwave frequency bands is given in Table 6.2. In the near future combined active and passive systems, such as AQUARIUS (launched in June 2011) and SMAP (planned launch in 2014), will offer new opportunities in microwave remote sensing. Passive and active measurements in the microwave region of the spectrum have mainly been used to characterize biophysical parameters of the plant canopy, such as shape, size and distribution of plant elements, water content, height of the vegetation, LAI, above ground biomass, and number of plants (Chukhlantsev *et al.*, 2003; Della Vecchia *et al.*, 2007; Moran *et al.*, 1997; Paloscia and Pampaloni, 1988). In addition, passive microwave methods at low frequencies (X-, C-, and L-band) have typically been used to detect bare or vegetated surface soil moisture content (Calvet *et al.*, 2011; Guglielmetti *et al.*, 2008; Jackson and Schmugge, 1989; Jackson *et al.*, 1982; Jonard *et al.*, 2011b; Njoku and Entekhabi, 1996; Schmugge *et al.*, 1974; Wigneron *et al.*, 2003). Additionally, low frequency active systems have been used to study the effect of vegetation on the retrieval of land surface properties. The effect of vegetation on the recovery of soil moisture was studied by Mätzler (1990), Serbin and Or (2005), Joseph *et al.* (2008),

and Joseph *et al.* (2010b). O'Neill *et al.* (1996) used both active and passive microwave sensors for soil moisture estimation through vegetation. Vegetation transmissivity and scattering were characterized by using L-band radar data. The vegetation parameters were then used for soil moisture retrieval based on a radiative transfer approach utilizing passive microwave data. However, limited attention has been given to the use of microwave methods to detect water stress in agricultural canopies despite the advantages of these methods compared to optical and infra-red (IR) multi or hyperspectral sensors (Detar *et al.*, 2006). These include the ability of providing time critical remotely sensed observations, such as at night time or when cloud cover is present (McNairn and Brisco, 2004) and the ability to sense the entire canopy as opposed to just the leaves. Ferrazzoli (2002) briefly reviewed the use of SAR for agricultural purposes. In addition to describing the historical evolution from ground-based measurements, to airborne measurements, and finally satellite platforms he addressed and discussed the identification of useful radar configurations and the development of relationships between backscattering and variables for seven selected crops.

Despite the extensive body of literature available on the subject of remote sensing and vegetation, no attempt has been made to evaluate and analyze in depth the use of active and passive microwave methods to characterize crop canopies, specifically in relation to stress phenomena. This review has three main objectives:

- to review the use of microwave methods to characterize crop canopies with specific attention to stress-related properties such as vegetation water content and leaf water potential;
- to analyze the effect of confounding factors on the retrieval of drought conditions or water stress in crop canopies;
- to formulate future avenues of research related to water stress recognition in vegetation using microwave methods.

The chapter is organized in 8 sections. In section two, we will present an overview of the theory and models that were developed to interpret signal propagation of microwave systems (passive and active) in above ground agricultural vegetation properties. Section three addresses the characterization of crop canopies using ground-based measurements with specific attention to diurnal and seasonal dynamics of backscattering in canopies. Section four mainly deals with the characterization of crop canopies from air- and spaceborne remote sensing observations. In section five, we discuss the relationship between dielectric properties of the vegetation and soil plant water relationships, whereby these relationships are essential for the interpretation of the diurnal and seasonal changes in emissivity and backscattering. Section six discusses the factors controlling microwave signals obtained from crop canopies with a specific focus on water stress phenomena. Finally, we end our review with the topic of multi-sensor measurements and an outlook section presenting conclusions and avenues for further research needs.

Table 6.1: List of spaceborne microwave sensors.

| **Name** | **Platform** | **Frequency (GHz)** | **Spatial resolution** | **Temporal resolution (d)** | **Active (A)/ Passive (P)** |
|---|---|---|---|---|---|
| AMSR-E | AQUA | 6.925, 10.65, 18.7 23.8, 36.5, 89.0 | 56, 38, 21, 24, 12, 5.4 km | 1 | P |
| ASCAT | MetOp | 5.255 | 25 to 50 km | 2 | A |
| PALSAR | ALOS | 1.27 | 9 to 157 m | 46 | A |
| AQUARIUS | AQUARIUS/SAC-D | 1.26 (A), 1.413 (P) | 76 to 156 km | 7 | A and P |
| ASAR | ENVISAT | 5.331 | 30 to 1000 m | 5 | A |
| COSMO-SkyMed | COSMO-SkyMed | 9.6 | 1 to 100 m | 0.5, 4, 16 | A |
| ERS-SAR | ERS-1 & ERS-2 | 5.3 | 30 m | 3, 35, 176 | A |
| JERS-1-SAR | JERS-1 | 1.3 | 18 m | 44 | A |
| RADARSAT 1 & RADARSAT 2 | RADARSAT 1 & RADARSAT 2 | 5.405 | 10 m | 24 | A |
| SIR-A | Space Shuttle | 1.28 | 40 m | – * | A |
| SIR-C/X | Space Shuttle | 1.25, 5.3, 9.6 | 10 to 30 m | – * | A |
| SMAP | SMAP | 1.26 (A), 1.41 (P) | 1 to 3 km (A), 40 km (P) | 2 to 3 | A and P |
| MIRAS | SMOS | 1.4 | 35 to 60 km | 3 | P |
| SSM/I | SSM/I | 19.35, 22.2, 37.0, 85.5 | 13 to 69 km | 0.5 | P |
| SeaWinds | QuickSCAT | 13.4 | 25 km | 1 | A |
| Tandem-L | Tandem-L | 1.2 | 3 to 20 m | 8 | A |
| TanDEM-X | TanDEM-X | 9.65 | 1 to 18 m | 2 to 4 | A |
| TerraSAR-X | TerraSAR-X | 9.65 | 1 to 18 m | 2 to 4 | A |
| WindSAT | Coriolis | 6.8, 10.7, 18.7, 23.8, 37.0 | 8 to 71 km | 8 | P |

* A temporal resolution is not given, because the missions took several days. SIR-A was a mission from 12 to 14 Nov. 1981 and SIR-C/X was a mission from 9 to 20 Apr. 1994 and from 30 Sept. to 11 Oct. 1994.

Table 6.2: Standard IEEE microwave frequencies and nomenclature.

| Band designator | Frequency (GHz) | Wavelength in free space (cm) |
|---|---|---|
| L | 1–2 | 30–15 |
| S | 2–4 | 15–7.5 |
| C | 4–8 | 7.5–3.8 |
| X | 8–12 | 3.8–2.5 |
| Ku | 12–18 | 2.5–1.7 |
| K | 18–27 | 1.7–1.1 |
| Ka | 27–40 | 1.1–0.75 |
| V | 40–75 | 0.75–0.40 |
| W | 75–110 | 0.40–0.27 |

## 6.2 Measurements principles and general modeling approaches

This section provides a general overview of the measurement principles of passive and active systems, and a brief description of electromagnetic wave propagation, attenuation, and scattering in vegetation canopies. Specific attention will be given to models specifically designed to predict emission or backscattered signals from crop canopies. Only a brief overview of the theory and the various models is provided. For more detailed information the reader will be referred to the original citations. In the presentation, we make a distinction between passive and active systems as each system measures different properties of the canopy. Microwave radiometers provide the brightness temperature, $T_{\mathrm{B}}$, of the surface whereas active radar systems measure the backscattering coefficient, $\sigma^0$.

### 6.2.1 Passive systems

For land surfaces low frequency microwave radiometry can be used as an indirect method to measure the complex dielectric permittivity $\varepsilon = \varepsilon' + i\varepsilon''$ of a bare soil, which can be used as a proxy for the estimation of the soil moisture content (e.g., Hong and Shin, 2011; Hornbuckle *et al.*, 2003; Saleh *et al.*, 2007; Schneeberger *et al.*, 2004; Wigneron *et al.*, 1995). The determination of the permittivity, $\varepsilon$, is typically based on the measurement of thermal radiance emitted from the Earth surface in a given frequency band (Njoku and Entekhabi, 1996). At specific frequency, the intensity of the received radiation (thermal emission) is proportional to the thermodynamic temperature $T_{\mathrm{s}}$ [K] and the emissivity $E_{\mathrm{S}}$ of the soil, which can be expressed by the Rayleigh-Jeans approximation of Planck's law. According to this equation, the radiance is proportional to the physical temperature of the object, and therefore, denoted as brightness temperature, $T_{\mathrm{B}}$ [K] (Njoku and Entekhabi, 1996; Wigneron *et al.*, 2001). As a consequence, the brightness temperature of a soil surface observed

for example by a radiometer operating at L-band can then be expressed as Eq. (2.4) (Jackson, 1993; Wigneron *et al.*, 2001).

However, in the presence of vegetation, Eq. (2.4) is no longer applicable because absorption, emission, and scattering by the vegetation canopy need to be considered in the formulation of the radiative transfer model (see also Figure 6.1). Therefore, $T_{\mathrm{B}}$ for one polarization of a soil-vegetation system can be expressed by:

$$T_{\mathrm{B}} = T_{\mathrm{v}}(1 - R_{\mathrm{v}} - \gamma) + E_{\mathrm{s}}\, T_{\mathrm{s}}\, \gamma + T_{\mathrm{s}}(1 - R_{\mathrm{v}} - \gamma)(1 - E_{\mathrm{s}})\gamma \tag{6.1}$$

where $T_{\mathrm{v}}$ is the vegetation temperatures [K], $R_{\mathrm{v}}$ is the vegetation canopy reflectivity, $\gamma$ is the transmissivity of the vegetation canopy, $E_{\mathrm{s}}$ is the surface emissivity, $T_{\mathrm{s}}$ [K] is the effective physical temperature of the soil, and $p$ refers to the polarization (horizontal or vertical) (Chukhlantsev *et al.*, 2003).

At low frequencies (L-band) and for low vegetation, a zero-order solution of radiative transfer equation, called Tau-Omega model, can be used and is expressed by:

$$T_{\mathrm{B},p} = (1 - \omega_p)(1 - \gamma_p)(1 + \gamma_p\, R_{\mathrm{s},p})T_{\mathrm{v}} + (1 - R_{\mathrm{s},p})\gamma_p\, T_{\mathrm{s}} \tag{6.2}$$

where $R_{\mathrm{s}}$ is the soil reflectivity and $\omega$ the single scattering albedo. The attenuation in the vegetation layer as described by the vegetation attenuation factor $\gamma$ (or vegetation transmissivity) can be defined in terms of the optical depth ($\tau$) and incidence angle ($\vartheta$) by (Wigneron *et al.*, 2007):

$$\gamma_p = \exp(-\tau_p / cos\vartheta) \tag{6.3}$$

Jackson and O'Neill (1990) showed that a linear relationship between the optical depth ($\tau$) and the vegetation water content ($VWC$ [kg m$^{-2}$]) exists:

$$\tau_p = b_p\, VWC \tag{6.4}$$

where $b$ is a regression coefficient which is frequency and polarization dependent and characteristic for the type of canopy (Jackson and Schmugge, 1991; Van de Griend and Wigneron, 2004).

In general, the Tau-Omega model is a good approximation at low frequencies such as L-band and has been intensively used to model microwave emissions from uniformly vegetated land surface at this frequency (Hornbuckle *et al.*, 2003; Joseph *et al.*, 2010b; O'Neill *et al.*, 1996; Wigneron *et al.*, 2004). Within the SMOS and SMAP communities, a modified version of the Tau-Omega model is used and is called the L-band Microwave Emission of the Biosphere (L-MEB) model (Wigneron *et al.*, 2007).

Only few physically based radiative transfer models were developed which account for the vegetation explicitly. These models are mainly used to correct for the vegetation influence in order to improve soil moisture observations in forest stands (Della Vecchia *et al.*, 2006; Ferrazzoli and Guerriero, 1996). Only few approaches were made to physically model agricultural crops such as the explicit model presented by Schwank *et al.* (2005) who showed that changes in the plant geometry (here induced by a hail storm over glover grass) will greatly influence measured brightness temperatures.

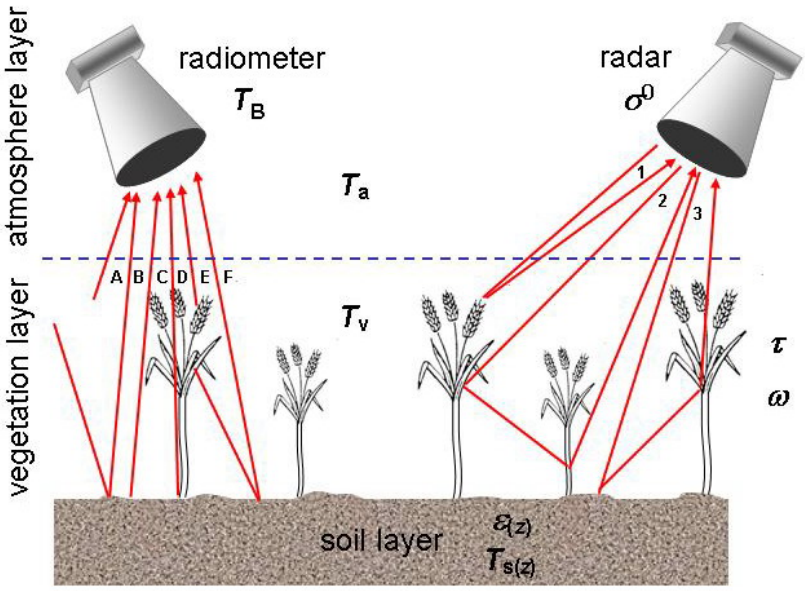


Figure 6.1: Schematic illustration of the different components of the passive and active signals measured by radiometer and radar, respectively. $T_{\mathrm{B}}$ is the brightness temperature measured by the radiometer, $\sigma^0$ is the backscattering coefficient measured by the radar, $T_{\mathrm{a}}$ is the temperature profile of the atmosphere layer, $T_{\mathrm{v}}$ is the temperature profile of the vegetation layer, $\tau$ is the vegetation optical depth, $\omega$ is the single scattering albedo of the vegetation layer, $T_{\mathrm{s}}(z)$ is the temperature profile in the soil, and $\varepsilon(z)$ is the dielectric permittivity profile in the soil. **1** represents the signal emitted by the radar and reflected on the vegetation canopy, **2** is the radar signal reflected by the vegetation stems to the radar antenna, **3** is the radar signal reflected by the soil surface and then the vegetation to the radar antenna, **A** is the passive microwave signal emitted from the atmosphere, **B** is the microwave emission from the atmosphere and reflected by the soil to the radiometer antenna, **C** is the microwave emission from the soil, **D** is the microwave emission from soil transmitted to the radiometer antenna through the vegetation layer, **E** is the microwave emission from the vegetation canopy, and **F** is the microwave emission from the vegetation canopy reflected by the soil to the radiometer antenna.

### 6.2.2 Active systems

Active systems such as radars or scatterometers are typically used to define the backscattering coefficient of the land surface. The backscattering coefficient, which is the effective scattering area of the target per unit area, is directly proportional to the ratio of the backscattered to the emitted energy. For a soil-vegetation system (Figure 6.1), the backscattering coefficient is generally expressed as:

$$\sigma^0 = \sigma_{\mathrm{s}}^0 \, \gamma^2 + \sigma_{\mathrm{v}}^0 (1 - \gamma^2) + \sigma_{\mathrm{sv}}^0 \tag{6.5}$$

where $\sigma_{\mathrm{s}}^0$ and $\sigma_{\mathrm{v}}^0$ are the backscattering coefficients of the soil and vegetation canopy, respectively, and $\sigma_{\mathrm{sv}}^0$ is the backscattering coefficient of the vegetation layer including the reflection from the soil and the attenuation by the vegetation (Chukhlantsev *et al.*, 2003).

In the early years of radar application over vegetation, empirical models were developed using regression analysis of the radar backscattering on plant moisture, plant height, and the moisture content of the underlying soil (Bush and Ulaby, 1976; Ulaby and Bush, 1976a,b). However, no knowledge about the physical processes was assumed or incorporated into the empirical models.

During the last decades physically based models were developed to describe the propagation, scattering, and attenuation of the electromagnetic waves in the vegetation layer. A detailed treatment and overview of models and microwave remote sensing theories is given by Ulaby *et al.* (1986) and Fung (1994). Chukhlantsev *et al.* (2003) distinguished two fundamentally different types of model approaches: (1) the continuous layer models with a randomly distributed dielectric constant (the so-called cloud models) and (2) models assuming a set of randomly distributed lossy scatters representing the different constituents of the vegetation such as leaves, stalks, branches, and trunks.

In 1978, Attema and Ulaby (1978) developed a cloud model for radar backscattering from vegetation. In this model, it is assumed that the vegetation is mainly composed of water which is surrounded by a large air volume. Therefore, the vegetation water can be represented by a water cloud whose water droplets are held in place by the vegetation. The model is based on the assumption that the canopy "cloud" contains identical water droplets which are randomly distributed within the canopy. The model was successfully applied by Paris (1986), Prevot *et al.* (1993), Taconet *et al.* (1994), Wigneron *et al.* (2002), Maity *et al.* (2004), and Serbin and Or (2005) for different applications and crop stands. It has to be noted that various authors modified the "simple cloud model" to increase the complexity and as a consequence the overall performance of the model (Paris, 1986). Ulaby *et al.* (1990) developed the Michigan Microwave Canopy scattering model for forest systems which is a widely used model in active microwave remote sensing. This model was successfully adapted to agricultural crops by Touré *et al.* (1994).

Eom and Fung (1984) developed a scatter model based on the matrix doubling method for volume scattering and the Kirchhoff method for rough surface scattering. They assumed that the scattering from the vegetation is dominated by the leaves and therefore single leaves can be modeled by thin dielectric discs. Finally, the vegetation layer was modeled as a layer of leaves above an irregular

soil surface. Additionally, the phase function for a single leaf was computed by approximating an integral equation for the electric field. In order to obtain closed form equations strong assumptions have to be made. These include: (1) the field variation across the thickness of the leaf is negligible, and (2) the phase change across the surface of the leaf can be accounted for by integrating the static field. Thus, the model is a static approximation generalized to include phase changes across the leaf surface. Finally, the closed form solution for the scattering coefficient contains three terms. One term represents volume scattering, another term ground surface scattering attenuated by the vegetation, and the last term which accounts for surface-volume interactions. Further research included various modifications and improvements in order to increase the physical representation of the model for different crops and frequencies. For example, Della Vecchia *et al.* (2004) modeled the radar backscattering from a canopy with leaves described as curved rectangular dielectric sheets based on the Tor Vergata model (Bracaglia *et al.*, 1995). Stiles and Sarabandi (2000) developed a fully phase coherent scattering models for grassland and Marliani *et al.* (2002) for crops such as sunflower and wheat. For fully developed crops the canopy may become dense and multiple scatter effects may occur (Picard *et al.*, 2003), which needs an improved description of the radiative transfer by taking into account higher order effects (Ferrazzoli and Guerriero, 1996). Additionally, resolving radiative interactions with complex multi-layer objects often requires an explicit 3D modeling of radiation pathways via ray tracing methods (Battaglia *et al.*, 2006).

## 6.3 Characterization of crop canopies using ground-based measurements

### 6.3.1 Combined crop and microwave measurements

To gain information about the biophysical crop parameters, three different types of retrieval algorithms are in use either for passive or active systems. The first type is based on empirical functions (e.g., regression equations) between the quantity measured (emission or backscattering coefficient) and the biophysical parameter investigated, whereby these empirical equations are often only valid for the test site, the region, or the crop investigated. The second type of retrieving algorithms is based on neural network predictions. In this approach it is necessary to train the corresponding neural network by statistically representative sampling. In many cases such training is not always feasible. The third type of algorithms is based on the inversion of radiation models and it is most widely used. In this approach, the models relate the radiation parameters to environmental parameters such as the vegetation canopy (Chukhlantsev *et al.*, 2003). In the subsequent we will give a literature overview of studies that provide both microwave data obtained from ground-based systems and crop data. Additionally, we organized the discussion along the two major measurement systems.

### Active systems

Table 6.3 gives an overview of literature studies which provide information on ground-based radar backscattering measurements, crop canopy properties, and soil moisture content. Table 6.4 also provides information on the use of air- and spaceborne microwave platforms which are discussed in Section 6.4. In general, our analysis of literature dealing with crop characterization and stress detection showed that most studies used active systems. This is especially the case for the analysis of diurnal and seasonal dynamics observed in crop canopies as discussed in Sections 6.3.2 and 6.3.3. Although active and passive systems have both their advantages and disadvantages, active radar systems on air- and spaceborne platforms provide higher spatial resolution than passive systems. One reason could be the fact that mapping and characterizing canopies as well as detecting water stress phenomena typically requires a high spatial resolution due to the inherent heterogeneity of land cover. In case of soil moisture mapping this picture might look different. Due to the limited number of studies using passive systems, we refrained from including an explicit table in the text but referred to the relevant references in two separate subsections (Sections 6.3.1 and 6.3.2).

The majority of the experiments using active systems were conducted on cereals (wheat, sorghum), corn, soybean, alfalfa, ladyfinger, and tomato with frequencies ranging from L to X-band. Most experiments were performed under field conditions with natural rainfall or eventually irrigation. Typical biophysical parameters that were measured include leaf area index, biomass of the whole plant and its components, crop height, vegetation stage, vegetation water content, and soil moisture. In the 1970s, Ulaby and Bush (1976b) used a scatterometer in the frequency range of 8–18 GHz to monitor corn growth over a 4 month period. The authors found a good correlation between normalized plant water content (i.e., the ratio of mass of water in the plant to plant height) and the radar backscattering coefficient at incidence angles of 40° or more. Higher frequencies typically showed better correlations. Bush and Ulaby (1976) used the same setup to analyze the backscattering from alfalfa. They found that, at nadir, the backscattering coefficient was dependent on variations in plant height and soil moisture. Ulaby and Wilson (1985) used L-, C-, and X-band radars mounted on a boom truck to investigate canopy attenuation of winter wheat and soybeans. Attenuation data were acquired at 1.55, 4.75, and 10.2 GHz for HH- and VV-polarization at incidence angles of 20° and 50°. With radar systems, HH indicates co-polarized horizontal transmit and horizontal receive, whereas VV indicates co-polarized vertical transmit and vertical receive of the signal. The authors found that vegetation canopies are highly non-uniform and anisotropic at microwave frequencies. They also observed large differences between the HH- and VV-polarization measurements of canopy attenuation which indicated that the relative importance of ground emission and backscattering was polarization dependent. Recently, Prasad (2009) showed that the angular variation of scattering coefficient at X-band for the crop ladyfinger decreases as the plant grows since the effects of soil was masked by developing vegetation. The author also observed that scattering coefficients increased with LAI both for VV- and HH-polarization and that LAI and biomass are highly corre-

lated with backscattering (more than for plant height). As already observed by Ulaby and Bush (1976a) for corn crop, the author also noticed that at X-band, the effect of crop covered soil moisture in the retrieval of crop variables could be neglected at incidence angle of about 45° or higher.

In general, no specific attention was paid in determining parameters or variables that provide information on the water stress status of the canopy. Typical indicators such as soil water potential, leaf water potential, or chlorophyll content have only been measured sporadically. The study of Singh *et al.* (2003) is the only one available in literature that provides information between chlorophyll content of the leaves and backscattering measured in X-band. The wheat chlorophyll was shown to be sensitive to the radar backscattering coefficient at 40° incidence angle, and this sensitivity was higher for VV- than for HH-polarization. Forster *et al.* (1991) observed changes in X-band radar backscattering in water-stressed tomato canopies over several days. The dynamics in radar backscattering were correlated to the changes in leaf water potential observed during the recovery of the plant after wilting. Colpitts and Coleman (1997) also determined leaf water potential to identify the water status of the potato canopy and leaves in combination with diurnal measurements of backscattering.

**Passive systems**

For passive systems the vegetation cover attenuates soil emission and adds its own contribution to the emitted radiation, whereby the contribution of the vegetation depends on the vegetation characteristics (density and vegetation water content) and the frequency used for observation. For frequencies ranging between 1 to 5 GHz, the vegetation is semitransparent, and therefore, its influence on the soil moisture retrieval is reduced (Guglielmetti *et al.*, 2007; Wigneron *et al.*, 1995).

Numerous studies have shown the potential of microwave radiometers to estimate soil moisture and vegetation biomass (e.g., Jackson and Schmugge, 1989; Wegmüller, 1993). Soil moisture content and vegetation biomass were both retrieved over the growing season of soybean and wheat by Wigneron *et al.* (1995). The authors used multiple angle measurements of brightness temperature at L- and C-band and found that the retrieval process was more accurate and stable if both bands are analyzed simultaneously and if multiple observation angles (10 to 40°) were included in the analysis. Liu *et al.* (2002) investigated the retrieval of vegetation water content from the combined brightness temperatures at X-band and L-band using the crane-based PORTOS radiometer and an error propagation learning back propagation neural network. The combined use of both frequencies significantly outperformed the accuracy of single channel analysis.

Table 6.3: Overview of literature studies providing information on ground-based microwave radar measurements over crops and crop characteristics.

| Authors | Crops | | Radar measurements | | | Crop and Soil measurements* | | | | | | | | |
|---|---|---|---|---|---|---|---|---|---|---|---|---|---|---|
| | Crop type | Scale | Platform name<br>Frequency | Polarization<br>Incidence angle | Duration<br>Number | LAI | NP | BM | PH | LS | LT | WP | VWC | SMC |
| Ulaby and Batlivala (1976) | Sorghum | Field | 2–8 GHz | HH, VV<br>0–50° | 27 June–7 July 1974<br>(diurnal meas.) | − | − | − | + | − | − | − | − | + |
| Brakke *et al.* (1981) | Wheat,<br>corn,<br>sorghum | Field | 8.6, 13.0,<br>17.0, 35.6 GHz | HH, HV, VV<br>30, 50, 70° | 4-weekly scans<br>(1979) | + | + | + | + | − | − | + | + | + |
| Ulaby and Jedlicka (1984) | Corn,<br>sorghum,<br>wheat | Field | 8.6, 13.0,<br>17.0, 35.6 GHz | HH, HV, VV<br>30, 50, 70° | 7 meas. (1979) and<br>23 meas. (1980) | + | + | + | + | − | − | − | + | + |
| Wu *et al.* (1985a) | Winter wheat,<br>soybean,<br>corn | Field | X-band (10 GHz) | VV<br>30, 50° | Wheat: 2 d<br>Soybean: 2 d<br>Corn: 3 d | − | − | − | − | − | − | − | − | − |
| Paris (1986) | Corn | Field | 17 GHz | HH, VV<br>50° | Growing season<br>(25 meas.) | + | − | + | − | − | − | − | + | + |
| Brisco *et al.* (1990) | Wheat | Field | L-, C-, and K-band<br>(1.5, 5.17, 12.8 GHz) | HH, VV, HV<br>20–60° | 3 times 24–30 h<br>(Aug. 1987,<br>June–July 1988) | − | − | − | + | − | − | − | + | + |
| Bouman and van Kasteren (1990a) | Sugar-beet,<br>potato | Field | X-band (9.5 GHz) | VV, HH, HV, VH<br>10–80° | 1975–1981 | + | + | + | + | + | + | − | + | + |
| Bouman and van Kasteren (1990b) | Wheat,<br>barley,<br>oat | Field | X-band (9.5 GHz) | VV, HH<br>10–80° | 1975–1981 | − | − | − | − | − | − | − | − | − |
| Bouman (1991) | Sugar-beet,<br>potato,<br>wheat,<br>barley | Field | X-band (9.5 GHz) | VV, HH, HV, VH<br>10–80° | 1975–1981 | + | + | + | + | + | + | − | + | + |
| Forster *et al.* (1991) | Tomato | Pot | X-band | HH<br>25° | 12 d (daily) | − | − | − | − | − | − | + | + | − |
| Wegmüller (1993) | Corn,<br>wheat,<br>sugar-beet,<br>potato,<br>grass,<br>canola,<br>oat, rye | Field | RASAM<br>3–11 GHz | HH, VV,VH<br>0–70° | 1984–1989 | + | + | + | + | + | + | − | + | + |

* +, measurement performed; −, no measurement performed; LAI, leaf area index; NP, number of plant; BM, vegetation biomass ;PH, plant height; LS, leaf size; LT, leaf thickness; WP, water potential; VWC, vegetation water content; SMC, soil moisture content.

Table 6.3. Continued.

| Authors | Crops | | Radar measurements | | | Crop and Soil measurements* | | | | | | | | |
|---|---|---|---|---|---|---|---|---|---|---|---|---|---|---|
| | Crop type | Scale | Platform name<br>Frequency | Polarization<br>Incidence angle | Duration<br>Number | LAI | NP | BM | PH | LS | LT | WP | VWC | SMC |
| Colpitts and Coleman (1997) | Potato | Pot | L-, C-, and K-band<br>(45 MHz–26.5 GHz) | 0° | – | − | − | − | − | − | − | + | + | − |
| Chauhan and Lang (1999) | Alfalfa | Field | COMRAD<br>L-band (1.6 GHz) | HH, VV<br>10–60° | 5 d (June 1992) | − | + | − | + | + | + | − | + | + |
| Stiles and Sarabandi (2000) | Wheat | Field | L-, C-, X-band<br>(1.25, 5.3, 9.5 GHz) | VV, HH, HV<br>20–70° | – | + | + | + | + | + | + | − | + | + |
| Mattia *et al.* (2003) | Wheat | Field | C-band (5.3 GHz) | HH, VV<br>23–60 | Mar.–June 2001<br>(8 meas.) | − | + | + | + | + | − | − | − | + |
| Brown *et al.* (2003) | Wheat | Lab.<br>and field | GB-SAR<br>C-, X-band (Lab.)<br>L-, X-band (field) | VV, HH, VH<br>20–50° | June–July 1999 | + | + | + | + | + | − | − | + | + |
| Picard *et al.* (2003) | Wheat | Field | C-band | HH, VV<br>23–60° | Mar.–June 2001<br>(9 d) | − | + | + | + | − | − | − | + | + |
| Del Frate *et al.* (2004) | Wheat | Field | RASAM<br>3.1–10.2 GHz | VV, HH<br>10–70° | 1988 | − | − | + | + | − | − | − | − | + |
| Serbin and Or (2005) | Wheat | Greenh. | 1 GHz | 0° | 9 Mar.–7 May 2002<br>(every 30 min.) | + | + | + | + | − | − | − | + | + |
| Serbin and Or (2005) | Corn | Field | 1 GHz | VV<br>7.5, 17° | – | + | + | + | + | − | − | − | + | + |
| Gomez-Dans *et al.* (2006) | Wheat | lab. | GB-SAR<br>C-band (5.44 GHz) | HH, VV, HV<br>35–55° | June–July 1999 | − | − | − | + | − | − | − | − | − |
| Singh (2006) | Soybean | Field | X-band (9.5 GHz) | HH, VV<br>20–70° | 90 d<br>(every 10 d) | + | + | + | + | − | − | − | − | + |
| Della Vecchia *et al.* (2006) | Maize | Field | RASAM<br>C-band | HH, VV, HV, VH<br>30° | May–Oct. 1988 | + | + | + | + | + | + | − | + | + |
| Della Vecchia *et al.* (2008) | Maize | Field | RASAM<br>2.5–10.2 GHz | HH, VV, HV<br>20–50° | May–Oct. 1988<br>(23 meas. days) | − | − | + | + | − | − | − | + | + |
| Joseph *et al.* (2008) | Corn | Field | COMRAD<br>L-band (1.6 GHz) | HH, VV<br>15, 35, 55° | Apr.–Oct. 2002<br>(1 per week) | − | − | + | + | − | − | − | + | + |
| Prasad (2009) | Ladyfinger | Field | X-band (9.9 GHz) | HH, VV<br>20–70° | 90 d<br>(10 per day) | + | − | + | + | − | − | − | − | + |
| Joseph *et al.* (2010b) | Corn | Field | COMRAD<br>C-, L-band<br>(4.5, 1.6 GHz) | HH, VV<br>15, 35, 55° | Apr.–Oct. 2002<br>(1 per week) | − | − | + | + | − | − | − | + | + |

* +, measurement performed; −, no measurement performed; LAI, leaf area index; NP, number of plant; BM, vegetation biomass ;PH, plant height; LS, leaf size; LT, leaf thickness; WP, water potential; VWC, vegetation water content; SMC, soil moisture content.

Table 6.4: Overview of literature studies providing information on air- and spaceborne microwave radar measurements over crops and crop characteristics.

| Authors | Crops | | Radar measurements | | | Crop and Soil measurements* | | | | | | | | |
|---|---|---|---|---|---|---|---|---|---|---|---|---|---|---|
| | Crop type | Scale | Platform name<br>Frequency | Polarization<br>Incidence angle | Duration<br>Number | LAI | NP | BM | PH | LS | LT | WP | VWC | SMC |
| Prevot *et al.* (1993) | Wheat | Field | ERASME (airb.)<br>C-, X- band<br>(5.35, 9.65 GHz) | C-band:<br>HH, 15–30°<br>X-band:<br>VV, 30–45° | 1988 (4 d) | + | − | + | + | − | − | − | + | + |
| Bouman and Hoekman (1993) | Sugar-beet,<br>potato,<br>winter wheat | Field | DUTSCAT (airb.)<br>L-, C-, X-, Ku-band<br>(1.2, 3.2, 5.3, 9.6,<br>13.7, 17.25 GHz) | HH, VV<br>10–60° | 1988 (7 d) | + | − | + | + | + | + | − | + | + |
| Taconet *et al.* (1994) | Wheat | Field | ERASME (airb.)<br>C-, X-band<br>(5.35, 9.65 GHz) | HH, VV<br>20–40° | 16 June–28 July<br>1988 (4 dates)<br>21 Mar.–18 July<br>1989 (5 dates) | + | − | + | + | − | − | − | + | + |
| Bouman *et al.* (1999) | Sugar beet,<br>potato,<br>winter wheat | Field | ERS/SAR (spaceb.)<br>C-band (5.3 GHz) | VV<br>23° | 1992–1994 | + | − | − | − | − | − | − | | + |
| Cookmartin *et al.* (2000) | Wheat,<br>barley,<br>oilseed rape | Field | ERS-2/SAR<br>C-band (5.3 GHz) | VV<br>23° | 1997 (7 d) | + | + | − | + | + | + | − | + | + |
| Macelloni *et al.* (2001) | Wheat,<br>Sunflower | Field | AIRSAR (airb.)<br>P-, L-, C-band<br>EMISAR (airb.)<br>L-, C-band<br>SIR-C/X-SAR (spaceb.)<br>L-, C-/X-band<br>ERS-1/2/SAR (spaceb.)<br>C-band<br>JERS-1/SAR (spaceb.)<br>L-band | AIRSAR:<br>HH, VV, HV, VH<br>20, 35, 50°<br>EMISAR:<br>HH, VV, HV<br>45–50°<br>SIR-C/X-SAR:<br>HH, VV, HV,<br>VH/VV, 23–55°<br>ERS-1/2: VV, 23°<br>JERS-1: HH, 35° | Summer 1991<br>(AIRSAR)<br>Summer 1994<br>(EMISAR)<br>Apr., Oct. 1994<br>(SIR-C/X-SAR)<br>ERS-1/2 – JERS-1<br>(1992–1994) | + | + | + | + | + | + | − | + | + |
| Wigneron *et al.* (2002) | Sunflower | Field | ERASME (airb.)<br>ERS-2/SAR (spaceb.)<br>C-band | VV<br>20–23° | Oct. 1996–<br>Nov. 1997 | + | − | + | + | − | − | − | − | + |

* +, measurement performed; −, no measurement performed; LAI, leaf area index; NP, number of plant; BM, vegetation biomass ;PH, plant height; LS, leaf size; LT, leaf thickness; WP, water potential; VWC, vegetation water content; SMC, soil moisture content.

Table 6.4. Continued.

| Authors | Crops | | Radar measurements | | | Crop and Soil measurements* | | | | | | | | |
|---|---|---|---|---|---|---|---|---|---|---|---|---|---|---|
| | Crop type | Scale | Platform name<br>Frequency | Polarization<br>Incidence angle | Duration<br>Number | LAI | NP | BM | PH | LS | LT | WP | VWC | SMC |
| Blaes and Defourny (2003) | Winter wheat, sugar-beet, potato, maize | Field | ERS-1/2/SAR (spaceb.)<br>C-band | VV<br>23° | Mar.–July 1996 | + | − | − | + | − | − | − | − | + |
| Picard *et al.* (2003) | Wheat | Field | ERS/SAR (spaceb.)<br>C-band | VV<br>23° | Mar.–June 2000<br>(4 d) | − | + | + | + | − | − | − | + | + |
| Maity *et al.* (2004) | Cotton | Field | RADARSAT/SAR<br>C-band (5.3 GHz) | HH<br>36–42° | 2001 (3 d) | + | + | − | + | − | − | − | − | + |
| Del Frate *et al.* (2004) | Wheat | Field | ERS-2/SAR (spaceb.)<br>C-band | VV<br>23° | 1997 | + | − | + | − | + | − | − | + | + |
| Blaes *et al.* (2006) | Corn | Field | ENVISAT/SAR (spaceb.)<br>ERS-2/SAR (spaceb.)<br>RADARSAT/SAR (spaceb.)<br>C-band | HH, VV<br>15–45° | Jan.–<br>Sept. 2003 | + | + | + | + | + | + | − | + | + |
| Liu *et al.* (2006) | Winter wheat | Field | ENVISAT/ASAR (spaceb.)<br>C-band | HH, VV<br>42.5–45.2° | 2004 (Mar.–June) | + | − | + | − | − | − | − | + | + |
| Della Vecchia *et al.* (2006) | Wheat, maize | Field | ERS-2/SAR (spaceb.)<br>ENVISAT (spaceb.)<br>C-band | ERS:<br>VV, 20–25°<br>ENVISAT:<br>VV, 20–42° | 2001, 2003 | + | + | + | + | + | + | − | + | + |
| Baghdadi *et al.* (2009) | Sugarcane | Field | TerraSAR-X (spaceb.)<br>X-band (9.65 GHz)<br>ENVISAT/ASAR (spaceb.)<br>C-band<br>PALSAR/ALOS (spaceb.)<br>L-band (1.27 GHz) | TerraSAR:<br>HH, 39, 53°<br>ENVISAT:<br>VV, HH, HV<br>18–44°<br>PALSAR:<br>HH, HV,<br>36–43° | 2006–2008 | − | − | − | + | − | − | − | − | − |

* +, measurement performed; −, no measurement performed; LAI, leaf area index; NP, number of plant; BM, vegetation biomass ;PH, plant height; LS, leaf size; LT, leaf thickness; WP, water potential; VWC, vegetation water content; SMC, soil moisture content.

So far our knowledge about the sensitivity of the microwave measurements to the plant water stress is very limited. Paloscia and Pampaloni (1984) observed that microwave measurements at Ka-band were sensitive to plant stress. They found a correlation between a polarization index based on vertical and horizontal microwave measurements at Ka-band and a measured crop water stress index over corn. A correlation coefficient (R) of 0.92 was obtained for measurements performed with an incidence angle of 50°. Other authors treated the vegetation canopy more or less as an "interference factor" which hinders direct estimation of the soil moisture from microwave emission (e.g., Jackson and Schmugge, 1991; Joseph *et al.*, 2010b; Wigneron *et al.*, 1993, 2004).

### 6.3.2 Diurnal dynamics of backscattering in crop canopies

Since the late 1970s, various studies reported diurnal variations in the backscattering coefficient of crop canopies. This was attributed to variations in the dielectric properties of the canopy caused by changes in the vegetation moisture status (Brisco *et al.*, 1990; Ulaby and Batlivala, 1976) and to changes in the geometrical properties related to leaf orientation (Brisco *et al.*, 1990). A diurnal pattern in backscattering in a wheat canopy was observed by Brisco *et al.* (1990) using a truck-mounted L-, C-, and Ku-band scatterometer. However, these patterns were dependent on the frequencies investigated. The difference in patterns was explained by an increased geometric effect in the backscattering at higher frequency. The diurnal changes in backscattering were also dependent on the status of the crop. In the vegetative stage (June), diurnal changes were mostly controlled by the vegetation water content whereas at the senescing stage (July, August), diurnal backscattering changes were controlled by soil backscattering. They also observed that cross-polarization measurements (VH, HV) resulted in smaller diurnal changes of the backscattering than the copolarized channels (HH, VV), especially for C- and L-band frequencies. Forster *et al.* (1991) observed that the diurnal changes in X-band radar backscattering from water-stressed tomato canopy plants were dependent on frequency and incidence angles. Brakke *et al.* (1981) measured diurnal backscattering from ground-based microwave radar at Ku-band (13 GHz), VV-polarization and 50° incidence angle for wheat, corn, and sorghum. Surprisingly, they did not found any correlation between the backscattering and either leaf water potential or wind speed. However, their data set was relatively limited.

### 6.3.3 Seasonal dynamics of backscattering in crop canopies

Seasonal variations in the backscattering coefficient in crop canopies were also investigated by several authors. The backscattering coefficients of sugar beet and potato were determined by Bouman and van Kasteren (1990a) using X-band radar over a period of six years. They observed a saturation level in backscattering coefficients when crops reached a soil cover of 80%. Changes in the geometry of crop-soil system caused by strong winds, thinning of plants, as well as architecture of individual plants were found to affect backscattering.

The authors concluded that radar backscattering across the various years was highly variable due to interplay of different environmental factors influencing canopy geometry. Paris (1986) presented results of combined backscattering and biophysical parameters obtained during the growing season of corn. He found a clear power law relationship between the backscattering cross section of a corn leaf and its LAI. Peak values of canopy LAI coincided with measured backscattering coefficients observed at a 50° incidence angle both in HH- and VV-polarization. The time of the onset of the reproductive process in the corn plant was clearly detected in the temporal evolution of the backscattering coefficient. The surface soil moisture effect on the backscattering coefficient was insignificant at Ku-band (17 GHz) except at the end of the season when the corn was nearly transparent to the radiation.

## 6.4 Characterization of crop canopies using air- and spaceborne remote sensing

### 6.4.1 Active systems

Table 6.4 provides an overview of remotely sensed backscattering using aircraft and satellite platforms for agricultural crops. Most of these studies were conducted in the framework of large measurement campaigns operated at regional scale. A major difference with the experiments conducted using ground-based equipment is the fact that the obtained backscattering is typically related to averaged ground-based measurements of soils and vegetation obtained at different fields. Often the timing of ground-truth sampling shows a time lag with respect to the overpasses. This might not be a problem for quantities that differ only slightly in time lag such as LAI, biomass, and plant height. Evidence from diurnal measurements however shows that this might be different for vegetation water content and canopy structure. Latter may be strongly affected by stress effects and wind conditions and may lead to additional noise on measured signals which cannot be related to a specific process. Ferrazzoli (2002) concluded on the basis of a literature review, that correlations between backscattering and vegetation parameters obtained from airborne campaigns were not as good as the ones obtained from multi-temporal single-field ground-based observations.

A main motivation for using radar remote sensing is crop classification (Bouman and van Kasteren, 1990a) which is primarily based on the characterization of crop geometry. Hereby, differences in phenological development of, e.g., wheat, barley, and oats may lead to different temporal signatures in the backscattering. Skriver *et al.* (1999) found that the correlation between HH- and VV-polarization backscattering from C- and L-band SAR was suitable for discriminating between winter and spring crops, especially for C-band. Discrimination at early stages between both types of crops may help in further distinguishing individual crops belonging to one of these categories based on the temporal evolution of such correlations. Recently, Skriver *et al.* (2011) used short-revisit multi-temporal C- and L-band SAR data for crop classification. They found that multi-temporal acquisitions are very important for single- and

dual-polarization modes, and that cross-polarized backscattering provided best results.

Airborne and spaceborne radars have also been used to better understand the influence of vegetation on the signal backscattering. Brown *et al.* (1992) used airborne SAR data of different frequencies (L-, C-, and X-band) to measure backscattering from different canopies and found that correlation between C- and L-band and between X- and L-band data were very low indicating that the radar backscattering at the different frequencies was caused by different mechanisms. Especially, for vertical oriented crops such as wheat, a low correlation was found for X- and C-band, whereas the correlation was found to be acceptable for broad-leaved plants such as canola and field peas. Additionally, the backscattering determined at L-band was found to be more sensitive to the soil moisture content.

Several studies investigated the potential use of spaceborne radar for agricultural purpose, such as crop type mapping, crop condition assessment, soil tillage, crop residue mapping, soil moisture estimation, and to monitor crop growth (McNairn and Brisco, 2004). In the past, spaceborne SAR sensors (e.g., ERS-1, ERS-2, JERS-1, RADARSAT-1) were limited to a single frequency and polarization. In order to obtain enough information for agriculture applications, multi-channel radar observations were required.

Recently several improvements were made to increase the information content in the SAR data sets, such as the addition of polarizations (ASAR/ ENVISAT, RADARSAT-2), the use of additional frequencies (TerraSAR-X, COSMO-SkyMed, and PALSAR/ALOS), and the integration of SAR data with other frequencies and optical sensors which can provide additional crop and soils information (Clevers and vanLeeuwen, 1996; McNairn and Brisco, 2004). Nevertheless, information on the sensitivity of SAR measurements to crop condition indicators is still limited (McNairn and Brisco, 2004). Wigneron *et al.* (2002) found limitations in the retrieval of vegetation biomass of sunflower using ERS-2/SAR C-band data. This was attributed to the long revisit period (35 days) which was deemed not sufficient for monitoring of the sunflower vegetation cycle. In addition, accuracy of retrievals of the parametric growth curve was low. Recently, Baghdadi *et al.* (2009) examined the potential of three SAR sensors (TerraSAR-X, ASAR/ENVISAT, PALSAR/ALOS) operating at different frequencies (X-, C-, and L-band) for mapping the harvest of sugarcane. The authors showed a high correlation between backscattering coefficient and Normalized Difference Vegetation Index (NDVI) independently estimated from SPOT-4/5 images over the same fields. The best discrimination between ploughed and vegetated sugarcane fields was obtained by TerraSAR-X data. They also showed that cross-polarization channels have more potential than co-polarization channels for the detection of the sugarcane harvest.

A correct assessment of vegetation water content is essential for the accurate prediction of backscattering and emission from crop canopies as well as for the exact assessment of surface soil moisture content. In addition, vegetation water content could be an important indicator for the presence of water stress in crop canopies as well as the phenological stage of the canopy. Taconet *et al.* (1994) found a negative correlation between X-band backscattering and vegetation

water content in wheat from airborne radar with no dependency on the soil moisture content. Additionally, accuracies in estimated crop water content were the same at 20° and 40° incidence angle and higher for HH-polarization compared to VV-polarization. A saturation effect of the radar cross section was observed as the canopy becomes denser. Saatchi *et al.* (1994) developed an algorithm to retrieve canopy water content of natural grassland and pastures from airborne SAR data. Le Vine and Karam (1996) analyzed the dependence of attenuation in a vegetation canopy on frequency and plant water content in a synthetic study to examine the hypothesis that attenuation in vegetation is proportional to the water content of the canopy. Therefore, they used the concept of optical depth ($\tau$) with $\tau = bVWC$ (see Eq. (6.4)). The results indicated that the hypothesis is not unreasonable for canopies whose structure are small (leaves, stalks, stems, branches, etc.) compared to wavelength. This study was performed to find an appropriate correction of the measured signal for the vegetation canopy to retrieve soil moisture information instead of using the information for canopy characterization.

### 6.4.2 Passive systems

In the past, most of the studies carried out with air- or spaceborne radiometers were focused on the retrieval of soil moisture. The vegetation was systematically considered as an attenuation factor in the soil moisture retrieval (Njoku *et al.*, 2000; Wigneron *et al.*, 2004). Recently, several authors used spaceborne radiometer data to characterize the vegetation mostly based on vegetation indices which were derived from the data. These vegetation indices include Microwave Polarization Difference Temperatures (MPDT) (Choudhury and Tucker, 1987), Microwave Polarization Difference Index (MPDI) (Kirdyashev *et al.*, 1979; Becker and Choudhury, 1988), and Microwave Vegetation Indices (MVIs) (Shi *et al.*, 2008). Shi *et al.* (2008) developed a set of MVIs based on data from the Advanced Microwave Scanning Radiometer on the Earth Observing System (AMSR-E). The microwave vegetation indices were defined as the intercept ($a$) and slope ($b$) derived from a linear relationship between the brightness temperatures observed at two adjacent radiometer frequencies. The MVIs were correlated to the NDVI derived from Moderate Resolution Imaging Spectroradiometer (MODIS) data. They found that the MVIs can provide additional information on crop status since the microwave measurements were sensitive not only to the leafy part of the vegetation but also to the properties of the overall vegetation canopy. Similarly, Chen *et al.* (2009) found a new MVI for SMOS through the analysis of simulations by the AIEM model. The polarization difference for the bare surface emission signals at different view angles can be well characterized by a linear function with parameters that are dependent on the pair of view angles to be used. This makes it possible to minimize the surface emission signal and maximize the vegetation signal when using multi-angular SMOS measurements. Zhang *et al.* (2011) found that the MVIs are a function of vegetation water content or vegetation transmissivity. The $b$ parameter of MVIs decreased with increased vegetation water content but increased with increased vegetation transmissivity. Finally, the authors

used the MVIs for the correction of vegetation effects in soil moisture retrieval over areas with sparse vegetation in the Tibet Plateau. Li *et al.* (2010) analyzed the relationship between MPDT, MPDI, and MVIs for the case of cotton. They showed that MPDT and MPDI were negatively correlated to vegetation water content. For the specific case of cotton, they showed that MVIs are more suitable to retrieve vegetation water content. Jones *et al.* (2011) used passive microwave information from AMSR-E (Ku-band) to quantify global patterns and seasonal variability in vegetation optical depth (VOD) over a 6 year record (2003–2008). The VOD parameter showed significant correlation with vegetation indices and LAI obtained from MODIS optical-infrared data, and phenology cycles over 82% of the global domain. It has to be noted that dual-polarized and multi-angular L-band data from SMOS also have the ability to gain information on both soil moisture and VOD.

## 6.5 Canopy dielectric and plant water properties

### 6.5.1 Vegetation dielectric properties

As already stated above, backscattering and emission retrieved by active and passive systems are directly affected by the dielectric properties of the soil-plant system, and might therefore be used for early water stress detection in crop stands, because the amount of water in the crop canopy is generally the dominant factor controlling the dielectric properties (Nelson, 1991). Unfortunately, the dielectric properties also depend on measurement frequency, canopy and soil temperature, density and structure of the vegetation (Nelson, 1991), and on the salinity of the plant water (Ulaby and Jedlicka, 1984). Therefore, the relationship between dielectric permittivity and canopy water content is not straight forward. Amongst the first who systematically analyzed the dependency of dielectric permittivity and canopy water content were Ulaby and Jedlicka (1984) who treated the wet vegetation as a two-component mixture of bulk water (including air) and water. Based on these assumptions they developed two phase mixing models where the dielectric permittivity of the vegetation mixture (namely the stalk material), water, and bulk vegetation was assumed to differ in total amounts (and therefore differ in total influence to the overall signal). Unfortunately, none of the developed two-phase mixing models could describe measured data at X-band (8 GHz). As a consequence they increased the complexity of the models by using a three-component random-needle mixing model, where the bulk vegetation was used as a host material and the air and water as randomly orientated needle-like inclusions. This approach already agreed well with measured data at X-band (8 GHz). Finally, they proposed a four phase refractive mixing model consisting of the bulk vegetation as a host, and three additional types of inclusion such as (1) air, (2) free water with a fixed dielectric permittivity for the frequency range used, and (3) bound water with an ice-like dielectric permittivity. Applying this complex model the measured data were fitted as good as with the simpler three-phase

mixing model. Therefore, the authors concluded, that the problem of modeling the dielectric properties of water contained in a given material was not well understood at this times. Based on the work presented above, Ulaby and Elrayes (1987) developed a Debye-Cole dual-dispersion dielectric model consisting of a component that accounts for the volume fraction occupied by water in free form and another that accounts for the volume fraction occupied by the mixture comprised of water molecules bound to bulk-vegetation molecules. The model was again tested against measured data and showed excellent agreement over a wide range of moisture conditions and within the frequency range 0.2 to 20 GHz. Additionally, Ulaby and Elrayes (1987) found that the bound water content increases with decreasing total water content. In the following, varies authors developed mixing models for specific purposes or vegetation compartments such as the dielectric model for leaves as proposed by Mätzler (1994a) and for various plants such as Shrestha *et al.* (2005) and Shrestha *et al.* (2007).

### 6.5.2 Diurnal changes in plant water and dielectric properties

Within the biological and agronomy community it is widely known that diurnal changes of plant water content might occur as a consequence of water stress induced by high temperatures and/or shortening of available soil water. Ackley (1954) observed diurnal and seasonal changes in crop water content and water deficit of crops. He clearly demonstrated that leave water content drops to its minimum in the early afternoon and recovered during night time. In the following years various studies indicated that not only the water content but also the turgor pressure changed during the day (e.g., Acevedo *et al.*, 1979; Ackerson *et al.*, 1977; Allen *et al.*, 1998; Dutt and Gill, 1978; Ehrler *et al.*, 1978; Olsson and Milthorpe, 1983; Turner, 1974), whereby the changes were highly dependent on the crop type (Turner, 1974). From a plant physiological point of view it is also clear that the turgor pressure is much more sensitive to stress conditions than the total plant water content. This has been proven by studies from, e.g., Dutt and Gill (1978) who showed that even small changes in water content correspond to relatively large changes in turgor pressure. Additionally, Ehrler *et al.* (1978), Forster *et al.* (1991), and Olsson and Milthorpe (1983) showed the existence of a diurnal hysteretic effect in the leaf water potential as a function of the induced water stress in the soil. Hereby, the recovery of plant water potential tended to be slower for plants that are undergoing water stress compared to non-stressed plants.

Backscattering coefficients were also found to be sensitive to changes in leaf water potential as reported by Forster *et al.* (1991), Martin *et al.* (1989), and Siddique *et al.* (2000). However further research is needed to explore dependencies between canopy properties such as leaf water potential, leaf water content, and canopy geometry and radar backscattering. To complement the information from plant observations these dependencies need to be related to the observed water status in soil using soil moisture and soil matric potential measurements. In addition, the value of combined passive and active microwave measurements in characterizing the dynamics of canopy geometry needs to be

explored. There is evidence in literature that changes in canopy geometry may strongly contribute to the observed backscattering (see sections below). In addition geometric effects appear to be more important in backscattering from active microwave systems than in signals obtained by passive systems.

## 6.6 Factors controlling microwave signals of crop canopies

In this section, we will discuss the various factors that may lead to changes in the structure and function of crop canopies, and that therefore, may affect the observed microwave emission and backscattered signals. Some of these factors have already been addressed in previous sections and will only be briefly touched upon. The presentation below shows that many environmental factors may influence the observed microwave signals and that disentangling their influence needs both monitoring of these factors but also quantification of their effect on microwave signals. Especially, the identification of water stress phenomena may be confounded by other effects also inducing changes in canopy structure and function. Also, environmental controls such as soil moisture status and microclimatology may affect microwave signals. Identification of water stress may therefore require monitoring of all relevant parameters and properties affecting microwave emission and backscattering.

### 6.6.1 Water stress phenomena

The relation between water stress and microwave emissions and backscattering was already partly addressed in Section 6.3. In this sub-section we will mainly focus on the effect of water stress on crop canopy structure and function. It is well-known from crop physiology that water or drought stress in plants may lead to changes in the structure and function of the canopy, and thereby, affect the observed microwave emission or backscattering coefficient. Depending on the intensity and severity of this stress, the effects may range from fully reversible to irreversible. Despite this effect of plant water status on microwave emission of its canopy due to changes in its structural properties, there are practically no studies available in literature that allow relating water stress, the related changes in geometrical properties of the canopy, and, e.g., backscattering coefficients or microwave emission. Water stress effects that may be detected by microwave techniques include: (1) loss of turgor pressure in the leaves leading to the droop of leaves (Singh *et al.*, 2006), (2) reduced cell division and thus reduced stem elongation leading to changes in LAI and plant height (Song *et al.*, 2008), (3) changes in leaf structure to reduce transpiration losses (Moran *et al.*, 1989), and (4) reduced capability in tracking sun light (Moran *et al.*, 1989). Most of these effects, however, have typically been studied with optical and near-infrared sensors (Colwell, 1974; Moran *et al.*, 1989). Droop of ears in spring barley was observed by Cookmartin *et al.* (2000) using microwave methods. This droop of ears led to a substantial increase in their radar cross section. Most likely this effect was caused by stress conditions

but no clear evidence was given by the authors. The study by Colpitts and Coleman (1997) analyzed drought stress of a potato leaf using measurements in L-, C-, and Ku-band. Drought stress could directly be related to reduced leaf gravimetric water content and leaf thickness. They found only weak statistical relationships between complex relative permittivity and the gravimetric water content of a leaf, because the water-to-air ratio within the leaf remained nearly constant with changing water content (see also Section 6.5). In contrast, correlations were found between leaf permittivity and leaf thickness across the wavelengths used. The leaf thickness was found to be directly related to relative leaf water content, osmotic potential, water potential, and turgor pressure. These findings suggest that the canopy architecture will have a much stronger effect on radar backscattering than the permittivity.

### 6.6.2 Wind strength

It appears that the effect of wind strength on radar backscattering is important for measurements performed at high frequencies. These findings and the importance for retrieving canopy water stress from backscattering measurements of wind strength need however to be further validated. In early publications such as Brakke *et al.* (1981) no effect of wind speed on the radar backscattering measured at Ku-band and two different polarizations was found for corn, sorghum, and wheat. Wu *et al.* (1985b) observed strong fading of the backscattering signal in milo due to wind effects using X-band. Bouman and van Kasteren (1990a) used X-band to analyze factors that influence backscattering coefficient of potato and sugar beet and found that the architecture of individual beet plants and their distribution in space affected the radar backscattering. Especially, strong winds led to changes in canopy architecture, and therefore, will affect radar backscattering and may confound the quantification of water stress phenomenon.

### 6.6.3 Saturation effect

The quantification of saturation effect is mainly an issue for active systems, especially at higher frequencies. Saturation implies that the backscattering coefficient becomes insensitive to changes in canopy structure and function (Blaes *et al.*, 2006; Cookmartin *et al.*, 2000; Liu *et al.*, 2006; Taconet *et al.*, 1994). Occurrence of saturation effects have been related to the type of crop (Bouman and van Kasteren, 1990a; Ferrazzoli *et al.*, 1997), crop biomass (Bouman and van Kasteren, 1990a), crop cover (Bouman, 1991), crop height (McNairn *et al.*, 2000), and LAI (Blaes *et al.*, 2006; Ferrazzoli *et al.*, 1992) and may mask potential correlation between crop parameters and backscattering coefficient (Chen *et al.*, 2009). In addition, saturation has been observed at different polarizations and incidence angles (Chen *et al.*, 2009; Ferrazzoli *et al.*, 1992; McNairn and Brisco, 2004).

Only a few studies analyzed the effect of vegetation water content on the occurrence of saturation. Taconet *et al.* (1994) used the airborne scatterometer ERASME in C- and X-band, HH- and VV-polarization, and incidence

angles 15 to 45°. Backscattering coefficients were obtained for two years under different soil moisture conditions for wheat. Backscattering values obtained with X-band using HH-polarization saturated at vegetation water contents larger than 3 kg $m^{-2}$ and became highly variable for values larger than 4 kg $m^{-2}$. A similar pattern was observed for values observed in X-band using VV-polarization. Bouman (1991) used radar backscattering data at X-band to derive crop parameter from beet, potato, barley, and wheat. In case of beet, the backscattering coefficients obtained saturation values at a fraction cover of 0.8 with values ranging between 0 and −2 dB. Backscattering coefficients for potato were found to saturate at a similar fraction cover but with values ranging between −2 and −4 dB. For wheat and barley no saturation level could be observed. For beet, crop water content at the fraction cover of 0.8 was about 0.5 kg $m^{-2}$, whereby between 0.8 and full cover the crop water content increased up to 6 kg $m^{-2}$ and more indicating that radar backscattering no longer corresponded to changes in vegetation water content (their Figure 1 and Figure 7a). Therefore, the presence of saturation effect may mask the detection of water stress in plant canopies. Saturation effects may also be observed for microwave signals obtained from radiometers. Wigneron *et al.* (1993) used a multi-frequency radiometer (PORTOS) to monitor the microwave emission of a soybean field. Both soil moisture and biomass which was parameterized by the vegetation volume fraction were found to have a very significant effect on the evolution of the microwave signal. Increase in biomass led to saturation of the observed emissions at 5.05 GHz and 36.5 GHz but this effect was less pronounced at 1.4 GHz showing a continuous increase of the microwave signal.

### 6.6.4 Surface soil moisture content

Surface soil water content is a key variable in understanding mass and energy transfer processes between the land surface and the atmosphere, whereby passive and active microwave systems have extensively been used to determine its spatial and temporal dynamics. However, exact estimation of soil moisture content from emission or backscattering is hampered by the presence of a vegetation canopy. To overcome the problem of the confounding signal from the vegetation canopy, radiative transfer models were developed and applied which account for the all processes within the vegetation canopy (Hunt *et al.*, 2011; Joseph *et al.*, 2010b). The derivation of crop parameters from microwave methods may be hampered by the influence of the underlying soil and more explicit, by changes in the soil moisture content, especially for frequencies lower than C-band. In this respect, vegetation canopy models may be extremely valuable to derive properties that can provide information on the status of the canopy and more specifically of its water status.

Several findings have shown that the surface soil water status determines the intensity of the observed radar backscattering of cropped soil. For example, Ulaby *et al.* (1982a) found that at 50% of field capacity the backscattering of a radar operating at 4.25 to 4.75 GHz (10° incidence angle) was dominated by the vegetation. Additionally, radar backscattering seemed to be dominated by the return from the soil at higher moisture contents. Airborne scatterometer (X-

band with HH-polarization) data of wheat fields showed no clear dependence of the backscattering signal on soil water content (Taconet *et al.*, 1994). Additionally, a negative correlation between radar backscattering and vegetation water content was found for the frequency used. They found that at lower frequencies (C-band) and steep to medium incidence angles the radar backscattering comes from the underlying soil attenuated through the vegetation above. Similarly, Baghdadi *et al.* (2009) showed that for L-band measurements performed at 20° incidence angle over a fully grown sugarcane crop (50 cm high) the radar signal was no longer sensitive to surface roughness and the sensitivity to soil moisture content was low (around 0.04 dB/vol.%). Detecting crop emergence may be masked by dips and peaks in the backscattering caused by changes in soil moisture content (Bouman and van Kasteren, 1990a). Joseph *et al.* (2008) used the ratio between modeled bare soil backscattering and the vegetation water content to estimate surface soil moisture using dual-polarized L-band measurements (1.6 GHz). The authors also reported that the retrieval of soil moisture was found to be dependent on the view angle and polarization used, whereby they found best agreement at 35° view angle and VV-polarization. Encouraged by the positive results, Joseph *et al.* (2010b) used also successfully C-band data to estimate soil moisture. Contradictory to these findings, Schoups *et al.* (1998) reported that for S- and even C-band, radar signal becomes less sensitive to soil moisture content and surface roughness and more sensitive to canopy parameters.

Also the characterization of vegetation canopy using passive microwave measurements is affected by the surface soil moisture status. Hornbuckle and England (2004), e.g., reported that there was still a radiometric sensitivity in L-band to soil moisture even under corn having a biomass of 8.0 kg $m^{-2}$. One way to exclude the effect of soil moisture on the total emission and radar backscattering was the installation of a perfect reflector above the ground. Brunfeldt and Ulaby (1984) analyzed the effect of vegetation on microwave emission and radar backscattering in a systematical sense by applying this technique. Therefore, the soil between the crop rows was covered by a perfect reflector to block emissions from the soil and reflect downwelling radiation from the vegetation. Additionally, uncovered reference fields were used to validate their simplified radiative transfer model. Overall, the model performed well but the authors also clearly indicated that more research is needed to understand emission and reflection from crop stands. Calvet *et al.* (2011) analyzed the sensitivity of passive microwave observations to soil moisture content and vegetation water content for frequencies ranging between L- and W-band. They showed that for frequencies higher than L-band a larger sensitivity was observed to vegetation water content than to surface soil water content.

### 6.6.5 Biophysical crop parameter

Microwave methods have extensively been used to characterize biophysical crop parameter. Most of this work has been done by relating backscattering coefficients from active microwave methods to observed crop parameters under field conditions. In the subsequent, we will briefly present some major find-

ings regarding key parameters such as crop biomass, LAI, and plant geometry. Biomass and LAI will be discussed together as typically most microwave studies provide information on both quantities (Tables 6.3 and 6.4). Other properties such as plant height, crop cover, and growing stage will be referred to as we present these key parameters.

### Crop biomass and LAI

Many studies have shown that there is a clear interdependence between biomass, LAI and observed backscattering coefficients from active microwave systems. A large number of these studies are listed in Tables 6.3 and 6.4 and they provide regression equations and correlation coefficients to express the performance of the derived relationships. Rather than presenting in detail these relationships we would like to highlight some issues that are of importance when conducting microwave experiments to derive such dependencies. Analysis of these studies showed that canopy properties other than biomass and LAI may confound the expected relationship between both properties and the observed backscattering. These properties included the growing stage of the crop (Bouman and Hoekman, 1993; Bouman and van Kasteren, 1990a), the canopy structure and geometry (Bouman and Hoekman, 1993; Bouman and van Kasteren, 1990a), but also the soil moisture status (Brakke *et al.*, 1981; Brown *et al.*, 1992; Martin *et al.*, 1989; Mattia *et al.*, 2003), environmental conditions (Hoekman and Bouman, 1993), and management properties (Paris, 1983). It is therefore mandatory to monitor these confounding factors when trying to relate biomass and LAI to observed backscattering coefficients.

The specific growing stage of the crop has been shown to be an important factor determining the relationship between biomass, LAI and backscattering. The effect of growth stage was often related to geometry and saturation effects. C-band HH backscattering data from ASAR obtained over winter wheat was found to correlate very well with biomass ($R > 0.65$), LAI and other parameters such plant water content, leaf water content per unit leaf area, and specific growing stages such as regreening (Liu *et al.*, 2006). In the same study backscattering signals from VV-polarization were also analyzed but typically showed less correlation than values obtained with HH-polarization, independently of the growth stage. During booting and milking stages temporal changes in the correlation were observed with lower correlations both for HH and VV-polarization. On the other hand, pooling of regreening and booting data resulted in high correlations between C-band HH backscattering, biomass and LAI. Negative correlations between biomass and C-band HH and VV backscattering ($R = -0.52$ and $-0.44$) were found at booting. This was explained by changes in the canopy structure. The low correlations between biomass and also LAI observed from the C-band HH backscattering may be due to saturation. Blaes *et al.* (2006) showed that VV/HH polarization ratios obtained at incidence angles between 35 and 45° were able to assess the crop growth until saturation of the signal was reached (LAI of 4.6).

Several studies specifically focused on the analysis between LAI and backscattering coefficients. Ulaby and Jedlicka (1984) for example, studied the relation-

ship between LAI and backscattering measured at frequencies ranging between 8.6 and 35.6 GHz over corn, sorghum, and wheat. Most of the observed variation in canopy backscattering could be explained through variations in green LAI for cases where the LAI was greater than 0.5. For the wheat crop, the correlation was only good before head formation started. Again the authors observed an important contribution of the soil backscattering at early growth stages with low LAI (<0.5). The relationship between LAI of rice and C-band VV/HH backscattering ratio was analyzed by Chen *et al.* (2009) who found highest correlation for LAI values ranging between 1.7 and 3.5.

The above discussion of confounding factors showed that the effect of these parameters on backscattering depends also on the type of polarization and the incidence angles used. Singh (2006) performed ground-based X-band measurements at different angles and polarizations to analyze the relationship between biophysical parameters of soybean such as plant height, biomass, LAI, and crop covered soil moisture. He found the highest correlation between biomass and backscattering for incidence angles larger than 40° and VV-polarization. Lower angles were more affected by dynamics in soil moisture. Brown *et al.* (2003) used C- and X-band measurements to estimate the biomass of an outdoor wheat canopy. They showed that a two-channel C-band operating at moderate incidence angles was most appropriate to estimate biomass. The authors argued that biomass was expressed through its effect on extinction, rather than by its contribution to backscattering. Differential attenuation of soil backscattering by the HH- and VV-polarization, i.e., the difference between both polarizations, was found to best relate to biomass. However, the period with a large biomass increase was not captured. Mattia *et al.* (2003) used ground-based C-band backscattering measurements on wheat fields to derive relationship between wheat biomass and soil moisture. They showed that biomass could not be retrieved using VV-polarization with an incidence angle of 23° due to modulation from soil moisture. Better results were obtained for biomass prediction from backscattering when using the VV/HH ratio with an incidence angle of 40°. Maity *et al.* (2004) assumed a linear relationship between LAI and crop height for analysis with RADARSAT, whereby the increase in LAI and plant height led to an increase in backscattering. All studies analyzed suggest that the derivation of relationships between biomass and backscattering coefficient was most successful for larger incidence angles and that lower frequencies may result in better estimates.

**Effects of leaves, stems, and branches**

Most of the work on the effects of geometry and related plant parts on microwave signals has been done using active measurements systems and has focused on specific parts of the plants such as leaves, stems, and branches. Characterizing of these elements in terms of electromagnetic properties and shapes is essential for any mathematical modeling of backscattering coefficients. Several studies have shown that the leaf size and leaf geometry greatly influence the observed backscattering coefficients (Brown *et al.*, 2003; Karam and Fung, 1989; Wu *et al.*, 1985b). Paris (1986) was one of the first to include the leaf size

in a modified water cloud model to predict backscattering from a corn canopy and obtained an excellent fit between modeled and observed backscattering at a frequency of 17.5 GHz. Paloscia (1998) showed that the change in backscattering with vegetation water content was different for wide-leaf crops (grains) and crops with circular leaves (sunflowers). She concluded that crops with the same vegetation water content may result in different backscattering due to the geometry of the leaves. Cookmartin *et al.* (2000) showed that nonplanarity of leaves in oilseed rape was a considerable source of error in the physically-based radiative transfer model RT2. An additional mechanisms was observed by Della Vecchia *et al.* (2006) who reported that leaf curvature of maize and stem hollowness of wheat led to a reduction of backscattering and stem attenuation from C-band, respectively. Further theoretically analysis showed that these effects seem to be dependent on the growth stage of the crop. In addition to leaf shape and size, stem, ear, and branch properties also influence backscattering of radar signals. To overcome these problems and to allow interpretation of ERS-2 backscattering data, Cookmartin *et al.* (2000) developed an equivalent integrable first-order radiative transfer model which included a correct representation of attenuation by the stems and scattering by ears in cereals crops.

**Management practices**

Finally, also management practices may play an important role in analyzing backscattering signals. Paris (1983) found that radar backscattering coefficients were affected by row-directions among fields cropped with corn, soybean, alfalfa, and wood when using like-polarization at look angles between 5 and 25°. No effects were found for cross-polarization or look angles greater than 25° independent of the polarization. Additionally, wet surface soil water conditions, typical for irrigated crop systems, were less favorable than dry surface conditions to separate between crop types. The effect of row direction of, e.g., wheat and barley was smaller than the effect of row spacing. A close row spacing of 12.5 cm for wheat and barley resulted in relatively high backscattering values during early vegetative growth and low backscattering values at grain filling and ripening compared to larger row spacing. This effect of row spacing was only observed at low and medium frequencies. Even the removal or leaving-behind of crop residues as well as ploughing and harrowing of the stubble will influence the backscattering coefficient of X-band measurements as reported by Bouman and van Kasteren (1990a).

## 6.7 Multi-sensors measurements

For the characterization of crop conditions, i.e., type, status, height, etc., the utilization of more than one sensor type gives valuable information. Data acquired over the same site by different sensors are partially redundant, since they represent the same scene, and partially complementary, since the sensors have different characteristics and the physical mechanisms of diffusion are different (Le Hegarat-Mascle *et al.*, 2000). Several approaches have been pub-

lished to combine microwave data from several frequencies, active with passive microwave, or microwave data with optical data from visible, near infrared, and thermal spectra. These methods are discussed in the following. We will focus on the combination of active and passive systems and on the combination of microwave with optical/multispectral systems. However, real fusion techniques of disparate data which contributes to the understanding of the objects observed, as reviewed by Dong *et al.* (2009) and Pohl and van Genderen (1998), are rare.

### 6.7.1 Active and passive microwave sensors

In several early studies, passive and active microwave signatures of various agricultural crops were measured, e.g., by Brunfeldt and Ulaby (1984) and Hüppi (1987). At this stage, a strong focus was on the estimation of soil moisture, considering vegetation as a confounding factor only for soil moisture retrieval (Jackson *et al.*, 1982). Saatchi *et al.* (1994) developed an active/passive microwave scattering model for a grass canopy in order to explain the behavior of reduction in sensor sensitivity to soil moisture in the presence of a (wet) thatch layer. Chauhan (1997) used NASA's Airborne Synthetic Aperture Radar (AIRSAR) to estimate the vegetation opacity and surface roughness, whereas the brightness temperature was received by the Push-Broom Microwave Radiometer (PBMR). Hereby the study was mainly focused on the estimation of soil moisture, but they nicely showed the synergistic effect of active and passive microwave sensors to gain information about the status of cropped agricultural fields. As a consequence of the upcoming SMAP mission (Entekhabi *et al.*, 2010), a combined use of active and passive microwave data gains more attraction, whereby the focus of SMAP lies in the estimation of near surface soil moisture (Dorigo *et al.*, 2010).

An exception from the focus on soil moisture retrieval is the work of Wigneron *et al.* (1999), who simulated active and passive observations to investigate the surface characteristics over a soybean field. Soil and vegetation effects were best described by combining passive microwave data at L-band with multi-angle active microwave data at C-band. Similarly, Jin and Huang (1996) developed a model considering an agricultural crop stand as a layer of continuous random media with an underlying rough surface. They analyzed the correlations of active and passive microwave signatures for different crops and compared them to real measurements at 1.2 GHz. The results showed that simultaneous radar and radiometer observations can be efficiently used to monitor the development of agricultural crops. Moreover, they identified clusters in emissivity and backscattering which were used to separate different vegetation types. Oza *et al.* (2008) used SSM/I (passive) and QuickSCAT (active) data for the identification of rice growing stages from transplanting to maturity. While SSM/I was better able to identify the transplantation period, Quickscat was better able to predict the heading phase. Unfortunately, a real fusion of active and passive microwave data was not performed. A study using the ground-based radiometer-scatterometer system RASAM (Hüppi, 1987), and a feed forward neural network for biomass estimation of oat and wheat was presented by Jin and Liu (1997). This was also not a real data fusion, but they

jointly used active and passive microwave signals for the retrieval of biomass characteristics including canopy height, canopy water content, and dry matter fraction in an adequate accuracy.

### 6.7.2 Microwave and optical/multispectral sensors

While the microwave scattering process is influenced by the structural elements of the land cover, optical sensors provide either information on the chemical composition (hyperspectral sensors) or physical temperature (IR-sensors) of the scene. Therefore, a fusion of these two data sets is feasible, especially for characterization of the plant status (Huang *et al.*, 2010). Important fusion techniques are the principal component analysis (PCA) and the intensity-hue-saturation (IHS) transform. Additive Integration, Component Substitution and Intensity Modulation are fusion methods tested by Chibani (2006) using SPOT and RADARSAT-1 data. However, most studies just compared the microwave signals to vegetation indices (Baghdadi *et al.*, 2009; Hunt *et al.*, 2011; Jones *et al.*, 2011; Rosenthal *et al.*, 1985; Svoray and Shoshany, 2002).

Real combination or fusion of microwave and optical signals for the characterization of crop canopies are rare, but would provide reasonable information. In general, two categories of microwave and optical data fusion techniques are reported:

The first category includes approaches aiming at an enhanced land cover and land use discrimination. Hereby, methods such as IHS transform and PCA transfer the remote sensing data into a new system, which introduces severe radiometric distortions or where they even lose their physical meaning, but enhance the spatial separability of land cover classes. Wavelet-based methods (Amolins *et al.*, 2007) –and even the simplest– tend to produce better results than standard fusion schemes such as IHS and PCA. Typically, wavelet fusion schemes have been proposed to import detailed information from SAR into multispectral imagery. The advantage is that the multispectral information remains almost unchanged and the texture information from SAR will be transferred. For classification approaches, a significant change in the data characteristics can be accepted, because a classification traditionally makes use of the relative differences between the classes only. Horgan *et al.* (1992) as well as Vescovi and Gomarasca (1999) fused shuttle imaging radar and Landsat data for enhanced classification. Similarly, Smara *et al.* (1998) and Michelson *et al.* (2000) found higher class separabilities when Landsat TM and ERS-1 data were combined. Alparone *et al.* (2004) presented a similar study on the succession satellites Landsat ETM+ and ERS-2 data with a wavelet transform. Le Hegarat-Mascle *et al.* (2000) fused multi-temporal ERS images and multispectral Landsat images by the Dempster-Shafer evidence theory for unsupervised classification in order to use their complementarity in reducing confusion by getting more complete description of the land cover type features. Haack and Khatiwada (2010) applied a spectral signature extraction and Transformed Divergence approach for SIR-C and Landsat data. Hong *et al.* (2009) developed a combined IHS-Wavelet Fusion algorithm. Finally, McNairn *et al.* (2009)

analyzed the performance of different classification algorithms on fused data sets of Radarsat-1, ASAR, SPOT, and Landsat.

The second category includes approaches which aim at a more detailed identification of absolute crop conditions. A combined use of optical and radar remote sensing is presented in the paper by Dente *et al.* (2008), who assimilated LAI derived from MERIS and ASAR into a crop growth model for yield estimation. It has to be mentioned that the combination of microwave and optical data was only used for gap filling of time series within the study. Mangiarotti *et al.* (2008) used a bi-objective optimization method to assimilate ASAR backscattering and SPOT-Vegetation NDVI into a vegetation dynamics model to improve its predictions on biomass and LAI, whereas Hadria *et al.* (2010) performed a comparative analysis using time series of both FORMOSAT-2 and ASAR images for the monitoring of irrigated wheat crops in a semi-arid region in Morocco. Hereby, FORMOSAT-2 images were used to characterize the spatiotemporal variations of green LAI, which was incorporated into a simple canopy functioning model to provide spatial estimates of above-surface biomass and top-soil moisture. They found evidence that the signal reaches a saturation level from intermediate values of biomass water content (about 2000 g $m^{-2}$). Airborne Visible and Infrared Imaging Spectrometer (AVIRIS) and AirSAR data were fused by Huang *et al.* (2010) for the estimation of fractions of non-photosynthetic vegetation (grass and shrub). This approach may also give feasible information on the conditions of dried crops, e.g., cereals before harvest.

In general, the utilization of multi-sensor and multi-frequency information leads to a better characterization of the crop status. The mentioned approaches may be feasible to identify plant stress related differences to the normal crop growth. However, for this aim more work is needed on the development of new sensors and fusion algorithms in an applicable way.

## 6.8 Outlook

In this chapter we reviewed the use of microwave methods to characterize crop canopies using microwave methods and with specific focus on their ability to identify the presence of water-stress related phenomena. Our analysis of literature showed that practically no data set are available which provide both microwave measurements of the plant canopy (e.g., backscattering, optical depth) and detailed measurements of the physiological properties of the canopy, the soil moisture status, and the micro-climatic conditions in the canopy, and therefore, allow evaluating observed microwave signals in relation to stress phenomena. Measurements presented in literature and related to analyzing the effect of water stress on, e.g., microwave signals were typically conducted on single plants under lab conditions with little information on the soil and plant water status. Moreover, there are no data available that provide information on soil and plant water status in combination with microwave measurements at the field scale. Detailed temporal and spatially distributed information about the soil and plant water status is in our opinion essential when evaluating any remote sensing method used to assess the occurrence and presence of water stress

in plants. Microwave measurements should therefore be combined with measurements of soil water potential and soil moisture content in the root zone, micro-meteorological measurements within and above the canopy as well as physiological properties and quantities of the plant such as volume-pressure curves, vegetation water content, leaf water potential, and transpiration rate of the plant. The characterization of geometrical and structural properties of the canopy and their dynamical behavior is another essential element to assess the effect of water stress phenomena on microwave signals. Interpretation of such integrated data sets in combination with 3D functional-structural plant canopy models including the effects of physiological processes on the radiative transfer properties of the canopy will enable to improve early identification of stress and will help to disentangle the factors influencing observed microwave signals. It will help to better evaluate the importance of mapping the dynamics and spatial distribution of surface soil moisture in terms of identifying the occurrence of plant water stress at the field scale. Up to now it is not clear in how far information on surface soil moisture status is relevant in assessing early plant water stress.

A combination of different sensor technologies covering the full spectral range from optical to microwave will open new perspectives and generate new knowledge about the status of vegetation and more specifically crop canopies. A first attempt to combine this spectral range on one platform which was suitable for crop science applications was ESA's ENVISAT mission, launched in 2002. For future satellites there is a trend to develop specialized sensors on individual platforms, such as the 5 planned ESA Sentinels (1: C-Band SAR, 2: Superspectral, 3: Ocean, 4/5: Atmospheric Chemistry) will continue the work of actual missions. Moreover, German activities around TerraSAR-X, TanDEM-X, RapidEye, EnMAP and Tandem-L provides and will provide sound knowledge about plant conditions and will in combination be able to identify crop stress. Myneni and Choudhury (1993) already pointed at the potential of combining different sensor technologies. They stated that combining optical and microwave techniques will allow observing different responses of the plants due to water stress such as the diurnal response of water stress detectable by microwave methods but which does not occur in the pigment concentration. Moreover, a combination of optical and microwave data can be synergistically used to infer land surface properties and crop status. Also, optical data and their deduced parameters can be used for correction and interpretation of microwave observations.

Here a close cooperation between the soil, plant, and remote sensing communities may lead to new results. In addition, validation of these novel model approaches will require data which are presently not available in literature as already outlined above.

Assimilation of remotely sensed properties such as backscattering coefficient or brightness temperature may provide a unique opportunity to improve the estimate of biophysical properties as crop canopies such as LAI, dry matter, plant water content, and related leaf potential and others. First studies that use assimilation of remotely sensed microwave data have been developed recently in the field of hydrology (Draper *et al.*, 2011; Montzka *et al.*, 2011),

meteorology (Rasmy *et al.*, 2011), or for optical remote sensed data and the assimilation in crop functioning models (e.g., Weiss *et al.*, 2001). This avenue has, however, not been really pursued in the past for vegetation canopy properties for microwave frequencies but it provides a huge potential for remotely sensed data, especially for microwave data as they are available for almost all weather conditions. Within the field of microwave measurements, acquisition of backscattering data at different frequency bands may provide additional information on the status of the crop. Lopez-Sanchez and Ballester-Berman (2009) stated that a combination of low and high microwave bands, allows determining different properties of the plants and different scales of their component such as leaves, stems, and heads. Additionally, multipolarization (dual- and full-polarization), data exploits the sensitivity of the wave polarization to the orientation, shape, and dielectric properties of the elements in the scene. Therefore, polarimetry SAR interferometry (such as PolInSAR) seems to be the most promising tool to gain information for agricultural crop stands (Lopez-Sanchez and Ballester-Berman, 2009). Finally, PolInSAR yields information not only about the dielectric properties, shape and orientation of the whole plant constituents, but also about the vertical structure of the plant by means of information about the localization of the scattering centers.

# Chapter 7

# Conclusions and perspectives

## 7.1 Conclusions

Soil water content is widely recognized as a key component of the water, energy, and carbon cycles. In order to assess the spatiotemporal dynamics of SWC at the field scale, which typically corresponds to the management scale in agriculture, ground-penetrating radar and ground-based radiometer appear to be very promising tools for high-resolution mapping and monitoring. In this thesis, we investigated and further improved GPR and radiometer forward and inverse modeling approaches for SWC retrieval at the field scale. In particular, we focused on the improvement of the GPR and radiometer models by including roughness corrections and the validation of the methods in laboratory and field conditions.

In Chapter 2, an L-band radiometer and an off-ground GPR instrument were mounted on a mobile platform to map SWC over an agricultural bare field with a relatively high spatial variability in SWC. Additionally, ground-truth SWC was recorded by time-domain reflectometry within each radar and radiometer footprint. The results of the field survey indicated that high-resolution SWC mapping was feasible using radiometer and GPR data, whereby both instruments showed reliable SWC estimates compared to TDR measurements. Nevertheless, discrepancies were observed for both instruments, which were attributed to different sensing depths and areas as well as different sensitivities with respect to soil surface roughness. For GPR, we operated at sufficiently low frequencies (<0.8 GHz) for which the radar reflections were not affected by roughness. The RMSE between SWC measured by GPR and TDR was 0.038 $m^3$ $m^{-3}$ while the RMSE between radiometer and TDR SWC estimates was 0.020 $m^3$ $m^{-3}$ after accounting for roughness using an empirical model that required calibration with reference TDR measurements, whereby only one effective parameter set was used for the entire field. Additionally, Monte Carlo simulations were performed to evaluate the sensitivity of the roughness parameters with respect to the number of ground truths used for the model calibration.

The results of the Monte Carlo simulations indicated that around 20% of the ground-truth information is required to obtain a good roughness calibration to be applied for the entire field, which is much larger than the number of reference points reported in all field studies dealing with the calibration of large-scale remote sensing products. Overall, this study represents the first work comparing field-scale SWC maps over a bare rough surface using ground-based radiometer and advanced off-ground GPR simultaneously, and therefore, provides an essential step for the understanding of combined use of passive and active sensors for planed satellite missions such as SMAP and/or for calibration and validation purposes for such missions.

As stated above, the classical approach to deal with soil surface roughness for the advanced off-ground GPR is to focus on low frequency data only, which are less or not sensitive to roughness effects (see Chapter 2). Yet, limiting the GPR frequency range to low frequencies also limits the information content in the radar data and, hence, limits soil characterization capabilities such as range resolution. To partly overcome this issue, soil roughness effects can be directly accounted for in the electromagnetic model. In that respect, in Chapter 3, the full-wave GPR model of Lambot *et al.* (2004c) was combined with a roughness model derived from Kirchhoff scattering theory for the retrieval of surface SWC through signal inversion. For the validation of the extended model, radar data measured over a sandy soil with known roughness and water content were used. Additionally, soil surface roughness and soil water content were varied to cover a wide range of experimental conditions. For this setup the radar measurements were performed in the full frequency range between 1–3 GHz and the roughness amplitude standard deviation varied from 0 to 1 cm. The results showed that full-waveform inversion permits simultaneous reconstruction of the medium dielectric permittivity and the standard deviation of the surface roughness, but only when the layer thicknesses are known. Unfortunately, this is typically not the case in field applications. Nevertheless, we proposed a specific inversion strategy for field conditions, which is based on a surface reflection focused inversion, and which permitted the retrieval of the surface permittivity with an RMSE in terms of SWC of 0.034 $m^3$ $m^{-3}$ compared to an RMSE of 0.068 $m^3$ $m^{-3}$ for an analysis where roughness was neglected. In that case, roughness parameters should be independently determined, e.g., using a laser profiler. The proposed method appears to be promising for surface SWC mapping in reasonably rough environments with a roughness amplitude $< 1/4$ of the wavelength and constitutes a step forward for far-field radar applications in rough environments.

In Chapter 4, we analyzed in particular the effects of tillage practices on the spatial variation of soil properties such as surface soil water content, bulk soil electrical conductivity, and mechanical resistance using on-ground and off-ground GPR as well as electromagnetic induction (EMI). Hereby, the EMI was used to provide insights into the variability of the soil properties of the deeper layer (up to 2 m depth). Reference SWC measurements were performed using two different capacitance probes and reference soil sampling. The soil resistance was independently measured at three locations using an automated penetrometer. The data showed that tillage influences soil resistance (deeper

tillage decreases soil resistance), which could be partly seen in the on-ground GPR data. Additionally, reference SWC measurements (capacitance probes and soil sampling) were in a reasonable agreement with the water content estimates from off-ground GPR. The correlations between the GPR and capacitance probe data (RMSE between 0.040–0.045 $m^3$ $m^{-3}$, $R^2$ between 0.31–0.39) were very similar to the correlation observed in Chapter 2 between GPR and TDR data (RMSE of 0.038 $m^3$ $m^{-3}$, $R^2$ of 0.39). These limited agreements were attributed to the relatively large variability of surface SWC at the $m^2$ scale while the different characterization supports were inherently different. We observed as well that the tillage type influenced shallow surface water content, while deeper SWC seemed to be unaffected. Surface SWC was significantly larger in the reduced and the deep loosening tillages compared to the conventional tillage, which was partly explained by lower pore connectivity between the topsoil and the deeper layers after conventional tillage. Finally, the spatial distribution of the SWC was analyzed using geostatistical approaches. The spatial analysis showed that the variance of the SWC within the conventional tillage plots was larger than within the other plots, which was explained by a larger soil heterogeneity induced by the plowing process. In conclusion, this study confirms the potential of GPR and EMI for fast determination of the soil state variables at the field scale and for the characterization of agricultural management practices.

We evidenced in Chapters 2 and 4 the potential of GPR and radiometer to map the spatial variability of surface SWC at the field scale. However, given the large temporal variability of SWC, time-lapse measurements should be performed to satisfy the characterization needs of most environmental and agricultural applications. Yet, accurate modeling of water flow and solute transport in heterogeneous subsurface can also be obtained from detailed characterization of the soil hydraulic properties which are known to vary much slowly over time (Lambot *et al.*, 2004a; Vereecken *et al.*, 2010). In Chapter 5, we investigated the potential of GPR and L-band radiometer to identify the hydraulic properties (water retention curve) of a sand subject to hydrostatic equilibrium with a range of water table depths. At hydrostatic equilibrium, the vertical water content profile exhibits a continuous variation corresponding to the water retention curve of the soil. For both GPR and radiometer, all measurements were aggregated in an inversion scheme to reconstruct the vertical water content profiles, which were constrained using the van Genuchten water retention equation. The results showed that both active and passive microwave data contain sufficient information to estimate the sand water retention curve and its related hydraulic parameters. The results were in close agreement with reference TDR measurements. This study represents a first comparison between active and passive microwave systems to characterize the shallow soil hydraulic properties.

In Chapter 6, the use of microwave remote sensing methods for characterizing crop canopies and vegetation water-stress related phenomena was reviewed. The analysis includes both active and passive systems that are ground-based, airborne, or spaceborne. The meta-analysis indicated that the vast majority of studies used active microwave systems to characterize the crop canopy and

to identify water stress related phenomena. It was also shown that for the quantification of the effect of dynamic vegetation properties and particularly water-stress related processes improved models and more observational data are urgently needed to understand and interpret the microwave data. Integrated data sets providing the full information on both soil and plant status are still lacking, which has hampered the development and validation of mathematical models. Additionally, there is a need to link 3D-functional-structural crop models with radiative transfer models in order to better understand the effects of environmental and related physiological processes on microwave data and to better quantify the impact of water stress on microwave propagation and attenuation. Such modeling approaches should also incorporate both passive and active microwave methods due to their different sensitivities to structural elements within the crop canopy. Especially, the combination of different sensor technologies covering a wide spectral range from optical to the microwave region will have the potential to move forward our knowledge on the status of crop canopies and particularly water related stress phenomena. Finally, data assimilation schemes of remotely sensed properties such as backscattering coefficients or brightness temperature will help to improve the estimation and the understanding of the biophysical crop properties.

In conclusion, GPR and radiometer methods were successfully validated for high-resolution mapping and monitoring of SWC at the field scale. The problem of soil surface roughness on the retrieved signal was accounted for by using an optimized roughness model in the data processing scheme of the radiometer. For the advanced off-ground GPR, soil surface roughness was also accounted for in the GPR full-waveform inversion of laboratory data. This permitted to improve SWC estimations under laboratory conditions for reasonably rough environments. In addition, the GPR methodology was applied at the field scale to assess different agricultural management practices, whereby the high sensitivity of the off-ground GPR to the surface SWC allowed us to distinguish the effects of different tillage practices on the soil surface. Finally, GPR and radiometer data collected above a sand box were used to infer the soil water retention function. The estimated values from both techniques were in close agreement with reference TDR measurements. Although all field surveys performed in this thesis were on bare soils, the effect of vegetation on active and passive microwave signals was intensively discussed in the last chapter. Taking into account that a major part of the land surface is covered by vegetation, the effect of vegetation on microwave propagation remains a challenging issue in remote sensing of SWC.

## 7.2 Further perspectives

### 7.2.1 Potential applications

The studies presented in this thesis proved the valuable potential of GPR and radiometer for characterizing the variability of soil properties and state variables at the field scale. Environmental and agricultural applications such as precision agriculture could greatly benefit from these non-invasive, low cost,

and high-resolution characterizing techniques. GPR and radiometer mounted on a mobile platform can both accurately map and monitor the surface soil moisture (see Chapters 2 and 4) which is, for instance, particularly important during seedbed preparation and at the beginning of the growing season. These techniques can be used to guide precision irrigation and/or soil management practices in order to optimize crop productivity and maintain sustainability of soils. Combined with EMI and/or soil resistance measurements (see Chapter 4), information about the root zone could also be acquired, which is particularly interesting for water stress detection. Some improvement could however be performed for a better applicability of the GPR and radiometer systems to precision agriculture. For instance, the GPR setup investigated in this thesis was used with the antenna fixed at about 1.2 meter off the ground in far-field conditions. Lambot and André (2012) recently developed a new GPR model allowing to use the antenna in near-field conditions or on-ground, which permits to increase the penetration depth and the spatial resolution. For radiometer, the antenna can not be used close to the ground as the self-emission of the antenna would be reflected on the soil surface and added to the natural radiance emitted from the soil. For agricultural soil with relatively low and sparse vegetation and small soil roughness, the GPR technique seems to be more easily applicable for soil characterization due to its potential to be used close to the soil surface (better spatial resolution, larger penetration depth) and its shorter measurement integration time for real-time mapping (less than 1 ms for GPR compared to 3–10 s for radiometer). However, for agricultural soil with denser vegetation and larger surface roughness, the radiometer technique could be preferably used given the smaller influence of the vegetation and soil roughness on the measured radiance. Yet, some improvements still have to be performed to accurately account for these influences on the soil moisture retrieval (see section below).

As Robinson *et al.* (2008a) pointed out, soil water content information at the catchment scale is also highly important to understand hydrologic processes. Given the high SWC variability, SWC information over a large area with a high temporal and spatial resolution is needed for accurate hydrological modeling. An emergent technology at the catchment scale is the wireless sensor network. These networks can provide soil moisture information with a high temporal resolution over large areas (Bogena *et al.*, 2010). However, SWC information between sensors is missing as each sensor provides only very local measurements. GPR and radiometer measurements could then be combined to sensor networks for an optimal spatial and temporal resolution at the catchment scale (Minet, 2011).

At the global scale, spaceborne microwave measurements provide soil moisture information particularly relevant for climate prediction. Spaceborne remote sensing products are usually validated using ground-based observations such as sparse point data from manual sampling or sensor networks. Given the high spatial variability of SWC, the large contrast in support scales between spaceborne remote sensing and *in-situ* methods makes them hardly comparable (Minet *et al.*, 2012; Crow *et al.*, 2012). The two methods investigated in this thesis could be used to improve the validation of spaceborne data. For active

spaceborne data such as SAR data, GPR and radiometer can provide soil moisture maps with a spatial extent in the same order as the footprint of the SAR instrument (e.g., 3–100 m for RADARSAT-2). For passive spaceborne data, the comparison with ground-based GPR and radiometer data is more complicated due to the much larger footprint of the spaceborne radiometers (e.g., 50 km for SMOS) and could be performed, for instance, in combination with airborne measurements. In that framework, an attempt to validate the SMOS satellite data by using airborne and truck-mounted radiometers has recently been performed by Montzka *et al.* (2012). The radar and radiometer methods investigated in this thesis will be further applied for systematic spaceborne active and passive remote sensing product validation.

### 7.2.2 Future research

**Vegetation effect on soil moisture retrieval** An important challenge for SWC estimation using active and passive microwave remote sensing remains for the effect of vegetation. In this thesis, we did not investigate this problem but the different issues related to vegetation were presented in Chapter 6. In general for passive remote sensing systems, the soil moisture retrieval algorithms used over vegetated areas are based on a simplified zero-order radiative transfer equation called the tau-omega model. This model includes vegetation parameters which are known to be depend on vegetation structure, observation incidence angle, and polarization (Wigneron *et al.*, 2004). Sparse information about these parameters such as the vegetation optical depth (tau parameter) can be found in literature but only few vegetation types have already been investigated and, generally, only over limited times during the growing season. Therefore, the temporal evolution of the vegetation parameters, in particular the $b$ parameter used to describe the vegetation optical depth (see Eq. (6.4)), should be further investigated for different crop types to improve the accuracy of the SWC estimates. Tower-based radiometer measurements over different kinds of vegetation growing through a wire-grid are valuable experiments to be performed. The wire grid being used to shield the soil emission in order to separate the radiance originating from the soil and the vegetation. Such experiments will provide important information on how the seasonal development of various vegetation types affects the microwave signatures. Furthermore, diurnal variabilities of vegetation emission can be quantified accurately, and artificial conditioning of the vegetation, such as wetting, could be performed. In order to improve the interpretation of L-band signatures emitted from forests, which cover a significant part of the land surface, studies regarding the effect of the litter on the soil moisture retrieval from active/passive microwave sensors are needed. The sand box setup developed in this thesis is well suited to measure the emission and scattering of organic litter layers at various conditions in terms of water content, density, structure, and composition.

**Roughness effect on soil moisture retrieval** The roughness modeling problem was addressed in this thesis for both active and passive microwave systems. For GPR, we used a physically-based roughness model. The rela-

tively good agreement between the model and the laboratory measurements confirms the ability of the investigated model to describe the roughness effect on the radar signal. In a further step, the proposed approach should be validated in field conditions. However, the model is expected to provide less satisfactory results as the use of only one roughness parameter, i.e., the standard deviation in surface height, does not allow to accurately describe the complex surface roughness distributions observed in agricultural fields. Additional statistical parameters such as the autocorrelation function and the associated correlation length could then be added in the model for a better description of the roughness. Furthermore, as for most physically-based models (e.g., IEM), the investigated model assumes that surface roughness is a random stationary process, characterized through a unique spatial scale (Davidson *et al.*, 2000). However, surface roughness in agricultural fields generally exhibits periodic and oriented structures such as furrows (Völksch *et al.*, 2011; Völksch, 2011). Several attempts have already been made to enhance conventional models using for instance multiscale approaches (Beaudoin *et al.*, 1990; Mattia and Le Toan, 1999). Nevertheless, the higher complexity and number of parameters of such models will probably limit their operational use. An alternative strategy with an increasing interest is the use of calibrated or effective roughness parameters (Lievens *et al.*, 2011). This approach has already been successfully applied in this thesis to model the roughness effect for radiometer (see Chapter 2), using a relatively simple equation including two effective roughness parameters calibrated with soil moisture observations. This permits to keep a practical modeling concept and avoid issues with respect to field measurements of the surface roughness (Jester and Klik, 2005). A similar strategy could then be developed for roughness modeling in GPR data processing algorithms.

**Active and passive data fusion** New avenues of research have been recently opened by combining active and passive microwave data. As shown in this thesis, the influence of surface roughness on soil moisture retrieval is different for radar and radiometer and depends also on wavelength and incidence angle. The two microwave methods lead also to different characterization depths, which therefore results in different soil moisture products. Over cropped areas, for common remote sensing operating frequencies, radar data are also typically more sensitive to vegetation compared to radiometer data (Kurum *et al.*, 2009). This inherently leads to larger uncertainties in the soil moisture retrieval, but this high sensitivity can be used to characterize the vegetation itself. To overcome the individual limitations of the two approaches and benefit from their different sensitivities, the combined use of these two technologies seems to be a promising solution for soil moisture retrieval. For instance, information on the vegetation structure obtained from active systems could be used in the processing of passive microwave data to improve SWC retrieval (O'Neill *et al.*, 1996). Based on the higher accuracy of spaceborne radiometer soil moisture estimates and the finer spatial resolution obtained for radar observations, the NASA is preparing the launch of a new satellite (SMAP) combining both radar and radiometer instruments. Several algorithms have recently been proposed to merge L-band radiometer and radar data to obtain high-resolution soil mois-

ture estimates (Zhan *et al.*, 2006; Piles *et al.*, 2009; Das *et al.*, 2011). However, these methods only improve the spatial resolution of the radiometer soil moisture estimates and not the retrieval accuracy. New research should investigate the feasibility to merge radar and radiometer for increased resolution and accuracy in soil moisture retrieval using, for instance, a Bayesian data fusion framework (Bogaert and Fasbender, 2007; Fasbender *et al.*, 2008) which allows to account for several information sources about a same variable of interest such as the soil moisture in order to provide an optimal spatial prediction.

**Data assimilation in hydrological models** In Chapter 5, we showed that the soil hydraulic properties can be retrieved by combining the GPR/radiometer electromagnetic model with a soil hydraulic model. This was performed at hydrostatic equilibrium in a relatively homogeneous soil (sand box). Further research could also focus on the inversion of GPR and radiometer data for dynamic conditions, which inherently permit to retrieve more information from a system (e.g., hydraulic conductivity function). For GPR, Lambot *et al.* (2006b) and Jadoon *et al.* (2008) recently proposed a hydrogeophysical inversion method to retrieve soil hydraulic properties from time-lapse GPR data. A similar approach could be tested for time-lapse radiometer data. Over the last years, numerous studies have also focused on the improvement of hydrological model results through the assimilation of soil moisture data (Walker *et al.*, 2002; Pauwels *et al.*, 2002; De Lannoy *et al.*, 2007; Reichle *et al.*, 2008; Reichle, 2008). For spaceborne remote sensing, data assimilation systems with the ensemble Kalman filter have been successfully used to merged satellite active/passive surface soil moisture retrievals with information from a land surface model and antecedent meteorological data to provide better soil moisture estimates (Montzka *et al.*, 2011; Draper *et al.*, 2012). In a similar way, high-resolution GPR and radiometer soil moisture retrievals could be, for instance, assimilated in hydrological models for a better estimation of the hydrologic fluxes at the micro-catchment/field scale.

# Bibliography


Acevedo, E., Fereres, E., Hsiao, T. C., and Henderson, D. W. 1979. Diurnal growth trends, water potential, and osmotic adjustment of maize and sorghum leaves in the field. Plant Physiology, 64(3):476–480.

Ackerson, R. C., Krieg, D. R., Miller, T. D., and Zartman, R. E. 1977. Water relations of field-grown cotton and sorghum - Temporal and diurnal changes in leaf water, osmotic, and turgor potentials. Crop Science, 17(1):76–80.

Ackley, W. B. 1954. Seasonal and diurnal changes in the water contents and water deficits of Bartlett pear leaves. Plant Physiology, 29(5):445–448.

Allen, L. H., Valle, R. R., Jones, J. W., and Jones, P. H. 1998. Soybean leaf water potential responses to carbon dioxide and drought. Agronomy Journal, 90(3):375–383.

Alletto, L., Coquet, Y., and Justes, E. 2011. Effects of tillage and fallow period management on soil physical behaviour and maize development. Agricultural Water Management, 102(1):74–85.

Alparone, L., Baronti, S., Garzelli, A., and Nencini, F. 2004. Landsat ETM+ and SAR image fusion based on generalized intensity modulation. IEEE Transactions on Geoscience and Remote Sensing, 42(12):2832–2839.

Ament, W. S. 1953. Toward a theory of reflection by a rough surface. Proceedings of the Institute of Radio Engineers, 41(1):142–146.

Amolins, K., Zhang, Y., and Dare, P. 2007. Wavelet based image fusion techniques - An introduction, review and comparison. ISPRS Journal of Photogrammetry and Remote Sensing, 62(4):249–263.

André, F., van Leeuwen, C., Saussez, S., Van Durmen, R., Bogaert, P., Moghadas, D., de Resseguier, L., Delvaux, B., Vereecken, H., and Lambot, S. 2012. High-resolution imaging of a vineyard in south of France using ground-penetrating radar, electromagnetic induction and electrical resistivity tomography. Journal of Applied Geophysics, 78(0):113–122.

Annan, A. P. 2005. GPR methods for hydrogeological studies. In Hubbard, Y. R. and S.S., editors, *Hydrogeophysics*, pages 185–213. Springer, New York.

Attema, E. P. W. and Ulaby, F. T. 1978. Vegetation modeled as a water cloud. Radio Science, 13(2):357–364.

Baghdadi, N. and Zribi, M. 2006. Evaluation of radar backscatter models IEM, OH and Dubois using experimental observations. International Journal of Remote Sensing, 27(18):3831–3852.

Baghdadi, N., Zribi, M., Loumagne, C., Ansart, P., and Anguela, T. P. 2008. Analysis of TerraSAR-X data and their sensitivity to soil surface parameters over bare agricultural fields. Remote Sensing of Environment, 112(12):4370–4379.

Baghdadi, N., Boyer, N., Todoroff, P., El Hajj, M., and Begue, A. 2009. Potential of SAR sensors TerraSAR-X, ASAR/ENVISAT and PALSAR/ALOS for monitoring sugarcane crops on Reunion Island. Remote Sensing of Environment, 113(8):1724–1738.

Basso, B., Amato, M., Bitella, G., Rossi, R., Kravchenko, A., Sartori, L., Carvahlo, L. M., and Gomes, J. 2011. Two-dimensional spatial and temporal variation of soil physical properties in tillage systems using electrical resistivity tomography. Agronomy Journal, 102(2):440–449.

Battaglia, A., Ajewole, M. O., and Simmer, C. 2006. Evaluation of radar multiple-scattering effects from a GPM perspective. Part I: Model description and validation. Journal of Applied Meteorology and Climatology, 45(12):1634–1647.

Beaudoin, A., Letoan, T., and Gwyn, Q. H. J. 1990. SAR observations and modeling of the C-band backscatter variability due to multiscale geometry and soil-moisture. IEEE Transactions on Geoscience and Remote Sensing, 28(5):886–895.

Becker, F. and Choudhury, B. J. 1988. Relative sensitivity of Normalized Difference Vegetation Index (NDVI) and Microwave Polarization Difference Index (MPDI) for vegetation and desertification monitoring. Remote Sensing of Environment, 24(2):297–311.

Beckmann, P. and Spizzichino, A. 1987. *The scattering of electromagnetic waves from rough surfaces*. Springer Verlag, 2nd ed., Berlin, Germany.

Blaes, X. and Defourny, P. 2003. Retrieving crop parameters based on tandem ERS 1/2 interferometric coherence images. Remote Sensing of Environment, 88(4):374–385.

Blaes, X., Defourny, P., Wegmüller, U., Della Vecchia, A., Guerriero, L., and Ferrazzoli, P. 2006. C-band polarimetric indexes for maize monitoring based on a validated radiative transfer model. IEEE Transactions on Geoscience and Remote Sensing, 44(4):791–800.

Bogaert, P. and Fasbender, D. 2007. Bayesian data fusion in a spatial prediction context: a general formulation. Stochastic Environmental Research and Risk Assessment, 21(6):695–709.

Bogena, H. R., Herbst, M., Huisman, J. A., Rosenbaum, U., Weuthen, A., and Vereecken, H. 2010. Potential of wireless sensor networks for measuring soil water content variability. Vadose Zone Journal, 9(4):1002–1013.

Bouman, B. A. M. 1991. Crop parameter-estimation from ground-based X-band (3-cm wave) radar backscattering data. Remote Sensing of Environment, 37(3):193–205.

Bouman, B. A. M. and Hoekman, D. H. 1993. Multitemporal, multifrequency radar measurements of agricultural crops during the Agriscatt-88 campaign in the Netherlands. International Journal of Remote Sensing, 14(8):1595–1614.

Bouman, B. A. M. and van Kasteren, H. W. J. 1990a. Ground-based X-band (3-cm wave) radar backscattering of agricultural crops. 1. Sugar-beet and potato - Backscattering and crop growth. Remote Sensing of Environment, 34(2):93–105.

Bouman, B. A. M. and van Kasteren, H. W. J. 1990b. Ground-based X-band (3-cm wave) radar backscattering of agricultural crops. 2. Wheat, barley, and oats - The impact of canopy structure. Remote Sensing of Environment, 34(2):107–119.

Bouman, B. A. M., van Kraalingen, D. W. G., Stol, W., and van Leeuwen, H. J. C. 1999. An agroecological modeling approach to explain ERS SAR radar backscatter of agricultural crops. Remote Sensing of Environment, 67(2):137–146.

Bracaglia, M., Ferrazzoli, P., and Guerriero, L. 1995. A fully polarimetric multiple scattering model for crops. Remote Sensing of Environment, 54(3):170–179.

Brakke, T. W., Kanemasu, E. T., Steiner, J. L., Ulaby, F. T., and Wilson, E. 1981. Microwave radar response to canopy moisture, leaf-area index, and dry-weight of wheat, corn, and sorghum. Remote Sensing of Environment, 11(3):207–220.

Brisco, B., Brown, R. J., Koehler, J. A., Sofko, G. J., and Mckibben, M. J. 1990. The diurnal pattern of microwave backscattering by wheat. Remote Sensing of Environment, 34(1):37–47.

Brosten, T. R., Day-Lewis, F. D., Schultz, G. M., Curtis, G. P., and Lane, J. W. 2011. Inversion of multi-frequency electromagnetic induction data for 3D characterization of hydraulic conductivity. Journal of Applied Geophysics, 73(4):323–335.

Brown, R. J., Manore, M. J., and Poirier, S. 1992. Correlations between X-band, C-band, and L-band imagery within an agricultural environment. International Journal of Remote Sensing, 13(9):1645–1661.

Brown, S. C. M., Quegan, S., Morrison, K., Bennett, J. C., and Cookmartin, G. 2003. High-resolution measurements of scattering in wheat canopies - Implications for crop parameter retrieval. IEEE Transactions on Geoscience and Remote Sensing, 41(7):1602–1610.

Brunfeldt, D. R. and Ulaby, F. T. 1984. Measured microwave emission and scattering in vegetation canopies. IEEE Transactions on Geoscience and Remote Sensing, 22(6):520–524.

Bush, T. F. and Ulaby, F. T. 1976. Radar return from a continuous vegetation canopy. IEEE Transactions on Antennas and Propagation, 24(3):269–276.

Calvet, J. C., Wigneron, J. P., Walker, J., Karbou, F., Chanzy, A., and Albergel, C. 2011. Sensitivity of passive microwave observations to soil moisture and vegetation water content: L-band to W-band. IEEE Transactions on Geoscience and Remote Sensing, 49(4):1190–1199.

Cambardella, C. A., Moorman, T. B., Novak, J. M., Parkin, T. B., Karlen, D. L., Turco, R. F., and Konopka, A. E. 1994. Field-scale variability of soil properties in central Iowa soils. Soil Science Society of America Journal, 58(5):1501–1511.

Campbell, G. S., Calissendorff, C., and Williams, J. H. 1991. Probe for measuring soil specific-heat using a heat-pulse method. Soil Science Society of America Journal, 55(1):291–293.

Chanzy, A., Tarussov, A., Judge, A., and Bonn, F. 1996. Soil water content determination using digital ground penetrating radar. Soil Science Society of America Journal, 60:1318–1326.

Chanzy, A., Raju, S., and Wigneron, J. P. 1997. Estimation of soil microwave effective temperature at L and C bands. IEEE Transactions on Geoscience and Remote Sensing, 35(3):570–580.

Chauhan, N. S. 1997. Soil moisture estimation under a vegetation cover: Combined active passive microwave remote sensing approach. International Journal of Remote Sensing, 18(5):1079–1097.

Chauhan, N. S. and Lang, R. H. 1999. Radar backscattering from alfalfa canopy: a clump modelling approach. International Journal of Remote Sensing, 20(11):2203–2220.

Chen, J. S., Lin, H., Huang, C. D., and Fang, C. Y. 2009. The relationship between the leaf area index (LAI) of rice and the C-band SAR vertical/horizontal (VV/HH) polarization ratio. International Journal of Remote Sensing, 30(8):2149–2154.

Chen, K. S., Wu, T. D., Tsang, L., Li, Q., Shi, J. C., and Fung, A. K. 2003. Emission of rough surfaces calculated by the integral equation method with comparison to three-dimensional moment method simulations. IEEETransactions on Geoscience and Remote Sensing, 41(1):90–101.

Chibani, Y. 2006. Additive integration of SAR features into multispectral SPOT images by means of the a trous wavelet decomposition. ISPRS Journal of Photogrammetry and Remote Sensing, 60(5):306–314.

Choi, M. and Jacobs, J. M. 2007. Soil moisture variability of root zone profiles within SMEX02 remote sensing footprints. Advances in Water Resources, 30(4):883–896.

Choudhury, B. J. and Tucker, C. J. 1987. Monitoring global vegetation using Nimbus-7 37 GHz data - Some empirical relations. International Journal of Remote Sensing, 8(7):1085–1090.

Choudhury, B. J., Schmugge, T. J., Chang, A., and Newton, R. W. 1979. Effect of surface-roughness on the microwave emision from soils. Journal of Geophysical Research, 84(NC9):5699–5706.

Choudhury, B. J., Schmugge, T. J., and Mo, T. 1982. A parameterization of effective soil-temperature for microwave emission. Journal of Geophysical Research, 87(NC2):1301–1304.

Christiansen, L., Haarder, E. B., Hansen, A. B., Looms, M. C., Binning, P. J., Rosbjerg, D., Andersen, O. B., and Bauer-Gottwein, P. 2011. Calibrating vadose zone models with time-lapse gravity data. Vadose Zone Journal, 10(3):1034–1044.

Chukhlantsev, A. A., Shutko, A. M., and Golovachev, S. P. 2003. Attenuation of electromagnetic waves by vegetation canopies. Journal of Communications Technology and Electronics, 48(11):1177–1202.

Clevers, J. G. P. W. and vanLeeuwen, H. J. C. 1996. Combined use of optical and microwave remote sensing data for crop growth monitoring. Remote Sensing of Environment, 56(1):42–51.

Colpitts, B. G. and Coleman, W. K. 1997. Complex permittivity of the potato leaf during imposed drought stress. IEEE Transactions on Geoscience and Remote Sensing, 35(4):1059–1064.

Colwell, J. E. 1974. Vegetation canopy reflectance. Remote Sensing of Environment, 3:175–183.

Cookmartin, G., Saich, P., Quegan, S., Cordey, R., Burgess-Allen, P., and Sowter, A. 2000. Modeling microwave interactions with crops and comparison with ERS-2 SAR observations. IEEE Transactions on Geoscience and Remote Sensing, 38(2):658–670.

Corwin, D. L. and Lesch, S. M. 2005. Apparent soil electrical conductivity measurements in agriculture. Computers and Electronics in Agriculture, 46(1-3):11–43.

Crow, W. T., Berg, A. A., Cosh, M. H., Loew, A., Mohanty, B. P., Panciera, R., de Rosnay, P., Ryu, D., and Walker, J. P. 2012. Upscaling sparse ground-based soil moisture observations for the validation of coarse-resolution satellite soil moisture products. Reviews of Geophysics, 50:20.

Das, N. N., Entekhabi, D., and Njoku, E. G. 2011. An algorithm for merging SMAP radiometer and radar data for high-resolution soil-moisture retrieval. IEEE Transactions on Geoscience and Remote Sensing, 49(5):1504–1512.

Davidson, M. W. J., Le Toan, T., Mattia, F., Satalino, G., Manninen, T., and Borgeaud, M. 2000. On the characterization of agricultural soil roughness for radar remote sensing studies. IEEE Transactions on Geoscience and Remote Sensing, 38(2):630–640.

de Jeu, R. A. M., Wagner, W., Holmes, T. R. H., Dolman, A. J., van de Giesen, N. C., and Friesen, J. 2008. Global soil moisture patterns observed by space borne microwave radiometers and scatterometers. Surveys in Geophysics, 29(4-5):399–420.

De Lannoy, G. J. M., Verhoest, N. E. C., Houser, P. R., Gish, T. J., and Van Meirvenne, M. 2006. Spatial and temporal characteristics of soil moisture in an intensively monitored agricultural field (OPE(3)). Journal of Hydrology, 331(3-4):719–730.

De Lannoy, G. J. M., Houser, P. R., Pauwels, V. R. N., and Verhoest, N. E. C. 2007. State and bias estimation for soil moisture profiles by an ensemble Kalman filter: Effect of assimilation depth and frequency. Water Resources Research, 43(6):15.

Dean, T. J., Bell, J. P., and Baty, A. J. B. 1987. Soil-moisture measurement by an improved capacitance technique.1. Sensor design and performance. Journal of Hydrology, 93(1-2):67–78.

Debye, P. 1929. *Polar molecules*. Reinhold, New York.

Del Frate, F., Ferrazzoli, P., Guerriero, L., Strozzi, T., Wegmüller, U., Cookmartin, G., and Quegan, S. 2004. Wheat cycle monitoring using radar data and a neural network trained by a model. IEEE Transactions on Geoscience and Remote Sensing, 42(1):35–44.

Della Vecchia, A., Ferrazzoli, P., and Guerriero, L. 2004. Modelling microwave scattering from long curved leaves. Waves in Random Media, 14(2):S333–S343.

Della Vecchia, A., Saleh, K., Ferrazzoli, P., Guerriero, L., and Wigneron, J. P. 2006. Simulating L-band emission of coniferous forests using a discrete model and a detailed geometrical representation. IEEE Geoscience and Remote Sensing Letters, 3(3):364–368.

Della Vecchia, A., Ferrazzoli, P., Wigneron, J. P., and Grant, J. P. 2007. Modeling forest emissivity at L-band and a comparison with multitemporal measurements. IEEE Geoscience and Remote Sensing Letters, 4(4):508–512.

Della Vecchia, A., Ferrazzoli, P., Guerriero, L., Ninivaggi, L., Strozzi, T., and Wegmüller, U. 2008. Observing and Modeling Multifrequency Scattering of Maize During the Whole Growth Cycle. IEEE Transactions on Geoscience and Remote Sensing, 46(11):3709–3718.

Dente, L., Satalino, G., Mattia, F., and Rinaldi, M. 2008. Assimilation of leaf area index derived from ASAR and MERIS data into CERES-Wheat model to map wheat yield. Remote Sensing of Environment, 112(4):1395–1407.

Deroin, J. P., Company, A., and Simonin, A. 1997. An empirical model for interpreting the relationship between backscattering and arid land surface roughness as seen with the SAR. IEEE Transactions on Geoscience and Remote Sensing, 35(1):86–92.

Desilets, D., Zreda, M., and Ferre, T. P. A. 2010. Nature's neutron probe: Land surface hydrology at an elusive scale with cosmic rays. Water Resources Research, 46:7.

Detar, W. R., Penner, J. V., and Funk, H. A. 2006. Airborne remote sensing to detect plant water stress in full canopy cotton. Transactions of the Asabe, 49(3):655–665.

Dobrowolski, J. A. 1995. Optical properties of films and coatings. In Bass, M., Van Stryland, E. W., Williams, D. R., and Wolfe, W. L., editors, *Handbook of Optics*, volume I, pages 42.41–42.130. McGraw-Hill, New York.

Dong, J., Zhuang, D. F., Huang, Y. H., and Fu, J. Y. 2009. Advances in multi-sensor data fusion: algorithms and applications. Sensors, 9(10):7771–7784.

Dorigo, W. A., Scipal, K., Parinussa, R. M., Liu, Y. Y., Wagner, W., de Jeu, R. A. M., and Naeimi, V. 2010. Error characterisation of global active and passive microwave soil moisture datasets. Hydrology and Earth System Sciences, 14(12):2605–2616.

Draper, C., Mahfouf, J. F., Calvet, J. C., Martin, E., and Wagner, W. 2011. Assimilation of ASCAT near- surface soil moisture into the SIM hydrological model over France. Hydrology and Earth System Sciences, 15(12):3829–3841.

Draper, C. S., Reichle, R. H., De Lannoy, G. J. M., and Liu, Q. 2012. Assimilation of passive and active microwave soil moisture retrievals. Geophysical Research Letters, 39:5.

Dubois, P. C., Vanzyl, J., and Engman, T. 1995. Measuring soil-moisture with imaging radars. IEEE Transactions on Geoscience and Remote Sensing, 33(4):915–926.

D'Urso, G. and Minacapilli, M. 2006. A semi-empirical approach for surface soil water content estimation from radar data without a-priori information on surface roughness. Journal of Hydrology, 321(1-4):297–310.

Dutt, S. K. and Gill, K. S. 1978. Diurnal changes in leaf water potential of rice, barley and wheat. Biologia Plantarum, 20(6):472–474.

Ehrler, W. L., Idso, S. B., Jackson, R. D., and Reginato, R. J. 1978. Diurnal changes in plant water potential and canopy temperature of wheat as affected by drought. Agronomy Journal, 70(6):999–1004.

Elliott, J. A., Cessna, A. J., Nicholaichuk, W., and Tollefson, L. C. 2000. Leaching rates and preferential flow of selected herbicides through tilled and untilled soil. Journal of Environmental Quality, 29(5):1650–1656.

Entekhabi, D., Njoku, E. G., O'Neill, P. E., Kellogg, K. H., Crow, W. T., Edelstein, W. N., Entin, J. K., Goodman, S. D., Jackson, T. J., Johnson, J., Kimball, J., Piepmeier, J. R., Koster, R. D., Martin, N., McDonald, K. C., Moghaddam, M., Moran, S., Reichle, R., Shi, J. C., Spencer, M. W., Thurman, S. W., Tsang, L., and Van Zyl, J. 2010. The Soil Moisture Active Passive (SMAP) mission. Proceedings of the IEEE, 98(5):704–716.

Eom, H. J. and Fung, A. K. 1984. A scatter model for vegetation up to Ku-band. Remote Sensing of Environment, 15(3):185–200.

Ernst, J. R., Holliger, K., Maurer, H., and Green, A. G. 2006. Realistic FDTD modelling of borehole georadar antenna radiation: Methodolgy and application. Near Surface Geophysics, 4(1):19–30.

Escorihuela, M. J., Kerr, Y. H., de Rosnay, P., Wigneron, J. P., Calvet, J. C., and Lemaitre, F. 2007. A simple model of the bare soil microwave emission at L-band. IEEE Transactions on Geoscience and Remote Sensing, 45:1978–1987.

Escorihuela, M. J., Chanzy, A., Wigneron, J. P., and Kerr, Y. H. 2010. Effective soil moisture sampling depth of L-band radiometry: A case study. Remote Sensing of Environment, 114(5):995–1001.

Famiglietti, J. S., Devereaux, J. A., Laymon, C. A., Tsegaye, T., Houser, P. R., Jackson, T. J., Graham, S. T., Rodell, M., and van Oevelen, P. J. 1999. Ground-based investigation of soil moisture variability within remote sensing footprints during the Southern Great Plains 1997 (SGP97) Hydrology Experiment. Water Resources Research, 35(6):1839–1851.

Famiglietti, J. S., Ryu, D. R., Berg, A. A., Rodell, M., and Jackson, T. J. 2008. Field observations of soil moisture variability across scales. Water Resources Research, 44(1):16.

FAO. 2011. Climate change, water and food security. FAO Water Report 36, Rome.

Fasbender, D., Peeters, L., Bogaert, P., and Dassargues, A. 2008. Bayesian data fusion applied to water table spatial mapping. Water Resources Research, 44(12):9.

Ferrazzoli, P. 2002. SAR for agriculture: Advances, problems and prospects. Proceedings of the Third International Symposium on Retrieval of Bio- and Geophysical Parameters from SAR Data for Land Applications. ESA Special Publications.

Ferrazzoli, P. and Guerriero, L. 1995. Radar sensitivity to tree geometry and woody volume - a model analysis. IEEE Transactions on Geoscience and Remote Sensing, 33(2):360–371.

Ferrazzoli, P. and Guerriero, L. 1996. Passive microwave remote sensing of forests: A model investigation. IEEE Transactions on Geoscience and Remote Sensing, 34(2):433–443.

Ferrazzoli, P., Paloscia, S., Pampaloni, P., Schiavon, G., Solimini, D., and Coppo, P. 1992. Sensitivity of microwave measurements to vegetation biomass and soil-moisture content - A case-study. IEEE Transactions on Geoscience and Remote Sensing, 30(4):750–756.

Ferrazzoli, P., Paloscia, S., Pampaloni, P., Schiavon, G., Sigismondi, S., and Solimini, D. 1997. The potential of multifrequency polarimetric SAR in assessing agricultural and arboreous biomass. IEEE Transactions on Geoscience and Remote Sensing, 35(1):5–17.

Forster, R., Martin, C., and Moore, R. 1991. Radar backscatter correlation with leaf water potential of water-stressed tomato canopies. In *IEEE International Symposium on Geoscience and Remote Sensing (IGARSS)*, pages 2269–2272.

Friedman, S. P. 2005. Soil properties influencing apparent electrical conductivity: a review. Computers and Electronics in Agriculture, 46(1-3):45–70.

Fung, A. K. 1994. *Microwave scattering and emission models and their applications*. Artech House, Boston.

Fung, A. K., Li, Z., and Chen, K. S. 1992. Backscattering from a randomly rough dielectric surface. IEEE Transactions on Geoscience and Remote Sensing, 30(2):356–369.

Galagedara, L. W., Redman, J. D., Parkin, G. W., Annan, A. P., and Endres, A. L. 2005. Numerical modeling of GPR to determine the direct ground wave sampling depth. Vadose Zone Journal, 4:1096–1106.

Garrido, F., Ghodrati, M., and Chendorain, M. 1999. Small-scale measurement of soil water content using a fiber optic sensor. Soil Science Society of America Journal, 63(6):1505–1512.

Giannopoulos, A. and Diamanti, N. 2008. Numerical modelling of ground-penetrating radar response from rough subsurface interfaces. Near Surface Geophysics, 6(6):357–369.

Gloaguen, E., Giroux, B., Marcotte, D., and Dimitrakopoulos, R. 2007. Pseudo-full-waveform inversion of borehole GPR data using stochastic tomography. Geophysics, 72(5):J43–J51.

Gomez-Dans, J. L., Quegan, S., and Bennett, J. C. 2006. Indoor C-band polarimetric interferometry observations of a mature wheat canopy. IEEE Transactions on Geoscience and Remote Sensing, 44(4):768–777.

Goovaerts, P. 1999. Geostatistics in soil science: state-of-the-art and perspectives. Geoderma, 89(1-2):1–45.

Govender, M., Dye, P. J., Weiersbye, I. M., Witkowski, E. T. F., and Ahmed, F. 2009. Review of commonly used remote sensing and ground-based technologies to measure plant water stress. Water SA, 35(5):741–752.

Grant, J. P., Van de Griend, A. A., Schwank, M., and Wigneron, J. P. 2009. Observations and modeling of a pine forest floor at L-band. IEEE Transactions on Geoscience and Remote Sensing, 47(7):2024–2034.

Greacen, E. L. 1981. Soil water assessment by the neutron method. CSIRO, Melbourne, Australia.

Grote, K., Hubbard, S., and Rubin, Y. 2003a. Field-scale estimation of volumetric water content using ground-penetrating radar ground wave techniques. Water Resources Research, 39(11):14.

Grote, K., Hubbard, S. S., and Rubin, Y. 2003b. Field-scale estimation of volumetric water content using GPR ground wave techniques. Water Resources Research, 39(11):1321, doi:1310.1029/2003WR002045.

Guglielmetti, M., Schwank, M., Mätzler, C., Oberdorster, C., Vanderborght, J., and Flühler, H. 2007. Measured microwave radiative transfer properties of a deciduous forest canopy. Remote Sensing of Environment, 109(4):523–532.

Guglielmetti, M., Schwank, M., Mätzler, C., Oberdorster, C., Vanderborght, J., and Flühler, H. 2008. FOSMEX: Forest soil moisture experiments with microwave radiometry. IEEE Transactions on Geoscience and Remote Sensing, 46(3):727–735.

Haack, B. N. and Khatiwada, G. 2010. Comparison and integration of optical and quadpolarization radar imagery for land cover/use delineation. Journal of Applied Remote Sensing, 4.

Hadria, R., Duchemin, B., Jarlan, L., Dedieu, G., Baup, F., Khabba, S., Olioso, A., and Le Toan, T. 2010. Potentiality of optical and radar satellite data at high spatio-temporal resolutions for the monitoring of irrigated wheat crops in Morocco. International Journal of Applied Earth Observation and Geoinformation, 12:S32–S37.

Heimovaara, T. J. and Bouten, W. 1990. A computer-controlled 36-channel time domain reflectometry system for monitoring soil-water contents. Water Resources Research, 26(10):2311–2316.

Hoekman, D. H. and Bouman, B. A. M. 1993. Interpretation of C-band and X-band radar images over an agricultural area, the Flevoland test site in the Agriscatt-87 campaign. International Journal of Remote Sensing, 14(8):1577–1594.

Hong, G., Zhang, Y., and Mercer, B. 2009. A wavelet and IHS integration method to fuse high resolution SAR with moderate resolution multispectral images. Photogrammetric Engineering and Remote Sensing, 75(10):1213–1223.

Hong, S. and Shin, I. 2011. A physically-based inversion algorithm for retrieving soil moisture in passive microwave remote sensing. Journal of Hydrology, 405(1-2):24–30.

Horgan, G. W., Glasbey, C. A., Soria, S. L., Gozalo, J. N. C., and Alonso, F. G. 1992. Land-use classification in central Spain using SIR-A and MSS imagery. International Journal of Remote Sensing, 13(15):2839–2848.

Hornbuckle, B. K. and England, A. W. 2004. Radiometric sensitivity to soil moisture at 1.4 GHz through a corn crop at maximum biomass. Water Resources Research, 40(10).

Hornbuckle, B. K., England, A. W., De Roo, R. D., Fischman, M. A., and Boprie, D. L. 2003. Vegetation canopy anisotropy at 1.4 GHz. IEEE Transactions on Geoscience and Remote Sensing, 41(10):2211–2223.

Huang, S. L., Potter, C., Crabtree, R. L., Hager, S., and Gross, P. 2010. Fusing optical and radar data to estimate sagebrush, herbaceous, and bare ground cover in Yellowstone. Remote Sensing of Environment, 114(2):251–264.

Huisman, J. A., Sperl, C., Bouten, W., and Verstraten, J. M. 2001. Soil water content measurements at different scales: accuracy of time domain reflectometry and ground penetrating radar. Journal of Hydrology, 245:48–58.

Huisman, J. A., Snepvangers, J. J. J. C., Bouten, W., and Heuvelink, G. B. M. 2002. Mapping spatial variation in surface soil water content: comparison of ground-penetrating radar and time domain reflectometry. Journal of Hydrology, 269:194–207.

Huisman, J. A., Hubbard, S. S., Redman, J. D., and Annan, A. P. 2003a. Measuring soil water content with ground penetrating radar: A review. Vadose Zone Journal, 2:476–491.

Huisman, J. A., Snepvangers, J. J. J. C., Bouten, W., and Heuvelink, G. B. M. 2003b. Monitoring temporal development of spatial soil water content variation: Comparison of ground penetrating radar and time domain reflectometry. Vadose Zone Journal, 2:519–529.

Hunt, E. R., Li, L., Yilmaz, M. T., and Jackson, T. J. 2011. Comparison of vegetation water contents derived from shortwave-infrared and passive-microwave sensors over central Iowa. Remote Sensing of Environment, 115(9):2376–2383.

Hüppi, R. 1987. *RASAM: A radiometer-scatterometer to measure microwave signatures of soil, vegetation and snow*. Ph.D. thesis, University of Bern.

Huyer, W. and Neumaier, A. 1999. Global optimization by multilevel coordinate search. Journal of Global Optimization, 14(4):331–355.

Jabro, J. D., Sainju, U. M., Stevens, W. B., Lenssen, A. W., and Evans, R. G. 2009. Long-term tillage influences on soil physical properties under dryland conditions in northeastern Montana. Archives of Agronomy and Soil Science, 55(6):633–640.

Jackson, T. J. 1993. Measuring surface soil-moisture using passive microwave remote-sensing. Hydrological Processes, 7(2):139–152.

Jackson, T. J. and O'Neill, P. E. 1990. Attenuation of soil microwave emission by corn and soybeans at 1.4 GHz and 5 GHz. IEEE Transactions on Geoscience and Remote Sensing, 28(5):978–980.

Jackson, T. J. and Schmugge, T. J. 1989. Passive microwave remote-sensing system for soil-moisture - Some supporting research. IEEE Transactions on Geoscience and Remote Sensing, 27(2):225–235.

Jackson, T. J. and Schmugge, T. J. 1991. Vegetation effects on the microwave emission of soils. Remote Sensing of Environment, 36(3):203–212.

Jackson, T. J., Schmugge, T. J., and Wang, J. R. 1982. Passive microwave sensing of soil-moisture under vegetation canopies. Water Resources Research, 18(4):1137–1142.

Jackson, T. J., Le Vine, D. M., Swift, C. T., Schmugge, T. J., and Schiebe, F. R. 1995. Large-area mapping of soil-moisture using the ESTAR passive microwave radiometer in Washita92. Remote Sensing of Environment, 54(1):27–37.

Jackson, T. J., Schmugge, J., and Engman, E. T. 1996. Remote sensing applications to hydrology: soil moisture. Hydrological Sciences, 41((4)):517–530.

Jadoon, K., Slob, E., Vanclooster, M., Vereecken, H., and Lambot, S. 2008. Uniqueness and stability analysis of hydrogeophysical inversion for time-lapse ground penetrating radar estimates of shallow soil hydraulic properties. Water Resources Research, (44):W09421, doi:09410.01029/02007WR006639.

Jadoon, K. Z., Lambot, S., Slob, E. C., and Vereecken, H. 2011. Analysis of horn antenna transfer functions and phase-center position for modeling off-ground GPR. IEEE Transactions on Geoscience and Remote Sensing, 49(5):1649–1662.

Jester, W. and Klik, A. 2005. Soil surface roughness measurement - methods, applicability, and surface representation. Catena, 64(2-3):174–192.

Jiang, L. M., Shi, J. C., Tjuatja, S. B., Dozier, J., Chen, K. S., and Zhang, L. X. 2007. A parameterized multiple-scattering model for microwave emission from dry snow. Remote Sensing of Environment, 111(2-3):357–366.

Jin, Y. Q. and Huang, X. Z. 1996. Correlation of temporal variations of active and passive microwave signatures from vegetation canopy. IEEE Transactions on Geoscience and Remote Sensing, 34(1):257–263.

Jin, Y. Q. and Liu, C. 1997. Biomass retrieval from high-dimensional active/passive remote sensing data by using artificial neural networks. International Journal of Remote Sensing, 18(4):971–979.

Jonard, F., André, F., Ponette, Q., Vincke, C., and Jonard, M. 2011a. Sap flux density and stomatal conductance of European beech and common oak trees in pure and mixed stands during the summer drought of 2003. Journal of Hydrology, 409:371–381.

Jonard, F., Weihermüller, L., Jadoon, K. Z., Schwank, M., Vereecken, H., and Lambot, S. 2011b. Mapping field-scale soil moisture with L-band radiometer and ground-penetrating radar over bare soil. IEEE Transactions on Geoscience and Remote Sensing, 49(8):2863–2875.

Jonard, F., Weihermüller, L., Vereecken, H., and Lambot, S. 2012. Accounting for soil surface roughness in the inversion of ultrawideband off-ground GPR signal for soil moisture retrieval. Geophysics, 77(1):H1–H7.

Jones, M. O., Jones, L. A., Kimball, J. S., and McDonald, K. C. 2011. Satellite passive microwave remote sensing for monitoring global land surface phenology. Remote Sensing of Environment, 115(4):1102–1114.

Joseph, A. T., van der Velde, R., O'Neill, P. E., Lang, R. H., and Gish, T. 2008. Soil moisture retrieval during a corn growth cycle using L-band (1.6 GHz) radar observations. IEEE Transactions on Geoscience and Remote Sensing, 46(8):2365–2374.

Joseph, A. T., van der Velde, R., O'Neill, P. E., Choudhury, B. J., Lang, R. H., Kim, E. J., and Gish, T. 2010a. L-band brightness temperature observations over a corn canopy during the entire growth cycle. Sensors, 10(7):6980–7001.

Joseph, A. T., van der Velde, R., O'Neill, P. E., Lang, R., and Gish, T. 2010b. Effects of corn on C- and L-band radar backscatter: A correction method for soil moisture retrieval. Remote Sensing of Environment, 114(11):2417–2430.

Karam, M. A. and Fung, A. K. 1989. Leaf-shape effects in electromagnetic-wave scattering from vegetation. IEEE Transactions on Geoscience and Remote Sensing, 27(6):687–697.

Karam, M. A., Fung, A. K., Lang, R. H., and Chauhan, N. S. 1992. A Microwave-Scattering Model for Layered Vegetation. IEEE Transactions on Geoscience and Remote Sensing, 30(4):767–784.

Kemna, A., Binley, A., Ramirez, A., and Daily, W. 2000. Complex resistivity tomography for environmental applications. Chemical Engineering Journal, 77(1-2):11–18.

Kerr, Y. H., Waldteufel, P., Wigneron, J. P., Delwart, S., Cabot, F., Boutin, J., Escorihuela, M. J., Font, J., Reul, N., Gruhier, C., Juglea, S. E., Drinkwater, M. R., Hahne, A., Martin-Neira, M., and Mecklenburg, S. 2010. The SMOS mission: New tool for monitoring key elements of the global water cycle. Proceedings of the IEEE, 98(5):666–687.

Kerr, Y. H., Waldteufel, P., Richaume, P., Wigneron, J. P., Ferrazzoli, P., Mahmoodi, A., Al Bitar, A., Cabot, F., Gruhier, C., Juglea, S. E., Leroux, D., Mialon, A., and Delwart, S. 2012. The SMOS Soil Moisture Retrieval Algorithm. IEEE Transactions on Geoscience and Remote Sensing, 50(5):1384–1403.

Kirdyashev, K. P., Chukhlantsev, A. A., and Shutko, A. M. 1979. Microwave radiation of grounds with vegetative cover. Radiotekhnika I Elektronika, 24(2):256–264.

Kong, J. A. 1990. *Electromagnetic wave theory*. Second edition, Wiley, New York.

Kosutic, S., Husnjak, S., Filipovic, D., and Bogunovic, M. 2001. Influence of different tillage systems on soil water availability in the Ap-horizon of an Albic Luvisol and yield in north-west Slavonia, Croatia. Bodenkultur, 52(3):215–223.

Kovar, J. L., Barber, S. A., Kladivko, E. J., and Griffith, D. R. 1992. Characterization of soil-temperature, water-content, and maize root distribution in 2 tillage systems. Soil Tillage Research, 24(1):11–27.

Kulasekera, P. B., Parkin, G. W., and von Bertoldi, P. 2011. Using soil water content sensors to characterize tillage effects on preferential flow. Vadose Zone Journal, 10(2):683–696.

Kurum, M., Lang, R. H., O'Neill, P. E., Joseph, A. T., Jackson, T. J., and Cosh, M. H. 2009. L-band radar estimation of forest attenuation for active/passive soil moisture inversion. IEEE Transactions on Geoscience and Remote Sensing, 47(9):3026–3040.

Lagarias, J. C., Reeds, J. A., Wright, M. H., and Wright, P. E. 1998. Convergence properties of the Nelder-Mead simplex method in low dimensions. Siam Journal on Optimization, 9(1):112–147.

Lambot, S. and André, F. 2012. Full-wave modeling of near-field radar data to reconstruct planar layered media. IEEE Transactions on Geoscience and Remote Sensing, Submitted.

Lambot, S., Javaux, M., Hupet, F., and Vanclooster, M. 2002. A global multilevel coordinate search procedure for estimating the unsaturated soil hydraulic properties. Water Resources Research, 38(11):1224, doi:1210.1029/2001WR001224.

Lambot, S., Antoine, M., van den Bosch, I., Slob, E. C., and Vanclooster, M. 2004a. Electromagnetic inversion of GPR signals and subsequent hydrodynamic inversion to estimate effective vadose zone hydraulic properties. Vadose Zone Journal, 3(4):1072–1081.

Lambot, S., Slob, E. C., van den Bosch, I., Stockbroeckx, B., Scheers, B., and Vanclooster, M. 2004b. Estimating soil electric properties from monostatic ground-penetrating radar signal inversion in the frequency domain. Water Resources Research, 40:W04205, doi:04210.01029/02003WR002095.

Lambot, S., Slob, E. C., van den Bosch, I., Stockbroeckx, B., and Vanclooster, M. 2004c. Modeling of ground-penetrating radar for accurate characterization of subsurface electric properties. IEEE Transactions on Geoscience and Remote Sensing, 42:2555–2568.

Lambot, S., Antoine, M., Vanclooster, M., and Slob, E. C. 2006a. Effect of soil roughness on the inversion of off-ground monostatic GPR signal for noninvasive quantification of soil properties. Water Resources Research, 42:W03403, doi:03410.01029/02005WR004416.

Lambot, S., Slob, E. C., Vanclooster, M., and Vereecken, H. 2006b. Closed loop GPR data inversion for soil hydraulic and electric property determination. Geophysical Research Letters, 33:L21405, doi:21410.21029/22006GL027906.

Lambot, S., Weihermüller, L., Huisman, J. A., Vereecken, H., Vanclooster, M., and Slob, E. C. 2006c. Analysis of air-launched ground-penetrating radar techniques to measure the soil surface water content. Water Resources Research, 42:W11403, doi:11410.11029/12006WR005097.

Lambot, S., Slob, E., and Vereecken, H. 2007. Fast evaluation of zero-offset Green's function for layered media with application to ground-penetrating radar. Geophysical Research Letters, 34:L21405, doi:21410.21029/22007GL031459.

Lambot, S., Binley, A., Slob, E., and Hubbard, S. 2008a. Ground penetrating radar in hydrogeophysics. Vadose Zone Journal, 7(1):137–139, doi: 110.2136/vzj2007.0180.

Lambot, S., Slob, E., Chavarro, D., Lubczynski, M., and Vereecken, H. 2008b. Measuring soil surface water content in irrigated areas of southern Tunisia using full-waveform inversion of proximal GPR data. Near Surface Geophysics, 6:403–410.

Lambot, S., André, F., Slob, E. C., and Vereecken, H. 2012. Effect of antenna-medium coupling in the analysis of ground-penetrating radar data. Near Surface Geophysics, In Press.

Landron, O., Feuerstein, M. J., and Rappaport, T. S. 1996. A comparison of theoretical and empirical reflection coefficients for typical exterior wall surfaces in a mobile radio environment. IEEE Transactions on Antennas and Propagation, 44(3):341–351.

Larson, K. M., Small, E. E., Gutmann, E. D., Bilich, A. L., Braun, J. J., and Zavorotny, V. U. 2008. Use of GPS receivers as a soil moisture network for water cycle studies. Geophysical Research Letters, 35(24):5.

Lawrence, H., Demontoux, F., Wigneron, J. P., Paillou, P., Wu, T. D., and Kerr, Y. H. 2011. Evaluation of a numerical modeling approach based on the finite-element method for calculating the rough surface scattering and emission of a soil layer. IEEE Geoscience and Remote Sensing Letters, 8(5):953–957.

Le Hegarat-Mascle, S., Quesney, A., Vidal-Madjar, D., Taconet, O., Normand, M., and Loumagne, C. 2000. Land cover discrimination from multitemporal ERS images and multispectral Landsat images: a study case in an agricultural area in France. International Journal of Remote Sensing, 21(3):435–456.

Le Vine, D. M. and Karam, M. A. 1996. Dependence of attenuation in a vegetation canopy on frequency and plant water content. IEEE Transactions on Geoscience and Remote Sensing, 34(5):1090–1096.

Ledieu, J., De Ridder, P., De Clercq, P., and Dautrebande, S. 1986. A method of measuring soil moisture by time domain reflectometry. Journal of Hydrology, 88:319–328.

Li, Y., Zhang, L., Jiang, L., Zhang, Z., and Zhao, T. 2010. Evaluation of vegetation indices based on microwave data by simulation and measurements. In *IEEE International Symposium on Geoscience and Remote Sensing (IGARSS)*, pages 3311–3314.

Lievens, H., Verhoest, N. E. C., De Keyser, E., Vernieuwe, H., Matgen, P., Alvarez-Mozos, J., and De Baets, B. 2011. Effective roughness modelling as a tool for soil moisture retrieval from C-and L-band SAR. Hydrology and Earth System Sciences, 15(1):151–162.

Liu, L. Y., Wang, J. J., Bao, Y. S., Huang, W. J., Ma, Z. H., and Zhao, C. J. 2006. Predicting winter wheat condition, grain yield and protein content using multi-temporal EnviSat-ASAR and Landsat TM satellite images. International Journal of Remote Sensing, 27(4):737–753.

Liu, S. F., Liou, Y. A., Wang, W. J., Wigneron, J. P., and Lee, J. B. 2002. Retrieval of crop biomass and soil moisture from measured 1.4 and 10.65 GHz brightness temperatures. IEEE Transactions on Geoscience and Remote Sensing, 40(6):1260–1268.

Lopez-Sanchez, J. M. and Ballester-Berman, J. D. 2009. Potentials of polarimetric SAR interferometry for agriculture monitoring. Radio Science, 44.

Lu, D. S. 2006. The potential and challenge of remote sensing-based biomass estimation. International Journal of Remote Sensing, 27(7):1297–1328.

Macelloni, G., Paloscia, S., Pampaloni, P., and Ruisi, R. 2001. Airborne multifrequency L- to Ka-band radiometric measurements over forests. IEEE Transactions on Geoscience and Remote Sensing, 39(11):2507–2513.

Mahboubi, A. A., Lal, R., and Faussey, N. R. 1993. 28 years of tillage effects on 2 soils in Ohio. Soil Science Society of America Journal, 57(2):506–512.

Maity, S., Patnaik, C., Chakraborty, M., and Panigrahy, S. 2004. Analysis of temporal backscattering of cotton crops using a semiempirical model. IEEE Transactions on Geoscience and Remote Sensing, 42(3):577–587.

Mangiarotti, S., Mazzega, P., Jarlan, L., Mougin, E., Baup, F., and Demarty, J. 2008. Evolutionary bi-objective optimization of a semi-arid vegetation dynamics model with NDVI and sigma(0) satellite data. Remote Sensing of Environment, 112(4):1365–1380.

Marliani, F., Paloscia, S., Pampaloni, P., and Kong, J. A. 2002. Simulating coherent backscattering from crops during the growing cycle. IEEE Transactions on Geoscience and Remote Sensing, 40(1):162–177.

Marquardt, D. W. 1963. An algorithm for least-squares estimation of nonlinear parameters. Journal of the Society for Industrial and Applied Mathematics, 11:431–441.

Martin, R. D., Asrar, G., and Kanemasu, E. T. 1989. C-band scatterometer measurements of a tallgrass prairie. Remote Sensing of Environment, 29(3):281–292.

Mattia, F. and Le Toan, T. 1999. Backscattering properties of multi-scale rough surfaces. Journal of Electromagnetic Waves and Applications, 13(4):493–527.

Mattia, F., Le Toan, T., Picard, G., Posa, F. I., D'Alessio, A., Notarnicola, C., Gatti, A. M., Rinaldi, M., Satalino, G., and Pasquariello, G. 2003. Multitemporal C-band radar measurements on wheat fields. IEEE Transactions on Geoscience and Remote Sensing, 41(7):1551–1560.

Mätzler, C. 1990. Seasonal evolution of microwave-radiation from an oat field. Remote Sensing of Environment, 31(3):161–173.

Mätzler, C. 1994a. Microwave (1-100 GHz) dielectric model of leaves. IEEE Transactions on Geoscience and Remote Sensing, 32(4):947–949.

Mätzler, C. 1994b. Passive microwave signatures of landscapes in winter. Meteorology and Atmospheric Physics, 54(1-4):241–260.

Mätzler, C. 2006. *Thermal microwave radiation: Applications for remote sensing*. IET Electromagnetic Waves series 52. The Institution of Engeneering and Technology, London.

Mätzler, C. and Standley, A. 2000. Relief effects for passive microwave remote sensing. International Journal of Remote Sensing, 21(12):2403–2412.

Mätzler, C., Weber, D., Wuthrich, M., Schneeberger, K., Stamm, C., Wydler, H., and Flühler, H. 2003. ELBARA, the ETH L-band radiometer for soil-moisture research. In *IEEE International Symposium on Geoscience and Remote Sensing (IGARSS)*, pages 3058–3060.

McNairn, H. and Brisco, B. 2004. The application of C-band polarimetric SAR for agriculture: a review. Canadian Journal of Remote Sensing, 30(3):525–542.

McNairn, H., van der Sanden, J. J., Brown, R. J., and Ellis, J. 2000. The potential of RADARSAT-2 for crop mapping and assessing crop condition. In *Second International Conference on Geospatial Information in Agriculture and Forestry*. Lake Buena Vista, Florida.

McNairn, H., Shang, J. L., Jiao, X. F., and Champagne, C. 2009. The contribution of ALOS PALSAR multipolarization and polarimetric data to crop classification. IEEE Transactions on Geoscience and Remote Sensing, 47(12):3981–3992.

McNeill, J. D. 1980. Electromagnetic terrain conductivity measurement at low induction numbers. Technical Note TN-6, Geonics Limited, Ontario.

Mialon, A., Wigneron, J. P., de Rosnay, P., Escorihuela, M. J., and Kerr, Y. H. 2012. Evaluating the L-MEB model from long-term microwave measurements over a rough field, SMOSREX 2006. IEEE Transactions on Geoscience and Remote Sensing, 50(5):1458–1467.

Michalski, K. A. and Mosig, J. R. 1997. Multilayered media Green's functions in integral equation formulations. IEEE Transactions on Antennas and Propagation, 45(3):508–519.

Michelson, D. B., Liljeberg, B. M., and Pilesjo, P. 2000. Comparison of algorithms for classifying Swedish landcover using Landsat TM and ERS-1 SAR data. Remote Sensing of Environment, 71(1):1–15.

Michot, D., Benderitter, Y., Dorigny, A., Nicoullaud, B., King, D., and Tabbagh, A. 2003. Spatial and temporal monitoring of soil water content with an irrigated corn crop cover using surface electrical resistivity tomography. Water Resources Research, 39(5):20.

Minet, J. 2011. *High resolution soil moisture mapping by a proximal ground penetrating radar - A numerical, laboratory and field evaluation*. Ph.D. thesis, Université catholique de Louvain, Belgium.

Minet, J., Lambot, S., Slob, E. C., and Vanclooster, M. 2010. Soil surface water content estimation by full-waveform GPR signal inversion in the presence of thin layers. IEEE Transactions on Geoscience and Remote Sensing, 48(3):1138–1150.

Minet, J., Wahyudi, A., Bogaert, P., Vanclooster, M., and Lambot, S. 2011. Mapping shallow soil moisture profiles at the field scale using full-waveform inversion of ground penetrating radar data. Geoderma, 161(3-4):225–237.

Minet, J., Bogaert, P., Vanclooster, M., and Lambot, S. 2012. Validation of ground penetrating radar full-waveform inversion for field scale soil moisture mapping. Journal of Hydrology, 424-425(0):112–123.

Mittelbach, H., Casini, F., Lehner, I., Teuling, A. J., and Seneviratne, S. I. 2011. Soil moisture monitoring for climate research: Evaluation of a low-cost sensor in the framework of the Swiss Soil Moisture Experiment (SwissSMEX) campaign. Journal of Geophysical Research-Atmospheres, 116:11.

Mo, T. and Schmugge, T. J. 1987. A parameterization of the effect of surface-roughness on microwave emission. IEEE Transactions on Geoscience and Remote Sensing, 25(4):481–486.

Mo, T., Schmugge, T. J., and Wang, J. R. 1987. Calculations of the microwave brightness temperature of rough soil surfaces: Bare field. IEEE Transactions on Geoscience and Remote Sensing, 25(1):47–54.

Monerris, A., Benedicto, P., Vall-Ilossera, M., Camps, A., Santanach, E., Piles, M., and Prehn, R. 2008. Assessment of the topography impact on microwave radiometry at L-band. Journal of Geophysical Research-Solid Earth, 113(B12):9.

Montzka, C., Moradkhani, H., Weihermüller, L., Hendricks Franssen, H.-J., Canty, M., and Vereecken, H. 2011. Hydraulic parameter estimation by remotely-sensed top soil moisture observations with the particle filter. Journal of Hydrology, 399(2011):410–421.

Montzka, C., Bogena, H., Weihermüller, L., Jonard, F., Bouzinac, C., Kainulainen, J., Balling, J. E., Loew, A., dall Amico, J., Rouhe, E., Vanderborght, J., and Vereecken, H. 2012. Brightness temperature and soil moisture validation at different scales during the SMOS validation campaign in the Rur and Erft catchments, Germany. IEEE Transactions on Geoscience and Remote Sensing, In Press.

Moran, M. S., Pinter, P. J., Clothier, B. E., and Allen, S. G. 1989. Effect of water-stress on the canopy architecture and spectral indexes of irrigated alfalfa. Remote Sensing of Environment, 29(3):251–261.

Moran, M. S., Vidal, A., Troufleau, D., Qi, J., Clarke, T. R., Pinter, P. J., Mitchell, T. A., Inoue, Y., and Neale, C. M. U. 1997. Combining multifrequency microwave and optical data for crop management. Remote Sensing of Environment, 61(1):96–109.

Moran, M. S., Peters-Lidard, C. D., Watts, J. M., and McElroy, S. 2004. Estimating soil moisture at the watershed scale with satellite-based radar and land surface models. Canadian Journal of Remote Sensing, 30(5):805–826.

Moskal, L. M. and Zheng, G. 2009. Retrieving leaf area index (LAI) using remote sensing: Theories, methods and sensors. Sensors, 9(4):2719–2745.

Müller, M., Kurz, G., and Yaramanci, U. 2009. Influence of tillage methods on soil water content and geophysical properties. Near Surface Geophysics, 7(1):27–36.

Myneni, R. B. and Choudhury, B. J. 1993. Synergistic use of optical and microwave data in agrometeorological applications. Advances in Space Research, 13(5):239–248.

Naujoks, M., Kroner, C., Weise, A., Jahr, T., Krause, P., and Eisner, S. 2010. Evaluating local hydrological modelling by temporal gravity observations and a gravimetric three-dimensional model. Geophysical Journal International, 182(1):233–249.

Ndiaye, B., Molenat, J., Hallaire, V., Gascuel, C., and Hamon, Y. 2007. Effects of agricultural practices on hydraulic properties and water movement in soils in Brittany (France). Soil Tillage Research, 93(2):251–263.

Nelson, S. O. 1991. Dielectric-properties of agricultural products - Measurements and applications. IEEE Transactions on Electrical Insulation, 26(5):845–869.

Njoku, E. G. and Entekhabi, D. 1996. Passive microwave remote sensing of soil moisture. Journal of Hydrology, 184(1-2):101–129.

Njoku, E. G., Wilson, W. J., Yueh, S. H., and Rahmat-Samii, Y. 2000. A large-antenna microwave radiometer-scatterometer concept for ocean salinity and soil moisture sensing. IEEE Transactions on Geoscience and Remote Sensing, 38(6):2645–2655.

Njoku, E. G., Jackson, T. J., Lakshmi, V., Chan, T. K., and Nghiem, S. V. 2003. Soil moisture retrieval from AMSR-E. IEEE Transactions on Geoscience and Remote Sensing, 41(2):215–229.

Noborio, K. 2001. Measurement of soil water content and electrical conductivity by time domain reflectometry: a review. Computers and Electronics in Agriculture, 31:213–237.

Oh, Y., Sarabandi, K., and Ulaby, F. T. 1992. An empirical-model and an inversion technique for radar scattering from bare soil surfaces. IEEE Transactions on Geoscience and Remote Sensing, 30(2):370–381.

Oleschko, K., Korvin, G., Munoz, A., Velazquez, J., Miranda, M. E., Carreon, D., Flores, L., Martinez, M., Velasquez-Valle, M., Brambila, F., Parrot, J. F., and Ronquillo, G. 2008. Mapping soil fractal dimension in agricultural fields with GPR. Nonlinear Processes in Geophysics, 15(5):711–725.

Olsson, K. A. and Milthorpe, F. L. 1983. Diurnal and spatial variation in leaf water potential and leaf conductance of irrigated peach-trees. Australian Journal of Plant Physiology, 10(3):291–298.

O'Neill, P. E., Chauhan, N. S., and Jackson, T. J. 1996. Use of active and passive microwave remote sensing for soil moisture estimation through corn. International Journal of Remote Sensing, 17(10):1851–1865.

Oza, S. R., Panigrally, S., and Parihar, J. S. 2008. Concurrent use of active and passive microwave remote sensing data for monitoring of rice crop. International Journal of Applied Earth Observation and Geoinformation, 10(3):296–304.

Paloscia, S. 1998. An empirical approach to estimating leaf area index from multifrequency SAR data. International Journal of Remote Sensing, 19(2):361–366.

Paloscia, S. and Pampaloni, P. 1984. Microwave remote-sensing of plant water-stress. Remote Sensing of Environment, 16(3):249–255.

Paloscia, S. and Pampaloni, P. 1988. Microwave polarization index for monitoring vegetation growth. IEEE Transactions on Geoscience and Remote Sensing, 26(5):617–621.

Panciera, R., Walker, J. P., Kalma, J. D., Kim, E. J., Saleh, K., and Wigneron, J. P. 2009. Evaluation of the SMOS L-MEB passive microwave soil moisture retrieval algorithm. Remote Sensing of Environment, 113(2):435–444.

Paris, J. F. 1983. Radar backscattering properties of corn and soybeans at frequencies of 1.6, 4.75, and 13.3 GHz. IEEE Transactions on Geoscience and Remote Sensing, 21(3):392–400.

Paris, J. F. 1986. The effect of leaf size on the microwave backscattering by corn. Remote Sensing of Environment, 19(1):81–95.

Pauwels, V. R. N., Hoeben, R., Verhoest, N. E. C., De Troch, F. P., and Troch, P. A. 2002. Improvement of TOPLATS-based discharge predictions through assimilation of ERS-based remotely sensed soil moisture values. Hydrological Processes, 16(5):995–1013.

Pellarin, T., Wigneron, J. P., Calvet, J. C., Berger, M., Douville, H., Ferrazzoli, P., Kerr, Y. H., Lopez-Baeza, E., Pulliainen, J., Simmonds, L. P., and Waldteufel, P. 2003. Two-year global simulation of L-band brightness temperatures over land. IEEE Transactions on Geoscience and Remote Sensing, 41(9):2135–2139.

Pellerin, L. 2002. Applications of electrical and electromagnetic methods for environmental and geotechnical investigations. Surveys in Geophysics, 23(2-3):101–132.

Picard, G., Le Toan, T., and Mattia, F. 2003. Understanding C-band radar backscatter from wheat canopy using a multiple-scattering coherent model. IEEE Transactions on Geoscience and Remote Sensing, 41(7):1583–1591.

Pierdicca, N., Pulvirenti, L., and Marzano, F. S. 2010. Simulating topographic effects on spaceborne radiometric observations between L and X frequency bands. IEEE Transactions on Geoscience and Remote Sensing, 48(1):273–282.

Piles, M., Entekhabi, D., and Camps, A. 2009. A Change Detection Algorithm for Retrieving High-Resolution Soil Moisture From SMAP Radar and Radiometer Observations. IEEE Transactions on Geoscience and Remote Sensing, 47(12):4125–4131.

Pinel, N., Bourlier, C., and Saillard, J. 2007. Forward radar propagation over oil slicks on sea surfaces using the Ament model with shadowing effect. Progress in Electromagnetics Research-Pier, 76:95–126.

Pinter, P. J., Hatfield, J. L., Schepers, J. S., Barnes, E. M., Moran, M. S., Daughtry, C. S. T., and Upchurch, D. R. 2003. Remote sensing for crop management. Photogrammetric Engineering and Remote Sensing, 69(6):647–664.

Pohl, C. and van Genderen, J. L. 1998. Multisensor image fusion in remote sensing: concepts, methods and applications. International Journal of Remote Sensing, 19(5):823–854.

Prasad, R. 2009. Retrieval of crop variables with field-based X-band microwave remote sensing of ladyfinger. Advances in Space Research, 43(9):1356–1363.

Prevot, L., Dechambre, M., Taconet, O., Vidalmadjar, D., Normand, M., and Galle, S. 1993. Estimating the characteristics of vegetation canopies with airborne radar measurements. International Journal of Remote Sensing, 14(15):2803–2818.

Pulliainen, J. and Hallikainen, M. 2001. Retrieval of regional snow water equivalent from space-borne passive microwave observations. Remote Sensing of Environment, 75(1):76–85.

Pulvirenti, L., Pierdicca, N., and Marzano, F. S. 2011. Prediction of the error induced by topography in satellite microwave radiometric observations. IEEE Transactions on Geoscience and Remote Sensing, 49(9):3180–3188.

Quesney, A., Le Hegarat-Mascle, S., Taconet, O., Vidal-Madjar, D., Wigneron, J. P., Loumagne, C., and Normand, M. 2000. Estimation of watershed soil moisture index from ERS/SAR data. Remote Sensing of Environment, 72(3):290–303.

Rasmy, M., Koike, T., Boussetta, S., Lu, H., and Li, X. 2011. Development of satellite land data assimilation system coupled with mesoscale model in the Tibetan plateau. IEEE Transactions on Geoscience and Remote Sensing, 49(8):2847–2863.

Rautiainen, K., Lemmetyinen, J., Pulliainen, J., Vehvilainen, J., Drusch, M., Kontu, A., Kainulainen, J., and Seppanen, J. 2012. L-Band Radiometer Observations of Soil Processes in Boreal and Subarctic Environments. IEEE Transactions on Geoscience and Remote Sensing, 50(5):1483–1497.

Reedy, R. C. and Scanlon, B. R. 2003. Soil water content monitoring using electromagnetic induction. Journal of Geotechnical and Geoenvironmental Engineering, 129(11):1028–1039.

Reichle, R. H. 2008. Data assimilation methods in the Earth sciences. Advances in Water Resources, 31(11):1411–1418.

Reichle, R. H., Crow, W. T., Koster, R. D., Sharif, H. O., and Mahanama, S. P. P. 2008. Contribution of soil moisture retrievals to land data assimilation products. Geophysical Research Letters, 35(1):6.

Rhoades, J. D., Raats, P. A. C., and Prather, R. J. 1976. Effects of liquid-phase electrical conductivity, water content, and surface conductivity on bulk soil electrical conductivity. Soil Science Society of America Journal, 40:651–655.

Richard, G., Rouveure, R., Chanzy, A., Faure, P., Chanet, M., Marionneau, A., Regnier, P., and Duval, Y. 2010. Using proximal sensors to continuously monitor agricultural soil physical conditions for tillage management. In *Proximal Soil Sensing*, Progress in Soil Science, pages 313–321. Springer, Dordrecht.

Ritsema, C. J., Kuipers, H., Kleiboer, L., van den Elsen, E., Oostindie, K., Wesseling, J. G., Wolthuis, J. W., and Havinga, P. 2009. A new wireless underground network system for continuous monitoring of soil water contents. Water Resources Research, 45:9.

Robinson, D. A., Jones, S. B., Wraith, J. M., Or, D., and Friedman, S. P. 2003. A review of advances in dielectric and electrical conductivity measurement in soils using time domain reflectometry. Vadose Zone Journal, 2:444–475.

Robinson, D. A., Schaap, M. G., Or, D., and Jones, S. B. 2005. On the effective measurement frequency of time domain reflectometry in dispersive and nonconductive dielectric materials. Water Resources Research, 41(2):9.

Robinson, D. A., Binley, A., Crook, N., Day-Lewis, F. D., Ferre, T. P. A., Grauch, V. J. S., Knight, R., Knoll, M., Lakshmi, V., Miller, R., Nyquist, J., Pellerin, L., Singha, K., and Slater, L. 2008a. Advancing process-based watershed hydrological research using near-surface geophysics: a vision for, and review of, electrical and magnetic geophysical methods. Hydrological Processes, 22(18):3604–3635.

Robinson, D. A., Campbell, C. S., Hopmans, J. W., Hornbuckle, B. K., Jones, S. B., Knight, R., Ogden, F., Selker, J., and Wendroth, O. 2008b. Soil moisture measurement for ecological and hydrological watershed-scale observatories: A review. Vadose Zone Journal, 7(1):358–389.

Roisin, C. J. C. 2007. A multifractal approach for assessing the structural state of tilled soils. Soil Science Society of America Journal, 71(1):15–25.

Rosenbaum, U., Huisman, J. A., Weuthen, A., Vereecken, H., and Bogena, H. R. 2010. Sensor-to-sensor variability of the ECH(2)O EC-5, TE, and 5TE sensors in dielectric liquids. Vadose Zone Journal, 9(1):181–186.

Rosenthal, W. D., Blanchard, B. J., and Blanchard, A. J. 1985. Visible infrared microwave agriculture classification, biomass, and plant height algorithms. IEEE Transactions on Geoscience and Remote Sensing, 23(2):84–90.

Rubin, Y. and Hubbard, S. 2005. *Hydrogeophysics*, volume 50 of *Water Science and Technology Library Series*. Springer, Dordrecht.

Ryu, D. and Famiglietti, J. S. 2005. Characterization of footprint-scale surface soil moisture variability using Gaussian and beta distribution functions during the Southern Great Plains 1997 (SGP97) hydrology experiment. Water Resources Research, 41(12):13.

Saatchi, S. S., Le Vine, D. M., and Lang, R. H. 1994. Microwave backscattering and emission model for grass canopies. IEEE Transactions on Geoscience and Remote Sensing, 32(1):177–186.

Sai, B. and Ligthart, L. P. 2004. GPR phase-based techniques for profiling rough surfaces and detecting small, low-contrast landmines under flat ground. IEEE Transactions on Geoscience and Remote Sensing, 42(2):318–326.

Saleh, K., Wigneron, J. P., Waldteufel, P., de Rosnay, P., Schwank, M., Calvet, J. C., and Kerr, Y. H. 2007. Estimates of surface soil moisture under grass covers using L-band radiometry. Remote Sensing of Environment, 109(1):42–53.

Samouelian, A., Cousin, I., Tabbagh, A., Bruand, A., and Richard, G. 2005. Electrical resistivity survey in soil science: a review. Soil Tillage Research, 83(2):173–193.

Sauer, T. J., Clothier, B. E., and Daniel, T. C. 1990. Surface measurements of the hydraulic-properties of a tilled and untilled soil. Soil Tillage Research, 15(4):359–369.

Schmugge, T., Gloersen, P., Wilheit, T., and Geiger, F. 1974. Remote-sensing of soil-moisture with microwave radiometers. Journal of Geophysical Research, 79(2):317–323.

Schmugge, T. J., Kustas, W. P., Ritchie, J. C., Jackson, T. J., and Rango, A. 2002. Remote sensing in hydrology. Advances in Water Resources, 25(8-12):1367–1385.

Schneeberger, K., Schwank, M., Stamm, C., de Rosnay, P., Mätzler, C., and Flühler, H. 2004. Topsoil structure influencing soil water retrieval by microwave radiometry. Vadose Zone Journal, 3(4):1169–1179.

Schoups, G., Troch, P. A., and Verhoest, N. 1998. Soil moisture influences on the radar backscattering of sugar beet fields. Remote Sensing of Environment, 65(2):184–194.

Schwank, M. and Mätzler, C. 2006. Air-to-soil transition model. In *Thermal microwave radiation: Applications for remote sensing*, IET Electromagnetic Waves series 52, pages 287–301. The Institution of Engeneering and Technology, London.

Schwank, M., Stahli, M., Wydler, H., Leuenberger, J., Mätzler, C., and Flühler, H. 2004. Microwave L-band emission of freezing soil. IEEE Transactions on Geoscience and Remote Sensing, 42(6):1252–1261.

Schwank, M., Mätzler, C., Guglielmetti, M., and Flühler, H. 2005. L-band radiometer measurements of soil water under growing clover grass. IEEE Transactions on Geoscience and Remote Sensing, 43(10):2225–2237.

Schwank, M., Guglielmetti, M., Mätzler, C., and Flühler, H. 2008. Testing a new model for the L-band radiation of moist leaf litter. IEEE Transactions on Geoscience and Remote Sensing, 46(7):1982–1994.

Schwank, M., Völksch, I., Wigneron, J. P., Kerr, Y. H., Mialon, A., de Rosnay, P., and Mätzler, C. 2010a. Comparison of two bare-soil reflectivity models and validation with L-band radiometer measurements. IEEE Transactions on Geoscience and Remote Sensing, 48(1):325–337.

Schwank, M., Wiesmann, A., Werner, C., Mätzler, C., Weber, D., Murk, A., Völksch, I., and Wegmüller, U. 2010b. ELBARA II, an L-band radiometer system for soil moisture research. Sensors, 10(1):584–612.

Schwank, M., Wigneron, J. P., Lopez-Baeza, E., Völksch, I., Mätzler, C., and Kerr, Y. H. 2012. L-band radiative properties of vine vegetation at the MELBEX III SMOS cal/val site. IEEE Transactions on Geoscience and Remote Sensing, 50(5):1587–1601.

Schwen, A., Bodner, G., and Loiskandl, W. 2011a. Time-variable soil hydraulic properties in near-surface soil water simulations for different tillage methods. Agricultural Water Management, 99(1):42–50.

Schwen, A., Bodner, G., Scholl, P., Buchan, G. D., and Loiskandl, W. 2011b. Temporal dynamics of soil hydraulic properties and the water-conducting porosity under different tillage. Soil Tillage Research, 113(2):89–98.

Seneviratne, S. I., Luthi, D., Litschi, M., and Schar, C. 2006. Land-atmosphere coupling and climate change in Europe. Nature, 443(7108):205–209.

Seneviratne, S. I., Corti, T., Davin, E. L., Hirschi, M., Jaeger, E. B., Lehner, I., Orlowsky, B., and Teuling, A. J. 2010. Investigating soil moisture-climate interactions in a changing climate: A review. Earth-Science Reviews, 99(3-4):125–161.

Serbin, G. and Or, D. 2005. Ground-penetrating radar measurement of crop and surface water content dynamics. Remote Sensing of Environment, 96(1):119–134.

Sherlock, M. D. and McDonnell, J. J. 2003. A new tool for hillslope hydrologists: spatially distributed groundwater level and soil water content measured using electromagnetic induction. Hydrological Processes, 17(10):1965–1977.

Shi, J. C., Chen, K. S., Li, Q., Jackson, T. J., O'Neill, P. E., and Tsang, L. 2002. A parameterized surface reflectivity model and estimation of bare-surface soil moisture with L-band radiometer. IEEE Transactions on Geoscience and Remote Sensing, 40(12):2674–2686.

Shi, J. C., Jackson, T., Tao, J., Du, J., Bindlish, R., Lu, L., and Chen, K. S. 2008. Microwave vegetation indices for short vegetation covers from satellite passive microwave sensor AMSR-E. Remote Sensing of Environment, 112(12):4285–4300.

Shi, J. C., Du, Y., Du, J. Y., Jiang, L. M., Chai, L. N., Mao, K. B., Xu, P., Ni, W. J., Xiong, C., Liu, Q., Liu, C. Z., Guo, P., Cui, Q., Li, Y. Q., Chen, J., Wang, A. Q., Luo, H. J., and Wang, Y. H. 2012. Progresses on microwave remote sensing of land surface parameters. Science China-Earth Sciences, 55(7):1052–1078.

Shrestha, B. L., Wood, H. C., and Sokhansanj, S. 2005. Prediction of moisture content of alfalfa using density-independent functions of microwave dielectric properties. Measurement Science and Technology, 16(5):1179–1185.

Shrestha, B. L., Wood, H. C., and Sokhansanj, S. 2007. Modeling of vegetation permittivity at microwave frequencies. IEEE Transactions on Geoscience and Remote Sensing, 45(2):342–348.

Siddique, M. R. B., Hamid, A., and Islam, M. S. 2000. Drought stress effects on water relations of wheat. Botanical Bulletin of Academia Sinica, 41(1):35–39.

Singh, D. 2006. Scatterometer performance with polarization discrimination ratio approach to retrieve crop soybean parameter at X-band. International Journal of Remote Sensing, 27(19):4101–4115.

Singh, D., Yamaguchi, Y., Yamada, H., and Singh, K. P. 2003. Retrieval of wheat chlorophyll by an X-band scatterometer. International Journal of Remote Sensing, 24(23):4939–4951.

Singh, V., Pallaghy, C., and Singh, D. 2006. Phosphorus nutrition and tolerance of cotton to water stress. I. Seed cotton yield and leaf morphology. Field Crop Science, 96:191–198.

Skriver, H., Svendsen, M. T., and Thomsen, A. G. 1999. Multitemporal C- and L-band polarimetric signatures of crops. IEEE Transactions on Geoscience and Remote Sensing, 37(5):2413–2429.

Skriver, H., Mattia, F., Satalino, G., Balenzano, A., Pauwels, V. R. N., Verhoest, N. E. C., and Davidson, M. 2011. Crop classification using short-revisit multitemporal SAR data. IEEE Journal of Selected Topics in Applied Earth Observations and Remote Sensing, 4(2):423–431.

Slob, E., Sato, M., and Olhoeft, G. 2010. Surface and borehole ground-penetrating-radar developments. Geophysics, 75(5):A103–A120.

Slob, E. C. and Fokkema, J. 2002. Coupling effects of two electric dipoles on an interface. Radio Science, 37(5):1073, doi:1010.1029/2001RS002529.

Smara, Y., Belhadj-Aissa, A., Sansal, B., Lichtenegger, J., and Bouzenoune, A. 1998. Multisource ERS-1 and optical data for vegetal cover assessment and monitoring in a semi-arid region of Algeria. International Journal of Remote Sensing, 19(18):3551–3568.

Soldovieri, F., Hugenschmidt, J., Persico, R., and Leone, G. 2007. A linear inverse scattering algorithm for realistic GPR applications. Near Surface Geophysics, 5(1):29–41.

Song, Y., Birch, C., and Hanan, J. 2008. Analysis of maize canopy development under water stress and incorporation into the ADEL-Maize model. Functional Plant Biology, 35:925–935.

Steelman, C. M. and Endres, A. L. 2010. An examination of direct ground wave soil moisture monitoring over an annual cycle of soil conditions. Water Resources Research, 46:16.

Stiles, J. M. and Sarabandi, K. 2000. Electromagnetic scattering from grassland Part I: A fully phase-coherent scattering model. IEEE Transactions on Geoscience and Remote Sensing, 38(1):339–348.

Strudley, M. W., Green, T. R., and Ascough, J. C. 2008. Tillage effects on soil hydraulic properties in space and time: State of the science. Soil Tillage Research, 99(1):4–48.

Svoray, T. and Shoshany, M. 2002. SAR-based estimation of areal aboveground biomass (AAB) of herbaceous vegetation in the semi-arid zone: a modification of the water-cloud model. International Journal of Remote Sensing, 23(19):4089–4100.

Taconet, O., Benallegue, M., Vidalmadjar, D., Prevot, L., Dechambre, M., and Normand, M. 1994. Estimation of soil and crop parameters for wheat from airborne radar backscattering data in C-bands and X-bands. Remote Sensing of Environment, 50(3):287–294.

Tan, C. S., Drury, C. F., Gaynor, J. D., Welacky, T. W., and Reynolds, W. D. 2002. Effect of tillage and water table control on evapotranspiration, surface runoff, tile drainage and soil water content under maize on a clay loam soil. Agricultural Water Management, 54(3):173–188.

Texier, S., Pamukcu, S., and Toulouse, J. 2005. Advances in subsurface water-content measurement with a distributed Brillouin scattering fibre-optic sensor. 17th International Conference on Optical Fibre Sensors, Pts 1 and 2, 5855:555–558.

Topp, G., Davis, J. L., and Annan, A. P. 1980. Electromagnetic determination of soil water content: Measurements in coaxial transmission lines. Water Resources Research, 16:574–582.

Topp, G. C., Davis, J. L., and Annan, A. P. 2003. The early development of TDR for soil measurements. Vadose Zone Journal, 2(4):492–499.

Touré, A., Thomson, K. P. B., Edwards, G., Brown, R. J., and Brisco, B. G. 1994. Adaptation of the mimics backscattering model to the agricultural context - Wheat and canola at L and C bands. IEEE Transactions on Geoscience and Remote Sensing, 32(1):47–61.

Tramblay, Y., Bouvier, C., Martin, C., Didon-Lescot, J. F., Todorovik, D., and Domergue, J. M. 2010. Assessment of initial soil moisture conditions for event-based rainfall-runoff modelling. Journal of Hydrology, 387(3-4):176–187.

Turner, N. C. 1974. Stomatal behavior and water status of maize, sorghum, and tobacco under field conditions. 2. Low soil-water potential. Plant Physiology, 53(3):360–365.

Ulaby, F. T. and Batlivala, P. P. 1976. Diurnal-variations of radar backscatter from a vegetation canopy. IEEE Transactions on Antennas and Propagation, 24(1):11–17.

Ulaby, F. T. and Bush, T. F. 1976a. Corn growth as monitored by radar. IEEE Transactions on Antennas and Propagation, 24(6):819–828.

Ulaby, F. T. and Bush, T. F. 1976b. Monitoring wheat growth with radar. Photogrammetric Engineering and Remote Sensing, 42(4):557–568.

Ulaby, F. T. and Elrayes, M. A. 1987. Microwave dielectric spectrum of vegetation. 2. Dual-dispersion model. IEEE Transactions on Geoscience and Remote Sensing, 25(5):550–557.

Ulaby, F. T. and Jedlicka, R. P. 1984. Microwave dielectric-properties of plant materials. IEEE Transactions on Geoscience and Remote Sensing, 22(4):406–415.

Ulaby, F. T. and Wilson, E. A. 1985. Microwave attenuation properties of vegetation canopies. IEEE Transactions on Geoscience and Remote Sensing, 23(5):746–753.

Ulaby, F. T., Moore, M. K., and Fung, A. K. 1981. *Microwave remote sensing: active and passive*, volume Vol. I: Fundamentals and radiometry. Addison Wesley, Boston, MA.

Ulaby, F. T., Aslam, A., and Dobson, M. C. 1982a. Effects of vegetation cover on the radar sensitivity to soil-moisture. IEEE Transactions on Geoscience and Remote Sensing, 20(4):476–481.

Ulaby, F. T., Moore, M. K., and Fung, A. K. 1982b. *Microwave remote sensing: active and passive*, volume Vol. II: Radar remote sensing and surface scattering and emission theory. Artech House, Boston, MA.

Ulaby, F. T., Moore, M. K., and Fung, A. K. 1986. *Microwave remote sensing: active and passive*, volume Vol. III: From theory to applications. Artech House, Norwood, MA.

Ulaby, F. T., Sarabandi, K., Mcdonald, K., Whitt, M., and Dobson, M. C. 1990. Michigan microwave canopy scattering model. International Journal of Remote Sensing, 11(7):1223–1253.

Van de Griend, A. A. and Wigneron, J. P. 2004. The b-factor as a function of frequency and canopy type at h-polarization. IEEE Transactions on Geoscience and Remote Sensing, 42(4):786–794.

van der Kruk, J., Vereecken, H., Diamanti, N., and Giannopoulos, A. 2010. Influence of interface roughness and heterogeneities on the waveguide inversion of dispersive GPR data. In *13th International Conference on Ground Penetrating Radar (GPR 2010)*. IEEE, Lecce, Italy.

van Genuchten, M. T. 1980. A closed-form equation for predicting the hydraulic conductivity of unsaturated soils. Soil Science Society of America Journal, 44:892–898.

van Overmeeren, R. A., Sariowan, S. V., and Gehrels, J. C. 1997. Ground penetrating radar for determining volumetric soil water content: results of comparative measurements at two test sites. Journal of Hydrology, 197:316–338.

Vereecken, H., Kamai, T., Harter, T., Kasteel, R., Hopmans, J., and Vanderborght, J. 2007. Explaining soil moisture variability as a function of mean soil moisture: A stochastic unsaturated flow perspective. Geophysical Research Letters, 34(22):6.

Vereecken, H., Huisman, J. A., Bogena, H., Vanderborght, J., Vrugt, J. A., and Hopmans, J. W. 2008. On the value of soil moisture measurements in vadose zone hydrology: A review. Water Resources Research, 44:21.

Vereecken, H., Weynants, M., Javaux, M., Pachepsky, Y., Schaap, M. G., and van Genuchten, M. T. 2010. Using pedotransfer functions to estimate the van Genuchten-Mualem soil hydraulic properties: A review. Vadose Zone Journal, 9(4):795–820.

Verhoest, N. E. C., Lievens, H., Wagner, W., Alvarez-Mozos, J., Moran, M. S., and Mattia, F. 2008. On the soil roughness parameterization problem in soil moisture retrieval of bare surfaces from synthetic aperture radar. Sensors, 8(7):4213–4248.

Vescovi, F. D. and Gomarasca, M. A. 1999. Integration of optical and microwave remote sensing data for agricultural land use classification. Environmental Monitoring and Assessment, 58(2):133–149.

Völksch, I. 2011. *Ground-based remote sensing of land surfaces - The influence of periodic patterns and relief on thermal microwave emission*. Ph.D. thesis, University of Bern, Switzerland.

Völksch, I., Schwank, M., and Mätzler, C. 2011. L-Band reflectivity of a furrowed soil surface. IEEE Transactions on Geoscience and Remote Sensing, 49(6):1957–1966.

Voronovich, A. G. 1985. Small-slope approximation in wave scattering by rough surfaces. Soviet Phys-JETP, 62:65–70.

Wagner, W., Bloschl, G., Pampaloni, P., Calvet, J. C., Bizzarri, B., Wigneron, J. P., and Kerr, Y. 2007. Operational readiness of microwave remote sensing of soil moisture for hydrologic applications. Nordic Hydrology, 38(1):1–20.

Walker, J. P., Willgoose, G. R., and Kalma, J. D. 2002. Three-dimensional soil moisture profile retrieval by assimilation of near-surface measurements: Simplified Kalman filter covariance forecasting and field application. Water Resources Research, 38(12):13.

Wang, J. R. and Choudhury, B. J. 1981. Remote-sensing of soil-moisture content over bare field at 1.4 GHz frequency. Journal of Geophysical Research, 86(NC6):5277–5282.

Wegmüller, U. 1993. Signature research for crop classification by active and passive microwaves. International Journal of Remote Sensing, 14(5):871–883.

Weihermüller, L., Huisman, J. A., Lambot, S., Herbst, M., and Vereecken, H. 2007. Mapping the spatial variation of soil water content at the field scale with different ground penetrating radar techniques. Journal of Hydrology, 340:205–216.

Weiss, M., Troufleau, D., Baret, F., Chauki, H., Prevot, L., Olioso, A., Bruguier, N., and Brisson, N. 2001. Coupling canopy functioning and radiative transfer models for remote sensing data assimilation. Agricultural and Forest Meteorology, 108(2):113–128.

Westermann, S., Wollschläger, U., and Boike, J. 2010. Monitoring of active layer dynamics at a permafrost site on Svalbard using multi-channel ground-penetrating radar. Cryosphere, 4(4):475–487.

Western, A. W., Grayson, R. B., and Bloschl, G. 2002. Scaling of soil moisture: A hydrologic perspective. Annual Review of Earth and Planetary Sciences, 30:149–180.

Wigneron, J. P., Kerr, Y., Chanzy, A., and Jin, Y. Q. 1993. Inversion of surface parameters from passive microwave measurements over a soybean field. Remote Sensing of Environment, 46(1):61–72.

Wigneron, J. P., Chanzy, A., Calvet, J. C., and Bruguier, W. 1995. A simple algorithm to retrieve soil-moisture and vegetation biomass using passive microwave measurements over crop fields. Remote Sensing of Environment, 51(3):331–341.

Wigneron, J. P., Ferrazzoli, P., Calvet, J. C., Kerr, Y., and Bertuzzi, P. 1999. A parametric study on passive and active microwave observations over a soybean crop. IEEE Transactions on Geoscience and Remote Sensing, 37(6):2728–2733.

Wigneron, J. P., Laguerre, L., and Kerr, Y. H. 2001. A simple parameterization of the L-band microwave emission from rough agricultural soils. IEEE Transactions on Geoscience and Remote Sensing, 39(8):1697–1707.

Wigneron, J. P., Fouilhoux, M., Prevot, L., Chanzy, A., Olioso, A., Baghdadi, N., and King, C. 2002. Monitoring sunflower crop development from C-band radar observations. Agronomie, 22(6):587–595.

Wigneron, J. P., Calvet, J. C., Pellarin, T., Van de Griend, A. A., Berger, M., and Ferrazzoli, P. 2003. Retrieving near-surface soil moisture from microwave radiometric observations: current status and future plans. Remote Sensing of Environment, 85(4):489–506.

Wigneron, J. P., Parde, M., Waldteufel, P., Chanzy, A., Kerr, Y., Schmidl, S., and Skou, N. 2004. Characterizing the dependence of vegetation model parameters on crop structure, incidence angle, and polarization at L-band. IEEE Transactions on Geoscience and Remote Sensing, 42(2):416–425.

Wigneron, J. P., Kerr, Y., Waldteufel, P., Saleh, K., Escorihuela, M. J., Richaume, P., Ferrazzoli, P., de Rosnay, P., Gurney, R., Calvet, J. C., Grant, J. P., Guglielmetti, M., Hornbuckle, B., Mätzler, C., Pellarin, T., and Schwank, M. 2007. L-band Microwave Emission of the Biosphere (L-MEB) Model: Description and calibration against experimental data sets over crop fields. Remote Sensing of Environment, 107(4):639–655.

Wollschläger, U., Gerhards, H., Yu, Q., and Roth, K. 2010. Multi-channel ground-penetrating radar to explore spatial variations in thaw depth and moisture content in the active layer of a permafrost site. Cryosphere, 4(3):269–283.

Wu, L. K., Moore, R. K., and Zoughi, R. 1985a. Sources of scattering from vegetation canopies at 10 GHz. IEEE Transactions on Geoscience and Remote Sensing, 23(5):737–745.

Wu, L. K., Moore, R. K., Zoughi, R., Aftfi, A., and Ulaby, F. T. 1985b. Preliminary results on the determination of the sources of scattering from vegetation canopies at 10 GHz. International Journal of Remote Sensing, 6(2):299–313.

Yao, T., Wierenga, P. J., Graham, A. R., and Neuman, S. P. 2004. Neutron probe calibration in a vertically stratified vadose zone. Vadose Zone Journal, 3(4):1400–1406.

Yarovoy, A. G., Vazouras, C. N., Fikioris, J. G., and Ligthart, L. P. 2004. Numerical simulations of the scattered field near a statistically rough air-ground interface. IEEE Transactions on Antennas and Propagation, 52:780–789.

Zhan, X. W., Houser, P. R., Walker, J. P., and Crow, W. T. 2006. A method for retrieving high-resolution surface soil moisture from hydros L-band radiometer and radar observations. IEEE Transactions on Geoscience and Remote Sensing, 44(6):1534–1544.

Zhang, S. L., Li, P. R., Yang, X. Y., Wang, Z. H., and Chen, X. P. 2011. Effects of tillage and plastic mulch on soil water, growth and yield of spring-sown maize. Soil Tillage Research, 112(1):92–97.

Zreda, M., Desilets, D., Ferre, T. P. A., and Scott, R. L. 2008. Measuring soil moisture content non-invasively at intermediate spatial scale using cosmic-ray neutrons. Geophysical Research Letters, 35(21):5.

Zribi, M., Taconet, O., Le Hégarat-Mascle, S., VidalMadjar, D., Emblanch, C., Loumagne, C., and Normand, M. 1997. Backscattering behavior and simulation comparison over bare soils using SIR-C/X-SAR and ERASME 1994 data over Orgeval. Remote Sensing of Environment, 59(2):256–266.

# Appendices

# Publications and conferences

## Publications in international peer-reviewed journals

- Jonard M., André F., Jonard F., Mouton N., Procès P., and Ponette Q. **2007**. Soil carbon dioxide efflux in pure and mixed stands of oak and beech, *Annals of Forest Science*, 64, 1-9.
- André F., Jonard M., Jonard F., and Ponette, Q. **2011**. Spatial and temporal patterns of throughfall volume in a deciduous mixed-species stand, *Journal of Hydrology*, 400, 244-254.
- Jonard F., Weihermüller L., Jadoon K.Z., Schwank M., Vereecken H., and Lambot S. **2011**. Mapping field-scale soil moisture with L-band radiometer and ground-penetrating radar over bare soil, *IEEE Transactions on Geoscience and Remote Sensing*, 49(8), 2863-2875.
- Jonard F., André F., Ponette Q., Vincke C. and Jonard M. **2011**. Sap flux density and stomatal conductance of European beech and common oak trees in pure and mixed stands during the summer drought of 2003, *Journal of Hydrology*, 409, 371-381.
- Jonard F., Weihermüller L., Vereecken H., and Lambot S. **2012**. Accounting for soil surface roughness in the inversion of ultrawideband off-ground GPR signal for soil moisture retrieval, *Geophysics*, 77(1), H1-H7.
- Vereecken H., Weihermüller L., Jonard F., and Montzka C. **2012**. Characterization of crop canopies and water stress related phenomena using microwave remote sensing methods: A review, *Vadose Zone Journal*, 11(2). DOI: 10.2136/vzj2011.0138ra.
- Montzka C., Bogena H., Weihermüller L., Jonard F., Bouzinac C., Kainulainen J., Balling J. E., Löw A., Dall'Amico J., Rouhe E., Vanderborght J., and Vereecken H. **2012**. Brightness temperature and soil moisture validation at different scales during the SMOS Validation Campaign in the Rur and Erft catchments, Germany, *IEEE Transactions on Geoscience and Remote Sensing*, in press. DOI: 10.1109/TGRS.2012.2206031.

- Jonard, F., Mahmoudzadeh, M., Roisin, C., Weihermüller, L., André, F., Minet, J., Vereecken, H., and Lambot, S. **2012**. Characterization of tillage effects on the spatial variation of soil properties using ground-penetrating radar and electromagnetic induction, *Geoderma*, under review.

- Dimitrov M., Kostov K. G., Jonard F., Jadoon K.Z., Schwank M., Weihermüller L., Hermes N., Vanderborght J., and Vereecken H. New improved algorithm for sky calibration of L-band radiometers JÜLBARA and ELBARA II, *IEEE Transactions on Geoscience and Remote Sensing*, to be submitted.

## Book chapter

- Minet J., Jadoon K.Z., Jonard F., Mahmoudzadeh M.R., Tran P.A. and Lambot S. **2012**. Advanced ground-penetrating radar for soil moisture retrieval, in: Multiscale Hydrologic Remote Sensing: Perspectives and Applications, CRC Press.

## International conferences and workshops

- Jonard F., Schwank M., Weihermüller L., Vereecken H., and Lambot S. Mapping field scale soil moisture with L-band radiometer and off-ground GPR over a rough surface, *2010 11th Specialist Meeting on Microwave Radiometry and Remote Sensing of the Environment (MicroRad)*, Washington, DC, USA, March 2010.

- Jonard F., Weihermüller L., Jadoon K.Z., Schwank M., Vereecken H., and Lambot S. Mapping soil moisture of a bare soil using L-band radiometer and advanced GPR, *Geophysical Research Abstracts, Vol. 12, EGU2010-836-6, EGU General Assembly*, Vienna, Austria, May 2010.

- Jonard F., Weihermüller L., Vereecken H., and Lambot S. Mapping field scale soil moisture with L-band radiometer and ground penetrating radar, *ESA, iLEAPS, EGU joint Conference-Topical Conference Earth Observation for Land-Atmosphere Interaction Science*, ESA-ESRIN, Frascati, Italy, November 2010.

- Montzka C., Bogena H., Weihermüller L., Jonard F., Dimitrov M., Bouzinac C., Kainulainen J., Balling J. E., Rouhe E., Vanderborght J., and Vereecken H. Analyses of brightness temperatures on different spatial scales during the SMOS validation campaign in the Rur catchment, Germany, *SMOS Validation and Retrieval Team Workshop*, ESA-ESRIN, Frascati, Italy, November 2010.

- Jonard F., Montzka C., Bogena H., Hasan S., and Vereecken H. SMAP validation activities of the Agropshere Institute in the Rur catchment,

Germany, *SMAP Cal/Val Workshop*, Oxnard, California, USA, May 2011.

- Jonard F., Weihermüller L., Schwank M., Vereecken H., and Lambot S. Soil moisture retrieval using L-band radiometer and ground-penetrating radar, *2011 IEEE International Geoscience and Remote Sensing Symposium (IGARSS) – Proceedings*, Vancouver, Canada, July 2011, pp. 3093-3096.

- Montzka C., Bogena H., Weihermüller L., Jonard F., Dimitrov M., Bouzinac C., Kainulainen J., Balling J. E., Vanderborght J., and Vereecken H. Radiobrightness validation on different spatial scales during the SMOS validation campaign 2010 in the Rur catchment, Germany, *2011 IEEE International Geoscience and Remote Sensing Symposium (IGARSS) – Proceedings*, Vancouver, Canada, July 2011, pp. 3760-3763.

- Jonard F., Montzka C., Weihermüller, L., and Vereecken H. Ground-based radiometer activities at the Agropshere Institute, *ELBARA II Workshop for data processing and quality control*, ESA-ESTEC, Noordwijk, The Netherlands, November 2011.

- Jonard F., Mahmoudzadeh M.R., Roisin C., Weihermüller L., André F., M., Vereecken H., and Lambot S. Using geophysical techniques to characterize tillage effect on soil properties, *PhD Student Day of the Graduate Schools ENVITAM and GEPROC*, Gembloux, Belgium, February 2012 (2nd Price - Best Poster Award).

- Dimitrov M., Kostov K. G., Jonard F., Jadoon K.Z., Schwank M., Weihermüller L., Hermes N., Vanderborght J., and Vereecken H. New improved algorithm for sky calibration of L-band radiometers JÜLBARA and ELBARA II, *2012 12th Specialist Meeting on Microwave Radiometry and Remote Sensing of the Environment (MicroRad) – Proceedings*, Villa Mondragone, Italy, March 2012.

- Jonard F., Weihermüller L., Jadoon K.Z., Schwank M., Vereecken H., and Lambot S. Estimating soil hydraulic properties using passive and active microwave data, *2012 12th Specialist Meeting on Microwave Radiometry and Remote Sensing of the Environment (MicroRad)*, Villa Mondragone, Italy, March 2012.

- Jonard F., Weihermüller L., Schwank M., Jadoon K.Z., Vereecken H., and Lambot S. Estimating soil hydraulic properties using L-band radiometer and ground-penetrating radar, *2012 IEEE International Geoscience and Remote Sensing Symposium (IGARSS) – Proceedings*, Munich, Germany, July 2012.

- Vereecken H., Bogena H., Weuthen A., Rosenbaum U., Huisman J.A., van der Kruk J., Hendricks Franssen H.-J., Montzka C., Jonard F., and Vanderborght J. Soil water content and hydrological fluxes in terrestrial systems: from measurement to prediction, *2nd International Conference on Hydropedology*, Leipzig, Germany, July 2012.

# About the author

François Jonard was born in Uccle, Belgium, on 20 August 1979. In 2002, he earned an M.Sc. degree in environmental engineering, with a specialization in water and forestry, at the Faculty of Biological, Agricultural and Environmental Engineering of the Université catholique de Louvain (UCL, Belgium). During his Master's degree, he participated in a six-month study exchange at the Faculty of Forestry, University of Moncton (UMCE, Canada). He wrote his Master thesis on the characterization of ammonium retention in forest soils (Belgian Ardennes) under the supervision of Prof. Bruno Delvaux (UCL).

From 2003 to 2004, he worked at the Earth and Life Institute (UCL) as a research assistant on forest hydrology modeling. In 2005, he earned a Master's degree in business administration at the Louvain School of Management (UCL). From 2006 to 2009, he was a Consultant with the European Commission in the fields of geographic information systems (GIS) and remote sensing applied to environmental issues.

In 2009, François Jonard obtained a three-year PhD grant from Forschungszentrum Jülich (FZJ, Germany) funded by the German Research Foundation (DFG) through Transregional Collaborative Research Centre 32. He started his PhD research programme at the Institute of Bio- and Geosciences – Agrosphere (FZJ), under the supervision of Prof. Sébastien Lambot. In his PhD project, he aimed to develop and apply inverse and forward modeling approaches for soil water content retrieval based on ground-penetrating radar and microwave radiometry. During his PhD research, he spent three months at NASA's Goddard Space Flight Center (GSFC, USA), working in the context of the NASA's upcoming Soil Moisture Active and Passive (SMAP) mission. In addition to his research, he gave lectures in GIS and remote sensing for students enrolled in the Bachelor's programme in agronomy at the Haute Ecole de la Province de Liège (HEPL, Belgium).

# Summary

Soil water content is widely recognized as a key component of the water, energy and carbon cycles and knowledge of its spatiotemporal distribution is in particular needed for developing optimal and sustainable environmental and agricultural management strategies. In that context, we analyzed and further developed advanced ground-penetrating radar (GPR) and microwave radiometry techniques for high-resolution mapping and monitoring of shallow soil water content at the field scale.

First, far-field ultra-wideband GPR and L-band radiometer were used for mapping soil water content over two test sites with bare soils and the results were compared to reference ground truths. For GPR, soil water content was derived from full-wave inversion focusing on the surface reflection while for radiometer a radiative transfer model was used. Both techniques provided relatively good results, especially for reconstructing spatial moisture patterns in relation to topography and forced conditions (differential irrigation and soil tilth). Nevertheless, absolute estimates were subject to inherent discrepancies that were attributed to the different characterization scales and local variability.

Second, we addressed the roughness modeling problem. For GPR, we combined the full-wave GPR model with a roughness model derived from the Kirchhoff scattering theory. Laboratory experiments showed that this approach performs well for roughness amplitudes reaching up to one fourth the wavelength. For the radiometer, we used an empirical equation which requires calibrating ground truths. This approach was successfully validated in field conditions.

Finally, GPR and radiometer measurements were performed over a sand box subject to hydrostatic equilibrium with a range of water table depths. For each technique, all measurements were aggregated in an inversion scheme to reconstruct the vertical water content profiles, which were constrained using the van Genuchten water retention equation. The results were in close agreement with reference time-domain reflectometry measurements.

Our results open promising research and application perspectives for the joint use of active and passive microwave remote sensing for soil moisture retrieval. In that respect, we addressed new avenues for characterizing crop canopies and water-stress related phenomena.

*Born in Uccle, Belgium, on 20 August 1979, François Jonard holds an M.Sc. degree in environmental engineering from the Université catholique de Louvain. He pursued his doctoral research at Forschungszentrum Jülich, Germany, in the framework of a research project funded by the German Research Foundation (DFG).*